Hydro-elastic response of ship structures to slamming induced whipping

Proefschrift

ter verkrijging van de graad van doctor
aan de Technische Universtiteit Delft,
op gezag van de Rector Magnificus prof.ir. K.C.A.M. Luyben,
voorzitter van het College van Promoties,
in het openbaar te verdedigen op 23 februari 2010 om 15:00 uur
door

Johannes Tewes TUITMAN

maritiem ingenieur,
geboren te Rotterdam.

Dit proefschrift is goedgekeurd door de promotor:

Prof.dr.ir. R.H.M. Huijsmans

Samenstelling promotiecommissie:

Rector Magnificus	voorzitter
Prof.dr.ir. R.H.M. Huijsmans	Technische Universiteit Delft, promotor
Prof.dr.ir. R. Benedictus	Technische Universiteit Delft
Prof.dr.ir. H. Bijl	Technische Universiteit Delft
Prof.dr. O.M. Faltinsen	Norwegian University of Science and Technology
Prof.dr. P. Temarel	University of Southampton
dr. Š Malenica	Bureau Veritas
dr.ir. M. Kaminski	MARIN
Prof.dr.ir. J.A. Pinkster	Technische Universiteit Delft, reservelid

keywords: slamming, whipping, structrual response, seakeeping

ISBN 978-90-9025031-1

The research reported in this thesis has been supported by TNO and has been partly funded by the Ministry of Defence of the Netherlands.

Summary

Hydro-elastic response of ship structures to slamming induced whipping

by Johan Tuitman

Slamming induced whipping can significantly increase the structural loading of ships. Although this is well-known, the whipping contribution to the structural loading is rarely taken into account when computing the structural loading. An exception are the "dynamic loading" factors found in Classification Societies rules. Currently there are no commercial tools available to compute the seakeeping response including slamming induced whipping. This is the main reason for not accounting for the effects of whipping. Extensive research has been done on the subject of slamming impact and whipping response but an integral and computationally efficient method is not yet available for ship structure designers.

This is the starting point for this research presented in this thesis. The objective of this thesis is: "*The development of a practical method to calculate the global and local response of the ship structure due to the seakeeping loading including the slamming loading. This method should contain the full hydro-elastic coupling.*" This method is developed by combining well-known components and new tools.

The concept of generalised modes is used to solve the hydro-elastic seakeeping problem. All degrees of freedom of the ship structure are described by mode shapes using this approach, even the rigid-body modes. The number of degrees of freedom may be arbitrary selected by the user. The flexible mode shapes of the structure are obtained from either a 3D-FEM analysis or a 1D-FEM analysis using a beam model of the ship structure. The seakeeping response of all modes, rigid and flexible, is solved simultaneously which ensures a full account for the hydro-elastic coupling.

The seakeeping response is solved in the time domain using a 3D surface integration method. The time domain allows one to include non-linear load components and to calculate the transient response with relative ease. The non-

linear Froude-Krylov and non-linear hydrostatic loads are taken into account to improve the seakeeping and internal load predictions. The diffraction and radiation loads are kept linear to allow for reasonably fast computations. The linear diffraction and radiation coefficients are solved in the frequency domain using a 3D boundary element method. This hydro-elastic approach allows one to compute the transient whipping response. The springing response can only be partially predicted because springing is often caused by additional non-linear load components which are not included in the presented theory.

Since fast and robust, non-empirical 3D methods are not yet available for the calculation of the slamming loads, the slamming loads are solved using 2D methods. The first of the two used methods is the Generalised Wagner Model (GWM). This is the most accurate of the two methods. The second method is the Modified Logvinovich Model (MLM) which is much faster compared to the GWM. The drawback of using these 2D methods is that the slamming loading can only be computed accurately for head seas and near head sea conditions. The computation of the slamming loads is directly integrated into the time domain seakeeping calculation. At every time step the slamming loads are computed based on the actual relative motions, and the computed slamming loads are taken into account for the solution of the resulting motions.

Insight into the global response of the ship structure is obtained by using the modal approach for computing the seakeeping response. However, it is difficult to compute the local structural response of a ship structure using the modal method. Therefore, the local structural response is computed by transferring the seakeeping loads to the 3D-FEM model of the structure and solving the response using the FEM method. The method used ensures that the hydrodynamic loads at the structural model are well balanced by the applied nodal acceleration loads, thus ensuring a consistent FEM solution. These nodal acceleration loads allow one to include the effect of whipping even when a quasi-static FEM approach is used.

The developed methodology is verified and validated using different ships, results of model experiments and the results of one full-scale sea trial. All verifications show that the developed approach gives the expected results and that the presented theory is consistent. The slamming forces are verified using model experiments of a container ship and an aluminium model. This validation shows that it is necessary to take into account the static bow wave generated by the blunt bow of the container ship when computing the slamming loads to a reasonable accuracy. The validations using experiments with the aluminium model show that the contribution of the added mass on the natural frequency is well predicted, even for conditions with forward speed. The calculated slamming loads and resulting whipping response compare well with the experimental results of the aluminium model. Stresses measured during a sea trial of the M-Frigate of the Royal Netherlands Navy are also used to validate the developed methodology. The computed spectral energy of the wave frequency and the

whipping response are close to the spectra measured. The Weibull fits of the extremes of the calculated and measured stresses shows very good agreement, the hog/sag ratio is also well predicted. The stresses are slightly overpredicted for the highest speed.

Two ultra large container ships are used for a case study. Design values such as the expected ultimate bending moment and fatigue loading are calculated based on the computed bending moment or stress history. It is shown that the seakeeping response should be calculated for at least 750 wave encounters in order to accurately compute the design values. The developed seakeeping method is fast and robust enough to compute the design values for all cells of a scatter diagram. The expected ultimate bending moment and fatigue damage are calculated based on a life-time of thirty years with both North Atlantic and World wide scatter diagrams. It is shown that the slamming induced whipping and the computed springing response reduce the predicted fatigue lifetime by about forty percent and increase the expected ultimate bending moment by about twenty percent. This shows the importance of accounting for these effects when computing the design values for such flexible ships.

It can be concluded that a practical method to calculate the global and local response of the ship structure due to the seakeeping loading including the slamming loading and whipping has been developed. It is shown that the developed method can be applied to calculate the design values for a complete scatter diagram. The validations shows that the predictions are reasonably accurate.

Samenvatting

Hydro-elastische responsie van scheepsconstructies door slamming geïndiceerde whipping
(Hydro-elastic response of ship structures to slamming induced whipping)

door Johan Tuitman

Whipping responsie ten gevolge van slammingsimpact, ook wel paaltjes pikken genoemd, kan de belasting van scheepsconstructies aanzienlijk vergroten. Hoewel dit algemeen bekend is, wordt de door slamming geïndiceerde whipping bijna nooit meegenomen tijdens het berekenen van de structurele belasting, behalve dan middels de "dynamische belasting" factoren die de regels van de klassebureaus voorschrijven. De belangrijkste reden om de slammingsimpact en whipping responsie niet te berekenen is dat commerciële beschikbare programma's voor zeegangsberekening dit niet kunnen. Er is uitgebreid onderzoek gedaan op het gebied van slammingsbelasting en whipping responsie maar er is nog geen integrale methode beschikbaar die efficiënte berekeningen toelaat voor de ontwerper van scheepsconstructies.

Het doel van het onderzoek dat in dit proefschrift is beschreven is "*Het ontwikkelen van een praktische methode voor het berekenen van de globale en locale responsie van scheepsconstructies door zeegangsbelasting waar ook slamming belasting voorkomt. De methode moet de volle hydro-elastische koppeling bevatten.*". Deze methode is ontwikkeld door het combineren van verschillende bekende componenten en een aantal nieuwe componenten.

Het concept van gegeneraliseerde vrijheidsgraden wordt gebruikt om het hydro-elastische zeegangsprobleem op te lossen. Volgens dit concept worden alle vrijheidsgraden beschreven door trilvormen, zelfs de starre lichaamsbewegingen. Het aantal vrijheidsgraden kan arbitrair door de gebruiker gekozen worden. De flexibele trilvormen worden verkregen van een berekening met de Eindige Elementen Methode (EEM) middels een 3D-model of een 1D-balk-model van de scheepsconstructies. De zeegangsresponsie van alle vrijheidsgraden, flexibel en star, wordt gelijktijdig opgelost zodat een volle hydro-elastische koppeling

wordt verkregen.

De zeegangsresponsie wordt berekend in het tijddomein gebruikmakend van een 3D-oppervlakte-integratiemethode. In de tijddomein kunnen de niet-lineaire belastingen en transiënte responsie relatief eenvoudig berekend worden. De Froude-Krylov en hydrostatische krachten worden niet-lineair berekend om de voorspelling van bewegingen en interne krachten te verbeteren. De diffractie en radiatiekrachten worden lineair berekend om de rekentijd beperkt te houden. De coëfficiënten voor de lineaire diffractie en radiatie krachten worden opgelost in het frequentiedomein met een 3D-boundary-elementen-methode. De hydro-elastische aanpak maakt het mogelijk om transiënte whipping te bepalen. De springing responsie kan maar gedeeltelijk bepaald worden omdat springing vaak veroorzaakt wordt door niet-lineaire belastingscomponenten welke niet in rekening worden gebracht in de gepresenteerde theorie.

Omdat hiervoor nog geen snelle, betrouwbare en niet-empirische 3D-methode beschikbaar is, worden 2D-methodes gebruikt voor het berekenen van slammingskrachten. De eerste van de twee gebruikte methodes is de Generalised Wagner Model (GWM). Deze methode is de meest nauwkeurige die gebruikt wordt. De andere is de Modified Logvinovich Model (MLM) welke veel sneller en iets stabieler is in vergelijking met de GWM methode. Het gebruik van deze 2D-methode heeft als nadeel dat slammingskrachten alleen voor kopgolven of bijna kopgolven nauwkeurig bepaald kunnen worden. De berekening van slammingskrachten is geïntegreerd in de zeegangsberekening. De slammingskrachten worden op elke tijdstap berekend op basis van de actuele relatieve snelheid en de slammingskrachten worden in rekening genomen bij het oplossen van de bewegingen.

De gebruikte modale aanpak voor de zeegangsberekening geeft inzicht in de globale responsie van de scheepsconstructies. Het is echter lastig om met de modale aanpak inzicht te krijgen in de lokale responsie van de constructie. De lokale responsie wordt daarom berekend door de zeegangskrachten over te zetten op het 3D-EEM-model van de constructie en vervolgens de responsie op te lossen met de EEM-methode. De gebruikte methode zorgt dat de zeegangskrachten gebalanceerd worden door de versnellingskrachten werkend in de knooppunten van het EEM-mesh. Dit zorgt dat de EEM oplossing consistent is. De knooppuntsversnellingskrachten zorgen dat de effecten van whipping worden meegenomen, zelfs bij het gebruiken van een quasi-statische EEM-oplossing.

De ontwikkelde methodiek is geverifieerd en gevalideerd met verschillende schepen, resultaten van modelproeven en het resultaat van één ware grootte meting. Alle verificaties laten zien dat de gebruikte aanpak de verwachte resultaten geeft en dat de gepresenteerde theorie consistent is. De slammingskrachten zijn gevalideerd met resultaten van de modelexperimenten met een containerschip en met een model van aluminium. Deze validatie met het containerschip laat zien dat het voor de volle boeg van het containership noodzakelijk is om rekening te houden met de statische boeggolf om de slam-

mingskrachten redelijk te voorspellen. De validatie met een aluminiummodel laat zien dat invloed van toegevoegde massa op de eigenfrequentie van het schip juist berekend wordt, zelfs met voorwaartse snelheid. Voor het aluminiummodel komen de berekende slammingbelasting en de geresulteerde whippingresponsie goed overeen met de experimentele resultaten. De spanning gemeten tijdens een ware grootte meting met het M-fregat van de Koninklijke Marine is ook gebruikt voor validatie van de ontwikkelde methodiek. De berekende spectrale energie voor de golffrequentie en whippingresponsie komen goed overeen met de gemeten spectra's. De Weibull fits van de extremen van de berekening en de metingen komen goed overeen, de hog/sag ratio wordt goed voorspeld. Voor de hoogste snelheid zijn de voorspelde spanningen wat hoger dan wat blijkt uit de metingen.

Twee zeer grote containerschepen zijn gebruikt voor casestudies. Ontwerpwaarden als het maximaal verwachte buigendmoment en de vermoeiingsschade worden berekend op basis van het berekend buigendmoment- of spanningshistorie. Het blijkt dat de signalen voor minstens 750 golfontmoetingen berekend moeten worden om de ontwerpwaarden nauwkeurig te kunnen berekenen. De ontwikkelde zeegangsberekeningsmethode is snel en betrouwbaar genoeg om de ontwerpwaarden voor alle cellen van een wave scatter diagram te berekenen. Het verwachte maximale buigendmoment en vermoeiingsschade is berekend voor een levensduur van dertig jaar gebruik makend van het Noord-Atlantisch en wereldwijd scatter diagram. Deze casestudies laten zien dat de slamming geïndiceerde whipping en springing de voorspelde vermoeiingslevensduur met ongeveer veertig procent reduceert en het maximaal verwachte buigendmoment met ongeveer twintig procent vergroot. Dit laat zien hoe belangrijk het is deze effecten mee te nemen voor berekeningen van de ontwerpwaarden voor zulke flexibele schepen.

Het kan geconcludeerd worden dat een praktische methode voor de berekening van de globale en lokale responsie van de scheepsconstructies door zeegangsbelasting met slammingbelasting ontwikkeld is. De ontwikkelde methode kan gebruikt worden voor het berekenen van de ontwerpwaarden voor een compleet scatterdiagram. De validatie laat zien dat voorspellingen redelijk accuraat zijn.

Contents

Nomenclature

Abbreviations

BEM Boundary Element method

BVP Boundary Value Problem

FE Finite Element

FEM Finite Element Method

FK Froude-Krylov

FPSO Floating Production Storage and Offloading

FRF Frequency Response Functions

GWM Generalised Wagner Model

MARIN Maritime Research Institute Netherlands

MEOB Former electronic and optic services of RNlN

MLM Modified Logvinovich Model

OSE Optimal State Estimation

RAO Response Amplitude Operator

RNlN Royal Netherlands Navy

SI Le Système International d'Unités

SN Stress-Number of cycles or Wöhler curve

SPH Smooth Particle Hydrodynamics

SWBM Still Water Bending Moment

VOF Volume of Fluid method

General notation

a	Scalar
$\vec{a}$	Vector
$\mathbf{a}$	Matrix
$\dot{a}$	First time derivative of a
$\ddot{a}$	Second time derivative of a
$a^\star$	Variable a is defined in the body reference frame
$a^\diamond$	Variable a is defined in the hydro reference frame
a	Variable a is defined in the Earth reference frame
$\vec{a}_{\mathbb{R}3}$	Vector defined for the three rigid-body translations or rotations
$\vec{a}_{\mathbb{R}6}$	Vector defined for the six rigid-body translations and rotations

Greek symbols

α	Deadrise angle
β_s	The β parameter of the SN-curve
ε	Phase angle
ζ	Wave elevation
ζ_a	Wave amplitude
ζ_{tot}	Total wave elevation
λ	Complex eigenvalue
μ	Heading angle of ship
$\vec{\xi}$	Modal displacement
$\vec{\xi}_a$	Response amplitude operator (RAO) for motions
$\vec{\xi}_r$	Rigid body rotation
ξ_r	Relative displacement
$\vec{\xi}_{sw}$	Still water displacements
$\vec{\xi}_t$	Rigid body translation

$\vec{\xi}_u$	Complex modal participations to the natural mode shapes
ρ	Density of the fluid
σ	Stress
Φ	Velocity potential in the fluid
φ	Space dependent part of the velocity potential in the fluid
$\bar{\varphi}$	Still water fluid flow potential
φ_D	Diffracted potential
φ_I	Incident potential
φ_R	Radiation potential
ω_e	Encounter frequency
ω_n	Modal frequency
ω_p	Angular peak frequency
ω	Frequency

Roman symbols

0	Origin of coordinate system
$\mathbf{A}$	Hydrodynamic added mass
A_{bz}	Effective shear area in z direction
a_n	Area of a panel
$\mathbf{B}$	Hydrodynamic damping
$\mathbf{C}_u$	User defined stiffness
$\mathbf{B}_u$	User defined damping
$\mathbf{c}_e$	Stiffness matrix for elastic modes
$\mathbf{c}_h$	Restoring by hydrostatics
$\mathbf{C}_m$	Gravity contribution to the hydrostatic restoring
$\mathbf{C}_{te}$	Stiffness matrix for all modes
D_f	Total fatigue damage

E	Elasticity modulus
$\mathcal{F}$	Fourier transform
$\vec{f}_{\text{beam}}$	Force by beam element(s)
$\vec{f}_{\text{cor}}$	Coriolis forces
$\vec{F}_D$	Diffraction force
$\vec{f}_{\text{diff}}$	Diffraction force
$\vec{f}_{\text{fkhs}}$	Froude-Krylov and hydrostatic force
$\vec{f}_{\text{grav}}$	Gravity force
$\vec{F}_I$	Incident wave force
$\vec{F}_{int}$	Internal loads
$\vec{f}_{\text{rad}}$	Frequency dependent part of radiation force
$\vec{f}_{\text{res}}$	Resulting force at section
$\vec{f}_{\text{sd}}$	Force by spring/damper element(s)
$\vec{f}_{\text{slam}}$	Slamming loading
$\vec{f}_{sw}$	Still water force vector
$\vec{f}_t$	Total force vector
$\vec{G}$	Location of the center of gravity
G	Shear modulus
g	Gravity acceleration
$\mathbf{h}$	Mode shapes
$\vec{H}$	Displacement
$H_{1/3}$	Significant wave height
$\mathbf{h}_e$	Elastic mode shapes
$\mathbf{h}_r$	Rigid body mode shapes
$\mathbf{h}_s$	Scaled mode shapes at slamming sections
$\vec{i}$	Unit vector in surge direction

ib	Body number
I_{by}	Moment of inertia of cross section
I_{bmy}	Mass moment of inertia of cross section
is	Section number
$\vec{j}$	Unit vector in sway direction
$\mathbf{K}$	Retardation or memory function
$\vec{k}$	Unit vector in heave direction
k	Wave number
K_s	The K parameter of the SN-curve
k_w	Weibull shape parameter
$\vec{l}$	Unit vector in roll direction
$\mathbf{m}$	Mass matrix
$\vec{m}$	Unit vector in pitch direction
M	Maximum moment
m	Mass
M_0	Mean value of bending moment
M_c	Weibull scale parameter
M_y	Bending moment
m_b	Mass per unit length
$\mathbf{m}_e$	Genuine mass matrix for elastic modes
$\mathbf{M}_i$	Mass matrix of point
$\vec{n}$	Normal
$\vec{n}$	Unit vector in yaw direction
Nc_i	Maximum umber of cycles within amplitude range i
nc_i	Number of cycles within amplitude range i
P	Probability

p	Pressure
p_D	Diffraction pressure
p_{fk}	Froude-Krylov pressure
p_{hs}	Hydrostatic pressure
p_I	Incident wave pressure
p_R	Radiation pressure
$\vec{r}_f$	Elastic contribution to deformation at point at body
$\vec{r}_p$	Location of point p
$\vec{r}_{p_r}$	Euler rotations at point p
$\mathbf{S}$	Matrix to distinguish between the mode shapes
S_b	Wetted surface
S_ζ	Spectral value of wave energy
t	Time
$\mathbf{T}_b$	Transformation matrix from the Earth frame to the body frame
$\mathbf{T}_{br}$	Transformation matrix from the Earth frame to the body frame for derivatives of Euler angles
$\mathbf{T}_e$	Transformation matrix from the body frame to the Earth frame
$\mathbf{T}_{er}$	Transformation matrix from the body frame to the Earth frame for derivatives of Euler angles
T_p	Peak period of wave
t_{return}	Return period of wave-train
$\mathbf{T}_s$	Transformation matrix from the slamming section frame to the body frame
U	Forward speed of body
V	Volume of the body
$\vec{W}$	Velocity vector of steady flow
x_w	Distance in the wave direction

Chapter 1

Introduction

Slamming is an impulsive hydrodynamic impact load, working on the ship structure, as the ship impacts with the waves. The ship structure can start to vibrate due to this slamming impact. Such transient vibration of the ship structure is called *whipping*. A measurement of a typical slamming induced whipping event is presented in Figure 1.1. This figure shows the measured stress at the weather deck during a full scale sea trial of the M-frigate of the Royal Netherlands Navy. The response of the ship structure to the non-impulsive wave loads is, in general, quasi-static. These are the low frequency (or wave frequency oscillations) in the stress shown in Figure 1.1. At time step 1357 [s], the ship undergoes a slamming impact. As can be noted, the ship structure starts to vibrate due to this impact resulting in high frequency oscillations in the stress signal.

The whipping response clearly increases the stress at the first minimum of the wave frequency stress after the slamming impact. Due to the low structural and hydrodynamic damping, following wave related extrema are also increased by the whipping response. Slamming and the resulting whipping response was shown to occur regularly during these measurements. It is clear that the slamming induced whipping causes a significant increase in the loading of the ship structure. The slamming loading does not only increase the global loads, but the resulting pressure will also increase the loads at the local shell structure.

The whipping response, as shown in Figure 1.1, is well known for many ship types [3, 1]. Part of the structural damage of ships is attributed to slamming loading and whipping response [40]. An example is the accident of the MSC Napoli in the English Channel on 18 January 2007 [6]. This ship experienced a structural failure because the actual loading of the structure exceeded the design load. It is assumed that the whipping response played a role in the accident by significantly increasing the structural loading [6].

Although it is well known that slamming can have a significant contribution to the structural loading, it is rarely taken into account in the design of the ships. The Classification Societies rules give some "dynamic loading" factors,

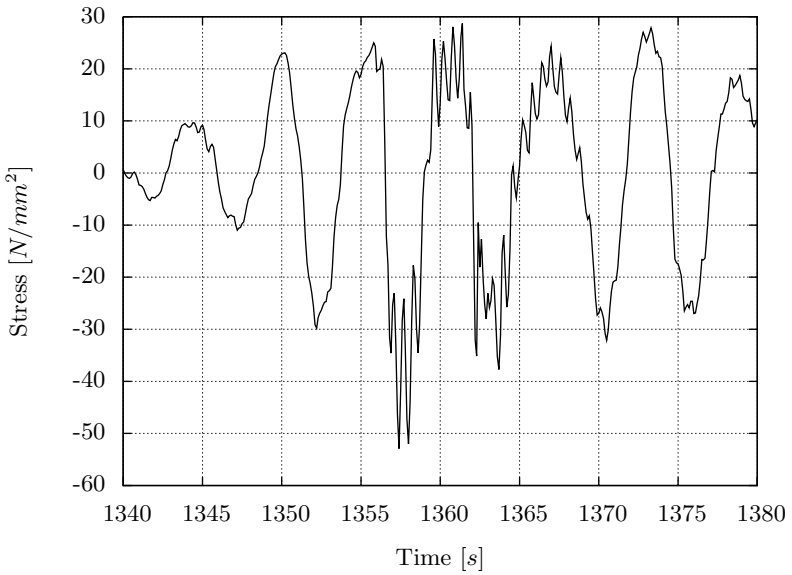

Figure 1.1: Measured stress during full scale trials of the M-frigate of the Royal Netherlands Navy.

but these factors are empirical ones and their domain of validity is not yet fully understood.

When performing seakeeping computations to calculate the structural loading, these slamming and whipping effects are rarely included. The main reason for not including the slamming and whipping in seakeeping loads and response calculations is the difficulty to do this correctly. Currently there is, to the author's knowledge, no commercial tool available which allows to include slamming and whipping in seakeeping calculations in a computationally efficient way such that the results can be used to calculate design values and predict the performance of the ship structure during its life-time.

This is the starting point for the research presented in this thesis. The objective of this thesis is "*The development of a practical method to calculate the global and local response of the ship structure due to the seakeeping loading including the slamming loading. This method should contain the full hydro-elastic coupling*". The development of such a method will be explained in this thesis. In addition, verification, validations and case studies, based on the developed theory will be presented.

The calculation of the loading and response of a ship in a sea remains a difficult subject. It is necessary to simplify some of the physics to be able to develop a method which is practical whilst maintaining a reasonable accuracy. The presented method is a combination of some well known components which

were already developed and some new tools. The presented method is set up such that the different components of the calculations are coupled in a consistent manner.

The method starts with the calculation of the natural modes of the ship structure. Next, the seakeeping problem is solved in the time domain. The response of both the rigid and flexible mode shapes are solved simultaneously. This is a *hydro-elastic* calculation. A separate module calculates the impulsive slamming loading during the seakeeping calculation. The motions of the rigid and flexible modes and the internal loads are the main result of the seakeeping calculations.

This hydro-elastic approach will also compute some *springing* response of the ship structure. Springing is the structural vibration which is caused by the non-impulsive hydrodynamic loading. The computation of the springing response is not the goal of this thesis but it cannot be "turned off" when performing a hydro-elastic analyse. Springing due to linear excitation is expected to be computed correctly. However, the springing response is often attributed to non-linear wave excitation components which are not be correctly computed using the presented method.

Design values like maximum expected bending moment and fatigue damage can be obtained by performing a Weibull extrapolation and undertaking a Rainflow count of the calculated bending moment or stress history. The design values can only be calculated with reasonable accuracy if the computed signal contains enough extrema. As will be shown in this thesis, the signal should be computed for about two hours to obtain accurate predictions. Knowing the design values for a single sea state is not enough to know the design loads of a ship, that is at least the values for a complete scatter diagram are needed. The method to calculate the seakeeping response should be reasonably fast and robust to be able to perform these two hour simulations for every cell of a scatter diagram. Only head waves and a single loading condition will be considered in this thesis. Much more computations are needed if allowing for different headings and/or loading conditions.

The local response of the ship structure due to the seakeeping and slamming loads can be investigated by transferring the calculated loads to a 3D Finite Element (FE) model and solving the structural response within the Finite Element Method (FEM) package. As the FEM analysis requires significant computing time, the local response can currently only be investigated for a limited number of slamming events.

The remainder of this chapter gives a more detailed introduction in the approach used in this thesis. The approach to compute the seakeeping response is explained in the first section. The seakeeping problem is solved using generalised modes. This concept is presented in the second section. The third section gives an introduction about the coupling between the seakeeping and structural calculations. The different meshes used to solve the seakeeping response are

explained in the fourth section. The fifth section gives an introduction to the computation of the internal loads. The computation of the slamming loads is presented in the sixth section. The seventh gives an introduction on how the design values are computed. An outline of this thesis is given in the last section of this chapter.

1.1 Seakeeping method

There are many different approaches available to calculate the seakeeping response of a ship. This response can be calculated using a 2D strip theory method, a 3D Boundary Element Method (BEM) or even a full 3D volume of fluid (VOF) or smooth particle hydrodynamics (SPH) method. Only the strip theory and BEM methods are robust and fast enough to be useful for the goal of this thesis.

One of the goals is to create a coupling with a 3D structural FE-model. For this purpose, it is necessary to be able to calculate the seakeeping response for complex 3D natural modes and to calculate the pressure at every wetted element of the 3D-FE model. This will be difficult to achieve when using 2D strip theory. The 3D-BEM is much more suitable to be coupled to a 3D-FEM. The 3D-BEM is also more accurate than 2D strip theory methods for zero speed problems. It is difficult to tell which of the two methods will be more accurate for forward speed problems. Both the 2D strip theory and the 3D-BEM have different corrections for forward velocity but currently neither can solve the forward speed problem exactly in a reasonable calculation time. The 3D-BEM is therefore selected for the computation of the seakeeping response. A 3D-BEM method using pulsating Green's sources is used.

The seakeeping calculation can be performed in both the frequency domain and the time domain. The frequency domain allows for fast calculation of linear seakeeping problems. However, when non-linear loads and/or impulsive loads are introduced it is more convenient, or even necessary, to perform the calculations in the time domain. Furthermore, it is also possible to account for large displacements in the time domain. Slamming is clearly a non-linear and impulsive load which makes calculations in the time domain necessary. It is generally known that at least the non-linear hydrostatics and Froude-Krylov forces should be included in the calculation to be able to predict the internal loading correctly for severe sea states. It would be best to also include the non-linear radiation and diffraction loads, but this is currently too complex and expensive to compute. Therefore, the linear radiation and diffraction coefficients computed in the frequency domain are used to compute these forces in the time domain.

1.2 Generalised modes

The seakeeping response of a ship is the combination of the rigid-body motion and the flexible response of the structure. The structural deformations remain very small in most seakeeping problems. This allows to exclude the (flexible) structural response for normal seakeeping calculations. The structural response can be computed after the rigid-body seakeeping calculation. This separate calculation results in some parts of the calculations being done twice. It also results in a lot of bookkeeping and the uncoupled approach will not fully account for all hydro-elastic effects. Therefore, in this thesis the calculation of the structural response will be directly incorporated into the seakeeping calculation using the modal approach.

The *modal approach* is a common way of calculating the dynamic response of structures. A number of pre-calculated elastic modes are used to described the structural response. The natural modes of the ship structure are often used but artificial mode shapes may also be used.

For an unconstrained structure in air, one can solve the rigid-body response and the dynamic response of the structure separately as long as the flexible response does not influence the loading at the structure. This separation is not valid for seakeeping problems. The hydrodynamics couple the rigid and flexible modes which may make it necessary to solve the response using both the rigid and flexible modes simultaneously. This coupled calculation is called a *hydro-elastic* calculation. It is necessary to use the hydro-elastic approach when the motions of the flexible modes influence the loading at the structure.

The concept of *generalised modes* is a convenient methodology to formulate the hydro-elastic problem. All degrees of freedom are described by mode shapes by this concept, even the rigid-body modes. Those generalised modes can have any shape and can be used to describe both rigid-body modes and flexible modes. For normal single rigid-body seakeeping calculations, six modes are used with mode shapes that represent surge, sway, heave, roll, pitch and yaw. The flexible modes are added to the set of rigid modes for hydro-elastic calculations. This is illustrated in Figure 1.2.

The concept of generalised modes is not limited to hydro-elastic calculations for single ships. For example, the concept can also be used for multi-body calculations. The six rigid modes are added for every ship, for example, for ship A and B shown in Figure 1.3.

Bishop and Price[4] introduced the use of additional modes to describe the flexibility of the ship hull in seakeeping calculations when they developed the theory of hydroelasticity for ships. Their methodology was based on strip theory for the seakeeping and a beam model to calculate the flexible response. This methodology has been adapted by many other authors for hydro-elastic calculations. The methodology has been extended to compute the seakeeping using a 3D-BEM by other authors.

Figure 1.2: Generalised modes for a ship with two flexible modes.

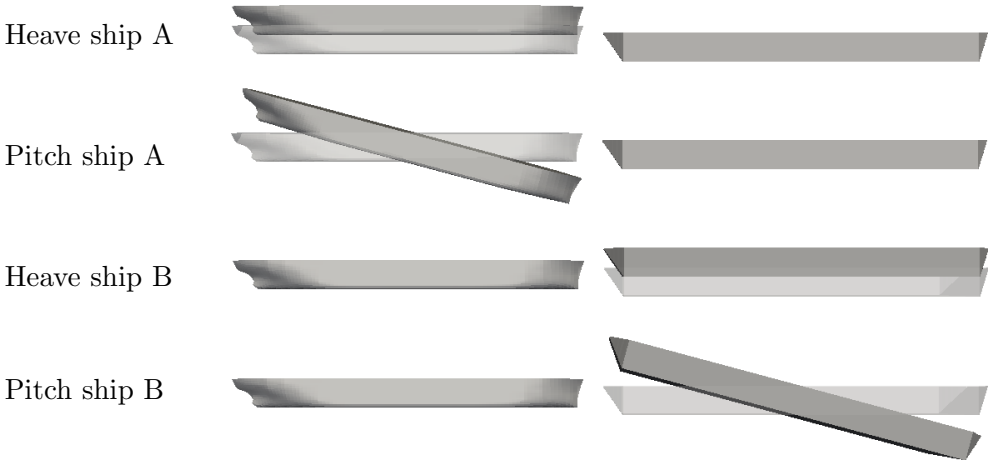

Figure 1.3: Generalised modes for a multi-body problem.

Newman [37] introduced the concept of generalised modes and showed that a wide variety of hydrodynamic problems can be handled using the generalised modes concept. A linear frequency domain 3D-BEM method was utilised for the hydrodynamic calculations. Results for flexible body, multi-bodies and connected bodies were presented.

For this thesis, the concept of generalised modes will also be used for the time domain where large amplitude of motions are allowed. Some additions to the original concept of generalised modes, which was developed for the frequency domain, will be necessary to be able to account for the large amplitude of motions.

1.3 Structural response

A direct coupling between the seakeeping code and the structural solver is avoided by using the modal approach. The dry mode shapes are calculated by a structural solver and these mode shapes are transfered to the hydrodynamic mesh. The modal response is calculated by the seakeeping program, which includes the effect of added mass on the modal response and can be used to obtain resulting motions, bending moments, stresses, etc.

The natural modes of the ship structure are calculated using the FE method. Two methods are implemented for the presented theory: The first method uses a 1D beam model of the ship structure. It is relatively easy to create a beam model of the ship structure. The beam model allows for calculation of the global bending moment. However, the beam model will not be accurate for complex mode shapes like torsion of a large container ship. The second method is a coupling with commercial 3D-FEM codes. The 3D model allows for computation of complex mode shapes. However, the creation of a 3D model of the ship structure requires much more effort than is needed for a beam model.

Only the global structural response can be calculated by the modal approach because only a limited number of modes are used. For calculation of the local response it is necessary to transfer the seakeeping loads to the structural model and calculate the structural response within the structural program.

The local structural response can only be calculated using the 3D-FE method. For this purpose, the seakeeping, slamming and inertial loads of a selected event are transfered to the FEM program. The FEM program solves the structural response.

1.4 Meshes

The developed method requires various meshes to model the geometry of the ship. The first mesh is the *hydrodynamic mesh*. This is the BEM mesh used to solve the linear Boundary Value Problem (BVP). The hydrodynamic mesh models the wetted part of the ship hull in still water. The mesh might contain panels at the inner free surface (i.e. the surface lid) to suppress so-called irregular frequencies. The hydrodynamic mesh must be created such that the mesh size does not vary much in order to ensure a stable solution of the BVP. There are no connectivity requirements between the elements of the hydrodynamic mesh. The hydrodynamic mesh should also model the part above the still water line of the hull if the mesh is used for the time domain seakeeping calculation.

The second mesh is the *structural mesh*, this is the 3D-FEM mesh of the outer hull and weather deck. Although the structural mesh describes the same geometry as the hydrodynamic mesh, the two meshes are usually very different

from each other due to the different requirements for the BEM and FEM calculation. There is usually a larger difference in element size and shape as the structural mesh has connectivity requirements and the FEM solution is less sensitive to local size and shape differences. The structural mesh does usually not have a separation for the parts below and above the still water line in contrast to the hydrodynamic mesh.

The last mesh is the *integration mesh*. This mesh is used to integrate the pressures within the seakeeping programs for calculation of the modal loading and response. By default the hydrodynamic mesh will be used as the integration mesh. When internal loads are calculated the panels of the integration mesh will be cut at the cross section for the internal loads calculation before it is used. This ensures that the hydrodynamic coefficients are integrated exactly up to the location of the cross section. The structural mesh will be used as the integration mesh when the seakeeping forces are to be transferred to the 3D-FEM model. This avoids mapping problems between the results of the seakeeping calculation and the FEM program. It also ensures that the total load in both calculations is equal. The integration mesh may also be cut at the still water plane in order to ensure correct integration of the linear hydrodynamic coefficients.

1.5 Internal loads

The internal loads in the ship structure are calculated to be able to judge whether or not the structure can withstand the seakeeping loads. The internal loads can be calculated using two approaches. The first approach is integrating the difference between the internal and the external forces up to the plane for which the internal loads are to be calculated. The second approach is using modal participation factors to compute the internal loads. The first approach is the most accurate approach, it can also be used for rigid bodies and it provides all six load components. The second approach is less accurate, it can only be used if elastic modes are included in the calculation and this approach as provided within the presented implementation only provides the horizontal and vertical internal loadings. The results of the modal approach will converge to the correct results, which are also obtained when using the direct integration approach, if many elastic modes are included in the calculation. Both methods are implemented to allow one to verify the calculated internal loads by comparing the results of both methods.

The modal approach for computation of the internal loads is a post-processing step of the calculated modal amplitudes. The implementation of the direct integration method is more complicated and this approach is therefore explained in more detail. Figure 1.4 illustrates the approach to calculate the internal loads at two transversal cuts using the direct integration method. The ship is divided into three sections using the defined cuts. The difference be-

tween the internal and external forces are integrated over the section length for every section separately. The internal loads at the cuts are obtained by adding the resulting loading at all sections before or after the cut. Both integration directions should result in the same internal load.

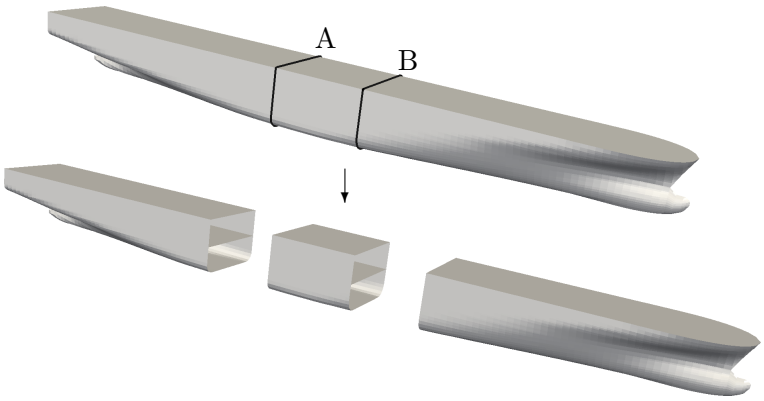

Figure 1.4: Approach used to compute the internal loads at sections A and B.

The calculation of the external force at the sections requires that all force components are also calculated for every section separately. The internal forces in the sections are due to acceleration of the mass. This should also include the accelerations of the elastic mode shapes. The internal forces of a section are calculated by computing the mass matrix for the section and multipling this sectional mass matrix with the acceleration vector. By including the elastic modes, the whipping contribution on the internal loads will be included.

1.6 Slamming loads

Different types of slamming can be defined [9]:

Bow-flare slamming occurs with relative high velocity between the bow-flare and the water surface.

Bottom slamming occurs when an emerged part of the bottom re-enters the water surface.

Breaking wave impact occurs when the ship sails into a breaking wave.

Wet-deck slamming occurs when the waves hit the wet deck of for example a catamaran or an offshore structure.

The focus of this thesis is on mono-hull ships. Therefore, wet-deck slamming is not considered here. The breaking wave impact is also not considered. Thus, only the bow-flare and bottom slamming are considered.

The research on slamming impact was started in 1929 by von Karman [58]. He investigated the loading at landing of seaplanes and proposed to model the impact as a collision with the added mass of the structure. Wagner [59] showed a few years later that one should also account for the pile-up of the fluid surface during the slamming event.

Research on slamming impacts is still ongoing. Many methods have been developed. Starting from 2D empirical methods to full 3D VOF and SPH methods. An overview of the available methods can be found in [9, 40]. The 2D and 3D empirical methods are not used as the range of validity of these methods is not fully clear. Most of the empirical methods can also not compute the local pressure which is needed to compute the loading at the structural model.

To the author's knowledge, there is currently no non-empirical 3D method available which can calculate the slamming loads for an arbitrary bow shape, fast and robust enough to be used for the goals of this thesis. Therefore, the slamming forces are calculated using 2D methods in this thesis. The 2D strip approach is illustrated in Figure 1.5. The bow of the ship is divided into multiple sections. A 2D section is located at the center of every section as shown by the thick line in the figure. The user controls the location and orientation of these sections.

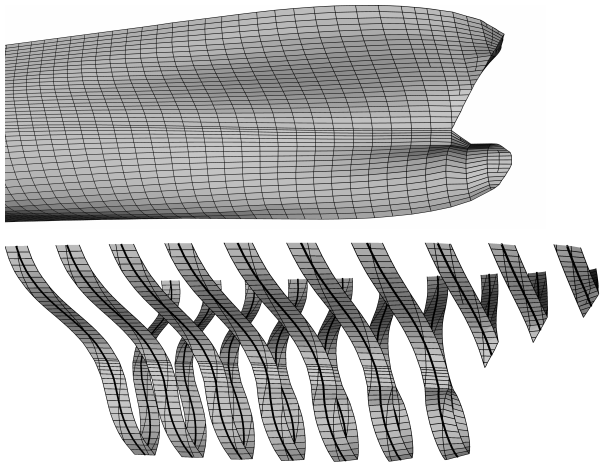

Figure 1.5: 2D sections for a slamming calculation.

Two 2D methods for calculation of the slamming force are coupled to the seakeeping program. The first is the Generalised Wagner Model (GWM) [62], which uses a BEM approach to solve the weakly nonlinear Wagner impact

problem. The other method is the Modified Logvinovich Model (MLM) [23]. This method is based on the Wagner theory of impact of a flat-disc but approximately accounts for both the body shape and the nonlinear terms in the Bernoulli equation for the hydrodynamic pressure.

The GWM method has a wider domain of validity and calculates the pressure loading along the whole section. The MLM method is much faster and more robust.

These 2D methods can handle a large range of bow shapes and are fast and robust enough to perform long term simulations. However, the methods will never be able to calculate the 3D problem fully correctly. A partial 3D correction is made by integrating the slamming pressure calculated by the 2D methods over the 3D geometry. The main disadvantages of the used 2D methods is that they seem to be only valid for head seas and near head sea conditions.

1.7 Design values

Being able to calculate the seakeeping and whipping response in a single sea state does not give the information needed to design a ship. Information like expected maximum bending moment and fatigue loading for different sea states and operation conditions should be known.

Linear frequency domain theory allows for relatively fast calculation of these design values for a complete scatter diagram. This is because the solution for the different cells of the scatter diagram are basically a summation of the same frequency domain solution. For the approach used in this thesis, the nonlinearities require the use of time domain calculations which require one to compute the design values for every cell of the scatter diagram separately.

Also the calculation of the design values for a single sea state is much more computationally intensive when using time domain calculations compared to the frequency domain. The expected extreme bending moment can be calculated using a Rayleigh distribution based on the calculated response spectrum when using the frequency domain. For the time domain it is necessary to generate a time trace that is long enough to be able to compute a Weibull extrapolation with reasonable accuracy.

It will be shown how the design values can be calculated using the results of the time domain calculations with sufficient accuracy and in an acceptable calculation time.

1.8 Outline of this thesis

The theory of the developed methodology is explained in part I of this thesis. The verifications, validations and case studies using the developed theory are presented in part II of this thesis.

Specifically, the formulation of the hydro-elastic problem is explained in the second chapter. It is explained how the input required for solving the hydro-elastic seakeeping problem is created. The mesh, mode shapes, the mass and stiffness matrices, and the hydrostatic restoring matrix are examples of the input needed to solve the hydro-elastic problem.

The third chapter explains the computation of the seakeeping response, internal loads and natural frequencies in the frequency domain. The linear added mass, damping and diffraction forces computed in the frequency domain are used to solve the seakeeping problem in the time domain. The approach for solving the seakeeping problem in the time domain is explained in the fourth chapter. Identification of the motions and internal loads are the main results of the seakeeping calculation. The slamming computation is directly integrated into the seakeeping calculation to be able to compute whipping responses.

The fifth chapter presents the backgrounds of the two 2D methods which are used to compute the slamming loading. The coupling between the slamming calculation and the seakeeping computation is also explained in this chapter. The approach to transfer the seakeeping and slamming loads to a 3D FEM model is presented in the sixth chapter. This allows one to evaluate the local structural response using the loads predicted by the seakeeping and slamming calculation. The computation of the design values using the results of the time domain seakeeping calculation is explained in the seventh chapter. In this chapter it is investigated how the design values can be computed accurately while minimising the computational effort.

The last five chapters, part II, present verification, validation and case studies of the presented theory. Specifically, the eighth chapter presents verification and case studies for two ultra large container ships. The hydro-elastic response and multi-body results are verified and validated in chapter nine. Barges or floaters with flexible connections are considered for this verification and validation. Chapter ten presents a validation of the computed wet natural frequencies, slamming impact and whipping response using experimental results for an aluminium ship model. The computed slamming loading is validated in the eleventh chapter using measured slamming forces during model experiments with a container ship. The last validation is presented in chapter twelve. The measured stresses during a full scale trial of a frigate in severe sea conditions with the occurrence of slamming and whipping is used in this chapter to validate the presented method. This chapter also verifies the calculation of the load cases for a 3D FEM computation in order to obtain the local structural response of the ship.

Part I

Theory

Chapter 2

Formulating the hydro-elastic problem

The first step in performing a hydro-elastic calculation is the preparation of all the input required to solve the hydro-elastic seakeeping problem in the frequency and/or the time domain. The meshes, mode shapes, the mass and stiffness matrices, hydrostatic restoring matrix, 2D slamming sections are examples of the information created in this pre-processing phase. This chapter describes the approach used to prepare all the input and formulates the hydro-elastic problem.

2.1 Overview of approach

The hydro-elastic problem is formulated by a number of programs each with their own specific tasks. Figure 2.1(a) illustrates the approach used to formulate a seakeeping problem for a single rigid-body. The hydrodynamic mesh is created by an existing external program, the pre-processor adds the rigid-body mode shapes and other information needed to solve the seakeeping problem. The pre-processor is capable of combining the input of multiple bodies to formulate a multi-body problem, see Figure 2.1(b).

The structural flexibility is taken into account by adding the natural mode shapes of the structure to the rigid-body modes. These natural modes are calculated using the FE method based on either a beam model or a 3D model of the ship structure. This approach is shown in Figure 2.2. Figure 2.2(a) illustrates the beam approach: a dedicated program solves the structural FEM problem and calculates the elastic mode shapes. Figures 2.2(b) and (c) illustrate the coupling with the 3D-FEM: the results from a computation using commercial FEM code are read by a program which projects the mode shapes onto the seakeeping meshes. It is also possible to extract the hull lines from the 3D-FEM model, see Figure 2.2(c). This can be used when the hydrodynamic hull

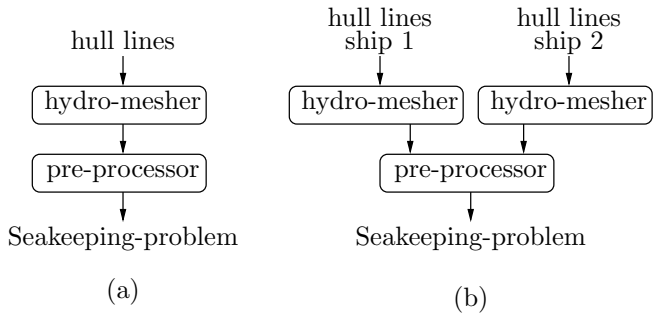

Figure 2.1: Creating rigid-body (a) and multi-body (b) input.

lines are not available or when the seakeeping loads are to be transferred to the 3D-FEM model. This ensures that the hydrodynamic mesh and the structural mesh describe the same geometry which is essential when one wants to transfer the seakeeping loads to the 3D-FEM model.

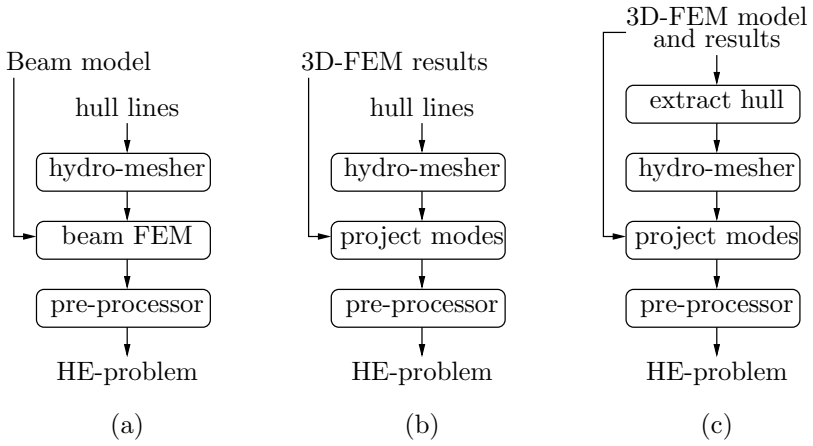

Figure 2.2: Creating input for flexible body.

The ship can also be balanced in still water. The reason for balancing is explained first. Figure 2.3 shows the calculated midship bending of a 360 $[m]$ container ship in still water. This time domain calculation includes the non-linear hydrostatic and gravity forces. The hydro-elastic problem is defined using the approach as illustrated in Figure 2.2(a). The bending moment is set such that zero is equal to the still water bending moment (SWBM) at the initial, undeformed, condition. The still water condition results in excitation of the modes, the ship starts to whip due to this loading. The whipping response is slowly damped and the ship finds its static, deformed, condition where the

moment due to the structural deformation compensates the SWBM.

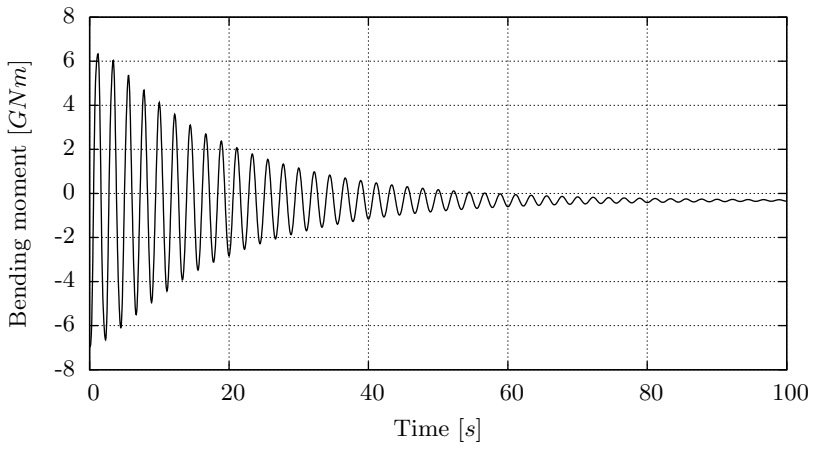

Figure 2.3: Midship bending moment of a 360 $[m]$ container ship in still water when using an unbalanced model.

The initial whipping response is significant for this very large flexible ship. The amplitude of displacement at the bow is about one metre. One has to wait until this initial whipping response has been damped out before the intended time domain analysis can start. Note also that the bending moment signal does not approach zero (the SWBM at the start) at the end of the calculation in Figure 2.2. The deformation in still water results in a slightly different SWBM than that found for the undeformed ship. This difference makes the post-processing more difficult. This initial whipping problem is solved by balancing the ship in still water before doing the hydro-elastic computation.

Figure 2.4 illustrates the approach for balancing the ship and for the computation of 2D-slamming sections. The "elastic modes" program can be either the beam program or the 3D-FEM interface. It is also possible to only balance the ship or only add the slamming sections. Both programs can also be used for rigid ships.

The balancing program calculates the displacements of all degrees of freedom such that all the modes are in equilibrium in still water. A new, balanced, mesh is created using these modal displacements. This approach ensures a correct draught and trim and it ensures that the flexible modes are balanced.

The 2D slamming sections are created by cutting through the 3D integration mesh. These sections will be used by the slamming module in the time domain program. Both the slamming sections and the balanced mesh result in new points for which the modal displacements are not yet known. Note that adding new points does not change the natural mode shapes, but the program for computing (2D beam) or projecting (3D-FEM) the flexible mode shapes has to

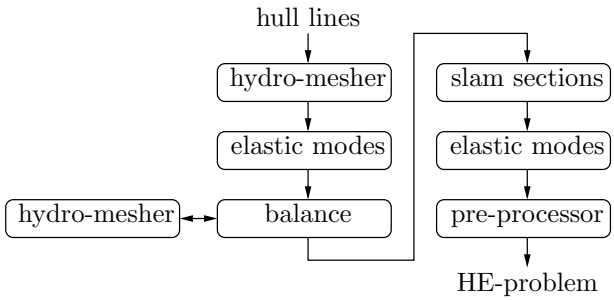

Figure 2.4: Creating input for a balanced flexible body with slamming sections.

be rerun in order to obtain the mode shapes for the new points.

A number of commercial programs are used in the pre-processing phase. AMG [26] is used to create the hydrodynamic mesh and TRIDENT [34] or NASTRAN are used to solve the 3D-FEM problem. These programs are used as black boxes and the approach used by these programs will not be explained it this thesis. As the current version of AMG is not capable of creating the hydrodynamic mesh for vessels built from only flat plates, like FPSO's, an additional program has been developed to create the hydrodynamic mesh for such ships. This program is not explained in this thesis as the method used is straightforward.

The next sections of this chapter explain the different steps and programs used in more detail. The creation of the 2D-slamming sections will be explained in Chapter 5.

2.2 Coordinate system and mode shapes

The coordinate system and the description of the mode shapes are introduced first. Figure 2.5 illustrates the coordinate system used. Unit vector $\vec{i}$ points in the surge direction, $\vec{j}$ in the sway direction and $\vec{k}$ in the heave direction. Vectors $\vec{l}, \vec{m}$ and $\vec{n}$ are the unit vectors in the roll, pitch and yaw directions, respectively. The origin of the coordinate system is denoted by O and the location of the center of gravity by $\vec{G}$.

For every location on the body, the matrix $\mathbf{h}(x, y, z)$ provides the transformation between the Cartesian system and the modal system which is based on the generalised modes

$$\mathbf{h}(x, y, x) = \left[\vec{h}_1^T, \vec{h}_2^T, \ldots, \vec{h}_{\text{ndof}}^T\right], \tag{2.1}$$

with

$$\vec{h}_i(x, y, z) = \left[h_{i,x} \cdot \vec{i}, h_{i,y} \cdot \vec{j}, h_{i,z} \cdot \vec{k}, h_{i,\phi} \cdot \vec{l}, h_{i,\theta} \cdot \vec{m}, h_{i,\psi} \cdot \vec{n}\right], \tag{2.2}$$

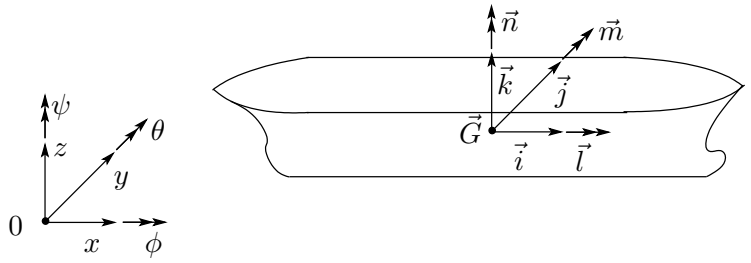

Figure 2.5: The axis system used.

where subscript i denotes the mode number. Note that $\mathbf{h}(x, y, z)$ is a collection of all mode shapes.

The displacement of a point on a body is, for small displacements, given as

$$\vec{H}(x, y, z) = \mathbf{h}(x, y, z) \cdot \vec{\xi}, \tag{2.3}$$

where $\vec{\xi}$ is the vector of the modal displacements.

The gradient of the mode shape vector is needed to calculate the hydrostatic restoring and the so-called m_j-terms for the calculation of the hydrodynamic coefficients. Only the modal translations and rotations are obtained from the structural model but the derivatives needed to calculate the gradient are not available for the structural model. Therefore, the spatial derivatives of the mode shapes, which indicate local rotations are estimated by the rotation angle. The strains are assumed to have negligible influence on the hydrostatics and hydrodynamics, so they are set to zero. The resulting estimation of the gradient of a mode shape is

$$\nabla \vec{h}_i = \begin{bmatrix} \frac{\partial h_{i,x}}{\partial x} & \frac{\partial h_{i,y}}{\partial x} & \frac{\partial h_{i,z}}{\partial x} \\ \frac{\partial h_{i,x}}{\partial y} & \frac{\partial h_{i,y}}{\partial y} & \frac{\partial h_{i,z}}{\partial y} \\ \frac{\partial h_{i,x}}{\partial z} & \frac{\partial h_{i,y}}{\partial z} & \frac{\partial h_{i,z}}{\partial z} \end{bmatrix} \approx \begin{bmatrix} 0 & -h_{i,\theta} & h_{i,\psi} \\ h_{i,\theta} & 0 & -h_{i,\phi} \\ -h_{i,\psi} & h_{i,\phi} & 0 \end{bmatrix}. \tag{2.4}$$

2.3 Extracting cross sections

The first step in formulating the hydro-elastic problem could be the extraction of the geometry of the 3D-FEM model. The extracted cross sections are used to create the hydrodynamic mesh.

Figure 2.6 shows an example of the extraction of the cross sections from a 3D-FEM model of a container ship. The thick black lines are the extracted cross sections. The cross sections are translated and/or rotated when the FEM model does not have the desired position and/or orientation for the seakeeping calculation.

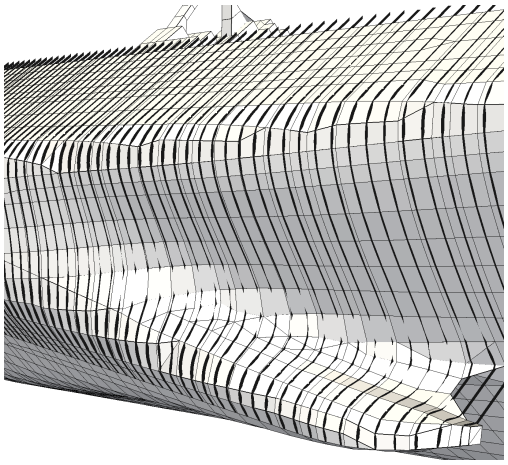

Figure 2.6: Cross sections created from a 3D-FEM model.

Figure 2.7 illustrates how a single cross-section is created by cutting through a 3D-FEM model of a different ship. Points are created at every element boundary encountered. Only the FEM panels of the outer hull are considered. These panels are identified by their module or part number. The points found in this way are interconnected by a line resulting in a piecewise 2D curve. The knuckle points are identified using a threshold angle for this curve. The curve is smoothed between the endpoints and the knuckle points using a smoothed spline[1]. The cross-section is made by creating a new curve which follows these smoothed splines.

2.4 Creating 3D sections and Gauss points

The calculation of the flexible mode shapes and the projection of the mode shapes onto the hydrodynamic and integration mesh is the next step of the pre-processing when a flexible ship is considered. Prior to projecting the mode shapes, the complete integration mesh must be available. The integration mesh is therefore created before projecting the mode shapes.

The user can select whether the hydrodynamic or the structural mesh is used as a basis for the integration mesh. The integration mesh is divided into 3D sections to allow for internal and external load calculations. The second step is the creation of the Gauss points at the panels of the integration mesh. These Gauss points will be used to integrate the pressure to modal forces during the seakeeping calculations. This can be done only if the modal displacements and rotations at each of the Gauss points are known. Therefore, these Gauss

[1]Routine `smooth.f` from `www.netlib.org` is used for this smoothing.

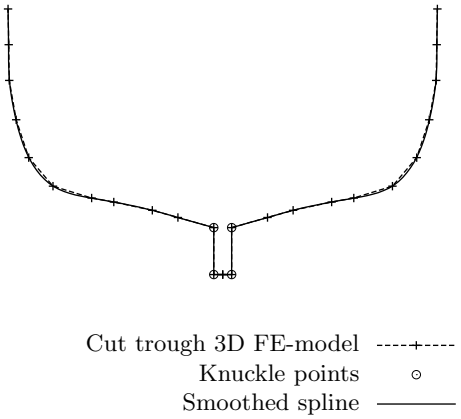

Figure 2.7: Create cross section

points are also created before projecting the mode shapes.

2.4.1 3D ship sections

The ship is divided into 3D sections by cutting through the integration mesh using planes. A cutting plane is defined by a point and a normal vector which allows any orientation and location of the cutting plane. An example of 3D sections created using two transversal cuts and one longitudinal cut is shown in Figure 2.8. These 3D sections can, for example, be used to calculate the internal load at amidships and the external force at the upper part of the bow section.

Figure 2.8: Example of 3D sections.

The 3D sections can be created at three stages of the pre-processing phase. The integration mesh will change due to the cuts through the mesh. The programs for projecting the flexible mode shapes will create the 3D sections before projecting the flexible mode shapes by default. This ensures that the projected mode shapes are valid for the "cut" integration mesh. The disadvantage of creating the 3D sections by the mode shape programs is that the horizontal cuts will be slightly bent after the mesh is balanced. This can be avoided by creating the 3D sections after the balanced integration mesh is created. Note that

the mode shapes have to be projected again after the mesh is balanced, so the mode shapes will also be valid for the integration mesh with 3D sections when created after the balancing. The last possibility is to create the 3D sections in the last pre-processing program. This can be used for rigid bodies which are not balanced.

A cut through the mesh is made for all cut-planes defined by the user. Figure 2.9 shows the different possibilities for cutting through panels. These new panels should have a reasonable aspect ratio to allow for accurate integration over the new panels.

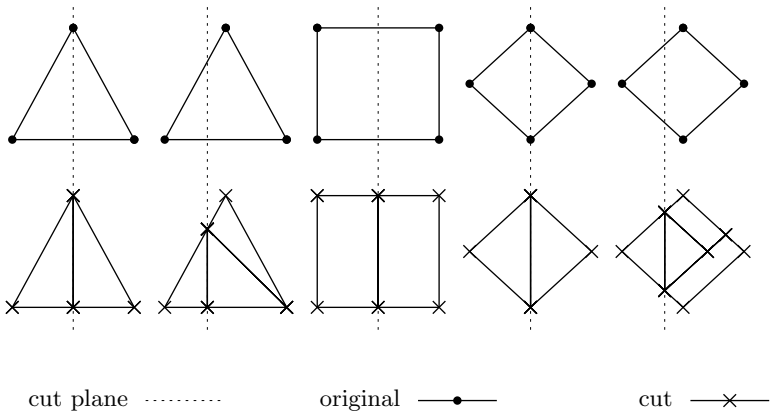

Figure 2.9: Different cuts through panels.

The 3D sections created are numbered automatically. This numbering is not straightforward since any number of arbitrary cut-planes can be defined. The approach for numbering the 3D sections is illustrated in Figure 2.10. The total ship has section number zero at the start. The first division into 3D sections is made in (a). The section number is increased by one at one side of the section. The section number is increased by two at the other side. Two and four are added to the section numbers for the next cut (b). This continues until all 3D sections are created (c). The section numbers are compressed after all 3D sections have been created (d). This ensures that the section numbering is continuous and always starts from one. A list with the contributing 3D sections for the internal loads at the cuts is also created. For example, sections 1, 2, 4 and 5 will contribute to the loading at the midship section when integrating from the forward direction. Sections 3 and 6 will contribute to the loading at midship when integrating from the aft.

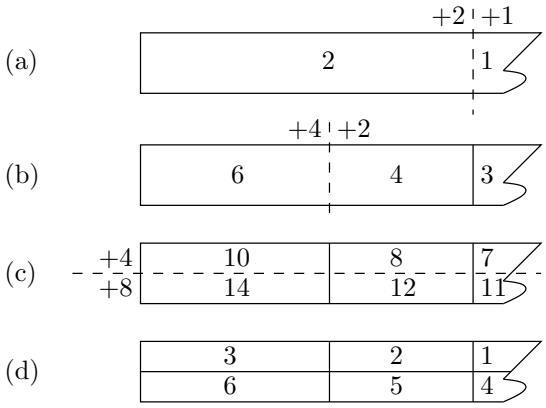

Figure 2.10: Section numbering.

2.4.2 Gauss points

All integrals over the surface are numerically solved using the Gauss quadrature. The mathematical background of the integration using Gauss points can be found in Appendix A. Using the Gauss integration allows the user to control the accuracy of the integration by changing the number of Gauss points per panel instead of changing the mesh. This is important when the structural mesh is used as integration mesh because it is usually difficult to change this 3D-FE mesh.

The number of Gauss points per panel is based on the panel size. The number of Gauss points for a panel is chosen such that the associated area of one Gauss point does not exceed the user defined threshold. An example of the resulting distribution of Gauss points can be found in Figure 2.11. The larger panels have more Gauss points than the smaller panels which results in a more uniform accuracy of the integration over the surface compared to using a fixed number of Gauss points per panel. The pressure distribution is not taken into account for choosing for the number of Gauss points because the pressure distribution is unknown a priori and changes constantly during the time domain calculations.

The integration with Gauss points will not be accurate if there are discontinuities in the pressure distribution. Discontinuities in pressure the distribution will occur at the still water line for the linear calculations. For example, the pressure of the incoming wave will have the highest amplitude just below the still water line and is zero above the still water line according to the linear theory. This discontinuity will usually not affect the integration as the hydrodynamic mesh does not have any panel that crosses the still water line. However, when a structural mesh is used as the integration mesh, the integration becomes inaccurate as the structural mesh usually does not account for

the location of the still water line. A solution is to cut the mesh at the still water line if the structural mesh is used as the integration mesh.

This is illustrated using the structural mesh shown in Figure 2.11. The original panel distribution (a) does not account for the still water line. The cut at the still water line (b) ensures that none of the panels cross the still water line. The resulting heave force of a artificial pressure distribution is calculated using a different number of Gauss points per panel. The resulting force and the pressure distribution are equal to

$$F_z = \iint_{S_b} p_t(z) n_z \, \mathrm{d}s, \tag{2.5}$$

with

$$p_t(z) = \begin{cases} 1 & z \leq 0 \\ 0 & z > 0 \end{cases}. \tag{2.6}$$

The resulting heave force can be found in Figure 2.12. The resulting force changes with the number of Gauss points for the original mesh and hardly converges to the final value. The number of used Gauss points has much less influence on the calculated force if a cut at the still water line is applied. This shows that the structural mesh can be used as the integration mesh only if a cut is made at the still water line. It will be explained in Chapter 6 how the nodal force at the original FE mesh can be calculated if the integration mesh has been cut.

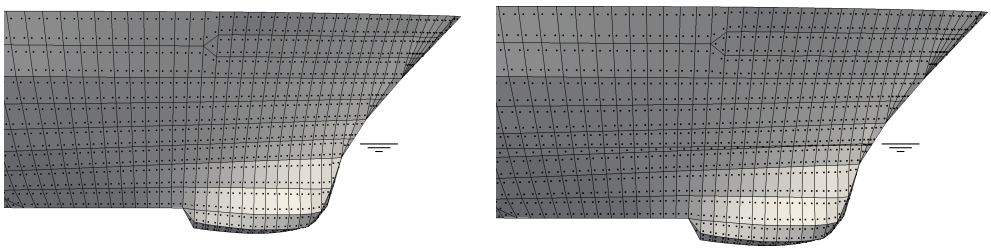

(a) (b)

Figure 2.11: Original FE mesh (a) and the same mesh with a cut at the still water line (b).

2.5 Obtaining mode shapes from 3D-FEM

The dry natural mode shapes of the ship structure may be calculated using an 3D-FE method. Commercial FEM programs are used to calculate the dry flexible mode shapes of the structural model. These mode shapes have to be

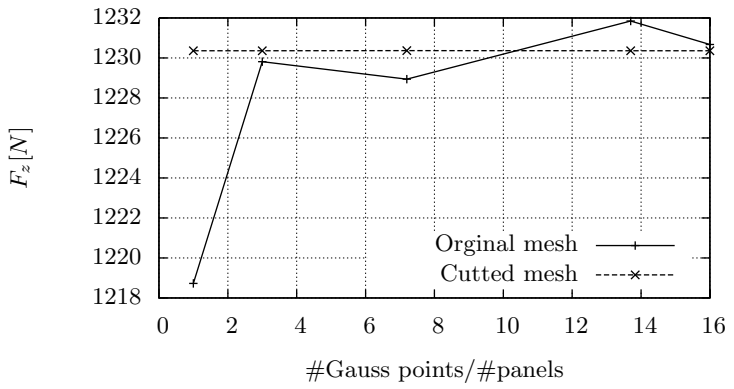

Figure 2.12: Resulting heave force when integrating with different numbers of Gauss points.

transfered to the hydrodynamic and structural meshes used for the seakeeping calculation. In addition, the accompanying mass and structural stiffness matrices and the gravity contribution to the hydrostatic restoring also needs to be computed.

The elastic modes shapes are mass normalised by the FEM program. The modal mass matrix is equal to the identity matrix after this normalisation. Using these mode shapes can give some accuracy problems in the time domain calculation. The rigid-body translations and rotations are added to the flexible mode shapes for the seakeeping calculations. The unit rigid-body translations are one metre and the unit rotations are one radian. For very large ships, the associated mass for these rigid rotations can be in the order of $10^{13}[kg]$ while the modal mass for the flexible modes is $1[kg]$. Such large differences in mass of the rigid-body modes and the mass of the elastic modes can lead to an ill-conditioned system of equations used to solve the seakeeping response[2]. This is avoided by scaling the elastic mode shapes such that the modal mass has the same order of magnitude as the modal mass of the rigid-body modes.

The solution of the FEM program usually contains not only the elastic mode shapes but also rigid-body mode shapes. It is essential for the time domain calculation that these rigid-body modes shapes are not transfered to the seakeeping program. The rigid-body modes from the FEM solution will usually be a combination of the rigid modes like surge, sway, etc. The seakeeping program cannot account for large amplitude motions if those mixed FEM rigid modes are provided. The internal loads can also not be computed using these mixed modes when using the direct integration method as the rigid-body modes

[2]The same difference in order of magnitude will also be found in the calculated forces and the stiffness matrix. This will also introduce inaccuracies.

are used to obtain the loading in the Cartesian system.

Some FEM programs allow to include the infinite frequency added mass in the FEM calculation when solving the vibrational eigenvalue problem. A BEM method for the computation of the full added mass is included in these FEM programs. This full added mass matrix is added to the structural mass before solving for the eigenvalues. Including the added mass makes it easier to find the relevant mode shapes. The mode shapes are found starting from the lowest frequency. The first few modes are the global and relevant modes. However, at a certain frequency local modes, which are not relevant for the seakeeping problem, will be found. It is difficult to obtain global modes with a higher frequency than the first local modes as there are many more local modes than global modes. In general, the inclusion of the added mass will lower the frequency of the global modes more than the frequency of the local modes. This makes it easier to find the global modes which are the most relevant for the hydro-elastic seakeeping problem.

Including the added mass to the FEM calculation will result in elastic mode shapes which contain rigid-body components. These modes are no longer orthogonal to the rigid-body mode shapes. Orthogonality between the rigid and elastic modes is assumed for the theory used of the time domain calculation. This requires one to remove the rigid-body components from the elastic mode shapes if they are computed with the inclusion of the added mass. The rigid-body component is simply the translation or rotation of the total mass by the modal displacement.

Note that the inclusion of the added mass in the FEM computation is not used in this thesis. The above discussion is only to explain what should be done when the added mass would be included in the FEM computation.

2.5.1 Projection of the mode shapes

An example of the projection of the mode shapes for a container ship is shown in Figure 2.13. Figure 2.13(a) shows the undeformed structural mesh and (b) the hydrodynamic mesh. Figure 2.13(c) shows the displacements of the first torsional mode for both the FEM mesh and the projected mode shape at the hydrodynamic mesh. The FEM mesh is visualised using a wire frame, the hydrodynamic mesh is the gray colored mesh. The projected mode shape of the hydrodynamic mesh is very close to the original mode shape of the structural mesh. This indicates that the projection procedure as will be explained below gives correct results.

The methodology described in [30] is used to project the mode shapes. This methodology has been enhanced to make the method more robust. All quads (four node elements) of the FEM mesh are divided into triangles to simplify the projection of the mode shapes. This is shown in Figure 2.14(a) and (b). The mode shapes are projected to all points describing the geometry of the

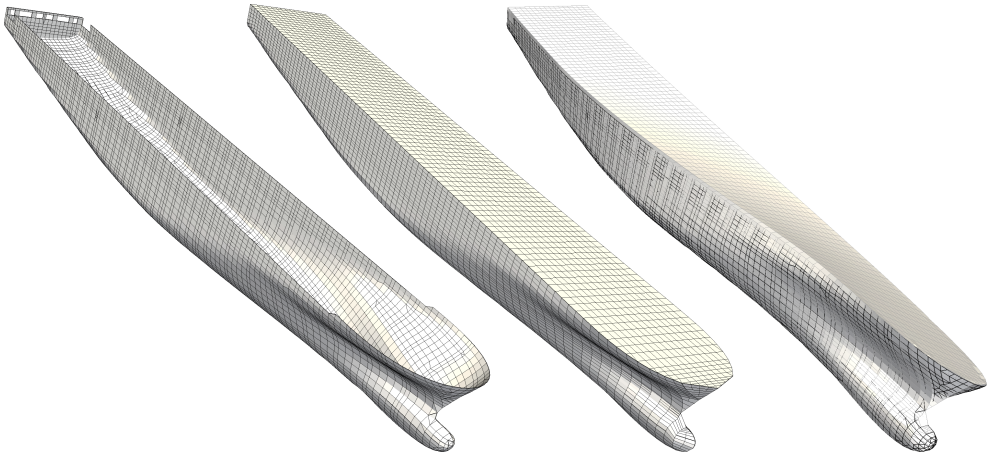

Figure 2.13: Transfer of mode shapes from the FEM mesh to the hydrodynamic mesh.

ship. The first step in projecting the mode shapes at a single point is to find the closest FEM panel. All FEM panels attached to the fifteen nearest nodes and panel centers are selected. This selection is shown in Figure 2.14(c), the cross indicates the location for the mode shape projection. A smaller number of panels could be selected in this case, but for very curved parts, like the bulb, this amount appeared to be necessary to ensure that the closest panel is always included in the selection.

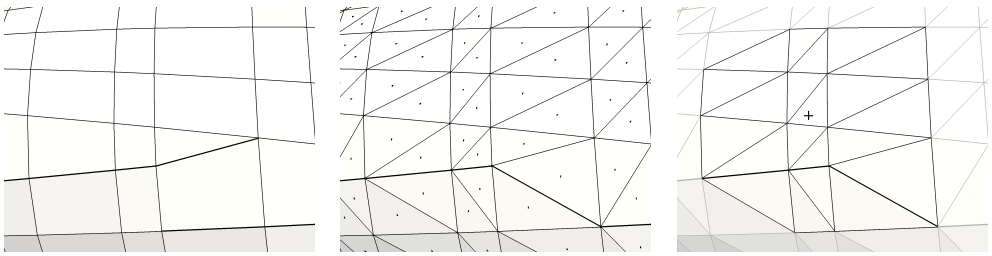

Figure 2.14: Preparing and selecting FEM panels.

The location p to transfer the mode shapes to is projected onto all selected elements. The approach for this projection is shown in Figure 2.15, where p' indicates the projection point. First, it is tried to project the point onto the panel by moving the point along the panel normal (a). If this projection falls

outside the element, it is tried to project the point onto one of the panel edges (b). The closest node is used as the projection point if this is also not possible (c). This projection is repeated for all selected elements. The projection point which is closest to the original point is used to transfer the mode shapes. The mode shape displacements of all three nodes are interpolated if the projection point is located at the element. An interpolation between the two nodes is used if the projection point is located at the element edge. When the projection point is a node, the mode shape displacement of this node will be used without any interpolation.

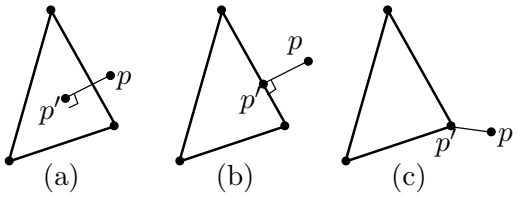

Figure 2.15: Finding the projection point.

The procedure described above will become inaccurate when the projection point is not close to the original point. This will be the case for the deck panels of the hydrodynamic mesh shown in Figure 2.13(b). Another mapping procedure is applied for the points for which the distance to the projection point is larger than the average element diagonal of the structural mesh. The mode shapes of the 3D-FEM results are first simplified to beam-like deformations using a virtual beam. The simplified mode shape will only depend on the longitudinal coordinate. This beam-like mode shape allows one to calculate the mode shape at every location at the ship. It should be noted that this approach is only valid if the global modal displacements are "beam-like", but this is usually the case for ship structures.

Figure 2.16 illustrates the calculation of the simplified mode shapes using a virtual beam. The ship and "beam" are divided into 30 longitudinal sections (a). The average rotations of the nodal FEM mode shapes are calculated for every section. A smoothed spline is created using these averaged sectional values for all three rotations (b). The next step is to calculate the average translations. The beam translation of a node is the translation of the original FEM mode shape minus the translation due to the beam rotation. A smoothed spline is created for the translation using the average translation for each section. The mode shape can now be calculated for every point. Figure 2.14 shows that the mode shape of the deck panels is continuous and connects well to the sides of the ship. This shows that this beam-wise projection approach gives reasonable mode shapes.

Only the nodes attached to the outer hull are considered for calculating the

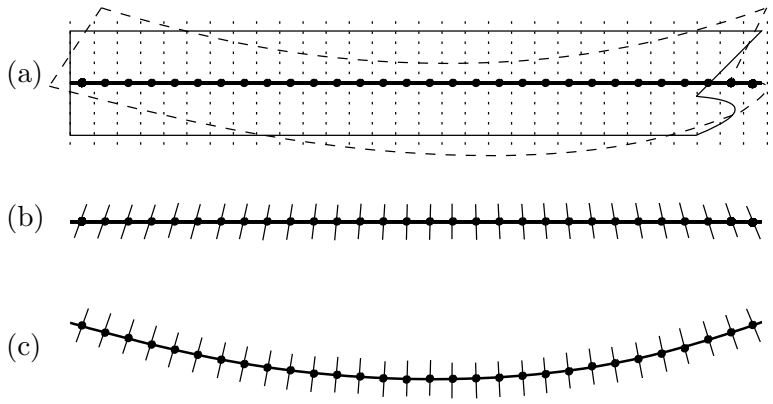

Figure 2.16: Simplified mode shapes.

simplified mode shapes. This is because some of the 3D-FEM mode shapes can be very localised. These local displacements should not be mapped onto the virtual beam model as this model should only describe the global displacements by the mode shapes. The outer hull is normally stronger and stiffer than the internal structure. Therefore, the local modes are usually not present at the outer hull.

2.5.2 Mass and stiffness matrix

The mode shapes calculated by the 3D-FEM program are mass normalised. If the FE model does not conform to the SI units, the factor d_u should be used to convert the results to SI units. The mode shapes are scaled by d_s to obtain the same magnitude as the rigid-body modes, see Section 2.5.

The modal genuine mass matrix $\mathbf{m}_e$ and stiffness matrix $\mathbf{c}_e$ matrices for the flexible modes are equal to

$$\mathbf{m}_e = d_s^2 \cdot d_u^2 \cdot \begin{bmatrix} 1 & & & & \\ & 1 & & 0 & \\ & & \ddots & & \\ & 0 & & 1 & \\ & & & & 1 \end{bmatrix}, \tag{2.7}$$

$$\mathbf{c}_e = d_s^2 \cdot d_u^2 \cdot \begin{bmatrix} \omega_{n(1)}^2 & & & & \\ & \omega_{n(2)}^2 & & 0 & \\ & & \ddots & & \\ & 0 & & \omega_{n(n-1)}^2 & \\ & & & & \omega_{n(n)}^2 \end{bmatrix}, \tag{2.8}$$

where ω_n are the (dry) modal frequencies. Equation (2.7) is only valid if a FE model without the added mass is used. Equation (2.11) could be used to compute the modal genuine mass matrix when the added mass is included in the FEM calculation.

The total mass and stiffness matrices for the body can be created by simply combining the rigid-body and flexible contributions because the modes are assumed to be orthogonal. The calculation of internal loads will require the mass matrices for the different sections. There will be a coupling between the rigid-body and elastic modes in the mass matrix of these individual sections. Therefore, the mass matrices for the sections have to be computed using the mass distribution and mode shapes of the FE model. First, the rigid-body mode shapes are added to the elastic FEM modes

$$\mathbf{h} = [\mathbf{h}_r, \mathbf{h}_e], \tag{2.9}$$

with $\mathbf{h}_r$ the rigid-body mode shapes for location $\vec{r} = (x, y, z)$ and $\mathbf{h}_e$ the elastic mode shapes from the FEM results defined by

$$\begin{aligned} \vec{h}_x &= \vec{i}, \\ \vec{h}_y &= \vec{j}, \\ \vec{h}_z &= \vec{k}, \\ \vec{h}_\phi &= \vec{i} \times (\vec{r} - \vec{G}) + \vec{l}, \\ \vec{h}_\theta &= \vec{j} \times (\vec{r} - \vec{G}) + \vec{m}, \\ \vec{h}_\psi &= \vec{k} \times (\vec{r} - \vec{G}) + \vec{n}. \end{aligned} \tag{2.10}$$

The modal mass matrix for the total body and individual sections is calculated using

$$\mathbf{m}_{is} = \sum_{i=1}^{N_{\text{nodes}_{is}}} \mathbf{h}_i \cdot \mathbf{M}_i \cdot \mathbf{h}_i^T, \tag{2.11}$$

where $\mathbf{M}_i$ is the mass matrix for the FEM node i, is is the number of the section[3] and N_{nodes} is the number of nodes at which masses are defined. The nodal mass is often lumped to a scalar mass M_i in the FEM method. The nodal mass matrix can be written in that case as

$$\mathbf{M}_i = \begin{bmatrix} M_i & 0 & 0 & 0 & 0 & 0 \\ 0 & M_i & 0 & 0 & 0 & 0 \\ 0 & 0 & M_i & 0 & 0 & 0 \\ 0 & 0 & 0 & 0 & 0 & 0 \\ 0 & 0 & 0 & 0 & 0 & 0 \\ 0 & 0 & 0 & 0 & 0 & 0 \end{bmatrix}. \tag{2.12}$$

The values of $\mathbf{M}_i$ or M_i are read from the mass matrix created by the FEM program.

The modal displacement causes a displacement of the structural mass in the gravity field. This displacement gives a contribution to the hydrostatic stiffness matrix of [28]

$$C_{m,ij} = g \iiint_V m(\nabla \vec{h}^j) h_z^i \, \mathrm{d}v, \tag{2.13}$$

where g is gravity acceleration, V the volume of the body and m the mass. The mass distribution and mode shapes from the FE model are used to compute this contribution. Equation (2.13) is simplified using equation (2.4) and the integral over the body is substituted by a summation of the nodal mass contributions. This results in

$$C_{m,ij,is} \approx g \sum_{i=1}^{N\text{nodes}_{is}} M_{i_{z,z}} \left(h_\theta^i \cdot h_x^j + \cdot h_\phi^i \cdot h_y^j \right), \tag{2.14}$$

where $M_{i_{z,z}}$ is the (z,z) or $(3,3)$ component of the M_i mass matrix.

2.6 Calculating mode shapes using a beam model

The natural modes of the ship structure can be calculated using an 1D-beam model when a 3D-FE model is not available. The program DYANA [25] is modified to fit the approach used in this thesis. This program is a predecessor of the 1D-FEM program described in [44].

[3] $is = 0$ is used to obtain the result for the total body.

The beam is divided into elements in the longitudinal direction, see Figure 2.17. The beam is located at the y and z-coordinate of the center of gravity. The element distribution is modified to better account for internal load calculations. More specifically, it is ensured that an element center is located exactly at the locations for internal load calculations in the longitudinal direction. This allows to calculate the modal participation factors for bending moments and shears force, at the desired locations, as these are only available at the element center. It also ensures that the correct mass is associated with the different sections for the internal load calculation.

Only the approach to compute vertical bending mode shapes is presented in this section. The horizontal bending modes can also be computed using the same approach but changing all vertical components to horizontal components. Torsion modes are not computed by this beam approach. Note that the programs presented in [25] and [44] do compute torsional modes using beam theory.

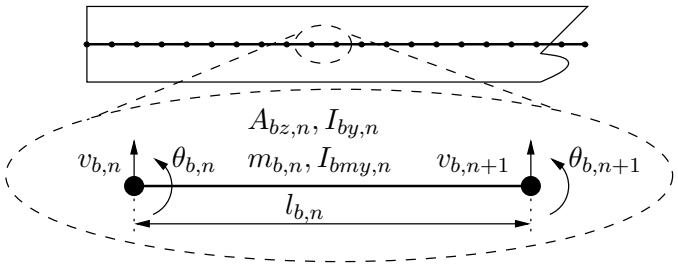

Figure 2.17: Beam model.

The degrees of freedom of one beam element is shown in Figure 2.17. Every node, indicated with subscript n, has one translation v_b in the z-direction and a rotation θ_b around the y-axis. Note the sign difference for the θ_b rotation compared to the coordinate system defined in Section 2.2.

The elasticity modulus E and shear modulus G are assumed to be constant for the whole beam. The following beam properties are interpolated for every beam element using the user defined distribution:

A_{bz}	effective shear area in the z-direction,
I_{by}	moment of inertia of the cross section,
m_b	mass per unit length,
I_{bmy}	mass moment of inertia of the cross section.

The mass and stiffness matrices have to be calculated to solve the eigenvalue

problem. Two auxiliary variables are used to compute these matrices

$$\beta_{b,n} = \frac{EI_{by,n}}{GA_{bz,n}l_{b,n}^2}, \tag{2.15}$$

$$\gamma_{b,n} = \frac{I_{bmy,n}}{m_{b,n}l_{b,n}^2}. \tag{2.16}$$

The stiffness matrix for a single element is equal to

$$\mathbf{C}_{b,n} = \frac{2EI_{by,n}}{1+12\beta_{b,n}l_{b,n}^3}\begin{bmatrix} 6 & 3l_{b,n} & -6 & 3l_{b,n} \\ 3l_{b,n} & 2(1+3\beta_{b,n})l_{b,n}^2 & -3l_{b,n} & (1-6\beta_{b,n})l_{b,n}^2 \\ -6 & -3l_{b,n} & 6 & -3l_{b,n} \\ 3l_{b,n} & (1-6\beta_{b,n})l_{b,n}^2 & -3l_{b,n} & 2(1+3\beta_{b,n})l_{b,n}^2 \end{bmatrix}. \tag{2.17}$$

The mass matrix for the element is

$$\mathbf{M}_{b,n} = \frac{M_{b,n}l_{b,n}}{(1+12\beta_{b,n})^2}\begin{bmatrix} M_{b,n_{1,1}} & M_{b,n_{1,2}} & M_{b,n_{1,3}} & M_{b,n_{1,4}} \\ M_{b,n_{1,2}} & M_{b,n_{2,2}} & M_{b,n_{2,3}} & M_{b,n_{2,4}} \\ M_{b,n_{1,3}} & M_{b,n_{2,3}} & M_{b,n_{1,1}} & -M_{b,n_{1,2}} \\ M_{b,n_{1,4}} & M_{b,n_{2,4}} & -M_{b,n_{1,2}} & M_{b,n_{2,2}} \end{bmatrix}, \tag{2.18}$$

with

$$M_{b,n_{1,1}} = \tfrac{13}{35} + \tfrac{42}{5}\beta_{b,n} + 48\beta_{b,n}^2 + \tfrac{6}{5}\gamma_{b,n}, \tag{2.19}$$

$$M_{b,n_{1,2}} = \left(\tfrac{11}{210} + \tfrac{11}{10}\beta_{b,n} + 6\beta_{b,n}^2\right) l_{b,n} + \gamma_{b,n}\left(\tfrac{1}{10} - 6\beta_{b,n}\right) l_{b,n}, \tag{2.20}$$

$$M_{b,n_{1,3}} = \tfrac{9}{70} + \tfrac{18}{5}\beta_{b,n} + 24\beta_{b,n}^2 - \tfrac{6}{5}\gamma_{b,n}, \tag{2.21}$$

$$M_{b,n_{1,4}} = -\left(\tfrac{13}{420} + \tfrac{9}{10}\beta_{b,n} + 6\beta_{b,n}^2\right) l_{b,n} + \gamma_{b,n}\left(\tfrac{1}{10} - 6\beta_{b,n}\right) l_{b,n}, \tag{2.22}$$

$$M_{b,n_{2,2}} = \left(\tfrac{1}{105} + \tfrac{1}{5}\beta_{b,n} + \tfrac{6}{5}\beta_{b,n}^2\right) l_{b,n}^2 + 2\gamma_{b,n}\left(\tfrac{1}{15} + \beta_{b,n} + 24\beta_{b,n}^2\right) l_{b,n}^2, \tag{2.23}$$

$$M_{b,n_{2,3}} = \left(\tfrac{13}{420} + \tfrac{9}{10}\beta_{b,n} + 6\beta_{b,n}^2\right) l_{b,n} - \gamma_{b,n}\left(\tfrac{1}{10} - 6\beta_{b,n}\right) l_{b,n}, \tag{2.24}$$

$$M_{b,n_{2,4}} = -\left(\tfrac{1}{140} + \tfrac{1}{5}\beta_{b,n} + \tfrac{6}{5}\beta_{b,n}^2\right) l_{b,n}^2 - \gamma_{b,n}\left(\tfrac{1}{30} + 2\beta_{b,n} - 24\beta_{b,n}^2\right) l_{b,n}^2. \tag{2.25}$$

The total mass matrix $\mathbf{M}_b$ and stiffness matrix $\mathbf{C}_b$ can be composed by adding the contributions of all the beam elements. The natural dry mode shapes are found by solving the eigenvalue problem

$$\left(\mathbf{C}_b - \omega^2\mathbf{M}_b\right)\vec{h}_b = \vec{0} \tag{2.26}$$

where ω is the angular frequency and $\vec{h}_b$ the corresponding mode shape. Note that the vector $\vec{h}_b$ only contains the degrees of freedom of the beam. The mode shapes are scaled such that the maximum displacement of the nodes is $1[m]$. This ensures that the flexible mode shapes have the same order of displacement

as the rigid-body mode shapes, see Section 2.5. The modal stiffness matrix is equal to

$$\mathbf{C}_e = \sum_{n=1}^{N_{\text{elements}}} \mathbf{h}_{b,n} \cdot \mathbf{C}_{b,n} \cdot \mathbf{h}_{b,n}^T. \tag{2.27}$$

The modal mass matrix should also include the contribution of the rigid-body mode shapes because of the coupling between the rigid-body modes and elastic modes for the mass matrices of the 3D ship sections. The first step is to change the elastic mode shapes at the nodes of the beam elements to account for all six degrees of freedom

$$\vec{h}_{b,n,\mathbb{R}6}^{\,i} = [0, 0, v_{b,n}^i, 0, -\theta_{b,n}^i, 0]^T. \tag{2.28}$$

The rigid-body mode shapes (2.10) are added to the elastic mode shapes using (2.9). The mass matrices for the total body and the sections are calculated using equation (2.11). The mass contribution to the hydrostatic stiffness matrix is calculated using (2.14).

The flexible modal displacement field has to be calculated for all points describing the geometry of the body. The beam mode shapes $\mathbf{h}_b$ are only known for the nodes of the beam model. This mode shape is interpolated in the x-direction to calculate the mode shape at the same x-location as point p but still on the y and z-coordinate of the center of gravity. The interpolated mode shape is denoted by $[v_{b,int_p}^i, \theta_{b,int_p}^i]$. The resulting mode shape for location x_p, y_p, z_p is

$$\vec{h}_p^{\,i} = [-\theta_{b,int_p}^i \cdot (z_p - G_z), 0, v_{b,int_p}^i, 0, -\theta_{b,int_p}^i, 0]^T. \tag{2.29}$$

The last step is to calculate the modal participation factors for the bending moment, $\vec{M}_{b,n}$ and shear force, $\vec{Q}_{b,n}$ of the centers of the beam elements

$$M_{b,n}^i = \frac{EI_{by,n}}{l_{b,n}} \left(\theta_{b,n+1}^i - \theta_{b,n}^i\right), \tag{2.30}$$

$$Q_{b,n}^i = \frac{6\beta_{b,n} GA_{bz,n}}{(1 + 12\beta_{b,n}) l_{b,n}} \left[2\left(v_{b,n}^i - v_{b,n+1}^i\right) + l_{b,n}\left(\theta_{b,n+1}^i + \theta_{b,n}^i\right)\right]. \tag{2.31}$$

2.7 Balancing

The next step is to balance the ship for the still water condition. Most ships have a SWBM which is in the same order as the wave bending moment. The SWBM will cause displacements of the elastic modes in the still water. The selected draft and trim may also be unbalanced with respect to the actual structural weight and the center of gravity, these motions are also balanced. It should be noted that it is assumed that the displacements needed to balance

the model remain small. Therefore, the initial draft and trim should be close to the correct values.

All panels will be displaced by the balancing procedure. This causes some complications for the hydrodynamic mesh. To solve the BVP accurately, it is necessary that none of the panels cross the still water plane. This is the case for the original hydrodynamic mesh but, due to the displacements caused by the balancing, the balanced mesh will have panels that cross the still water line. This problem is solved by creating a new hydrodynamic mesh based on the balanced geometry.

As an external program is used to create the hydrodynamic mesh, the displacements by balancing can only be applied by displacing the ship sections which are used to created the hydrodynamic mesh. Therefore, the hydrodynamic mesh can only be deformed with a beam-like shape. To ensure that the final balanced shape of the different meshes are equal, the whole balancing is done using shapes of a virtual beam. Only the displacements in the z-direction are considered, as this is the only direction in which the hydrostatic pressure changes.

2.7.1 Restoring matrix

The Newton-Raphson method is used to find the balanced displacements. The total restoring stiffness should be known to apply this method. The total restoring is the summation of the hydrostatic restoring and the structural stiffness. The total structural stiffness matrix is equal to

$$\mathbf{C}_{te} = \begin{bmatrix} \mathbf{0}_{6\times 6} & \mathbf{0}_{6\times \mathrm{nflex}} \\ \mathbf{0}_{\mathrm{nflex}\times 6} & \mathbf{C}_e \end{bmatrix}. \tag{2.32}$$

The hydrostatic restoring matrix can be calculated using the formulas presented in [37] and [28]. The formulations presented in these papers are equivalent but they are difficult to evaluate for the geometry of a real ship. The calculation of the restoring matrix is simplified by first calculating the contribution for every panel in its local axis system and then calculating the modal contribution using

$$\mathbf{C}_h = \mathbf{C}_m + \sum_{n=1}^{N_{\mathrm{panels}}} \mathbf{h}_n \cdot \mathbf{c}_{h,n} \cdot \mathbf{h}_n^T. \tag{2.33}$$

When applying the same simplifications for the gradient of the mode shape as described in Section 2.2, the contribution for a panel in its local axis system

can be written as

$$\mathbf{c}_{h,n} = a_n \cdot \rho \cdot g \cdot \begin{bmatrix} 0 & 0 & -n_x & 0 & -z \cdot n_z & z \cdot n_y \\ 0 & 0 & -n_y & z \cdot n_z & 0 & -z \cdot n_x \\ 0 & 0 & -n_z & -z \cdot n_y & z \cdot n_x & 0 \\ 0 & -z \cdot n_z & z \cdot n_y & 0 & 0 & 0 \\ z \cdot n_z & 0 & -z \cdot n_x & 0 & 0 & 0 \\ -z \cdot n_y & z \cdot n_x & 0 & 0 & 0 & 0 \end{bmatrix}, \quad (2.34)$$

where a_n is the area of the panel and $\vec{n}$ the normal.

The gravity contribution of the mass to the hydrostatic matrix $\mathbf{C}_m$ is calculated by the programs which calculate the structural mode shapes, see Sections 2.5 and 2.6. The matrix $\mathbf{C}_m$ can also be calculated using equation (2.14) for rigid bodies. The total mass matrix and the mode shapes at the center of gravity should be used in this case.

2.7.2 Balancing iteration

The balancing iteration is illustrated in Figure 2.18. Vector $\vec{\xi}_{sw}$ is the modal displacement needed to obtain an equilibrium of the forces in still water. This vector is set to zero at the start of the iterations.

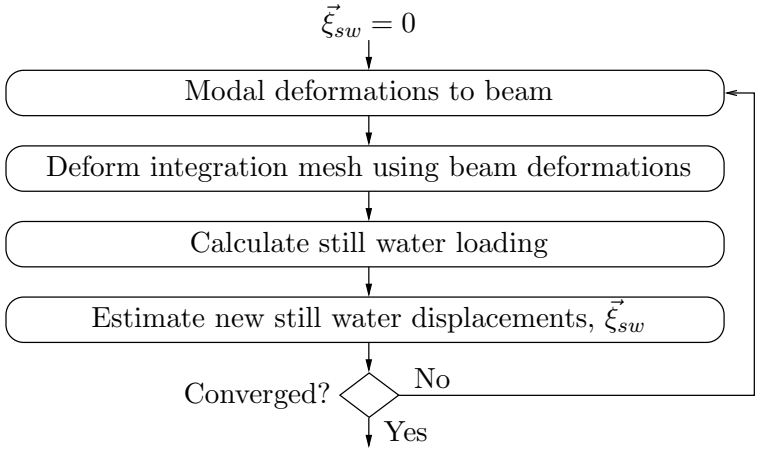

Figure 2.18: Finding balanced displacements.

The first step is to map the modal displacement to a virtual beam model. The same procedure to create a beam-like model of the mode shapes as explained in Section 2.5 is applied in this case. A deformed mesh is created in the second step by displacing all nodes of the integration mesh in the z-direction using the displacement of the virtual beam.

The resulting still water force is calculated in the third step. The still water hydrostatic force is equal to

$$f_{hs}^{i} = \iint_{S_b} \rho g z \vec{h}_i \vec{n} \, \mathrm{d}s, \tag{2.35}$$

where S_b is the wetted surface of the body. The gravity force $\vec{f}_{\text{grav}}$ is calculated using equation (4.58). The total still water force is equal to

$$\vec{f}_{sw} = \vec{f}_{hs} + \vec{f}_{\text{grav}} + \mathbf{C}_{te}\vec{\xi}_{sw}. \tag{2.36}$$

The resulting still water force will cause an additional modal displacement of

$$\Delta\vec{\xi}_{sw} = -\left(\mathbf{C}_{te} + \mathbf{C}_h\right)^{-1} \vec{f}_{sw}. \tag{2.37}$$

This gives a new estimation of the still water deformation

$$\vec{\xi}_{sw} = \vec{\xi}_{sw} + \Delta\vec{\xi}_{sw}. \tag{2.38}$$

All degrees of freedom which do not have a positive restoring value on the main diagonal, e.g. surge and sway, are excluded from equation (2.37). The still water deformation of these modes is set to zero.

The iteration is stopped when the norm of the vector $\Delta\vec{\xi}_{sw}$ is at least one million times smaller than the norm of the same vector at the first iteration step. It should be noted that the hydrostatic restoring matrix is only calculated using the original undeformed mesh. It would be more consistent to recompute this matrix every iteration step, however, this requires a lot more computational effort. As the static displacements should remain small, it is assumed that the hydrostatic restoring matrix will not change significantly and will give a good estimation for all iteration steps. The restoring matrix is only used to make an estimation for the next iteration, therefore, it is not essential to recompute this matrix for every iteration. The robustness of the iteration procedure is increased by scaling down the vector $\Delta\vec{\xi}_{sw}$ if the norm of vector $\Delta\vec{\xi}_{sw}$ is larger than the norm of the same vector in the previous iteration step.

2.7.3 New meshes

The new hydrodynamic mesh and integration mesh are created after the balanced deformations are found. The integration mesh is created by displacing all the nodes using the beam deformation. The hydrodynamic mesh has to be recreated to correctly account for the still water plane. All hull lines and definition points (e.g. bulb definition) are displaced using the beam deformations and the mesh program is run to create the new, deformed mesh.

The elastic mode shapes were projected onto the original hydrodynamic mesh and they should be projected again onto the new hydrodynamic mesh.

This is done by rerunning the program that projects the elastic mode shapes. Projecting the elastic mode shapes onto a deformed mesh is inconsistent as the structural model does not contain the still water deformations. The still water deformation is stored and read by the program that projects the elastic mode shapes. The program subtracts the still water deformation from the shape of the deformed mesh for every point before projecting the mode shapes. This ensures a consistent projection of the mode shapes.

The final still water displacement vector $\vec{\xi}_{sw}$ is stored as the internal loads by these displacements should be taken into account in the time domain seakeeping calculation.

The procedure described above can only be applied if it is possible to create a new deformed hydrodynamic mesh. This is not the case for ships that are built using only flat plates like FPSO's and barges. A different program has been developed for creating the hydrodynamic meshes for these ships. As this program can only create flat planes, it is not possible to create a deformed hydrodynamic mesh. For this case, the deformation vector is still calculated to get a compensating internal moment to avoid the whipping and deformation due to the SWBM during the time domain seakeeping calculation. This deformation vector is equal to

$$\vec{\xi}_{sw} = \mathbf{C}_{te}^{-1} \vec{f}_{sw}. \tag{2.39}$$

2.8 Pre-processor

The pre-processor formulates the final hydro-elastic problem. The first step is collecting the data from the previous programs and completing the input for each body. The second step is to put the information of all bodies present in the calculation into a final hydro-elastic problem definition.

2.8.1 Single body

The calculation of the elastic modes as explained in Sections 2.5 and 2.6 does not only provide the mode shapes, but also the mass matrix, structural stiffness matrix and the gravity contribution to the hydrostatics. This information must also be calculated for rigid bodies.

The rigid-body mode shapes are defined by equation (2.10). The structural stiffness matrix is equal to zero for rigid bodies. The mass matrix is

$$\mathbf{m} = \begin{bmatrix} M & 0 & 0 & 0 & 0 & 0 \\ 0 & M & 0 & 0 & 0 & 0 \\ 0 & 0 & M & 0 & 0 & 0 \\ 0 & 0 & 0 & M_{I_x} & 0 & 0 \\ 0 & 0 & 0 & 0 & M_{I_y} & 0 \\ 0 & 0 & 0 & 0 & 0 & M_{I_z} \end{bmatrix}, \tag{2.40}$$

with M the mass, and M_{I_x}, M_{I_y} and M_{I_z} the mass moment of inertia around the x, y and z-axis. The gravity contribution to the hydrostatics matrix is calculated using equation (2.14) based on matrix (2.40) and the mode shape at the center of gravity.

Note that this approach to calculate the values of rigid bodies does not allow one to calculate the internal loads because the mass distribution is not included. This mass distribution for rigid bodies can be obtained by running the programs to calculate the elastic modes but requesting to compute zero elastic modes.

The hydrostatic matrix has to be calculated for both rigid and flexible bodies. The calculation of the hydrostatic restoring matrix was already briefly introduced in Section 2.7.1. The presented approach is now extended to be able to calculate the hydrostatic restoring matrix for the different 3D sections needed to calculate the internal loads. It should be noted that the calculation of the hydrostatic matrix for generalised modes is still an open discussion in the literature, see [29]. The approach presented here shows, in general, good results and is validated for the rigid-body modes. However, it is difficult to validate the method for elastic modes and internal load calculations. Comparison between the internal loads calculated using the restoring matrix created with the presented method and well accepted methods for rigid bodies shows some small differences. It is not clear what causes these differences. The hydrostatic restoring matrix is not investigated further in this thesis as the hydrostatic restoring force will be calculated by integrating the hydrostatic pressure using the actual location of the body in the time domain. For this, the linear restoring matrix is not used.

The hydrostatic restoring matrix is defined in the Earth system. It is likely that there is an internal load at the boundaries of the 3D ship sections. The translation of this internal load due to the modal displacement will contribute to the restoring matrix. The internal load at the boundaries of a section is equal to

$$\vec{f}_{int,is} = -\iint_{S_b,is} \rho g z \vec{n} \, \mathrm{d}S - g \iiint_{V,is} m \, \mathrm{d}v. \tag{2.41}$$

The contribution of the internal force to the restoring is equal to

$$C_{int,ij,is} = \vec{f}_{int,is}(\nabla \vec{h}^j_{int,is})\vec{h}^i_{int,is}, \tag{2.42}$$

where $\vec{h}_{int,is}$ is the "mode shape" of the internal load. As it is difficult to calculate this mode shape, the contribution of the internal loads is estimated by integrating the contribution defined by (2.42) over the surface where the mode shapes are known. The integral over the surface will result in an internal load which is equal to the buoyancy. The gravity force should then be subtracted. In other words, to integrate the correct amount of internal force, a gravity

reduction factor is introduced

$$\vec{gr}_{is} = \frac{-\iint_{S_b,is} \rho g z \vec{n} \, \mathrm{d}S - g \iiint_{V,is} m \, \mathrm{d}v}{-g \iiint_{V,is} m \, \mathrm{d}v}. \tag{2.43}$$

The contribution of the internal load is estimated as

$$C_{int,ij,is} \approx \sum_{x,y,z} -\vec{gr}_{is} \rho g \iint_{S_b} z \vec{n} (\nabla \vec{h}^j) \vec{h}^i \, \mathrm{d}S. \tag{2.44}$$

The hydrostatic restoring matrix for a section is equal to

$$\mathbf{C}_{h,is} = \mathbf{C}_{m,is} + \mathbf{C}_{int,is} + \sum_{n=1}^{N\text{panels}_{is}} \mathbf{h}_n \cdot \mathbf{c}_{h,n} \cdot \mathbf{h}_n^T, \tag{2.45}$$

with $\mathbf{C}_{m,is}$ as defined in (2.14) and $\mathbf{C}_{h,n}$ equal to (2.34).

The next step is the creation of a set of dummy Gauss points. These dummy points will be used to evaluate the pressure from the calculated potential. The location of the original Gauss points cannot always be used to evaluate the pressure as these points may fall inside the hydrodynamic mesh. The hydrodynamic pressure will also depend on the gradient of the potential for forward speed problems. The gradient of the potential is discontinuous across the hydrodynamic mesh. The pressure can only be evaluated at or outside the hydrodynamic mesh due to this discontinuity. The Gauss points can fall inside the hydrodynamic mesh because the Gauss points are defined for the integration mesh. The integration mesh can be the structural (3D-FEM) mesh which should describe the same geometry but has usually a very different mesh compared to the hydrodynamic mesh. This difference between the meshes usually results that a part of the Gauss points will fall inside the hydrodynamic (BEM) mesh. This is illustrated in Figure 2.19

Figure 2.19 also shows the approach used to ensure that the dummy Gauss points are outside the hydrodynamic mesh but still close to the original position. The dummy points are first located at the location of the original Gauss point. The same projection procedure as described in Section 2.5.1 is used to make a projection of the dummy Gauss point onto the hydrodynamic mesh. This projection point is used to judge if the dummy point falls inside the hydrodynamic mesh. The dummy point will be moved slightly further than the projection point if the dummy point is inside the hydrodynamic mesh. This ensures that all dummy Gauss points are located outside the hydrodynamic mesh and can be used to evaluate the pressure.

The dummy Gauss points that are outside the hydrodynamic mesh are also moved to a position just outside the hydrodynamic mesh to ensure that the pressure is evaluated very close to the body surface.

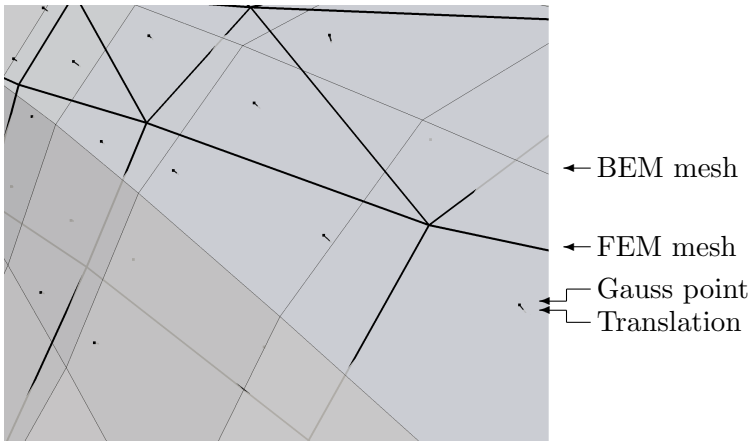

Figure 2.19: Translation of dummy Gauss points.

As a final note, it is assumed for the previous calculations that all bodies have at least the rigid-body modes. However, it is also possible to add bodies without any degree of freedom. This can be used to model fixed objects like the sides of a towing tank. The size of all matrices and vectors are zero for these bodies except for the meshes describing the geometry of the body.

2.8.2 Final hydro-elastic problem

The next step is to combine the separate bodies into one hydro-elastic problem. This step is also performed for single body problems.

The first step is to translate the bodies in the x and y-direction and rotate them around the z-axis to put each body in the correct relative position. Only the meshes have to be translated and rotated, the mode shapes only have to be rotated and all other matrices remain the same because they describe properties in the body system.

A single hydrodynamic and integration mesh is created from the meshes of the different bodies. It should be noted that, in general, a multi-body configuration has no axis of symmetry. The symmetric parts of the different bodies are also added to the final hydrodynamic mesh if the final problem has no symmetry. The final integration mesh will always contain the total geometry of the body or bodies, as using symmetry for the integration of the hydrodynamic forces hardly increases the calculation performance of the seakeeping programs.

The degrees of freedom of the different bodies are simply stacked on top of each other. For example, the final number of degrees of freedom will be twelve for a multi-body problem with two rigid ships. The first six modes will be the rigid-body modes of ship one and the second six are the rigid-body modes of

the second ship, recall Figure 1.3.

The final mode shapes are defined for all degrees of freedom and the total geometry of all bodies. These mode shapes are created by stacking the original mode shapes for the different bodies and setting the modal displacements vector to zero for all points of the other bodies.

Matrix $\mathbf{S}$ is introduced to distinguish between the different modes. This matrix is a collection of $\mathbf{S}_{ib}$ matrices which are defined for every body in the calculation

$$\mathbf{S} = [\mathbf{S}_1, \mathbf{S}_2, \ldots, \mathbf{S}_{N_{\text{bodies}}}], \tag{2.46}$$

where ib is the body number and N_{bodies} the total number of bodies.

The number of rows of the matrices is equal to the number of modes used. The number of columns of the $\mathbf{S}_{ib}$ matrix is equal to six, because it represent the six rigid-body modes. The matrix $\mathbf{S}$ will have the number of bodies times six columns. A one in the matrices maps the mode used to the rigid-body mode which it represents. All other elements of the matrix are zero. The row for a flexible mode will consist of only zeroes. This property of the $\mathbf{S}$ matrix is used to identify the flexible modes.

For calculations with only one rigid-body, the $\mathbf{S}$ matrix will be equal to $\mathbf{S}_1$ and has a size of six by six with ones on the main diagonal and all other elements are zero (the 6x6 identity matrix). For every flexible mode that is added to this ship, a row of zeroes is added to the $\mathbf{S}$ matrix, this matrix is illustrated in Figure 2.20(a). For a calculation with two rigid ships the $\mathbf{S}$ matrix has a size of twelve by twelve and the $\mathbf{S}_1$ and $\mathbf{S}_2$ twelve by six. This $\mathbf{S}$ matrix has ones at the main diagonal and all other elements are zero (the 12x12 identity matrix), see Figure 2.20(b).

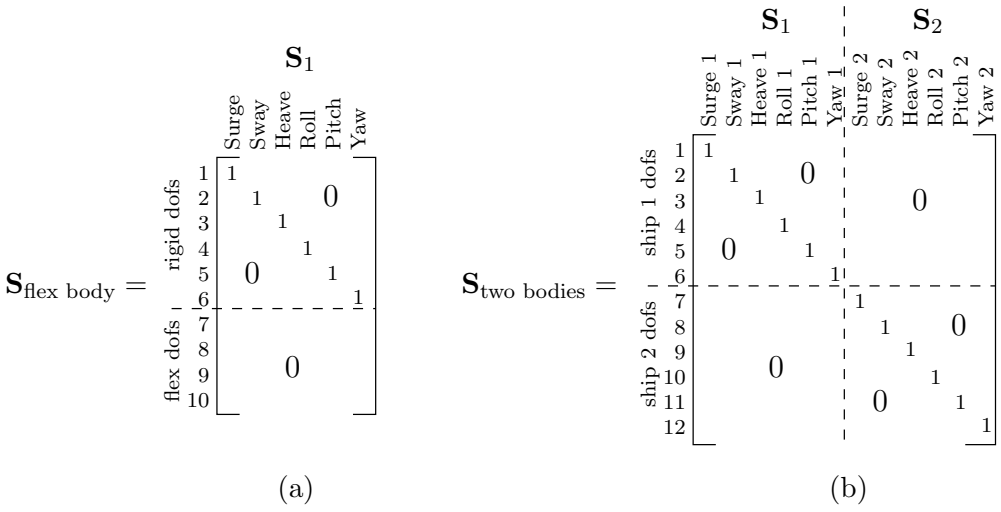

(a) (b)

Figure 2.20: Examples of the $\mathbf{S}$ matrix.

Let $\vec{y}$ be a vector which contains values in terms of all modal coordinates. The values for the rigid-body modes of body ib, $\vec{y}_{ib}$, are obtained by

$$\vec{y}_{ib} = \mathbf{S}_{ib}^T \cdot \vec{y}. \tag{2.47}$$

The vector in the modal coordinates can be created using values that are known for the rigid-body modes and values for the flexible modes $\vec{y}_f$ by

$$\vec{y} = \vec{y}_f + \sum_{ib=1}^{N_{\text{body}}} \left\{ \mathbf{S}_{ib} \cdot \vec{y}_{ib} \right\}. \tag{2.48}$$

Note that the vector $\vec{y}_f$ has the same size as the vector $\vec{y}$ and should have values equal to zero for the rigid modes. The rigid-body values usually correspond to the values in the Cartesian system.

The mass, structural stiffness and hydrostatic restoring matrices of the different bodies are also stacked into matrices for the complete problem. As there is no influence between the bodies for these matrices, these matrices are stacked like

$$\mathbf{P}_t = \begin{bmatrix} \mathbf{P}_1 & \mathbf{0} \\ \mathbf{0} & \mathbf{P}_2 \end{bmatrix}. \tag{2.49}$$

The stacking of the matrices of the different sections is done as

$$\mathbf{P}_{t,is} = \begin{cases} \begin{bmatrix} \mathbf{P}_{1,is_1} & \mathbf{0} \\ \mathbf{0} & \mathbf{0} \end{bmatrix} & \text{if } is \in \text{ body 1} \\ \\ \begin{bmatrix} \mathbf{0} & \mathbf{0} \\ \mathbf{0} & \mathbf{P}_{2,is_2} \end{bmatrix} & \text{if } is \in \text{ body 2} \end{cases}, \tag{2.50}$$

where is_1 and is_2 represent the original section numbering of the two bodies and is the section number for the total problem. The approach described by the previous two equations is applicable for any number of bodies.

Additional information necessary for solving the total hydro-elastic problem, like locations for internal loads calculations, modal participation factors for bending moments, shear forces or stresses, still water displacements vectors, center of gravity locations, etc. is also created by combining the values of the different bodies in this way.

Note that the different bodies are not coupled yet. The added mass and damping will create the hydrodynamic coupling between the bodies. In Chapter 4 it is explained how the bodies can be coupled mechanically in the time domain calculations. There are no mechanical couplings between the bodies in the frequency domain. However, the user can force a coupling by using an user defined stiffness matrix.

Chapter 3

Frequency domain

The frequency domain approach is convenient for solving a linear seakeeping response calculation. Knowing the response to waves with different frequencies allows one to calculate the response for different sea states using superposition. The frequency domain approach also allows for a direct spectral analysis which avoids long calculations in order to obtain statistics with sufficient accuracy. This makes a frequency domain analysis usually much faster compared to a time domain analysis for linear problems.

However, it is difficult to add non-linearities to the frequency domain calculation. The computation of transient responses, like slamming induced whipping, are also difficult to compute using the frequency domain approach. In this thesis, the non-linear seakeeping and whipping analysis will, therefore, be performed in the time domain where it is more convenient to account for the non-linearities and transient responses. Nevertheless, the approach used to solve the seakeeping response in the time domain requires the linear coefficients for the added mass, damping and diffraction force which are calculated in the frequency domain.

This chapter explains the calculation of these hydrodynamic coefficients and addresses the calculation of the ship motions, internal loads and wet natural frequencies in the frequency domain. The incoming waves are defined in the first section of this chapter. The approach to compute the hydrodynamic coefficients by solving the Boundary Value Problem (BVP) is explained in the second section. The third section explains the calculation of the response and internal loads. The approach for computing the wet natural modes is presented in the last section.

3.1 Incoming waves

The waves are assumed to be linear sinusoidal waves in deep water. Figure 3.1 shows the definition of the heading of the body μ towards the waves. A heading

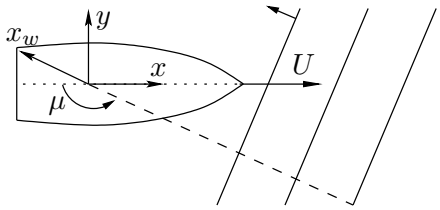

Figure 3.1: Wave definition.

of zero degrees results in following waves and 180 degrees results in head waves.

The total distance in the wave direction is

$$x_w = x\cos\mu + y\sin\mu, \tag{3.1}$$

and U is the mean forward speed of the ship.

The wave elevation ζ of a single wave component is equal to

$$\zeta(x_w, t) = \zeta_a \cos\left(\omega t - x_w k + \varepsilon\right), \tag{3.2}$$

with ζ_a the wave amplitude, ε the phase angle and k the wave number, such that,

$$k = \omega^2/g. \tag{3.3}$$

The body will encounter the waves at a different frequency ω_e due to its forward velocity, this is defined by

$$\omega_e = \omega - kU\cos\mu. \tag{3.4}$$

3.2 Hydrodynamic coefficients

The fluid motion around the body or bodies should be known in order to calculate the pressure at the hull and the resulting hydrodynamic coefficients. A few assumptions are made to be able to solve the fluid motions using a BVP:

- The fluid is assumed to be incompressible, inviscid, non-rotational and without surface tension.
- Body motions remain small.
- An infinite depth of the fluid is assumed.
- The fluid and body motions are harmonic.

The fluid motion is determined by solving a BVP using potential flow. This BVP is first formulated for the zero speed case. This zero speed solution is partly adapted to account for forward speed.

3.2.1 Zero speed problem

The total velocity potential in the fluid Φ is both time and space dependent [53, 21]. This potential can be split in a space and time dependent part

$$\Phi(x, y, z, t) = \Re\{\varphi(x, y, z)e^{-i\omega t}\}, \tag{3.5}$$

as the fluid motions are assumed to be harmonic in time.

The total velocity potential is decomposed into the incident, diffracted and for every degree of freedom the radiated components

$$\varphi = \varphi_I + \varphi_D - i\omega \sum_{j=1}^{N_{\text{dof}}} \vec{\xi}_j \cdot \varphi_{Rj}, \tag{3.6}$$

where

φ_I	incident potential,
φ_D	diffraction potential,
φ_{Rj}	j-th radiation potential,
N_{dof}	number of degrees of freedom.

The space dependent part of the incident wave potential is equal to

$$\varphi_I = \frac{-i\zeta_a g}{\omega} e^{k(z-ix_w)}. \tag{3.7}$$

The diffraction and radiation velocity potentials are solved using the following BVP

$$\begin{cases} \Delta\varphi = 0 & \text{in the fluid,} \\ -k\varphi + \dfrac{\partial\varphi}{\partial z} = 0 & z = 0, \\ \dfrac{\partial\varphi}{\partial\vec{n}} = V_n & \text{on } S_b, \\ \lim\left[\sqrt{kR}\left(\dfrac{\partial\varphi}{\partial R} - ik\varphi\right)\right] = 0 & R \to \infty, \end{cases} \tag{3.8}$$

where V_n denotes the normal velocity which depends on the considered potential

$$\frac{\partial\varphi_D}{\partial\vec{n}} = -\frac{\partial\varphi_I}{\partial\vec{n}}, \qquad \frac{\partial\varphi_{Rj}}{\partial\vec{n}} = \vec{h}_j\vec{n}. \tag{3.9}$$

The first equation of the BVP (3.8) ensures the conservation of mass. The second equation is the linearised free surface boundary condition. This condition ensures that the fluid velocity at the free surface is equal to the velocity of the free surface itself and that the pressure is equal to the ambient pressure which is set to zero. This surface boundary condition is linearised around $z = 0$. The third equation of (3.8) ensures that no fluid will cross the body boundary by setting the velocity of the fluid equal to the velocity of the body boundary

in the normal direction of the body surface. The last equation is the radiation condition which ensures that the diffracted and radiated potentials approach zero far away from the body.

This BVP is solved numerically by using constant source distributions over the hydrodynamic mesh panels. Pulsating Green's source functions are used. These fulfill the linearised free surface boundary condition and the radiation condition. The source strengths are solved by satisfying the body boundary condition at the centers of the hydrodynamic panels.

The Green's sources used will also satisfy the surface boundary condition at the "free surface" inside the body which can cause a kind of artificial resonance of the wave system inside the body. The frequencies where the resonances appear are so-called irregular frequencies. This resonance problem is alleviated by placing additional panels at the free surface inside the body.

The different pressure components are calculated from the potentials after solving the BVP by using the linearised Bernoulli equation $p = -\rho\Phi_t$ which leads to

$$p_I = i\omega\rho\varphi_I, \tag{3.10}$$

$$p_D = i\omega\rho\varphi_D, \tag{3.11}$$

$$p_{Rj} = i\omega\rho\varphi_{Rj}, \tag{3.12}$$

where p_I, p_D and p_{Rj} are the pressure by the incident wave, the diffraction pressure and the radiation pressure due to motions of the j^{th} mode, respectively.

The BVP (3.8) is solved for a range of frequencies which are relevant for the seakeeping problem. It is difficult to solve the BVP for very high frequencies due to the small wave lengths. The hydrodynamic mesh has to be very fine in order to solve the BVP at high frequencies, requiring a lot of computational effort and a significant amount of memory. The wet natural frequencies of the ship structure occur in the frequency range for which the BVP cannot be solved in a computationally efficient manner. Fortunately, the small wave length corresponding to such high frequencies results in a negligible hydrodynamic damping compared to the structural damping. This allows the use of the infinite frequency solution for these high frequencies. The surface boundary condition is set to $\varphi = 0$ to solve the BVP for the infinite frequency.

3.2.2 Adjustments for forward velocity

The above equations are only valid for zero speed problems. It is still very difficult to consistently solve the BVP for forward speed seakeeping problems, even for purely rigid-body problems. A few adjustments are made to the above equations to better account for the forward velocity. However, the presented approach does not fully account for the forward speed.

The first adjustment is to include the effort of forward speed via the encounter frequency (3.4). The second adjustment is to account for the contribution of the velocity in the body boundary condition. The still water fluid flow around the body due to the forward velocity has to be solved first. This potential $\bar{\varphi}$ is usually solved using a double body approach.

The velocity vector of the steady flow relative to the moving reference frame is [36]

$$\vec{W} = U\nabla\left(\bar{\varphi} - x\right). \tag{3.13}$$

This steady flow velocity can also be approximated by a uniform flow $\vec{W} = -U\vec{i}$ if the double body approximation is not available.

Due to the forward velocity the body boundary condition of equation (3.8) becomes [36]

$$\frac{\partial \varphi_{Rj}}{\partial \vec{n}} = \vec{h}_j\vec{n} + \frac{i}{\omega_e}\left\{(\nabla\vec{W})i\vec{h}_j - (\nabla\vec{h}_j)\vec{W}\right\} \tag{3.14}$$

Accounting for the forward velocity when evaluating of the pressure is the last adjustment of the zero speed equations

$$p = i\omega_e\rho\varphi - \rho\vec{W}\nabla\varphi. \tag{3.15}$$

The surface boundary condition remains equal to the zero speed condition. Two commercial programs, HYDROSTAR and PRECAL, are used to solve the double body flow, the BVP and to calculate the pressures. Unfortunately, both programs could not yet include the forward speed corrections of the body boundary condition and the pressure for the flexible modes at the time the calculations which are presented in this thesis were performed. Therefore, the forward velocity is only included via the encounter frequency for the results presented in this thesis.

3.2.3 Coefficients

The hydrodynamic coefficients for the total body and the sections are obtained by an integration of the pressure over the wetted surface, using the integration mesh. As explained in Section 2.8.1, the dummy Gauss points are used as the locations to evaluate the pressure. The pressure is integrated using the original Gauss points. The hydrodynamic coefficients are equal to

$$F_{i,I,is} = \iint_{s_B,is} p_I\vec{h}_i\vec{n}\,\mathrm{d}S, \tag{3.16}$$

$$F_{i,D,is} = \iint_{s_B,is} p_D\vec{h}_i\vec{n}\,\mathrm{d}S, \tag{3.17}$$

$$\omega_e A_{ij,is} + i\omega_e B_{ij,is} = \iint_{s_B,is} p_{Rj}\vec{h}_i\vec{n}\,\mathrm{d}S, \tag{3.18}$$

with

$\vec{F}_I$	incident wave force,
$\vec{F}_D$	diffraction force,
$\mathbf{A}$	hydrodynamic added mass,
$\mathbf{B}$	hydrodynamic damping.

3.3 Response

The motion response is calculated for each frequency for which the hydrodynamic coefficients are obtained. The internal loads due to the external loads and motions of the ship are also computed. The last part of the calculation of the response in the frequency domain is the investigation of the effect of hydro-elasticity.

3.3.1 Motions

The motions are solved using the Newton equation. When assuming harmonic motion the Newton equation can be written as

$$\begin{aligned}(\mathbf{m} + \mathbf{A}(\omega_e))\,\ddot{\vec{\xi}} + (\mathbf{B}\,(\omega_e) + \mathbf{B}_u)\,\dot{\vec{\xi}} + (\mathbf{C}_{te} + \mathbf{C}_h + \mathbf{C}_u)\,\vec{\xi} = \\ \big(\vec{F}_I(\omega_e) + \vec{F}_D(\omega_e)\big)\Re\{e^{-i\omega_e t}\},\end{aligned} \tag{3.19}$$

where $\mathbf{B}_u$ is the additional damping matrix and $\mathbf{C}_u$ is the additional stiffness matrix defined by the user. These matrices can, for example, be used to add structural damping and/or connect the separate bodies through springs.

A solution is found by writing the resulting harmonic motion as

$$\vec{\xi} = \vec{\xi}_a \cdot \Re\{e^{-i\omega_e t}\}, \tag{3.20}$$

where $\vec{\xi}_a$ is the complex response amplitude operator (RAO). The RAO for the modal motions is found by solving the following system of equations

$$\begin{aligned}\left\{-\omega_e^2\,(\mathbf{m} + \mathbf{A}(\omega_e)) - i\omega_e\,(\mathbf{B}\,(\omega_e) + \mathbf{B}_u) + (\mathbf{C}_{te} + \mathbf{C}_h + \mathbf{C}_u)\right\}\vec{\xi}_a = \\ \vec{F}_I(\omega_e) + \vec{F}_D(\omega_e).\end{aligned} \tag{3.21}$$

3.3.2 Internal loads

As discussed in Section 1.5, the internal loads can be calculated using two methods. The first method consist of integrating the internal and external forces up to the internal load plane. The second method uses the modal participation factors which are calculated if a beam model is used to model the structure, see Section 2.6.

The first method starts with computing the difference between the internal and external forces for every 3D ship section separately, see Section 2.4.1. The resulting force F_{res} at a 3D section is equal to

$$\begin{aligned}\vec{F}_{res,is} = \Big\{ &- \omega_e^2 \left(\mathbf{m}_{is} + \mathbf{A}_{is}(\omega_e)\right) - i\omega_e \left(\mathbf{B}_{is}\left(\omega_e\right) + \mathbf{B}_{u,is}\right) \\ &+ \left(\mathbf{C}_{te,is} + \mathbf{C}_{h,is} + \mathbf{C}_{u,is}\right) \Big\}\vec{\xi}_a - \vec{F}_{I,is}(\omega_e) - \vec{F}_{D,is}(\omega_e).\end{aligned} \tag{3.22}$$

The internal load at the plane $\vec{F}_{int,ic}$ is the summation of the resulting forces at all associated sections, see Section 2.4.1

$$\vec{F}_{int,ic} = \sum_{is=1}^{N_{\text{sections}}} \vec{F}_{res,is} \qquad \text{for } is \text{ associated to } ic. \tag{3.23}$$

This internal load vector is defined in the modal coordinate, see equation (2.1). However, the internal loads should be calculated in the Cartesian system. The load vector in the Cartesian system are the modal forces and moments of the rigid-body modes of the body ib for which the internal loads are calculated. These can be extracted using the matrix $\mathbf{S}$, see Section 2.8.2,

$$\vec{F}_{int,ic,\mathbb{R}6} = \mathbf{S}_{ib}^T \cdot \vec{F}_{int,ic}, \tag{3.24}$$

where $\mathbb{R}6$ indicates a vector in the Cartesian system.

The hydrodynamic forces, and thereby the internal loads, are defined with respect to the center of gravity. The moments of the internal loads at the location of the cut $\vec{p}_{ic}$ are

$$\vec{F}_{int,ic,\mathbb{R}6,(4:6),p_{ic}} = \vec{F}_{int,ic,\mathbb{R}6,(4:6)} + (\vec{G} - \vec{p}_{ic}) \times \vec{F}_{int,ic,\mathbb{R}6,(1:3)}. \tag{3.25}$$

The other method to obtain the internal loads uses the modal participation factors. Using (2.30) as modal participation factors will give the bending moment and (2.31) the shear force. The total force or moment is obtained by

$$F_{int,ic}^j = \sum_{i=1}^{N_{\text{dof}}} p_{f,ic,i}^j \xi_i, \tag{3.26}$$

with $p_{f,ic}^j$ the modal participation factors for an internal load and where j indicates the different load components for the same location. Since this approach gives an estimation of the internal loads, the results will converge to the correct internal load if many flexible modes are included in the calculation.

3.3.3 Contribution of elastic modes

The effect of hydro-elasticity can be investigated by separating the contributions of the rigid and elastic modes. The method described in [31] is used for

this separation. The quasi-static and dynamic structural responses are also separated in this method. The quasi-static assumption is often used when the seakeeping loads are transferred to a 3D-FEM method. The dynamic effects will usually not be accounted for in the 3D-FEM results by using the quasi-static assumptions.

The modes are divided into rigid-body and elastic modes, the motions are also separated into the structural quasi-static and the dynamic parts

$$\vec{\xi} = \begin{Bmatrix} \vec{\xi}^R \\ \vec{\xi}^E \end{Bmatrix} = \begin{Bmatrix} \vec{\xi}_0^R + \vec{\xi}_d^R \\ \vec{\xi}_0^E + \vec{\xi}_d^E \end{Bmatrix}. \tag{3.27}$$

The motion equation (3.21) is rewritten as

$$\left(\begin{bmatrix} \mathbf{RR} & \mathbf{RE} \\ \mathbf{ER} & \mathbf{EE} \end{bmatrix} + \begin{bmatrix} \mathbf{0} & \mathbf{0} \\ \mathbf{0} & \mathbf{C}_e \end{bmatrix} \right) \begin{Bmatrix} \vec{\xi}^R \\ \vec{\xi}^E \end{Bmatrix} = \begin{Bmatrix} \vec{F}^R \\ \vec{F}^E \end{Bmatrix}. \tag{3.28}$$

Matrix $\mathbf{R}$ indicates the rigid-body components of the left hand side of equation (3.21). The elastic components are in the matrix $\mathbf{E}$ except for the structural stiffness matrix $\mathbf{C}_e$. The structural quasi-static response is

$$\mathbf{RR} \cdot \vec{\xi}_0^R = F^R, \tag{3.29}$$

$$\mathbf{C}_e \cdot \vec{\xi}_0^E = F^E - \mathbf{ER} \cdot \vec{\xi}_0^R. \tag{3.30}$$

The structural dynamic part of the motion is solved by inserting equations (3.27), (3.29) and (3.30) into equation (3.28)

$$\left(\begin{bmatrix} \mathbf{RR} & \mathbf{RE} \\ \mathbf{ER} & \mathbf{EE} \end{bmatrix} + \begin{bmatrix} \mathbf{0} & \mathbf{0} \\ \mathbf{0} & \mathbf{C}_e \end{bmatrix} \right) \begin{Bmatrix} \vec{\xi}_d^R \\ \vec{\xi}_d^E \end{Bmatrix} = - \begin{Bmatrix} \mathbf{RE} \cdot \vec{\xi}_0^R \\ \mathbf{EE} \cdot \vec{\xi}_0^E \end{Bmatrix}. \tag{3.31}$$

The procedure is applied for the calculation of the internal loads for an ultra large container ship with a length of about 360 $[m]$. The midship bending moment is calculated based on the total, the quasi-static and the dynamic response. This is shown in Figure 3.2. Only the amplitudes are presented, the phase between the quasi-static and dynamic response causes the amplitude of the total response to be lower than the summation of the amplitude of the two contributions.

The bending moment at the first wet natural frequency at 2.8 $[rad/s]$ is clearly underestimated if the structural dynamics are not included in the calculation. However, the figure also shows that there is a minor dynamic amplification of the bending moment at 0.7 $[rad/s]$. A larger dynamic amplification at low frequency is found in [31] for a different ship. This amplification will be missed if the elastic modes are not included or when a quasi-static FEM solution is used. This shows the importance of performing a full hydro-elastic analysis for such flexible ships.

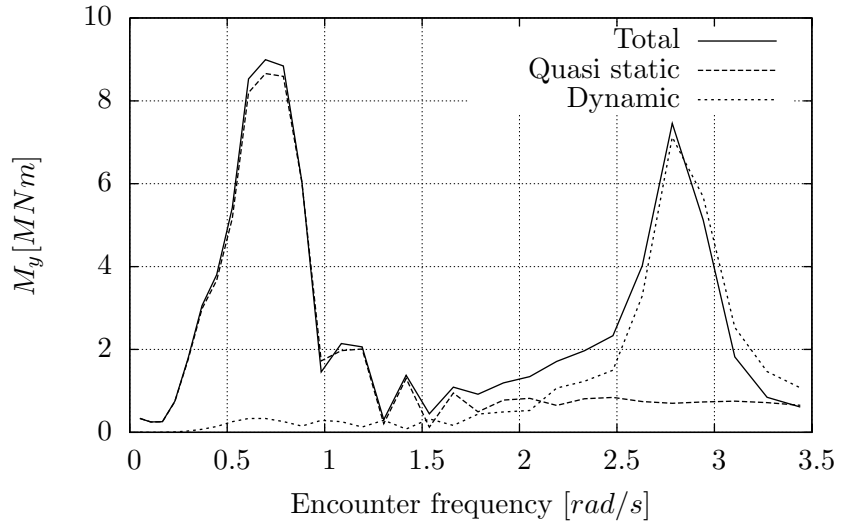

Figure 3.2: Dynamic amplification.

3.4 Wet natural modes

The wet natural frequencies and corresponding mode shapes can be obtained by solving the eigenvalue problem

$$\left\{-\lambda^2\left(\mathbf{m}+\mathbf{A}(\Im(\lambda))\right)-i\lambda\left(\mathbf{B}\left(\Im(\lambda)\right)+\mathbf{B}_u\right)+\left(\mathbf{C}_{te}+\mathbf{C}_h+\mathbf{C}_u\right)\right\}\vec{\xi}_u=\vec{0}, \tag{3.32}$$

with λ the complex eigenvalue and $\vec{\xi}_u$ the complex mode shape. It should be noted that the eigenvalue solution will always be a combination of the original, dry mode shapes. These will converge to the real wet mode shapes by using enough elastic mode shapes to solve this eigenvalue problem. The real wet natural mode shapes can be calculated directly if the hydrodynamic matrices would be added to the calculation of the structural or elastic modes. This method is not applied in this thesis due to the complexity and required calculation effort for this direct method.

The eigenvalue problem (3.32) cannot be solved directly as the hydrodynamic added mass and damping depend on the frequency. A numerical iteration scheme is used to find the eigenvalues. In the first iteration step the eigenvalues are solved using the hydrodynamic coefficients of the lowest frequency for which they have been solved. This solution reveals a set of eigenvalues whose size is equal to the number of used degrees of freedom. The added mass and damping corresponding to the first eigenvalue are inserted into equation (3.32) and the eigenvalues are solved again. This is continued until the first eigenvalue has converged, which is the case if the frequency for the used hydrodynamic

coefficients is found to be equal to the eigenvalue frequency. The same iteration is applied for the other eigenvalues that have been found in the first iteration step. These iterations are also redone using the eigenvalues based on the hydrodynamic coefficients for the other calculated frequencies as starting point of the iterations. The change of starting point for the iterations normally gives the same results, but due to the frequency dependent hydrodynamic coefficients there might be more eigenvalues than degrees of freedom in the system. Those might be missed if only one starting point would be used. Only the unique eigenvalues are kept after all iterations are finished.

The iteration procedure requires the hydrodynamic coefficients for a large range of frequencies. An interpolation is used if the required frequency falls between two calculated frequencies. The lowest frequency values are used if the requested frequency is lower than the lowest calculated frequency. The infinite frequency values are used when the requested frequency is higher than the highest calculated frequency.

The eigenvalue problem is solved using the first order routines from the EISPACK library. For this purpose, the second order eigenvalue problem (3.32) is changed to a first order problem by writing

$$\begin{bmatrix} \mathbf{0} & \mathbf{I} \\ -\mathbf{A}_t(\omega)^{-1}\mathbf{C}_t & -\mathbf{A}_t(\omega)^{-1}\mathbf{B}_t(\omega) \end{bmatrix} \begin{Bmatrix} \vec{\xi}_u \\ \lambda\vec{\xi}_u \end{Bmatrix} = \vec{0}, \tag{3.33}$$

where subscript t indicates the summation of the different contributions to the mass, damping and stiffness matrices. All eigenvalues are found as complex conjugate pairs when solving this first order eigenvalue problem: one of the pairs is the eigenvalue for the displacements and the other one for the velocities. Only the eigenvalues for the displacements are kept.

Chapter 4

Time domain

The prediction of the structural response of a ship sailing in a sea with the occurrence of slamming is the main objective of this thesis. The slamming loading is non-linear and the resulting whipping is a transient response. Solving the seakeeping problem in the time domain allows one to account relatively easily for non-linear loading and to calculate transient responses. This chapter explains the computation of the seakeeping response in the time domain.

The slamming loading often occurs in a severe sea state. The linear assumption that all seakeeping forces can be calculated using the still water condition may not hold for these conditions. It would be best to calculate all hydrodynamic force components using the actual position of the body in the waves. However, a different approach is used as it is too complex and too computationally intensive to compute all hydrodynamic forces using non-linear theory. Both the Froude-Krylov and the hydrostatic forces can be calculated relatively easily for the actual position of the body in the waves. The linear hydrodynamic coefficients computed in the frequency domain are used to calculate the other hydrodynamic force components. Fortunately, accounting only for the non-linearities in the Froude-Krylov and the hydrostatic loads already gives a reasonable estimation of the wave frequency non-linear structural loading. As will be shown in Chapter 12, the measured hog-sag ratio in the structural stresses during a full scale trail are well predicted using the presented approach.

The first section of this chapter explains the creation of the wave-train for the time domain calculation. The time domain calculation accounts for large amplitudes of motion. This requires different reference frames which make transformations between the different systems necessary. These reference frames and transformations are explained in the second section. The approach used to solve the equations of motion is discussed in the third section. The last section of this chapter describes the calculation of the different load components.

4.1 Waves

In contrast to the frequency domain calculation, the sea state is an input for the time domain calculation as the non-linearities prevent the use of superposition of the calculated response. The sea state is represented by a combination of single wave components. Only long crested seas are considered: all wave components have the same direction. The definition of a single wave component is given by equation (3.2). The total wave elevation ζ_{tot} of a wave-train, consisting of N_{wave} waves, is equal to

$$\zeta_{\text{tot}}(t, x_w) = \sum_{i=1}^{N_{\text{wave}}} \zeta_a(i) \cos\big(\omega(i)t - x_w k(i) + \varepsilon(i)\big). \tag{4.1}$$

The different wave components can be based on a sea spectrum or on measured wave elevations.

The frequencies of the wave components are distributed such that the encounter frequencies are equidistant (i.e. $\Delta\omega_e = (\omega_e(N_{\text{wave}}) - \omega_e(1))/N_{\text{wave}}$). The return period of the wave-train t_{return} is equal to

$$t_{\text{return}} = \frac{2\pi}{\Delta\omega_e}. \tag{4.2}$$

4.1.1 Wave components from spectrum

Only one wave spectrum type is used, the JONSWAP spectrum [21]. The spectrum is defined by

$$S_\zeta(\omega) = \frac{A \cdot g^2}{\omega^5} \cdot \exp\left(-\frac{5}{4}\left(\frac{\omega_p}{\omega}\right)^4\right) \cdot \gamma^r, \tag{4.3}$$

where

$$r = \exp\left(\frac{-\left(\frac{(\omega-\omega_p)}{\omega_p}\right)^2}{(2 \cdot s^2)}\right), \tag{4.4}$$

and

$$s = \begin{cases} 0.07 & \omega \leq \omega_p \\ 0.09 & \omega > \omega_p \end{cases}, \tag{4.5}$$

with

$S_\zeta(\omega)$	spectral value,
ω_p	angular peak frequency,
s	spectral width parameter,
γ	peakedness factor (3.3),
A	normalization factor calculated as $5.061 \cdot H_{1/3}^2/T_p^4 \cdot (1 - 0.287 \cdot \log(\gamma))$.

The Bretschneider wave spectrum [21] can be obtained by setting the γ factor to 1.0.

The amplitude of the different wave components are calculated using the spectral value. The spectral value is used to define the range of frequencies that are used to generate the wave-train. The wave components are distributed between the frequencies where the spectrum value is equal to one thousandth of the maximum value. Although the threshold of one thousandth is arbitrary, it ensures that the wave components that contain only very little energy are not used in the computation. The frequency distribution is shifted by a random number between $[-\frac{1}{2}\Delta\omega_e, \frac{1}{2}\Delta\omega_e]$ to add additional randomness of the resulting wave train by ensuring that the different wave realisations are built using components with slightly different frequencies.

The wave amplitude ζ_a is

$$\zeta_a(\omega) = \sqrt{2 \cdot S_\zeta(\omega) \cdot \Delta\omega}. \tag{4.6}$$

A uniform random distribution between 0 and 2π is used for the phase shift of the wave components ε.

4.1.2 Measured wave elevation

The wave components can also be based on a measurement of the wave elevations during a certain time-span. This is especially useful to reproduce towing tank experiments.

When the wave probe is at a fixed position the amplitude and phase of the different wave components can be obtained by a Fourier transform

$$[\zeta_a(\omega), \varepsilon_p(\omega)] = \mathcal{F}\big[\zeta_p(t)\big], \tag{4.7}$$

Using a wave probe attached to the towing carriage gives

$$[\zeta_a(\omega_e), \varepsilon_p(\omega_e)] = \mathcal{F}\big[\zeta_p(t)\big]. \tag{4.8}$$

The wave components with frequencies which are too high or too low to contribute significantly to the seakeeping response are usually removed from the Fourier results.

If the wave probe was attached to a moving towing carriage the encounter frequency is measured. The wave frequency in that case is equal to

$$\omega = \frac{-1 + \sqrt{1 - \frac{4\omega_e U \cos\mu}{g}}}{\frac{-2U\cos\mu}{g}}, \tag{4.9}$$

under the assumption of deep water, no following waves and linear waves.

Furthermore, the phases of the wave components have to be corrected for the location of the wave probe

$$\varepsilon(\omega_e) = \varepsilon_p(\omega_e) + k(\omega_e)x_{w_p}, \tag{4.10}$$

where x_{w_p} is the location of the wave probe, measured positively in the wave direction, and with respect to the origin of the coordinate system used for the seakeeping calculations. Deep water and sinusoidal wave are assumed for equation (4.10)

4.2 Reference frames and transformations

To be able to calculate the actual position of the ship accurately, it is necessary to account for large amplitudes of the motions. The large amplitudes of the motions result in different reference frames which introduce transformations of variables between the different systems. These different reference frames and the transformations are explained in this section. The theory for single body seakeeping described in [56] and [12] has been extended for the multi-body case to obtain these reference frames and transformations.

4.2.1 Reference frames

A number of different reference frames are used to solve the seakeeping problem with account for large amplitude motions and possible multiple bodies. Figure 4.1 illustrates, as example, the different reference frames used for a seakeeping problem with two bodies.

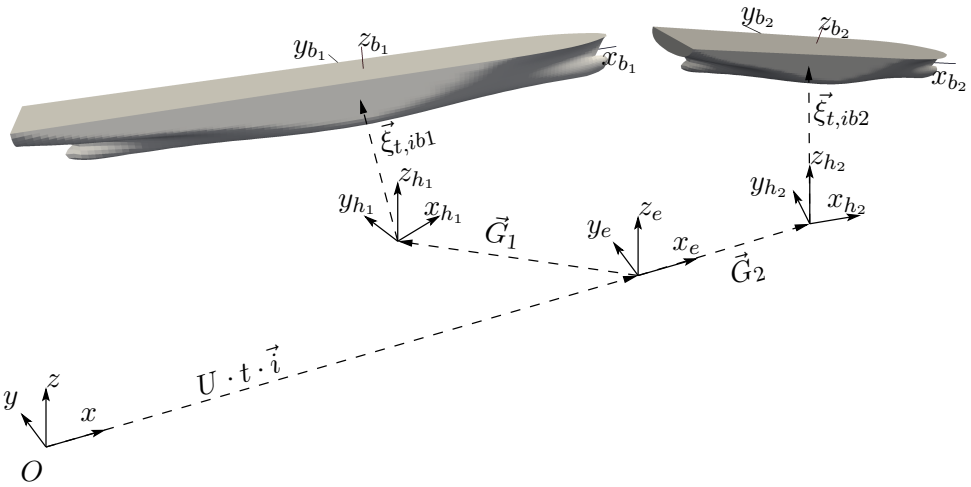

Figure 4.1: Reference frames.

The different reference frames are:

Fixed Earth system, xyz This system was defined in Section 2.2. The fixed Earth system points with the x-direction into the initial heading of the bodies. The origin of the system is located in the still water plane. The waves are defined with respect to this system, see Section 3.1.

Steady moving Earth system, $x_e y_e z_e$ The orientation of this system is equal to the fixed Earth system, however the system translates with the mean velocity of the ship(s) in the x-direction. This system is used to integrate the motions of the ship(s) over time. The rigid-body translations of the bodies $\xi_{t,ibn}$ are defined with respect to this reference frame but with an offset due to the original location of the center of gravity $\vec{G}_n$.

Hydrodynamic systems, $x_{h_{ib}} y_{h_{ib}} z_{h_{ib}}$ The "hydro system" is defined for every body. The origin of the system is the origin of the steady moving Earth system but with an offset equal to the original location of the center of gravity. The orientation of the hydro system is such that the z-axis remains upright but the system yaws with the ship. This system is used to compute the linear hydrodynamic forces. All quantities in this system are indicated by a superscript $^\diamond$.

Body systems, $x_{b_{ib}} y_{b_{ib}} z_{b_{ib}}$ A body system is defined for every body. The origin of the system is at the location of the center of gravity of the body. The x-axis is pointing to the bow, the y-axis to the port side and the z-axis is pointing upwards. The superscript * indicates quantities in this system.

All reference frames still exist when solving a single body problem. However, in that case, only one hydrodynamic and one body frame is defined.

4.2.2 Euler transformations

The differences in orientation of the reference frames requires several quantities to be transformed between the different systems. For this purpose, transformation matrices between the different reference frames are created. The transformation matrices for a single rigid-body are derived in this subsection. The results are generalised to the modal coordinate system in the next subsection.

The orthogonal transformation matrices can be created using either Euler angles or Euler parameters [16]. The Euler parameters are not expressed in quantities like roll, pitch and yaw. This makes it difficult to define the transformations to the hydro system. The Euler angles are expressed in the three rotations and will be used. The disadvantage of using Euler angles is that the transformations will become singular if one of the rotations is equal to 90

degrees. The degree of freedom for which the transformations will become singular if the rotation approaches 90 degrees depends on the sequence of the Euler angle rotations. The pitch rotation will cause a singularity for the sequence of rotations used in this thesis, but a pitch rotation of 90 degrees is not expected in normal seakeeping calculations.

Figure 4.2 shows the sequence of Euler rotations used. At the start the body reference frame has the same orientation as the Earth reference frame. The body frame is first rotated using the yaw angle, then the resulting frame is rotated with the pitch angle around the new y-axis. The last rotation is that of roll around the new x-axis of the resulting frame after the pitch rotation. It should be noted that the sequence of rotations is important as any other sequence of rotations will result in a different orientation of the body.

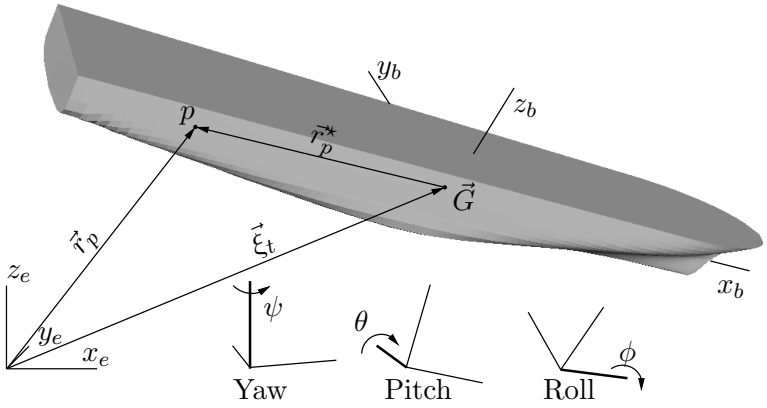

Figure 4.2: Euler transformation.

The location in the Earth reference frame of point p in Figure 4.2 is calculated using

$$\vec{r_p} = \xi_t + \mathbf{T}_{e\mathbb{R}3} \cdot \vec{r}_p^{\star}, \tag{4.11}$$

where $\vec{r}_p^{\star}$ is the vector from the center of gravity to point p, defined in the body system and $\mathbf{T}_{e\mathbb{R}3}$ is the transformation matrix from the body system to the Earth system. According to [24], the transformation matrix is equal to

$$\mathbf{T}_{e\mathbb{R}3} = \begin{bmatrix} \cos(\psi)\cos(\theta) & -\sin(\psi)\cos(\phi) + & \sin(\psi)\sin(\phi) + \\ & \cos(\psi)\sin(\theta)\sin(\phi) & \cos(\psi)\sin(\theta)\cos(\phi) \\ \sin(\psi)\cos(\theta) & \cos(\psi)\cos(\phi) + & -\cos(\psi)\sin(\phi) + \\ & \sin(\psi)\sin(\theta)\sin(\phi) & \sin(\psi)\sin(\theta)\cos(\phi) \\ -\sin(\theta) & \cos(\theta)\sin(\phi) & \cos(\theta)\cos(\phi) \end{bmatrix}. \tag{4.12}$$

The matrix $\mathbf{T}_{e\mathbb{R}3}$ is orthogonal, therefore the transformation from the Earth

system to the body system can be written as

$$\mathbf{T}_{b\mathbb{R}3} = \mathbf{T}_{e\mathbb{R}3}^{\mathrm{T}}. \tag{4.13}$$

Let $\vec{y}_{\mathbb{R}3}$ be a vector of a quantity defined in the Earth system. Vectors $\vec{y}^{\star}_{\mathbb{R}3}$ and $\vec{y}^{\diamond}_{\mathbb{R}3}$ are the vectors corresponding to the same quantity but defined in the body system and hydro systems, respectively. Using the definitions of the reference frames given in the previous section, the following transformations are defined

$$\vec{y}_{\mathbb{R}3} = \mathbf{T}_{e\mathbb{R}3}(\phi,\theta,\psi)\cdot\vec{y}^{\star}_{\mathbb{R}3}, \qquad \vec{y}^{\star}_{\mathbb{R}3} = \mathbf{T}_{b\mathbb{R}3}(\phi,\theta,\psi)\cdot\vec{y}_{\mathbb{R}3}, \tag{4.14}$$

$$\vec{y}_{\mathbb{R}3} = \mathbf{T}_{e\mathbb{R}3}(0,0,\psi)\cdot\vec{y}^{\diamond}_{\mathbb{R}3}, \qquad \vec{y}^{\diamond}_{\mathbb{R}3} = \mathbf{T}_{b\mathbb{R}3}(0,0,\psi)\cdot\vec{y}_{\mathbb{R}3}, \tag{4.15}$$

$$\vec{y}^{\diamond}_{\mathbb{R}3} = \mathbf{T}_{e\mathbb{R}3}(\phi,\theta,0)\cdot\vec{y}^{\star}_{\mathbb{R}3}, \qquad \vec{y}^{\star}_{\mathbb{R}3} = \mathbf{T}_{b\mathbb{R}3}(\phi,\theta,0)\cdot\vec{y}^{\diamond}_{\mathbb{R}3}. \tag{4.16}$$

Matrices are transformed in a similar fashion

$$\mathbf{y}_{\mathbb{R}3} = \mathbf{T}_{e\mathbb{R}3}(\phi,\theta,\psi)\cdot\mathbf{y}^{\star}_{\mathbb{R}3}\cdot\mathbf{T}^{\mathrm{T}}_{e\mathbb{R}3}(\phi,\theta,\psi), \tag{4.17}$$

$$\mathbf{y}_{\mathbb{R}3} = \mathbf{T}_{e\mathbb{R}3}(0,0,\psi)\cdot\mathbf{y}^{\diamond}_{\mathbb{R}3}\cdot\mathbf{T}^{\mathrm{T}}_{e\mathbb{R}3}(0,0,\psi), \tag{4.18}$$

$$\mathbf{y}^{\diamond}_{\mathbb{R}3} = \mathbf{T}_{e\mathbb{R}3}(\phi,\theta,0)\cdot\mathbf{y}^{\star}_{\mathbb{R}3}\cdot\mathbf{T}^{\mathrm{T}}_{e\mathbb{R}3}(\phi,\theta,0), \tag{4.19}$$

$$\mathbf{y}^{\star}_{\mathbb{R}3} = \mathbf{T}_{b\mathbb{R}3}(\phi,\theta,\psi)\cdot\mathbf{y}_{\mathbb{R}3}\cdot\mathbf{T}^{\mathrm{T}}_{b\mathbb{R}3}(\phi,\theta,\psi), \tag{4.20}$$

$$\mathbf{y}^{\diamond}_{\mathbb{R}3} = \mathbf{T}_{b\mathbb{R}3}(0,0,\psi)\cdot\mathbf{y}_{\mathbb{R}3}\cdot\mathbf{T}^{\mathrm{T}}_{b\mathbb{R}3}(0,0,\psi), \tag{4.21}$$

$$\mathbf{y}^{\star}_{\mathbb{R}3} = \mathbf{T}_{b\mathbb{R}3}(\phi,\theta,0)\cdot\mathbf{y}^{\diamond}_{\mathbb{R}3}\cdot\mathbf{T}^{\mathrm{T}}_{b\mathbb{R}3}(\phi,\theta,0). \tag{4.22}$$

The rotation axis for the Euler angles are not orthogonal because they are taken during a rotation process as shown in Figure 4.2. The same is true for their time derivatives. The transformation between the derivatives of the Euler angles $(\dot{\phi},\dot{\theta},\dot{\psi})$ and the angular velocities in the body reference frame (p,q,r) is [24]

$$\begin{bmatrix} p \\ q \\ r \end{bmatrix} = \mathbf{T}_{br\mathbb{R}3}(\phi,\theta,\psi)\cdot\begin{bmatrix} \dot{\phi} \\ \dot{\theta} \\ \dot{\psi} \end{bmatrix}, \tag{4.23}$$

with

$$\mathbf{T}_{br\mathbb{R}3}(\phi,\theta,\psi) = \begin{bmatrix} 1 & 0 & -\sin(\theta) \\ 0 & \cos(\phi) & \sin(\phi)\cos(\theta) \\ 0 & -\sin(\phi) & \cos(\theta)\cos(\phi) \end{bmatrix}. \tag{4.24}$$

Because this transformation is not orthogonal, the transformation matrix has to be inverted to obtain the inverse relation [24]

$$\begin{bmatrix} \dot{\phi} \\ \dot{\theta} \\ \dot{\psi} \end{bmatrix} = \mathbf{T}_{er\mathbb{R}3}(\phi,\theta,\psi)\cdot\begin{bmatrix} p \\ q \\ r \end{bmatrix}, \tag{4.25}$$

with

$$\mathbf{T}_{er\mathbb{R}3}(\phi,\theta,\psi) = \begin{bmatrix} 1 & \sin(\phi)\tan(\theta) & \cos(\phi)\tan(\theta) \\ 0 & \cos(\phi) & -\sin(\phi) \\ 0 & \sin(\phi)/\cos(\theta) & \cos(\phi)/\cos(\theta) \end{bmatrix}. \tag{4.26}$$

This is the matrix which causes the singularity for a pitch angle equal to $\pm\frac{\pi}{2}$ which is unlikely to happen during normal seakeeping calculations.

4.2.3 Transformation in modal coordinates

The Euler transformations are defined for the Cartesian system but most vectors and matrices are defined in the modal coordinates. Figure 4.3 illustrates the approach used to create a transformation matrix for vectors in modal coordinates. As an example, the modal vector $\vec{y}$ for two bodies both with elastic modes is transformed to the body system. The values corresponding to the elastic modes are not transformed as the elastic deformations are assumed to remain small. The values corresponding to the rigid-body modes are transformed using the Euler transformation with the rotation angles of the body.

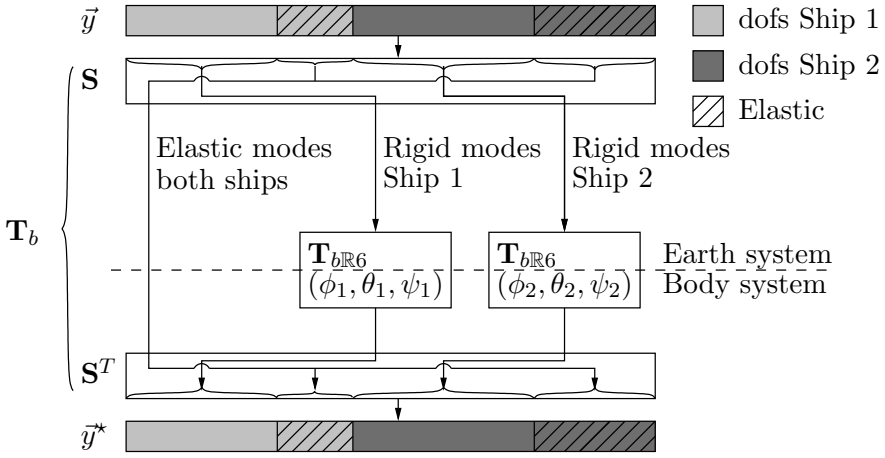

Figure 4.3: Example of the transformation of a vector to a different system.

The creation of the modal transformation matrix is the same for the matrix from the Earth system to the body system or the other way around. Therefore, the approach to create a general modal transformation matrix $\mathbf{T}$ is presented here. This matrix can be either $\mathbf{T}_e$ or $\mathbf{T}_b$.

The rigid-body vector has six components: three rotations and three translations. The transformation matrix for the six degrees of freedom corresponding to rigid-body modes of a single rigid-body is

$$\mathbf{T}_{\mathbb{R}6} = \begin{bmatrix} \mathbf{T}_{\mathbb{R}3} & \mathbf{0} \\ \mathbf{0} & \mathbf{T}_{\mathbb{R}3} \end{bmatrix}, \tag{4.27}$$

or

$$\mathbf{T}_{r\mathbb{R}6} = \begin{bmatrix} \mathbf{T}_{\mathbb{R}3} & \mathbf{0} \\ \mathbf{0} & \mathbf{T}_{r\mathbb{R}3} \end{bmatrix}. \tag{4.28}$$

The degrees of freedom corresponding to elastic modes are not transformed, this results in a modal transformation matrix for the elastic modes

$$\begin{cases} T^e_{ij} = 1 & \text{if } i \text{ is elastic and } i = j, \\ T^e_{ij} = 0 & \text{otherwise.} \end{cases} \tag{4.29}$$

The rigid-body modes are extracted using the matrix $\mathbf{S}$ defined in Section 2.8.2. The total transformation matrix is equal to

$$\mathbf{T} = \mathbf{T}^e + \sum_{ib=1}^{N\text{body}} \mathbf{S}_{ib} \cdot \mathbf{T}_{\mathbb{R}6,ib} \cdot \mathbf{S}^{\mathrm{T}}_{ib}, \tag{4.30}$$

or

$$\mathbf{T}_r = \mathbf{T}^e + \sum_{ib=1}^{N\text{body}} \mathbf{S}_{ib} \cdot \mathbf{T}_{r\mathbb{R}6,ib} \cdot \mathbf{S}^{\mathrm{T}}_{ib}, \tag{4.31}$$

when derivatives to the Euler angles are concerned.

4.2.4 Hydro reference frame

The diffraction and radiation forces are calculated using the linear hydrodynamic coefficients from the frequency domain calculation. Adding these forces to a calculation with large amplitudes of motion raises the question in which reference frame should these forces act? In the presented theory it is assumed that they act in the hydro system. The same assumption is made by [12] and [10]. This assumption seems to be the most consistent, but the full consistent solution would be to calculate those forces based on the actual position of the body in the water.

The idea behind the assumption that the linear hydrodynamic forces act in the hydro reference frame is illustrated in Figure 4.4. The ship is in the still water position in Figure 4.4(a). There is no difference between the body, hydro and Earth reference frame in that position. The ship has a severe roll angle in Figure 4.4(b). The body reference frame will roll with the ship, the hydro and Earth frames keep upright. The motion indicated by the dotted line is a combination of heave and sway when seen from the body reference frame and pure heave when observed from the hydro frame. Assuming that the hydrodynamic coefficients act in the body system would result in a combination of heave and sway induced added mass and damping for this motion. If the ship would be rolled 90 degrees, only the sway hydrodynamic coefficients would be used when using the body system. As the hydro frame keeps upright, this motion is pure heave and only the heave hydrodynamics contribute to the forces

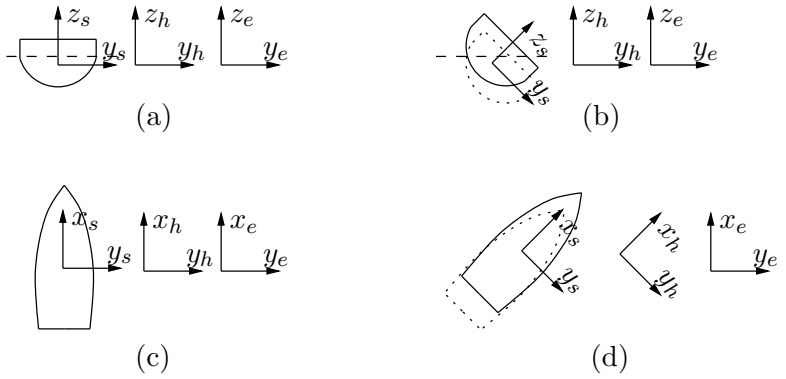

Figure 4.4: Orientation of linear hydrodynamic forces.

for this motion. This seems to be closer to the real hydrodynamics force than if one were to consider this motion to be partly sway.

The ship has a large yaw angle in Figure 4.4(d), the hydro frame is rotated with the yaw motion of the ship. Therefore, the indicated motion is still surge in the hydro frame. This would be a combination of surge and sway if the Earth system would be used. It should be noted that the diffraction force is still incorrect regardless of which frame is used as the diffraction force should depend on the actual heading of the ship. This could be corrected by calculating the diffraction force for a range of headings and by using the closest heading calculated or an interpolation between the calculated headings. This approach is not used in this thesis as mainly head sea conditions will be considered where the yaw motions are expected to remain small.

4.3 Equations of motion

In the time domain the equation of motion is the Cummins equation [8]

$$(\mathbf{A}(\infty)+\mathbf{m})\cdot\ddot{\vec{\xi}}+\mathbf{B}(\infty)\cdot\dot{\vec{\xi}}+\int_{-\infty}^{t}\mathbf{K}\,(t-\tau)\cdot\dot{\vec{\xi}}(\tau)\,\mathrm{d}\tau+\mathbf{C}_{te}\cdot\vec{\xi}=\vec{f}_h(t,\vec{\xi})+\vec{f}_q(t,\vec{\xi}), \tag{4.32}$$

where $\mathbf{K}(t-\tau)$ are retardation functions which account for the frequency dependent part of the hydrodynamic radiation force. The two force vectors $\vec{f}_h$ and $\vec{f}_q$ contain the remaining non-impulsive hydrodynamic forces and the impulsive hydrodynamic forces, respectively.

Equation (4.32) is the basic equation which is solved in the time domain, but the equation is not solved as presented here. Figure 4.5 illustrates the approach used to solve the seakeeping motions. The contribution of all components, except the inertia terms, are transfered to the right-hand side of the equation of

motion. The different force components are calculated in the most convenient reference frame, transferred to the body frame and added to the total force vector $\vec{f}_t^{\star}$. The calculation of the different force components is discussed in the next section.

Briefly, the accelerations are solved in the body system. Kinematic constraints, see Appendix B, are included in the calculation of the accelerations if they are defined. The forces and accelerations in the body system are used to calculate the internal loads. The accelerations are transformed to the Earth system where they are integrated to obtain velocities and displacements. Integration of the motion in the Earth system avoids the need to account for additional terms like centrifugal forces which will occur when the motions are integrated in the body system. The velocities and displacements are corrected for the kinematic constraints when defined. The motions are transformed to the different systems to allow for calculation of the forces for the next calculation step.

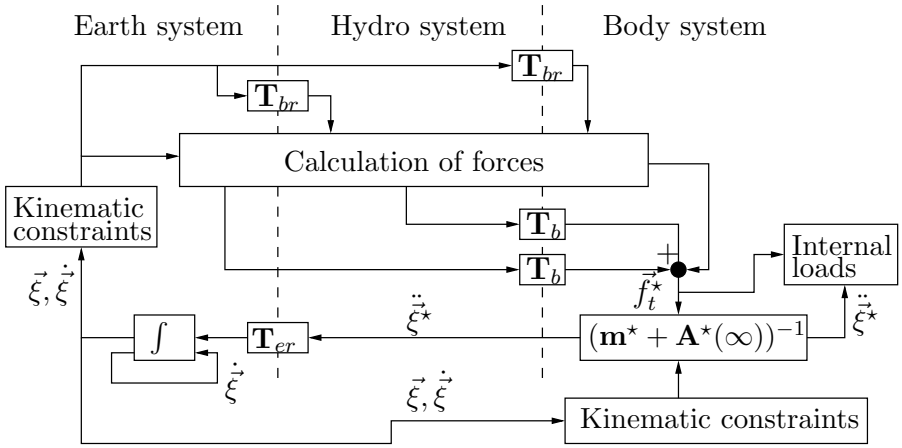

Figure 4.5: Computation scheme for solving the equations of motion.

4.3.1 Solving accelerations

The following system of equations is solved to obtain the accelerations in the body system

$$\begin{bmatrix} \mathbf{A}^{\star}(\infty) + \mathbf{m}^{\star} & \mathbf{\Phi}_{\xi}^{\star T} \\ \mathbf{\Phi}_{\xi}^{\star} & \mathbf{0} \end{bmatrix} \cdot \begin{bmatrix} \ddot{\vec{\xi}}^{\star} \\ \vec{\lambda} \end{bmatrix} = \begin{bmatrix} \vec{f}_t^{\star} \\ \vec{\gamma} \end{bmatrix}. \tag{4.33}$$

The $\vec{\lambda}, \mathbf{\Phi}_{\xi}^{\star}$ and $\vec{\gamma}$ are sets of Lagrange multipliers which account for kinematic constraints. The calculation of these Lagrange multipliers is explained in detail in Appendix B.

Note that both the added mass and the genuine mass in the above equation are defined in the body reference frame. The genuine mass is already defined in the body reference frame since it is attached to the body. The added mass is a linear hydrodynamic coefficient and is assumed to be defined in the hydro system. This matrix has to be transformed to the body system using equation (4.22).

4.3.2 Numerical time integration

The accelerations and velocities are integrated over time using a fourth-order Runge-Kutta scheme with a constant time step. This integration scheme is used because it requires a minimal number of function evaluations needed to obtain an accurate solution. The Runge-Kutta scheme is explained in detail as the coupling between the seakeeping and the slamming calculation depends on this integration scheme. This coupling with the slamming calculation is explained in Chapter 5.

The Runge-Kutta scheme is used to integrate both accelerations to velocities and velocities to displacements

$$\{\dot{\vec{\xi}}, \vec{\xi}\}_{n+1} = \{\dot{\vec{\xi}}, \vec{\xi}\}_n + \frac{1}{6} \cdot \Delta t \cdot \left(\vec{k}_1 + 2\vec{k}_2 + 2\vec{k}_3 + \vec{k}_4\right) + O(\Delta t^5), \tag{4.34}$$

with

$$\vec{k}_1 = \{\dot{\vec{\xi}}, \ddot{\vec{\xi}}\}(\{\dot{\vec{\xi}}, \vec{\xi}\}_n, t), \tag{4.35}$$

$$\vec{k}_2 = \{\dot{\vec{\xi}}, \ddot{\vec{\xi}}\}(\{\dot{\vec{\xi}}, \vec{\xi}\}_n + \frac{1}{2} \cdot \vec{k}_1, t + \frac{1}{2} \cdot \Delta t), \tag{4.36}$$

$$\vec{k}_3 = \{\dot{\vec{\xi}}, \ddot{\vec{\xi}}\}(\{\dot{\vec{\xi}}, \vec{\xi}\}_n + \frac{1}{2} \cdot \vec{k}_2, t + \frac{1}{2} \cdot \Delta t), \tag{4.37}$$

$$\vec{k}_4 = \{\dot{\vec{\xi}}, \ddot{\vec{\xi}}\}(\{\dot{\vec{\xi}}, \vec{\xi}\}_n + \vec{k}_3, t + \Delta t). \tag{4.38}$$

Figure 4.6 illustrates this Runge-Kutta scheme. Only the first step of the Runge-Kutta scheme (4.35) calculates the derivatives based on the real velocities and displacements. The scheme uses an estimation of the motions for the calculation of the derivatives at the second (4.36), third (4.37) and fourth (4.38) step. The velocities and displacements at the next time step are calculated using equation (4.34) which is based on the estimations of the four steps.

The velocities and displacements are different for every function evaluation of the Runge-Kutta integration. Therefore, the transformation matrices are recomputed and the velocities and displacements are corrected for the kinematic constraints (when defined) for every function evaluation.

Although there are four function evaluations, only the first step of the Runge-Kutta integration is based on the real motion of the ship. The solid black line in Figure 4.6 indicates the real motion of the ship. It is important

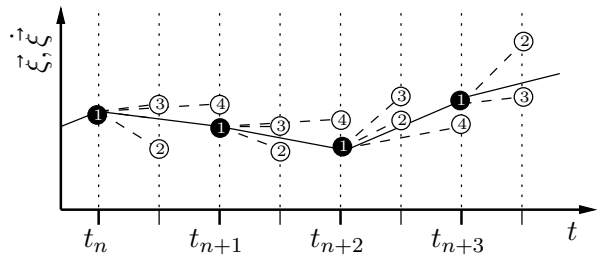

Figure 4.6: Fourth-order Runge-Kutta integration scheme.

that whenever the motion history is used in the calculation of a force component, for example the evaluation of the retardation functions, only the real velocities and displacements are used and not the intermediate estimations.

The motions are integrated using the Runge-Kutta scheme because this scheme gives the highest possible accuracy when using a fixed number of function evaluations. It could be argued that the Runge-Kutta scheme might not be good for transient responses, like whipping, because this scheme might slightly smooth the initial response to the slamming loading. However, the subsequent whipping response will not be smoothed. The main interest here is to evaluate the whipping response because the whipping will cause the loading of the global ship structure.[1] Therefore, the Runge-Kutta scheme is used to integrate the motions.

As an explicit integration scheme is used, the integration will become unstable when a too large time step is used. The maximum time step for a stable integration depends on the highest frequency in the system and the amount of damping. The stable time step is not computed and choice of the integration time step is left to the user. As the stable time step is mainly driven by the highest frequency, adding more flexible modes will reduce the stable time step and therefore increasing the required computation time.

4.3.3 Local motions

The calculation of the location of a point at a rigid-body in the Earth system is explained in Section 4.2.2. This approach is extended in this section to account for the generalised mode approach including flexible deformations.

Figure 4.7 illustrates how the location of a point in the Earth reference frame is obtained. Vector $\vec{r}_f^{\star}$ is the displacement vector due to the elastic deformation.

[1] The initial response would be interesting when looking at the local structural response. The local structural response cannot be calculated accurately using the presented theory as the modal approach does not have enough spatial resolution. The slamming loading should be transferred to a full 3D FEM-model in that case.

This vector is defined in the body frame as

$$\vec{r}_f^{\star} = \sum_{i=1}^{N_{\text{dof}}} \mathbf{h}_{p,t}^i \cdot \vec{\xi}_i \quad \text{when } \vec{\xi}_i \text{ is a flexible mode,} \tag{4.39}$$

where subscript t indicates the translation components of matrix $\mathbf{h}$. The rigid-body translations $\vec{\xi}_{t,ib}$ and rotations $\vec{\xi}_{r,ib}$ are obtained by equation (2.47). The location of a point p in the Earth reference frame is

$$\vec{r}_p = \vec{\xi}_{t,ib} + \mathbf{T}_{e\mathbb{R}3}(\vec{\xi}_{r,ib}) \cdot \left(\vec{r}_p^{\star} + \vec{r}_f^{\star}\right). \tag{4.40}$$

The Euler rotations to obtain the orientation of point $\vec{p}$ are

$$\vec{r}_{p_r} = \vec{\xi}_{r,ib} + \sum_{i=1}^{N_{\text{dof}}} \mathbf{h}_{p,r}^i \cdot \vec{\xi}_i \quad \text{when } \vec{\xi}_i \text{ is a flexible mode,} \tag{4.41}$$

where subscript r indicates the rotation components of matrix $\mathbf{h}$.

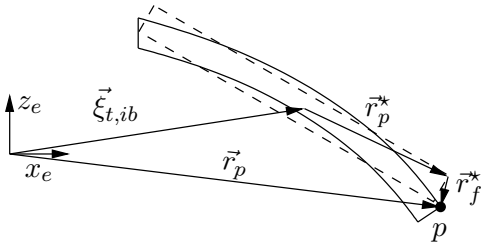

Figure 4.7: Location of point p.

The velocity of point p in the earth system is

$$\dot{\vec{r}}_p = \dot{\vec{\xi}}_{t,ib} + \mathbf{T}_{e\mathbb{R}3}(\vec{\xi}_{r,ib}) \left\{ \left(\mathbf{T}_{er\mathbb{R}3}(\vec{\xi}_{r,ib}) \cdot \dot{\vec{\xi}}_{r,ib} \right) \times \left(\vec{r}_p^{\star} + \vec{r}_f^{\star}\right) + \dot{\vec{r}}_f^{\star} \right\}, \tag{4.42}$$

with

$$\dot{\vec{r}}_f^{\star} = \sum_{i=1}^{N_{\text{dof}}} \mathbf{h}_{p,t}^i \cdot \dot{\vec{\xi}}_i \quad \text{when } \vec{\xi}_i \text{ is a flexible mode.} \tag{4.43}$$

Note that the vector $\dot{\vec{\xi}}_{r,ib}$ contains the time derivatives of the Euler angles. These cannot be used to calculate the rotational velocity of the body. This is the reason for first transforming this vector to the body system, then computing the rotation velocity in the body system and finally transforming it back to the Earth system in equation (4.42).

The acceleration in the Earth system is

$$\ddot{\vec{r}}_p = \ddot{\vec{\xi}}_{t,ib} + \mathbf{T}_{e\mathbb{R}3}(\vec{\xi}_{r,ib}) \left\{ \dot{\vec{\xi}}_{r,ib}^{\star} \times \left(\dot{\vec{\xi}}_{r,ib}^{\star} \times \vec{r}_p^{\star} \right) + \ddot{\vec{\xi}}_{r,ib}^{\star} \times \vec{r}_p^{\star} + \ddot{\vec{r}}_f^{\star} \right\}, \tag{4.44}$$

with

$$\ddot{\vec{r}}_f^{\star} = \sum_{i=1}^{N_{\text{dof}}} \mathbf{h}_{p,t}^i \cdot \ddot{\vec{\xi}}_i \quad \text{when } \vec{\xi}_i \text{ is a flexible mode,} \tag{4.45}$$

and

$$\dot{\vec{\xi}}_{r,ib}^{\star} = \mathbf{T}_{er\mathbb{R}3}(\vec{\xi}_{r,ib}) \cdot \dot{\vec{\xi}}_{r,ib}, \qquad \ddot{\vec{\xi}}_{r,ib}^{\star} = \mathbf{T}_{er\mathbb{R}3}(\vec{\xi}_{r,ib}) \cdot \ddot{\vec{\xi}}_{r,ib}. \tag{4.46}$$

The above equation gives the acceleration in the Earth system. The acceleration experienced by an observer at the point p is obtained by adding the gravity acceleration vector $[0, 0, -g]$ to the point acceleration and transforming the resulting acceleration back to the body system.

4.4 Loads

The total force vector used to solve the accelerations (4.33) is equal to

$$\begin{aligned} \vec{f}_t^{\star} = \vec{f}_{\text{fkhs}}^{\star} + \vec{f}_{\text{grav}}^{\star} + \vec{f}_{\text{sd}}^{\star} + \vec{f}_{\text{beam}}^{\star} + \vec{f}_{\text{slam}}^{\star} + \vec{f}_{\text{cor}}^{\star} + \\ \mathbf{T}_b(\phi,\theta,0)\left(-\mathbf{B}(\infty)\cdot\dot{\vec{\xi}}^{\diamond} - \vec{f}_{\text{rad}}^{\diamond} + \vec{f}_{\text{diff}}^{\diamond}\right) + \\ \mathbf{T}_b(\phi,\theta,\psi)\left(-\mathbf{B}_u\cdot\dot{\vec{\xi}} - \mathbf{C}_u\cdot\vec{\xi} - \mathbf{C}_e\cdot\vec{\xi}_{sw}\right), \end{aligned} \tag{4.47}$$

where

$\vec{f}_{\text{fkhs}}$	Froude-Krylov and hydrostatic force,
$\vec{f}_{\text{grav}}$	gravity force,
$\vec{f}_{\text{sd}}$	force by spring/damper element(s),
$\vec{f}_{\text{beam}}$	force by beam element(s),
$\vec{f}_{\text{slam}}$	slamming loading,
$\vec{f}_{\text{cor}}$	Coriolis forces [16],
$\vec{f}_{\text{rad}}$	frequency dependent part of radiation force,
$\vec{f}_{\text{diff}}$	diffraction force,
$\vec{\xi}_{sw}$	still water deformation (2.38).

Note that the beam elements of $\vec{f}_{\text{beam}}$ are used to connect the different bodies. These have nothing to do with the beam model described in Section 2.6 used for the computation of the elastic modes.

The calculation of the slamming force is explained in the next chapter. The computation of the other force components is explained in this section. The last part of this section deals with the calculation of the internal loads.

4.4.1 Radiation force

The frequency dependent part of the radiation force is calculated using the equation presented by Cummins [8]

$$\vec{f}^{\diamond}_{\text{rad},is} = \mathbf{B}^{\diamond}_{is}(\infty) \cdot \dot{\xi}(t) + \int_{-\infty}^{t} \mathbf{K}^{\diamond}_{is}(t-\tau) \cdot \dot{\vec{\xi}}^{\diamond} \, \mathrm{d}\tau, \tag{4.48}$$

where is indicates the different 3D ship sections, see Section 2.4.1.

It has been shown by [39] that the retardation functions, or memory functions, can be calculated using the frequency domain damping

$$\mathbf{K}^{\diamond}_{is}(t) = \frac{2}{\pi} \int_{0}^{\infty} (\mathbf{B}^{\diamond}_{is}(\omega_e) - \mathbf{B}^{\diamond}_{is}(\infty)) \cdot \cos(\omega_e \cdot t) \, \mathrm{d}\omega_e. \tag{4.49}$$

The damping curve is integrated up to the infinite frequency in equation (4.49). To be able to calculate the damping at high frequencies one needs very small panels and consequently a large amount of computational power to solve the hydrodynamic BVP in the frequency domain. Therefore, it is not feasible to calculate the damping curve up to the point where the damping becomes equal to its infinite value. The damping curve is extrapolated using a curve in the form of $\frac{a}{\omega_e^b} + c$, before the retardation functions are calculated. This extrapolation is explained in detail in Appendix C.

Equation (4.49) is a so-called Filon quadrature. There are toolboxes available to solve this equation for an arbitrary damping function. These toolboxes are not used as the semi-analytical method described below requires less computationally effort.

The damping values are only calculated for a range of frequencies. An estimation for the curve between the calculated frequencies has to be made. The damping curve is linearly interpolated between the calculated frequencies. This allows to solve equation (4.49) partly analytically which saves computation time. The retardation function is equal to

$$\mathbf{K}(t) = \frac{2}{\pi} \sum_{i=1}^{N_{\text{freq}}-1} \int_{\omega_e(i)}^{\omega_{e(i+1)}} (\mathbf{a}_i \cdot \omega_e + \mathbf{b}_i) \cos(\omega_e t) \, \mathrm{d}\omega_e, \tag{4.50}$$

where

$$\begin{cases} \mathbf{a}_i \cdot \omega_{e(i)} + b_i = \mathbf{B}\left(\omega_{e(i)}\right) - \mathbf{B}\left(\infty\right) \\ \mathbf{a}_i \cdot \omega_{e(i+1)} + b_i = \mathbf{B}\left(\omega_{e(i+1)}\right) - \mathbf{B}\left(\infty\right) \end{cases}. \tag{4.51}$$

The integral in equation (4.50) is solved analytically for each increment in ω_e

$$\int_{\omega_{e(i)}}^{\omega_{e(i+1)}} [\mathbf{a}_i \cdot \omega_e + \mathbf{b}_i] \cos(\omega_e t)\, d\omega_e = \frac{1}{t^2}\Big(-\mathbf{a}_i \cos(\omega_{e(i)} t) - \mathbf{a}_i \omega_{e(i)} t \sin(\omega_{e(i)} t) - \mathbf{b}_i t \sin(\omega_{e(i)} t) + \mathbf{a}_i \cos(\omega_{e(i+1)} t) + \mathbf{a}_i \omega_{e(i+1)} t \sin(\omega_{e(i+1)} t) + \mathbf{b}_i t \sin(\omega_{e(i+1)} t)\Big). \quad (4.52)$$

If t is equal to zero, the integral is simplified to

$$\frac{1}{2} a_i \omega_{e,(i+1)}^2 - \frac{1}{2} a_i \omega_{e,(i)}^2 + b_i \omega_{e,(i+1)} - b_i \omega_{e,(i)}. \quad (4.53)$$

The computed radiation force will only depend on a limited time span of the motion history to reduce the computation effort. This assumption is supported by the fact that waves generated by the motions much earlier in time are already far away from the ship and will not contribute significantly to the loading at the ship.

4.4.2 Froude-Krylov and non-linear hydrostatics

The pressures by the incoming waves and by the hydrostatics are calculated using the actual position of the body. The position of a point at the body is calculated using equation (4.40) which includes the deflection by both the rigid-body and flexible modes. The incoming waves are defined in Section 4.1.

Figure 4.8 illustrates the approximation used to describe the pressure in the incoming waves [56][2]. This is equal to

$$\begin{cases} p_{\text{fk}} = \sum_{i=1}^{\text{Nfreq}} \rho g \zeta_i(t, x_w, \omega) e^{k(\omega_i) z} & z < \min\big(0, \zeta_{\text{tot}}(t, x_w)\big), \\ p_{\text{fk}} = \rho g \zeta_{\text{tot}}(t, x_w) \left(1 - \dfrac{z}{\zeta_{\text{tot}}(t, x_w)}\right) & z \geq 0 \text{ and } z < \zeta_{\text{tot}}(t, x_w), \\ p_{\text{fk}} = 0 & z \geq \zeta_{\text{tot}}(t, x_w), \end{cases} \quad (4.54)$$

with $\zeta_{\text{tot}}(t, x_w)$ the total wave height, see equation (4.1). This equation is evaluated in the Earth reference frame. The pressure is set to zero above the wave surface. The pressure following from the incident wave potential (3.7) is used below the still water line. A linear interpolation is used above the still water line as the wave potential is not defined there.

[2] Many different approximations for the Froude-Krylov pressure can be found in the literature. This simple approximation is used as there is no general agreement on which approximation is the most accurate.

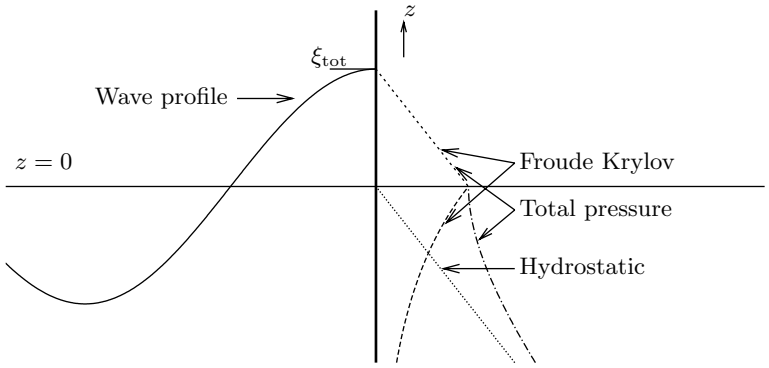

Figure 4.8: Froude-Krylov pressure.

The hydrostatic pressure is equal to

$$\begin{cases} p_{\text{hs}} = -\rho g z & z < \min\left(0, \zeta_{\text{tot}}(t, x_w)\right), \\ p_{\text{hs}} = 0 & z \geq 0 \text{ or } z \geq \zeta_{\text{tot}}(t, x_w). \end{cases} \tag{4.55}$$

Both the Froude-Krylov and hydrostatic pressure are integrated over the surface using the integration mesh with the Gauss points. The pressure is multiplied with the mode shape, the normal and the area associated with the Gauss points to obtain the modal force vector for the total body and the different 3D ship sections

$$f^{i\star}_{\text{fkhs},is} = \iint_{S_b,is} (p_{\text{fk}} + p_{\text{hs}})\, \vec{h}_i \vec{n}\, \mathrm{d}S. \tag{4.56}$$

Computation effort is reduced by first calculating the wave height around the body. All panels which are not wetted are excluded from the above calculations.

4.4.3 Diffraction force

The diffraction force is calculated using the complex RAO for the diffraction force $\vec{F}_D$ calculated in the frequency domain by equation (3.17). The diffraction force depends on the actual wave elevation around the body. The location of the body into the wave direction is equal to $x_{w,ib}$. The diffraction force in the time domain is equal to

$$\vec{f}^{\diamond}_{\text{diff},is} = \sum_{i=1}^{N_{\text{freq}}} \zeta_a(\omega_i) \cdot \Big(\Re(\vec{F}^{\diamond}_{D,is}(i)) \cdot \cos\left(\omega_i \cdot t + \varepsilon_\zeta(\omega_i) - x_{w,ib} \cdot k(\omega_i)\right) + \Im(\vec{F}^{\diamond}_{D,is}(i)) \cdot \sin\left(\omega_i \cdot t + \varepsilon_\zeta(\omega_i) - x_{w,ib} \cdot k(\omega_i)\right) \Big). \tag{4.57}$$

Note that $x_{w,ib}$ will be different for every body. Therefore, the above equation is evaluated for every degree of freedom separately and the $x_{w,ib}$ value of the corresponding body is used.

The frequencies of the wave components are usually different from the frequencies at which the hydrodynamic coefficients are calculated. The coefficients of the diffraction force at the wave frequencies are obtained by a linear interpolation of the calculated diffraction coefficients.

4.4.4 Gravitation force

The acceleration due to the gravity field is $-g$ in the heave direction, in the Earth reference frame. A gravity vector $\vec{g}_g$ for all modes is created using equation (2.48) with a rigid-body vector of $[0, 0, -g, 0, 0, 0]^{\mathrm{T}}$ for all bodies. The modal force due to the gravity acceleration is equal to

$$\vec{f}^{\star}_{\mathrm{grav},is} = \mathbf{m}^{\star}_{is} \cdot \mathbf{T}_b \cdot \vec{g}_g. \tag{4.58}$$

4.4.5 Coriolis force

The Coriolis force, due to rotation of the body, are calculated for every body and section separately [16]

$$\vec{f}^{\star}_{\mathrm{cor},ib,is} = -\dot{\vec{\xi}}^{\star}_{r,ib} \times \mathbf{m}^{\star}_{(\phi,\theta,\psi,is)} \cdot \dot{\vec{\xi}}^{\star}_{r,ib}. \tag{4.59}$$

The force vector is changed to a modal vector using equation (2.48).

4.4.6 Spring-damper element

A spring-damper element can be defined between two bodies or between one body and a point in the moving Earth frame. This is useful to model, for example, mooring lines between the bodies or for station-keeping.

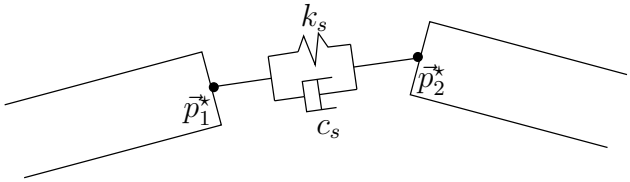

Figure 4.9: Spring-damper element.

Figure 4.9 shows a spring-damper element between two bodies. The element is attached at points $\vec{p}_1^{\star}$ and $\vec{p}_2^{\star}$. The position and velocity of these points in the

moving Earth frame can be calculated using equations (4.40) and (4.42). The force in the spring-damper element is equal to

$$f_{\text{sd0}} = k_s \left(||\vec{p}_1 - \vec{p}_2|| - l_{s0} \right) + b_s || \left(\dot{\vec{p}}_1 - \dot{\vec{p}}_2 \right) \cdot \vec{s}_n ||, \tag{4.60}$$

with l_{s0} is the original length of the spring and $\vec{s}_n$ a unit vector in the direction of the element

$$\vec{s}_n = \frac{\vec{p}_1 - \vec{p}_2}{||\vec{p}_1 - \vec{p}_2||}. \tag{4.61}$$

The force in the element may be set to zero for compression when the element is used to model mooring lines.

This results in a modal force of

$$\begin{cases} f^{i\star}_{\text{sd},is} = -\mathbf{T}_{b,\mathbb{R}3,ib1} \cdot f_{\text{sd0}} \cdot \vec{s}_n \cdot \vec{h}^i_{p_1} & \text{for } is \text{ body or section of } p_1, \\ f^{i\star}_{\text{sd},is} = \mathbf{T}_{b,\mathbb{R}3,ib2} \cdot f_{\text{sd0}} \cdot \vec{s}_n \cdot \vec{h}^i_{p_2} & \text{for } is \text{ body or section of } p_2, \\ f^{i\star}_{\text{sd},is} = 0 & \text{otherwise.} \end{cases} \tag{4.62}$$

The spring-damper element can also be connected to the moving Earth frame. In this case, vector $\vec{p}_2$ will be equal to the connection point in the steady moving Earth frame and $\dot{\vec{p}}_2$ will be zero in that case.

4.4.7 Beam element

Two bodies can be connected with a linear beam element. Note that this is not the beam model to compute the flexible modes. The user has to provide the stiffness matrix of the beam $\mathbf{C}_b$ which is a twelve by six matrix. The stiffness matrix provides the forces and moments at the connecting nodes based on the relative displacement and rotations between the two nodes. Using the $\mathbf{C}_b$ matrix as input allows the user to add any type of linear beam. A description of the stiffness matrix for a 3D-Euler beam can be found in [7].

As the beam element is designed to connect different floating bodies, it is assumed that the z-direction of the beam is located in the z-direction of the body frames and the x-direction of the beam is the line between the two connection points.

Figure 4.10 shows the beam in a deformed situation. It is necessary to define a local reference frame $z_m y_m z_m$ to compute the beam forces. The bodies may have also elastic deformations. This causes the orientation of the connecting node to be different from the body reference frame. Additional local reference systems are defined at the connecting nodes. The orientation of these points is calculated using (4.41) and the position of the connection points is obtained from (4.40).

The x_m-axis is located in the direction of the vector from p_1 to p_2. The y_m-axis is defined by the cross product with the average of vectors $\vec{z}_{p_1}$ and $\vec{z}_{p_1}$.

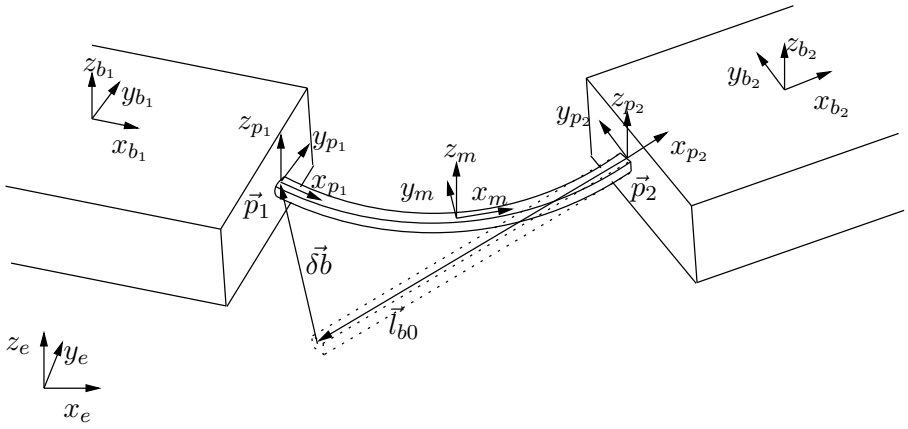

Figure 4.10: Connection via a deformed beam element.

This gives the beam reference frame the average roll of the two connection points. The z_m-axis is created using the cross product between the $\vec{x}_m$ and $\vec{y}_m$ unit vectors.

The deformation of the beam in the beam frame is

$$\delta\vec{b}_t^{\,m} = \mathbf{T}_{m,\mathbb{R}3}\left(\vec{p}_2 - \vec{p}_1 + \mathbf{T}_{p_2,\mathbb{R}3}^{\mathrm{T}} \cdot \vec{l}_{b0}\right), \tag{4.63}$$

$$\delta\vec{b}_r^{\,m} = \mathbf{T}_{m,\mathbb{R}3}\left(\vec{p}_{2,r} - \vec{p}_{1,r}\right). \tag{4.64}$$

The resulting force in the beam frame is equal to

$$\begin{Bmatrix} \vec{f}_{\mathrm{beam},p_1}^{\,m} \\ \vec{f}_{\mathrm{beam},p_2}^{\,m} \end{Bmatrix} = \mathbf{C}_b \cdot \begin{Bmatrix} \delta\vec{b}_t^{\,m} \\ \delta\vec{b}_r^{\,m} \end{Bmatrix}. \tag{4.65}$$

This results in a modal force of

$$\begin{cases} f_{\mathrm{beam},is}^{i\star} = \mathbf{T}_{b,\mathbb{R}6,ib1} \cdot \mathbf{T}_{m,\mathbb{R}6}^{\mathrm{T}} \cdot \vec{f}_{\mathrm{beam},p_1}^{\,m} \cdot \vec{h}_{p_1}^{\,i} & \text{for } is \text{ body or section of } p_1, \\ f_{\mathrm{beam},is}^{i\star} = \mathbf{T}_{b,\mathbb{R}6,ib2} \cdot \mathbf{T}_{m,\mathbb{R}6}^{\mathrm{T}} \cdot \vec{f}_{\mathrm{beam},p_2}^{\,m} \cdot \vec{h}_{p_2}^{\,i} & \text{for } is \text{ body or section of } p_2, \\ f_{\mathrm{beam},is}^{i\star} = 0 & \text{otherwise.} \end{cases} \tag{4.66}$$

4.4.8 Internal loads

The approach to calculate the internal loads in the time domain is almost equal to the approach used in the frequency domain, see Section 3.3.2.

The internal loads are calculated in the body system. The resultant force

at a 3D ship section is equal to

$$\begin{aligned}\vec{f}^{\star}_{\mathrm{res},is} = \vec{f}^{\star}_{\mathrm{fkhs},is} + \vec{f}^{\star}_{\mathrm{grav},is} + \vec{f}^{\star}_{\mathrm{sd},is} + \vec{f}^{\star}_{\mathrm{beam},is} + \vec{f}^{\star}_{\mathrm{slam},is} + \vec{f}^{\star}_{\mathrm{cor},is} + \\ \mathbf{T}_b(\phi,\theta,0)\left(-\mathbf{B}_{is}(\infty)\cdot\dot{\vec{\xi}}^{\diamond} - \vec{f}^{\diamond}_{\mathrm{rad},is} + \vec{f}^{\diamond}_{\mathrm{diff},is}\right) + \\ \mathbf{T}_b(\phi,\theta,\psi)\left(-\mathbf{B}_{u,is}\cdot\dot{\vec{\xi}} - \mathbf{C}_{u,is}\cdot\vec{\xi} - \mathbf{C}_{e,is}\cdot\vec{\xi}_{sw}\right) - \\ \left(\mathbf{m}^{\star}_{is} + \mathbf{A}^{\star}_{is}(\infty)\right)\ddot{\vec{\xi}}^{\star}.\end{aligned} \tag{4.67}$$

The internal load in the plane for the internal load calculation can be obtained using equations (3.24), (3.25) and resultant force (4.67) at the 3D ship sections.

The modal participation factors can also be used to calculate the internal loads in the time domain. In this case, equation (3.26) is used to compute the internal loads using the participation factors calculated for the structural beam model.

Chapter 5

Slamming loads

The slamming loads are calculated using two 2D methods because these methods are reasonable fast, robust and can calculate the slamming loads with reasonable accuracy.[1] The main focus of this chapter is the approach used to obtain a direct coupling between the seakeeping and the slamming calculation. The methodology for solving both problems is quite different. The seakeeping problem is fully solved as 3D but the slamming is solved using a 2D approach designed for drop test conditions. In general, the time scale of the slamming is much shorter than the time scale of the seakeeping problem. This makes it challenging to couple the calculation of both problems consistently. Note that the coupling is required to be able to solve hydro-elastic problems accurately.

The developed coupling allows one to account for relative roll motion. The relative roll motion usually occurs in oblique seas. Only one of the considered slamming prediction methods is able to account for these roll motions. However, after the coupling was implemented, it was found that the results obtained using this approach seem to be only accurate for near head sea cases. Numerical problems can occur during slamming calculations for headings larger than about thirty degrees from the head sea condition. In addition, the 2D approach used has not been validated against experimental data of drop tests which includes significant roll and sway velocity. In oblique seas, a relative roll and sway velocity will occur and without validation using drop tests or other experiments it cannot be judged if the slamming loading obtained by the 2D approach used is accurate. The author considers, therefore, the 2D approach used to be not suitable to calculate the slamming loads in real oblique seas.

There is not enough experimental data available in the open literature for a validation of the 2D slamming loads calculated in near head sea conditions. Therefore, the validations presented in this thesis are only for head sea conditions.

[1] The accuracy of the methods and their practical application is shown in the validations presented in chapters eight, ten, eleven and twelve.

The first section of this chapter gives more background about the two slamming calculation methods used. The second section gives an introduction of the approach used to couple the seakeeping program with the slamming calculation program and explains the creation of the two dimensional sections. The last section explains the coupling between the seakeeping and slamming calculation in detail.

5.1 Two dimensional slamming calculation

Two 2D methods for the calculation of the slamming loads are directly coupled to the seakeeping program. The first method is the Generalised Wagner Model (GWM) [62] which uses the BEM to solve the weakly nonlinear Wagner impact problem. The other method is the Modified Logvinovich Model (MLM) [23]. This method is based on the Wagner theory of impact of a flat-disc but approximately accounts for both the body shape and the nonlinear terms in the Bernoulli equation for hydrodynamic pressure.

Both methods are developed to calculate the slamming loads for a two dimensional section entering, or rather falling into, initial still water. Figure 5.1 shows a wedge shaped section with deadrise angle α entering still water. The dotted line indicates the still water line. The immersion of the section causes the nearby fluid surface to rise. Jet flows appear at the intersection between the fluid surface and the body. The resulting pressure distribution is sketched along the left-hand side of the wedge shown in Figure 5.1. A pressure peak is observed close to the intersection point c for low deadrise angles. The intersection point is located at the start of the jet flow where the pressure is equal to the ambient pressure. The challenging part of the slamming calculation is computing the uprise of the fluid surface, finding the intersection points and the computation of the pressure. An approximation can be used for the jet flow as it does not contribute significantly to the loading of the section.

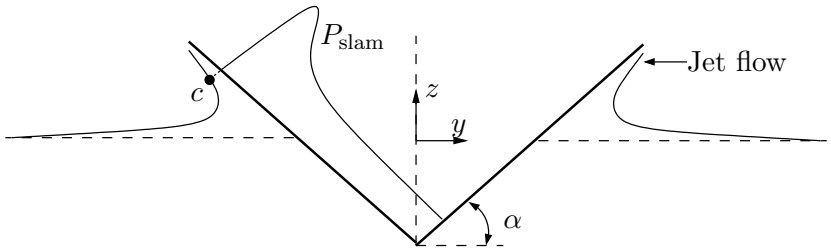

Figure 5.1: Slamming as a wedge shaped section enters still water.

Both methods allow only of sectional shapes which are monotonically increasing in width, for increasing draught. The section geometry may be asym-

metric, for example due to relative roll displacement. Both methods use a prescribed velocity profile. The velocity perpendicular to the still water line is the main input for the methods. The GWM also allows for roll and sway velocity. The methods can only handle the entry problem. The exit problem is not handled at all in this thesis. The slamming force is assumed to be zero during the exit phase.

Both methods assume the fluid to be incompressible, with non-rotational flow and with a velocity potential satisfying the Laplace equation

$$\frac{\partial^2 \varphi}{\partial y^2} + \frac{\partial^2 \varphi}{\partial z^2} = 0. \tag{5.1}$$

The effect of gravity is not included in the calculation. There will be no generation of waves due to the lack of gravity. It is also not possible to account for possible air entrapment in the slamming calculation.

Both methods cannot handle impact of flat bottom sections. The slamming force at flat bottom sections is estimated by using section shapes with a small curvature of the bottom part.

The GWM is very well validated by analytical solutions, experimental results of drop tests and comparison with CFD results in a number of reports and papers, examples are [62, 63, 47, 22]. The MLM method is also validated using experimental results and by using GWM results, see [23, 27]. The validations are mainly done for symmetric sections, some validation is available for asymmetric sections or symmetric sections with constant roll angle. However, to the author's knowledge, there is no validation work done for sections entering the water with roll and/or sway velocity. Only the calculated slamming force occurring during seakeeping in head seas will be validated in this thesis. The calculated 2D slamming force during drop tests is assumed to be already well validated and to be sufficiently accurate.

The main advantage of the MLM method is that the method is much faster compared to the GWM method. The MLM method is also more robust. However, the GWM method has a wider domain of validity. Where the MLM method can only be used for blunt section shapes, the GWM has been validated for wedge shaped sections with a deadrise angle up to 81 degrees. The approach used in this thesis to handle bulbous bows, changing them to be monotonically increasing in width, will result in relatively slender sections and the slamming loads at those sections can only be calculated accurately using the GWM model. It is advised to compare results using MLM and GWM for a few slamming events to judge if the MLM approach can be used for bows without a bulb.

5.1.1 Generalised Wagner Model

The program described in [46] is used to calculate the slamming pressure and resulting forces using the GWM method. This program is partly used as "black box". Therefore, the used theory and the numerical implementation is not fully explained here. These details can be found in [62].

A BEM is used by the GWM method to solve the velocity potential. The kinematic free-surface condition requires that the fluid particles remain at the free surface. This is automatically satisfied as the elevation of the free surface is obtained by integrating the fluid velocity at the free surface. The dynamic free-surface condition is applied at the exact free surface and is equal to

$$\frac{D\varphi}{Dt} = \frac{1}{2}\left[\left(\frac{\partial\varphi}{\partial y}\right)^2 + \left(\frac{\partial\varphi}{\partial y}\right)^2\right]. \tag{5.2}$$

The body boundary condition on the wetted body surface is equal to

$$\frac{\partial\varphi}{\partial\vec{n}} = \vec{v}\cdot\vec{n}, \tag{5.3}$$

where $\vec{n}$ is the normal of the surface and $\vec{v}$ is the velocity of the body surface.

Boundary elements are placed at both the wetted surface and the free surface. The element distribution for a symmetric problem is shown for some time steps of the calculation in Figure 5.2. The free surface elements are located at the still water surface at the first time step. This is because the initial potential, free surface velocity and displacement is set to zero for the first time step. The panel distribution at the body and at the free surface is refined near the intersection point. This allows to better account for large gradients of the pressure at the body and for the large curvature of the free surface. The total length of the free surface mesh is proportional to the wetted surface length to ensure that the fluid velocity at the endpoints of the free surface mesh is negligible.

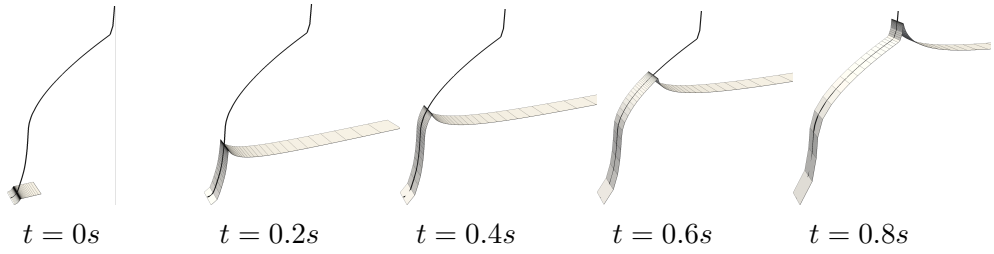

Figure 5.2: A GWM slamming calculation.

The BVP is solved for each time step of the slamming computation. The pressure at the body surface is calculated using the Bernoulli equation. The

forces are obtained by integration of the pressure. The velocity of the free surface is integrated to obtain the new position of the free surface. A new mesh is created using the updated position of the body and the free surface and the BVP is solved for the next time step. The size of the time step is based on the geometry at the intersection point and is different for every step.

5.1.2 Modified Logvinovich Model

The theory of the MLM method is described in [23] and [27]. The MLM method calculates the location of the contact or intersection points by solving the Wagner condition for the real shape of the section. The pressure is calculated using a flat plate assumption between the contact points and using also the non-linear terms in the Bernoulli equation.

The absence of the gravity contribution makes the uprise of the fluid surface only dependent on the immersion of the section and not the velocity history. This allows to a priori calculate the location of the contact points for a range of draughts before calculating the slamming loads.

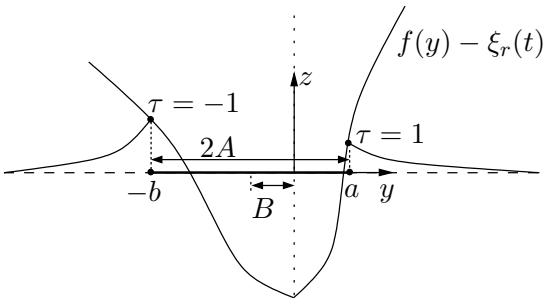

Figure 5.3: The definitions for the MLM method.

The location of the contact points $b(t)$ and $a(t)$ are shown in Figure 5.3. Both contact points are located at $z = 0$. The actual shape of the section is described by the function

$$z(y,t) = f(y) - \xi_r(t), \tag{5.4}$$

where $f(y)$ describes the section in the initial position and $\xi_r(t)$ is the relative displacement of the section in time. The wetted part lies between the contact points. The half width and the asymmetry characterization of the wetted part are

$$A(t) = \frac{1}{2}(a+b), \quad B(t) = \frac{1}{2}(a-b). \tag{5.5}$$

The location of the contact points can be found by solving the Wagner condition. A path over the wetted surface of the section is defined first. The actual shape of the section using a path from $\tau = -1$ to $\tau = 1$ is

$$G(\tau, t) = f\big(y(\tau, t)\big) - \xi_r(t), \quad y(\tau, t) = A(t)\tau + B(t). \tag{5.6}$$

This is used to write the Wagner condition

$$\int_{-1}^{1} G(\tau, t)\Big[\frac{1+\tau}{1-\tau}\Big]^{\frac{1}{2}} d\tau = 0, \tag{5.7}$$

$$\int_{-1}^{1} G(\tau, t)\Big[\frac{1-\tau}{1+\tau}\Big]^{\frac{1}{2}} d\tau = 0. \tag{5.8}$$

These last equations can be written as

$$\int_{-1}^{1} \frac{f\big(y(\tau, t)\big) d\tau}{\sqrt{1-\tau^2}} = \pi h(t), \qquad \int_{-1}^{1} \frac{f\big(y(\tau, t)\big)\tau d\tau}{\sqrt{1-\tau^2}} = 0. \tag{5.9}$$

Differentiating these equations in time and taking A as a new time-like variable results in a system of Ordinary Differential Equations (ODE)

$$\frac{\mathrm{d}h}{\mathrm{d}A} = \frac{1}{\pi}\Big[S_1 - S_0\frac{S_2}{S_1}\Big], \qquad \frac{\mathrm{d}B}{\mathrm{d}A} = -\frac{S_2}{S_1}, \tag{5.10}$$

where

$$S_n(A, B) = \int_{-1}^{1} \frac{f_y\big(y(\tau, t)\big)\,\tau^n d\tau}{\sqrt{1-\tau^2}}, \tag{5.11}$$

and f_y is the directional derivative of the section shape.

This system is solved by integrating h and B using a fourth order Runge-Kutta scheme, see Section 4.3.2, with equidistant steps of the variable A. As A is the half width of the wetted length, the maximum possible value of A is known in advance. The integration of variables h and B is done using a step size ΔA equal to one thousands of the length of A to ensure that the location of the contact points can be calculated accurately for all possible relative displacements of the section.

The initial values of h, B and A for solving equation (5.10) are zero if the section was fully emerged before the start of the slamming event. If the section did not fully emerge from the water, the initial values are calculated using the still water line at the time the relative velocity starts to point downwards.

The integral in equation (5.11) is solved using the points describing the geometry of the slamming section. The section shape is assumed to be linear

between the points defining the slamming section which makes the derivative of the function $f(y)$ constant for each segment of the section. This allows to calculate the integrals of equation (5.11) using the functions

$$\int_{\alpha}^{\beta} \frac{d\tau}{\sqrt{1-\tau^2}} = \arcsin\beta - \arcsin\alpha, \tag{5.12}$$

$$\int_{\alpha}^{\beta} \frac{\tau\, d\tau}{\sqrt{1-\tau^2}} = -\sqrt{1-\beta^2} + \sqrt{1-\alpha^2}, \tag{5.13}$$

$$\int_{\alpha}^{\beta} \frac{\tau^2\, d\tau}{\sqrt{1-\tau^2}} = \frac{1}{2}[\arcsin\beta - \arcsin\alpha] - \frac{1}{2}[\beta\sqrt{1-\beta^2} - \alpha\sqrt{1-\alpha^2}]. \tag{5.14}$$

The slamming pressure is solved for equidistant time steps. The relative displacement of the section at the time steps is known by integrating the provided velocity curve. The location of the contact points is known for a range of relative displacements. Linear interpolation based on the relative displacement is used to obtain the location of the contact points at the time step for which the slamming pressure is calculated.

The slamming pressure depends on the velocity of the contact points. These are

$$\dot{a} = \dot{\xi}_r \frac{\pi(S_1 - S_2)}{S_1^2 - S_0 \cdot S_2}, \tag{5.15}$$

$$\dot{b} = \dot{\xi}_r \frac{\pi(S_1 + S_2)}{S_1^2 - S_0 \cdot S_2}. \tag{5.16}$$

The pressure at the contact region is found by solving, or rather approximating, the potential around the flat plate analytically and using non-linear terms in the Bernoulli equation. This derivation can be found in [23]. The resulting pressure distribution is

$$P_{\text{slam}}(y,t) = \frac{1}{2}\rho\dot{\xi}_r\dot{a}\sqrt{\frac{b+y}{a-y}} + \frac{1}{2}\rho\dot{\xi}_r\dot{b}\sqrt{\frac{a-y}{b+y}} - \frac{1}{8}\rho\dot{\xi}_r^2\frac{(a-b-2x)^2}{(a-y)(b+y)(1+f_y^2(y))} - \frac{1}{2}\rho\dot{\xi}_r^2 + \rho\ddot{\xi}_r[\sqrt{(a-y)(b+y)} + f(y) - \xi_r(t)]. \tag{5.17}$$

This pressure becomes negative near the contact points. Only the positive pressure is considered

$$P_{\text{slam}}(y,t)^{(+)} = \begin{cases} P_{\text{slam}}(y,t) & P_{\text{slam}}(y,t) \geq 0 \\ 0 & P_{\text{slam}}(y,t) < 0 \end{cases}. \tag{5.18}$$

The vertical slamming force is

$$f_{\text{slam},z} = \int_{-b(t)}^{a(t)} P_{\text{slam}}(y,t)^{(+)} \, \mathrm{d}y. \tag{5.19}$$

5.2 Creation of slamming sections

The 2D slamming sections are created during the pre-processing phase described in Section 2.1. The creation of the 2D geometry of the slamming sections is explained in the first part of this section. Normals to the slamming sections scaled with the length of the sections are used to integrate the slamming pressure. The reasons for using these scaled normals and the calculation of the scaled normals are explained in the last two parts of this section.

5.2.1 Slamming section geometry

The 2D slamming sections are defined by the user by creating planes defined by reference points and normals to the planes. This allows to tilt, i.e. pitch, the sections to account better for the relative velocity at the bow. It also allows to give the section a yaw angle which can be used to define slamming sections perpendicular to the wave for oblique seas.

The transformation matrix between the body system and the orientation of a slamming section is defined as

$$\vec{p^s} = \mathbf{T}_s \cdot \vec{p^\star} + \vec{O^s}, \tag{5.20}$$

where point $\vec{p^s}$ is defined in the slamming section reference frame and $\vec{p^\star}$ is the same point observed in the body frame, see Figure 5.4. The transformation matrix consists of the three unit vectors of the slamming frame observed in the body frame, $\mathbf{T}_s = [\vec{e}_1, \vec{e}_2, \vec{e}_3]$ where $\vec{e}_1$ is the unit vector along the defined normal and $\vec{e}_2$ is a unit vector in direction $[-e_{1,y}, e_{1,x}, 0]$. The last vector is obtained by the cross product between the previous two, $\vec{e}_3 = \vec{e}_1 \times \vec{e}_2$.

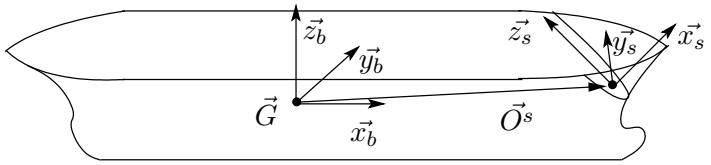

Figure 5.4: Slamming section reference frame.

Next, the integration mesh is transformed to the slamming section reference frame. The same approach as described in Section 2.3 is used to create the

geometry of the 2D slamming section. The section is defined in the plane $x_s = 0$ because the slamming section reference frame is used. The section geometry is smoothed. This smoothing is required as the slamming calculation is sensitive to distortions in the geometry which are usually present because of the meshed geometry used to create the sections.

Both slamming calculation methods can only handle sections that are monotonically increasing in width for an increasing draught. This will not be the case for bulbous bows. Figure 5.5 illustrates the modifications made for a bulbous bow. For further clarification, see also Figure 1.5. Some section cuts contain a part of the bulb which is detached from the bow part of the section. These separate bulb parts are removed. All inward inclined parts of the section will be removed when the bulb is attached to the bow part of the section. Removing the inclined parts of the section may not be such a crude approximation as the fluid flow will separate from the section at the inclined parts. This causes the actual fluid flow to follow the monotonically increasing section more than the original inclined section.

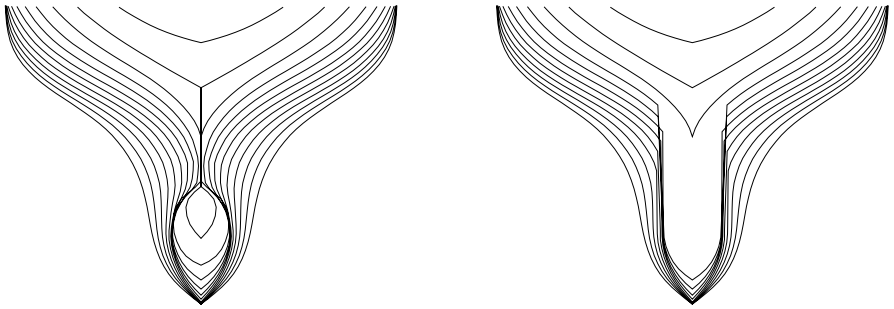

Figure 5.5: Removing the bulb and the inclining parts of the sections.

5.2.2 Pressure integration

After the slamming pressures are calculated using one of the 2D methods, the excitation of the 3D ship structure due to the slamming needs to be computed. A common approach is to calculate the slamming load as a single force vector acting in the section plane, multiply the force with the length of the section and calculate the response of the ship to this force. A different approach is used in this thesis. The excitation of all modes, including the flexible modes, is calculated by integrating the slamming pressure multiplied by the mode shape over the part of the 3D mesh which is associated with the 2D section. Figure 1.5 shows these sections of the 3D mesh used for the pressure integration. The

method has several advantages over the more traditional method:

- The orientation of the 2D slamming sections is defined by the user and is constant during the calculation. When the slamming loading is calculated as a single force in the plane of the section, the orientation of this force is also prescribed by the user when choosing the orientation of the slamming sections. By integrating the pressure over the 3D mesh, the orientation of the resulting slamming force depends on the 3D geometry of the ship and not on the orientation of the 2D sections. The verification in Section 8.2.4 will show that the calculated slamming force is not very sensitive to the selected orientation of the slamming section when using the pressure integration method. This is a favourable property since the direction of the relative velocity is not known in advance and will be different for every slamming event.

- The mode shape obtained from a beam model of a ship is reasonably constant over the 2D sections. This makes the traditional approach valid. The modal response to the single section force will be correct. Mode shapes from a 3D FEM model are usually not constant over the section. As the pressure distribution found for slamming is very variable in time and location, the modal excitation will also be variable. Projecting the pressure onto the mode shape is the only correct way to calculate the excitation of flexible modes obtained from a 3D-FEM computation.

- The loads at specific parts of the ship, e.g. a bow door, can only be obtained using the pressure integration method. This is not possible when a single force is used for every section except if the slamming sections exactly fits the part where the slamming force is required.

The modal excitation force by the slamming pressure integrated on the 3D mesh is equal to

$$\vec{f}_s^i = \sum_{\text{is}=1}^{N_{\text{slam}}} \iint_{S^s} p_s \cdot \vec{h}^i \cdot \vec{n} \, \mathrm{d}S^s, \tag{5.21}$$

where

N_{slam}	number of slamming sections,
p_s	slamming pressure,
S^s	surface of a slamming section,
$\vec{n}$	normal of 3D slamming section geometry.

Equation (5.21) is transformed into a line integral for every section to allow for fast and robust calculations of the modal slamming excitation

$$\vec{f}_s^i = \sum_{\text{is}=1}^{N_{\text{slam}}} \int_{L^s} p_s \cdot \vec{h}_s^i(l) \, \mathrm{d}l, \tag{5.22}$$

where L^s defines the contour of the section, and where

$$\mathbf{h}_s(l)\ \mathrm{d}l = \mathbf{h} \int \vec{n}\ \mathrm{d}w. \tag{5.23}$$

The integral on the right-hand side of equation (5.23) is performed over the length of the section. Note that it is assumed that the mode shape is constant over the section length. The value of $\mathbf{h}_s(l)$ does not change during the slamming calculation and is calculated in the pre-processing phase.

5.2.3 Slamming section scaled normal

The geometry of the 2D slamming sections is created in the pre-processing stage, see Figure 2.4. The program used does not only create the geometry, but it also generates the scaled normals. The mode shapes for the points of the slamming section will be generated by other programs during the pre-processing stage. The mode shapes and scaled normals will be combined by the seakeeping program using equation (5.23) to $\mathbf{h}_s(l)$, which is needed in equation (5.22).

Two methods are implemented to calculate the scaled normal vector $\frac{\int \vec{n}\ \mathrm{d}w}{\mathrm{d}l}$. The first method is fast but is not always accurate and robust. The second method is more accurate and robust but requires more computational effort.

For the first, fast method, are not only the 2D slamming sections created but also are intermediate sections at boundaries of the 2D sections, as is shown in Figure 5.6. These intermediate sections will be used to compute the scaled normal vector. However, this computation can only be accurate if the difference in geometry between the main and the intermediate sections remains small. This will not be the case if a section would include the upper intersection point of the bow with the bulb. This "bulb point" is indicated in Figure 5.6.

The first step of avoiding the "bulb point" to be at a section is to change the distance between the slamming sections before and after this point such that the boundary between two sections is located exactly at the "bulb point". Two intermediate sections are created at this "bulb point". One includes the bulb, which is used for creating the scaled normal for the section aft of the bulb point, and so the bulb is excluded for the other intermediate section used for the forward section. This ensures that the geometric differences between the main and the intermediate sections remain small.

The scaled normal vector is calculated for every point along the 2D section. Figure 5.7 illustrates how this vector is created. The section and the two intermediate sections are divided using an equal number of equidistant points (a). The width per length for every point of the section is calculated using the "panels" which are created by the points at the intermediate sections (b). The area of one panel is equal to $\frac{1}{2} \cdot ||\vec{v}_{s2} \times \vec{v}_{s3}||$ (c). The direction of the normal is obtained by the cross product of vectors $\vec{v}_{s2}$ and $\vec{v}_{s3}$. The width per length is

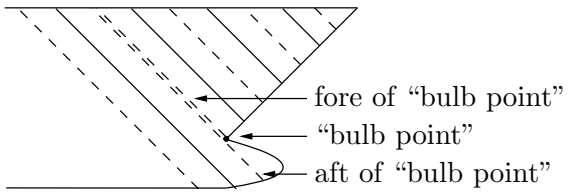

Figure 5.6: Intermediate sections.

equal to the area of the panel divided by the length of vector $\vec{v}_{s1}$. This gives the following formula for the scaled normal vector

$$\frac{\int \vec{n}\,\mathrm{d}w}{\mathrm{d}l} = \frac{1}{2} \cdot \frac{\vec{v}_{s2} \times \vec{v}_{s3}}{||\vec{v}_{s1}||}. \tag{5.24}$$

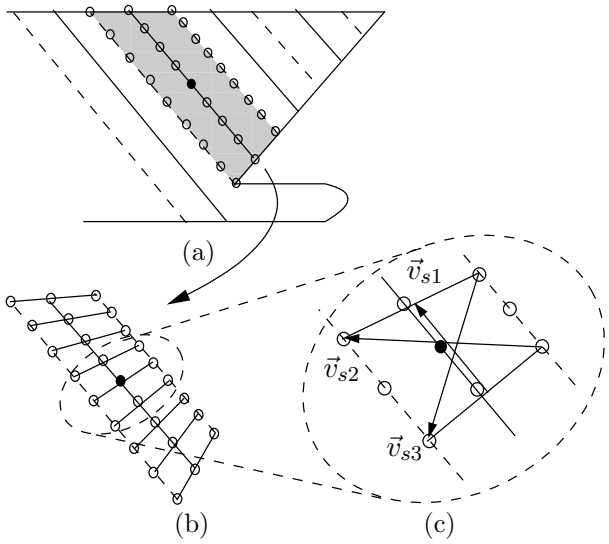

Figure 5.7: Creation of scaled normal vector with the fast method.

The second, accurate but intensive calculation method is illustrated in Figure 5.8. Every section is actually cut out of the 3D mesh. Then, for every point at the slamming section, the associated part of the section is cut out and the area times the normal is integrated over the resulting geometry and divided by the vector $\vec{v}_{s1}$ shown Figure 5.7. The associated part of one point of the 2D section is indicated with a darker gray color in Figure 5.8.

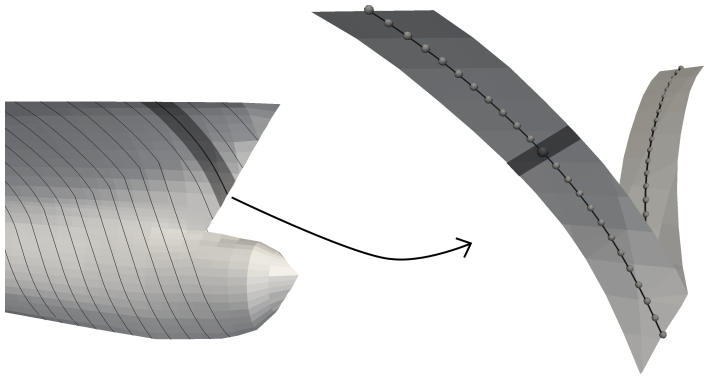

Figure 5.8: Creation of a scaled normal vector with the cutting method.

5.3 Coupling between seakeeping and slamming

The next step is the coupling between the seakeeping and the slamming program. An overview of the approach used is given in the first part of this section. The calculation of the relative velocity is explained in the second part. The third part explains when and how a slamming calculation is initialised. The coupling between the slamming calculation in the time integration scheme of the seakeeping program is the subject of the fourth part of this section. The last part explains the changes to the original slamming calculation programs which are necessary to be able to couple them to the seakeeping program.

5.3.1 Approach

Figure 5.9 illustrates the coupling between the seakeeping program and the slamming calculation program. The shapes of the 2D slamming sections, the mode shapes, the scaled normals and user settings are read at the initialisation at the start of the time domain seakeeping calculation. The box with the integral sign indicates the calculation of the accelerations and integration of the motions by the seakeeping program as explained in the previous chapter. The seakeeping program uses a time step Δt_{sk}. The slamming forces are computed using a much smaller time step Δt_{sl} which can be variable. This requires an additional integration within the slamming computation module.

It is checked if the conditions are met, to start a slamming calculation, at the start of every new time step in the seakeeping calculation. A slamming calculation is started if the relative velocity is above the user defined threshold and the slamming section should also have a minimum immersion which is also defined by the user. This minimum immersion is necessary to be able to start the GWM slamming computation. This check is performed for all defined slamming sections which are not active. The slamming calculation is initialised

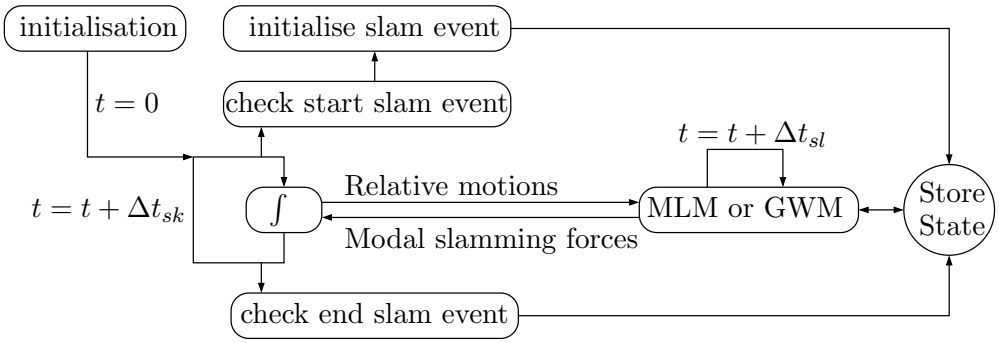

Figure 5.9: Approach for coupling between the seakeeping and the slamming calculations.

if the starting conditions are met.

The relative motions are calculated for the active slamming sections by the seakeeping program during the calculation of the load vector. The relative motion is the input for the slamming programs to calculate the modal slamming force for the current time step. Since, the slamming force depends on the history, i.e. uprise of the free-surface, the state of the different slamming sections is stored and used for the next time step.

When the calculations for the seakeeping time step are finished, it is checked if a slamming event should be ended. This will be the case if the relative velocity is lower than the user defined threshold. A too low relative velocity will cause instabilities of the GWM slamming computation.

Coupling the seakeeping and the slamming program will result in the fact that the effect of the added mass acceleration at the slamming sections is accounted for twice. It is included in a linear fashion in the radiation force and in a non-linear fashion in the slamming force. This double counting is not corrected as the non-linear slamming force is usually much higher than the linear radiation contribution.

5.3.2 Calculation of relative motion

The relative motion is calculated in the plane of the slamming sections as shown in Figure 5.10. The relative motion between the section and the undisturbed wave profile observed in the z-direction of the slamming section reference frame is used.

Due to the possibility of oblique seas, the relative motion may vary along the width of the section. This is illustrated in Figure 5.10, the intersection between the wave surface and the plane of the section is not a straight line. This effect cannot be taken into account for the slamming calculation as an initial still free surface is assumed for the slamming calculation. The relative

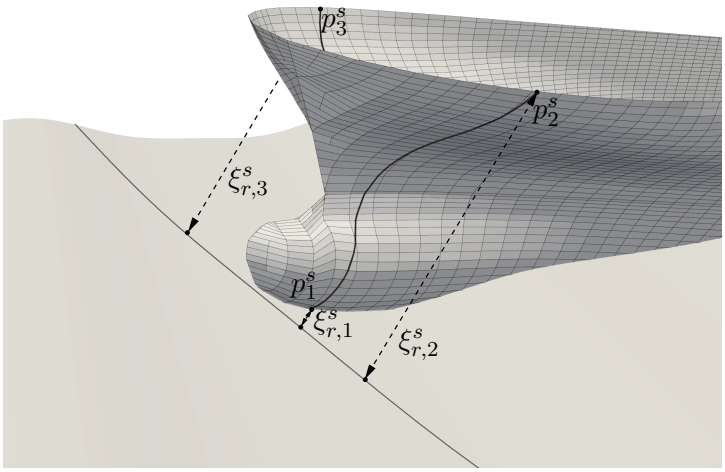

Figure 5.10: Relative displacement.

motion is calculated at three points and a linear interpolation function over the section is used to estimate the relative motion distribution over the section. One calculation point p_1^s is located at the lowest point of the section and the other two calculation points are located at the end points of the section, as shown in Figure 5.10. The interpolation function of the relative displacement at the section is

$$\begin{cases} a_d \cdot y_1^s + b_d \cdot z_1^s + c_d = \xi_{r,1}^s \\ a_d \cdot y_2^s + b_d \cdot z_2^s + c_d = \xi_{r,2}^s \\ a_d \cdot y_3^s + b_d \cdot z_3^s + c_d = \xi_{r,3}^s \end{cases}, \tag{5.25}$$

where y and z are the coordinates of the three points, superscript s indicates the slamming section reference frame and ξ_r the relative displacement. Solving this system of equations allows the calculation the of relative displacement at every point of the section using

$$\xi_r^s(y^s, z^s) = a_d \cdot y^s + b_d \cdot z^s + c_d. \tag{5.26}$$

The relative velocity distribution over the section is obtained by using the same approach.

The 2D slamming calculation methods can only handle motions of rigid sections. Therefore, a single velocity vector for the whole section is used as input for the slamming calculation. Note that the result of a slamming calculation is the pressure distribution which allows one to calculate the excitation for all modes even when a rigid section is assumed by the slamming calculation program. To obtain an average or rigid-body motion of the sections the average mode shape of the section with respect to the calculation points is calculated. Using this average mode shape and the calculation point coordinate in equations

(4.40) and (4.42) results in the average displacement and velocity for the section at the calculation points.

A numerical approach is used to calculate the relative motions. This is because the relative motions should be calculated in the plane of the slamming sections which may be tilted in the pitch direction and rotated in the yaw direction. The plane is also defined at a moving ship. The author is not aware of any analytical solution to compute the relative motions for this problem.

The relative displacement $\xi^s_{r,i}$ is the distance between the calculation points at the slamming section p^s_i and the intersection with the surface of the waves, see Figure 5.10. This intersection is found using a numerical iteration scheme. Figure 5.11 illustrates the numerical approach used to calculate the relative velocity. The relative displacement is calculated for a time step before and after the actual time step. The wave elevation is known for every time step, but the displacements of the ship are not known for the next time step. Therefore, the velocities of the ship are used to make an estimation of the displacement of the ship at the previous and next time steps. The relative velocity is equal to

$$\dot{\xi_r}(t) = \frac{\xi_r(t+\Delta t) - \xi_r(t-\Delta t)}{2\Delta t}, \tag{5.27}$$

with

$$\vec{\xi}(t \pm \Delta t) = \vec{\xi}(t) \pm \dot{\vec{\xi}}(t) \cdot \Delta t. \tag{5.28}$$

Note that the time step Δt used for computing this derivative is not necessarily the time step of the seakeeping computation. Therefore, the displacement at the previous time step is not necessarily known and is therefore also estimated.

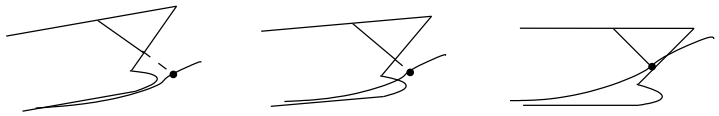

$\xi_r(t-\Delta t)$ $\quad$ $\xi_r(t)$ $\quad$ $\xi_r(t+\Delta t)$

$\vec{\xi} = \vec{\xi}(t) - \dot{\vec{\xi}}(t)\Delta t$ $\quad$ $\vec{\xi}(t)$ $\quad$ $\vec{\xi} = \vec{\xi}(t) + \dot{\vec{\xi}}(t)\Delta t$

Figure 5.11: Calculation of relative velocity.

The relative velocity calculated by equation (5.27) is used for the decision to start a slamming calculation. The relative velocity is the main input for the slamming calculation and a higher order differentiation scheme is used to obtain a smoother velocity input for the slamming calculation. This is important to obtain a stable slamming calculation. This higher order scheme is equal to

$$\dot{\xi_r}(t) = \frac{-\xi_r(t+2\Delta t) + 8\xi_r(t+\Delta t) - 8\xi_r(t-\Delta t) + \xi_r(t-2\Delta t)}{12\Delta t}, \tag{5.29}$$

again using the estimated displacements (5.28).

The MLM slamming calculation requires also the relative acceleration. The same approach as used to calculate the relative velocity is employed to calculate the relative accelerations. The displacement of the ship is estimated in this case by

$$\vec{\xi}(t \pm \Delta t) = \vec{\xi}(t) \pm \dot{\vec{\xi}}(t) \cdot \Delta t \pm \ddot{\vec{\xi}}(t) \cdot \Delta t^2, \tag{5.30}$$

and the relative acceleration is equal to

$$\ddot{\xi}_r(t) = \frac{\xi_r(t + \Delta t) - 2\xi_r(t) + \xi_r(t - \Delta t)}{2\Delta t}. \tag{5.31}$$

The relative motion is calculated in the slamming section reference system using the previous formulae. These relative motions cannot be used directly as the slamming calculation requires the motions in a different reference system which has a fixed orientation towards the water line. These differences in reference frames are illustrated in Figure 5.12. The origins of both systems are aligned.

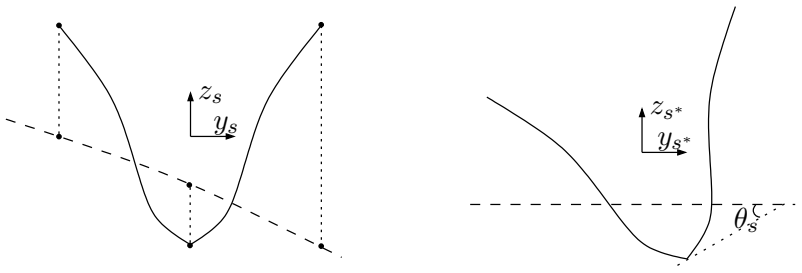

Figure 5.12: Difference between the slamming section system and the slamming calculation reference frame.

These differences in reference frames will only appear for calculations in conditions where relative roll motion occur. The systems will be aligned without relative roll displacement. The calculation as described below will be ignored for head sea calculations to reduce the computational effort.

The GWM slamming calculation is the only method which allows for relative roll motion. It was first tried to calculate the relative velocity in both the downward and sidewards direction. The combined sway, yaw and roll motions of the ship can cause a significant velocity in the sidewards direction at the intersection with the still water line. It appeared that the GWM is very sensitive to this sidewards velocity. The method fails to keep the intersection points at the correct position when the sidewards velocity is included. This problem causes the computed slamming force to be incorrect and resulted sometimes in numerical instabilities. This problem is avoided by not transferring the actual relative sidewards motions of the section but transferring instead a sidewards

velocity that compensates the roll induced sidewards motion at the still water line.

The intersection with the waterline is calculated using the linear interpolation function of equation (5.26)

$$\xi_r^s(y^s) = 0 = \frac{-c_d - a_d \cdot y^s}{b_d}. \tag{5.32}$$

This allows to calculate the relative roll angle as

$$\theta_s = \arctan\left(\frac{-a_d}{b_d}\right). \tag{5.33}$$

The relative velocity at the waterline is used as input for the slamming calculation. The relative velocity distribution at the waterline is found by substituting equation (5.32) into the interpolation function (5.25)

$$\dot{\xi}_r^s(y^s) = a_v \cdot y^s + b_v \cdot z_s + c_v, \tag{5.34}$$

$$\dot{\xi}_r^s(y^s) = a_v \cdot y^s + b_v \cdot \left(\frac{-c_d - a_d \cdot y_p}{b_d}\right) + c_v, \tag{5.35}$$

$$\dot{\xi}_r^s(y^s) = \left(a_v - \frac{b_v \cdot a_d}{b_d}\right) y_s - b_v \cdot \frac{c_d}{b_d} + c_v, \tag{5.36}$$

where a_v, b_v and c_v are the interpolation constants for the relative velocity distribution over the section. This allows one to calculate the relative velocity at the water line at $y^s = 0$ in both the z^s and θ^s direction

$$\dot{\xi}_{r,z}^s = -b_v \cdot \frac{c_d}{b_d} + c_v, \tag{5.37}$$

$$\dot{\xi}_{r,\theta}^s = a_v - \frac{b_v \cdot a_d}{b_d}. \tag{5.38}$$

The velocity y^s in the direction $\dot{\xi}_y^s$ is computed such that is cancels the sidewards velocity that is induced by the roll motion. This makes the slamming calculation more stable for oblique seas. The relative velocity in the slamming calculation system is equal to

$$\dot{\xi}_y^{s^*} = -\theta_s \cdot \xi_z^{s^*}, \tag{5.39}$$

$$\dot{\xi}_z^{s^*} = \dot{\xi}_{r,z}^s \cdot \cos(\theta) + \dot{\xi}_y^s \cdot \sin(\theta), \tag{5.40}$$

where the displacement in the z-direction of the slamming calculation frame equals

$$\xi_{z^{s^*}} = \frac{c_d}{\sqrt{a_d^2 + b_d^2}}. \tag{5.41}$$

5.3.3 Initialisation slamming calculation

A slamming calculation is initialised when the relative velocity is above a user defined threshold and the immersion of the section is larger than the user defined threshold. The slamming calculation is stopped as soon as the relative velocity drops below an user defined threshold, this can be a different value than used for starting the slamming calculation.

The choice of these thresholds has a large influence on the stability of the GWM slamming calculation. For low relative velocity, lower than $[1m/s]$ for normal ships, the calculation can become instable. The BEM problem of the GWM-method can only be formulated if the section has some initial immersion at the start of the calculation. Otherwise it would not be possible to create BEM-elements at the wetted geometry. If the initial immersion is very small, the GWM calculation will require much more computational effort in the initial stage of the slamming impact due to the small panel size resulting in a very small time step. Using a large initial immersion will neglect a part of the initial slamming impulse and a part of the uprise of the free surface for the remaining slamming calculation. The MLM calculation is stable as long as the relative velocity is directed downwards. MLM does not need any initial immersion to start the calculation.

The time step of the seakeeping calculation is usually quite large compared to the time scale of the slamming event. Figure 5.13 illustrates the approach for starting the slamming calculation. The top pictures show the relative displacement of the section for two successive time steps and the time step where the slamming calculation is started. The same relative displacement is plotted in the three graphs at the bottom. The small line in the section and the dashed line in the graphs indicated the user defined minimum immersion. At time step t_n the section is above the water so the slamming calculation is not started. At the next time step t_{n+1} the section is already in the water and the immersion is larger than the threshold. As shown in the figures on the right-hand side in Figure 5.13, an interpolation is made backwards in time until the relative displacement is equal to the threshold. The slamming calculation is started from that point.

The relative velocity also is a conditional for the start of a slamming calculation. The slamming section may have already enough relative displacement during a few seakeeping time steps before the relative velocity criteria is met. The slamming calculation will be initialised at the first interpolated time step where either the minimum immersion threshold is exactly met or at the time step where the relative velocity becomes larger than the minimum relative velocity threshold set by the user which is also used for stopping the slamming calculation. This initialisation may span multiple time steps of the seakeeping calculation. Only the slamming force of the last seakeeping time step will be transfered to the seakeeping program. The slamming forces obtained for

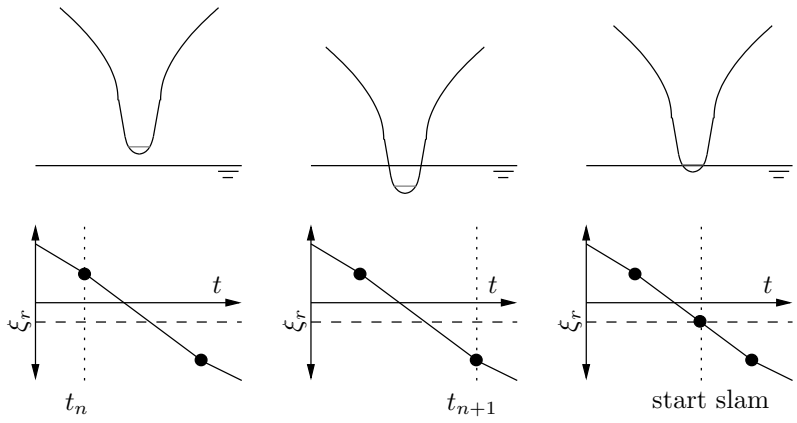

Figure 5.13: Moment of initialisation of slamming calculation.

previous time steps during initialisation are neglected for this case.

There are two reasons for starting the slamming calculation at the interpolated time step and not at the time step of the seakeeping calculation. The first reason is that otherwise the first part of the slamming impulse would be lost. The other reason is only applicable to the GWM. The GWM calculates the uprise of the free surface by integrating the velocity of the free surface during the slamming event. A correct prediction of the uprise is important for a correct calculation of the slamming force. A part of the uprise will be neglected by starting the calculation at a large immersion, lowering the calculated slamming force for the whole slamming event. The MLM model uses a semi-analytical solution for the uprise which is not affected by the starting point of the calculation.

5.3.4 Coupling the integration scheme

The coupling between the seakeeping calculation and the slamming calculation depends on the Runge-Kutta integration method used in the seakeeping calculation as described in Section 4.3.2. The time-scale of the slamming event is usually much smaller compared to the time-scale of the seakeeping problem. The duration of the slamming event is usually only a few time steps of the seakeeping calculations. In order to obtain the correct whipping amplitude, the impulse of the slamming should be integrated correctly.

Figure 5.14 shows the approach to integrate the slamming force. In this case the conditions for a slam event are satisfied at time step t_{n+1}. The slamming calculation is initialised at a time before time step t_{n+1} where the slamming conditions are exactly met, as explained in the previous section. The slamming calculation is continued until t_{n+1} after initialisation. There are many time

steps of the slamming calculation between the initialisation and t_{n+1}. The slam force f_{11} is the average slamming force between time steps t_n and t_{n+1} and is used to calculate the acceleration in the first Runge-Kutta step.

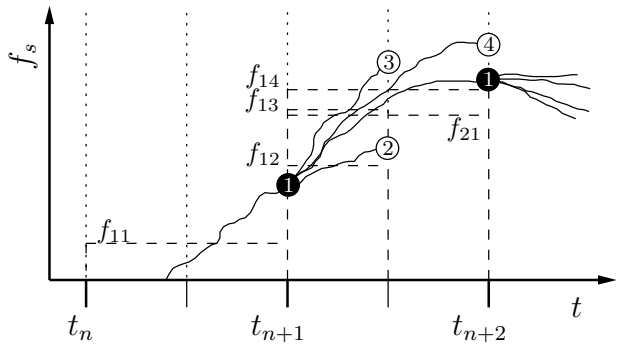

Figure 5.14: Integration of slamming force.

For the second Runge-Kutta step an estimation for the motions at $t_{n+1}+\frac{1}{2}\Delta t$ is made and the average slamming force from t_{n+1} until $t_{n+1}+\frac{1}{2}\Delta t$ is calculated, f_{12}. In the third Runge-Kutta step another estimation is made for the motions at $t_{n+1}+\frac{1}{2}\Delta t$. To calculate the slamming force associated with this new motion estimation, the slamming calculation is restarted in the state at t_{n+1} and re-run until $t_{n+1}+\frac{1}{2}\Delta t$ using the new estimation of the motions. f_{13} is the average slam force of this last calculation and is used to calculate the accelerations for the third Runge-Kutta step. For calculation of the average slamming force for the fourth Runge-Kutta step f_{14} and the first Runge-Kutta step for the next time step f_{21} the slamming calculation is run from the t_{n+1} until t_{n+2}.

The slamming calculation is started from the state at time step t_{n+2} for all Runge-Kutta steps to calculate the motions at t_{n+3}. The slamming calculation continues until the relative velocity drops below the user defined threshold.

This approach ensures that the slamming force is correctly integrated in time. The resulting impulse and whipping response should be independent of the selected time step of the seakeeping calculation when using a time step which is a few times smaller than the duration of the slamming events. This will not be the case if simply the actual force of the slam at the seakeeping time steps would be used. Using a time step which is in the same order as the slamming events will cause inaccuracies because the relative velocity curve will not be well described and/or the slamming events might be missed completely.

5.3.5 Coupling the slamming calculation method

All input necessary for the calculation of the slamming loads has been derived in the previous sections. This section describes the changes to the two methods

for calculation of the slamming loads to be able to couple them directly with the seakeeping calculation.

The modifications to the GWM, described in Section 5.1.1, are explained first. The coupling with the seakeeping integration scheme requires one to calculate the slamming loads between the time steps of the seakeeping calculation. The time step of the GWM is driven by the relative geometry between the section and the free surface. This results in the time step being different for every step of the slamming calculation. Figure 5.15 illustrates the actual coupling with the seakeeping calculation. This figure is an enlargement of Figure 5.14 with the lines of the intermediate Runge-Kutta steps removed. The small dots indicate the time steps of the GWM slamming calculation. In general, the time steps are much smaller compared to the average seakeeping time step. This allows one to run the GWM calculation until the first time step which is larger then the required time. This time step will also be the starting point for the next calculation. The average slamming load for a seakeeping time step is calculated using an integration of the slamming load with the trapezium rule between the first and last time step of the GWM calculation and dividing the result by the total time of the GWM calculation.

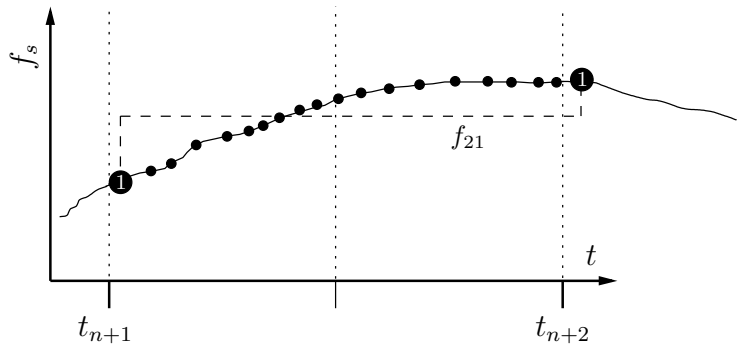

Figure 5.15: Integration of slamming force for GWM.

Equation (5.22) allows to calculate the modal force by a line integral. The mode shapes $\mathbf{h}_s(l)$ are available for all points describing the slamming section, see Section 5.2. However, the pressure is calculated for the GWM panels which have a different geometry for every time step. The approach to calculate the modal force is illustrated in Figure 5.16. The slamming section segments are divided into two segments and are associated to the nearest point. The average pressure at these new segments is calculated assuming a constant pressure at the GWM panels. The integral in equation (5.22) is computed by a summation of these average pressures multiplied by $\mathbf{h}_s(l)$ and the length of the new segments. Not only should the modal slamming forces for the body be calculated, but the modal forces at the different sections of the body are also required. The

summation of the slamming force is repeated for all 3D sections of the body for internal load calculation. Only the slamming section points present at the 3D sections are taken into account in order to calculate the sectional forces in order to compute the internal loads.

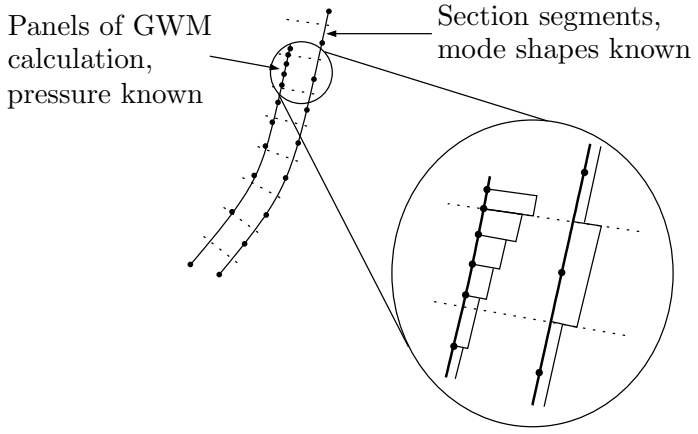

Figure 5.16: Calculation of modal force using GWM pressure.

The other slamming calculation method is the MLM method. The slamming pressure and resulting force can be calculated for every relative displacement and therefore every time step using the MLM method. This allows one to full compatibility with the time steps of the seakeeping calculation. The average slamming force during a seakeeping time step is calculated using twenty equidistant time steps in MLM.

Figure 5.17 illustrates the calculation of the modal force. The same approach as for the GWM is used. The average pressure is also calculated, but the MLM pressure is only defined at the flat plate at the still water line. This pressure is integrated as if it would act on the geometry of the slamming section. The MLM pressure is a continuous function and ten equidistant points for every segment of the slamming section are used to calculate the average pressure at a segment.

A part of the MLM pressure, see equation (5.18), is proportional to the relative accelerations. This part is usually referred to as added mass and normally all added mass contributions should be added to the left-hand side of the equation of motion. This approach is not followed for this MLM added mass as the equation of motion is only solved for the seakeeping time steps. These time steps are usually too large for an accurate integration of the contribution of this added mass. Another problem is that this added mass is in the slamming section reference frame and is defined relative to waves where the motions are solved in the Earth system. The accelerations found for the previous Runge-Kutta (prediction) step are used to calculate the contribution

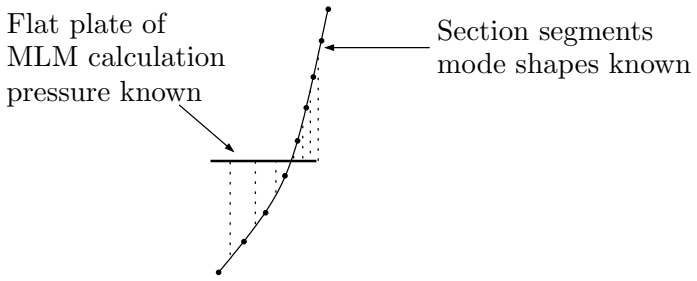

Figure 5.17: Calculation of modal force using MLM pressure.

of the added mass.

Chapter 6

Time domain seakeeping load to 3D-FEM

The seakeeping loads and responses are solved in the time domain using the theory presented in the fourth chapter. The response of the elastic modes is known from this computation and therefore the global structural response can be reconstructed. The local response of the ship structure to the sea loads, which can include slamming loading, cannot be derived accurately using the modal approach except when many relevant mode shapes are included in the seakeeping calculation.

The local structural response can be calculated by transferring the time history of the seakeeping loads to a 3D-FEM model and by solving the structural response within the FEM program. This chapter describes the transfer of all the hydro-elastic seakeeping loads, which contribute significantly to the structural response, to the FE model of the structure.

An introduction about the approach used is given in the first part of this chapter. A few geometric issues are discussed in the second part. The third part explains the calculation of the loading on the structural model.

6.1 Approach

The loads at the structural model are calculated by post-processing the compute seakeeping motions of both the rigid-body and flexible modes. The calculation of the loading at the structural model is quite similar to the calculation of the seakeeping loads as described in the fourth chapter. It would be possible to compute the structural loads directly during the seakeeping calculations, but there are two major disadvantages using that approach:

- The retardation function has to be evaluated for every wetted node of the structural mesh. This will be very computationally intensive.

- Usually, only a small part of the time domain calculation is selected to perform a structural analysis. This is usually the interval where the most extreme loading occurs. Using a post-processor allows to select only these events.

The hydrodynamic loads will be applied to the structural model as nodal forces instead of pressures at the panels. The main reason for using this approach is that the seakeeping theory accounts for large amplitude motions. As the linear hydrodynamic components are assumed to act in the hydro system, these force contributions should be transfered to the body system to be used in the structural calculation. This is illustrated in Figure 4.4. This cannot be done when pressure loading would be used as pressure loading cannot be transformed to a different reference frames. Another reason is that the different pressure integration routines of the FEM packages are avoided by using forces. These different routines might result in a slightly different total loading which will disturb the balance of forces at the structural model.

Only the main load components are transfered to the structural model. These are the Foude Krylov, hydrostatic, radiation, diffraction, slamming and acceleration components of the loading. Other force components like springs, damping, kinematic constraints, etc. are not transfered to the structural model as it is very difficult to know at which part of the ship these, mostly artificial, forces should act. Normally, these forces are relatively small compared to the main loads and the absence of these contributions will hardly influence the resulting (local) structural response. An exception is the roll damping. This damping can have significant influence on the roll motion in oblique seas and therefore the structural response. Thus, the calculation of structural loading as presented in this chapter should only be used for head sea cases and for cases where the contribution of the roll damping is negligible.

The structural response is solved by the FE program using a quasi-static approach. The whipping and springing response is taken into account by calculating the acceleration force at every structural node and by transferring these forces to the FEM load case. The dynamics of the local structure are not taken into account in the FEM calculation using this approach.

A quasi-static calculation using a FEM requires the addition of supports or constraints at some nodes. All six degrees of rigid-body motion should be suppressed by these supports without influencing the structural response.

Reaction forces will appear at the supports if the applied loading is not fully balanced. These reaction forces can influence the structural response. Most FE programs allow one to use “relief accelerations” to avoid these reaction forces. In that case, the FE program calculates rigid-body accelerations such that the model is fully balanced. The motions and thereby the accelerations are also a part of the seakeeping solution. Changing the resulting accelerations by using the “relief accelerations” will also change the structural response.

The presented approach ensures that the loading is well balanced and that the resulting accelerations are close to the original seakeeping accelerations, without using the relief accelerations. An important step for this is the use of the structural mesh to compute the seakeeping motion which is explained in the previous chapters. Interpolation between the hydrodynamic and structural mesh is avoided by using the structural mesh in the seakeeping calculation. Balanced loads are ensured by first computing the loading at the structural model and then recomputing the resulting accelerations when calculating the FE loading. There will be small differences between these accelerations and the original seakeeping accelerations since not all force components will be transfered. There will also be some differences in the radiation force because a different approach is used to calculate these forces for the structural loading in order to reduce the computation effort. This will be explained in Section 6.3.

The transfer of seakeeping loads to the structural model as presented in this chapter is only applicable to single body problems.

6.2 Nodal hydrodynamic coefficients

The hydrodynamic coefficients have to be calculated for every node at the structural mesh to be able to compute the nodal forces at the structural model. The calculation of these nodal values using the Gauss points integration is explained in Appendix A. This approach can directly be used if there are no sections defined. However, as explained in Section 2.4.1, panels will be cut if sections are defined. The hydrodynamic pressure is calculated and stored for every Gauss point of this mesh with cut panels after solving the BVP, see the third chapter. The modal displacements are also known for the Gauss points of the mesh with cut panels. Both the hydrodynamic coefficients and mode shapes have to be recomputed if the original structural mesh would be used to generate the Gauss points to compute the nodal values. This would also create a small difference between the coefficients used in the seakeeping calculation in for the calculation of the structural loading.

This re-computation is avoided by using the Gauss points of the cut panels to compute the coefficients at the nodes of the original or structural panels. The weight factors and Jacobian of the Gauss points of the cut panels are used in equation (A.10). However, the shape function in this equation are computed for the location of the Gauss points at the original panels. This is illustrated in Figure 6.1. A numerical procedure is used to calculate the local coordinates of the Gauss points at the original mesh to be able to compute the shape function at these points.

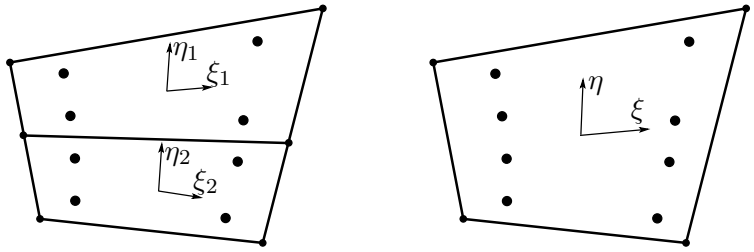

Figure 6.1: Gauss points at a cut panel and the original panel.

6.3 Loads

The computation of the total load case at the structural model is explained in the first part of this section. The other parts explain the calculation of the individual components of the total load vector.

6.3.1 Load case

As stated before, the total load vector which is exported to the FEM package is slightly different from the seakeeping load vector. The equation of motion is again solved to ensure balance between the hydrodynamic loading and acceleration forces at the structural model. The nodal contribution of all hydrodynamic force components are calculated first. These forces are based on the displacements and velocities calculated by the seakeeping program. The new acceleration is solved using

$$(\mathbf{A}^\star(\infty) + \mathbf{m}^\star) \cdot \ddot{\vec{\xi}}^\star = \vec{f}^\star_{\text{grav}} + \sum_{n=1}^{N\text{nodes}} \vec{f}^{\star,n}_{\text{fkhs}} + \vec{f}^{\star,n}_{\text{slam}} - \vec{f}^{\star,n}_{\text{rad}} + \vec{f}^{\star,n}_{\text{diff}}. \tag{6.1}$$

This equation is similar to equations (4.33) and (4.47). The superscript n indicates the force at the nodes of the structural mesh. The infinite added mass is still on the left-hand side to ensure that the hydrodynamic loading at the structural model is consistent with the accelerations.

The total hydrodynamic loading at the structural model is calculated after solving the motion equation

$$\vec{f}^{\star,n}_{\text{tot}} = \vec{f}^{\star,n}_{\text{fkhs}} + \vec{f}^{\star,n}_{\text{slam}} - \vec{f}^{\star,n}_{\text{rad}} - \vec{f}^{\star,n}_{A(\infty)} + \vec{f}^{\star,n}_{\text{diff}}. \tag{6.2}$$

The hydrodynamic loading is balanced by nodal acceleration forces

$$\vec{f}^{\star,n}_{\text{acc}} = m^{\star,n} \left(\vec{a}^{\star,n} + \vec{g}^\star \right), \tag{6.3}$$

where

$m^{\star,n}$ nodal mass,
$\vec{a}^{\star,n}$ accelerations in the body system at the node.

The acceleration at the nodes is calculated using equation (4.44) and transformed to the body reference frame.

The hydrodynamic and acceleration forces are combined and used as load case for the quasi-static FEM calculations.

6.3.2 Radiation force

The radiation force is the most difficult force component of the structural loading to compute. An approach could be to create and evaluate the retardation function for every structural node. This approach will result in exactly the same total radiation force as computed by the seakeeping program. However, the computation effort required for this approach is huge. Another approach could be to use the frequency domain RAO values. This will not be correct if it is based on the motion calculated in the frequency domain. Therefore, a Fourier transform on the calculated seakeeping velocity is used to obtain the amplitude and phases of the different frequencies in the time domain calculation. This approach results in a total radiation force which is very close to the radiation force calculated by the seakeeping program. There will be some differences because it is assumed that the linear hydrodynamic coefficients fully comply to the Kramers-Kronig relations for the creation of the retardation function (4.49), which is not always the case when forward speed is included. Also, the length and discretization of the retardation function may cause some differences. The discretized Fourier transform is the last source of possible differences between the results of the radiation force calculated using retardation functions or this frequency reconstruction.

The frequency content of the velocity in the hydro-reference frame is equal to

$$\dot{\vec{\xi}}^{f\diamond}(\omega) = \mathcal{F}\big(\dot{\vec{\xi}}^{\diamond}(t)\big). \tag{6.4}$$

The nodal force in the body reference frame due to radiation, with the contribution of the infinite frequency added mass subtracted, is

$$\vec{f}^{\star,n}_{\text{rad}} = \mathbf{T}_{b,\mathbb{R}3}(\phi,\theta,0) \cdot \sum_{j=1}^{N\text{freq}} \Big\{ \Re\left(\vec{F}^{\diamond,n}_R(j) - \vec{F}^{\diamond,n}_R(\infty)\right) \cdot \Re\left(\dot{\vec{\xi}}^{f\diamond}(j) \cdot e^{-i\omega_j t}\right) + \Im\left(\vec{F}^{\diamond,n}_R(j)\right) \cdot \Im\left(\dot{\vec{\xi}}^{f\diamond}(j) \cdot e^{-i\omega_j t}\right) \Big\}. \tag{6.5}$$

Force vector $\vec{F}^{\diamond,n}_R$ is the frequency domain nodal radiation force. Note that the contribution if the infinite damping is already included in equation (6.1). The nodal force due to the acceleration of the infinite frequency added mass is

$$\vec{f}^{\star,n}_{A(\infty)} = \mathbf{T}_{b,\mathbb{R}3}(\phi,\theta,0) \cdot \Re\left(\vec{F}^{\diamond,n}_R(\infty)\right) \cdot \ddot{\vec{\xi}}^{\diamond}. \tag{6.6}$$

6.3.3 Diffraction force

The diffraction force is only based on the actual position of the ship, see Section 4.4.3. The nodal diffraction force is computed using the same approach as used for the time domain calculation, see equation (4.57),

$$\vec{f}^{\star,n}_{\text{diff}} = \mathbf{T}_{b,\mathbb{R}3}(\phi,\theta,0)\cdot\sum_{j=1}^{N\text{freq}}\zeta_a(\omega(j))\Big\{\Re(\vec{F}^{\diamond,n}_D(j))\cos\big(\omega_j t+\varepsilon_\zeta(\omega_j)+x_w k(\omega_j)\big) + \Im(\vec{F}^{\diamond,n}_D(j))\sin\big(\omega_j t+\varepsilon_\zeta(\omega_j)+x_w k(\omega_j)\big)\Big\}, \quad (6.7)$$

with $\vec{F}^{\diamond,n}_D$ the nodal frequency domain diffraction coefficient.

6.3.4 Froude Krylov and hydrostatic force

The non-linear Froude Krylov and hydrostatic pressures are directly calculated in the body reference frame for the time domain calculation. The calculation of these pressures is explained in Section 4.4.2. The pressure is re-calculated using the same approach but equation (A.10) is used to compute the nodal forces.

6.3.5 Slamming force

The calculation of the slamming pressure is done exactly the same as described in the previous chapter. The average pressure at the slamming section nodes is multiplied with the scaled normals. This results in the forces at the slamming section nodes. These forces are multiplied with the shape functions at the location of the slamming section nodes to obtain the slamming force at the nodes of the structural mesh. The computed slamming force is already in the body system.

Chapter 7

Design values from non-linear calculations

Two important design values for ship structures are the maximum expected bending moment and the fatigue loading of the structure. Whipping induced by slamming and springing may have a significant contribution to the maximum bending moment and the fatigue load. The whipping response of the ship is calculated using non-linear time domain calculations which include the slamming loads. Although computing the springing response is not a goal of this thesis, it will be (partly) computed using the hydro-elastic approach. The design values should be computed for at least a part of the wave scatter diagram to get insight in the loading of the ship during its life. This requires to compute bending moment time traces for many different sea states.

Preforming these non-linear calculations for many conditions requires significant computational effort. It is investigated how the calculations can be performed and how the data can be analysed in order to minimise the calculation time needed to obtain accurate results for the design values. Only the "brute force" method is investigated. Using this method, the statistical values are obtained by only using the time traces. The results can only be accurate when using time traces of sufficient length. There are statistical methods available which combine the linear and non-linear results to reduce the calculation time significantly and still obtain the design values within a reasonable accuracy [20, 41]. These methods show good results but are not investigated or used within this thesis.

The first section of this chapter explains how the total fatigue damage and expected maximum bending moment are derived from the computed bending moment or stress history using the brute force method. How the design values can be computed in the most optimal way using the brute force method is investigated in the second section of this chapter.

7.1 Data analysis

Both the fatigue damage and the maximum expected bending moment are determined based on the bending moment signal. The fatigue analysis is explained in the first part of this section. The maximum moment analysis is explained in the second part. The last part of this section explains how one signal is created from multiple computations using different wave realisations for a single sea state.

7.1.1 Fatigue analysis

The total fatigue damage D_f is calculated based on the Palmgren-Miner linear damage hypothesis

$$D_f = \sum_{i=1}^{k} \frac{nc_i}{Nc_i}, \tag{7.1}$$

where nc_i is the number of cycles with amplitude range i that have occurred and Nc_i the number of cycles with amplitude range i that are allowed. The allowed number of cycles can be obtained by given Wöhler- or SN-curves presented as

$$N(\sigma) = \begin{cases} K_s^{-1}\sigma^{-\beta_s} & \sigma > \sigma_{\min} \\ \infty & \sigma < \sigma_{\min} \end{cases}. \tag{7.2}$$

This is a two segment curve where σ is the stress and K_s and β_s are the SN parameters. One- and three-segmented curves are also commonly used. For all the analyses presented in this thesis, a one segment curve is used. The one segment curve is obtained by setting $\sigma_{\min}$ to zero in equation (7.2).

The oscillations in the stress signal are counted using the rainflow count method. The algorithm proposed by Rychlik [14] is used to perform the rainflow count. This algorithm is equivalent to the original algorithm by Endo but is easier to implement. Figure 7.1 illustrates the definition of a rainflow cycle by Rychlik:

Rainflow cycle From each local maximum M one shall try to reach above the same level, in the backward and forward directions, with a as small downward excursion as possible. The minima, m^- and m^+, on each side are identified. That minimum which represents the smallest deviation from the maximum M is defined as the corresponding rainflow minimum m^{rfc}.

All min-max and max-min cycles are counted using the rainflow count. One full cycle is counted as the amplitude occurs both in the min-max and max-min count. It is normal that, when all full cycles are grouped together, some half-cycles are left over. The relative number of half cycles is reduced by mirroring

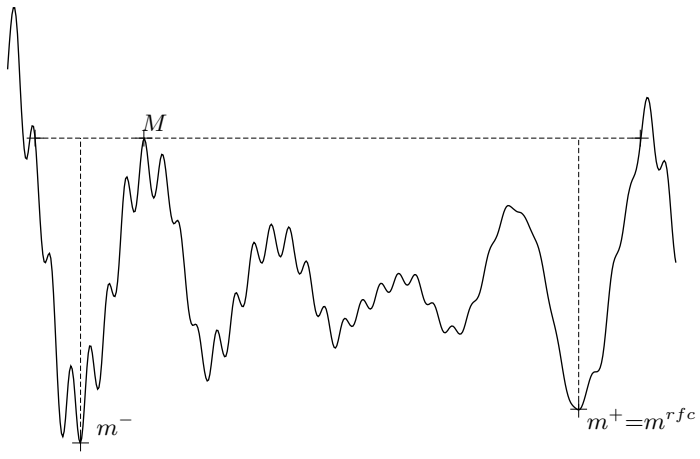

Figure 7.1: Rainflow count algorithm.

the data when the number of extremes is lower than one thousand. This makes the counting method more stable for a low number of cycles. As (almost) all cycles have a different amplitude, the nc_i in the Miner rule (7.1) will be 1 and k will be equal to the number of oscillations.

For the examples in this chapter, the stress at the deck is obtained using

$$\sigma_{\text{deck}} = S_{\text{cons}} \cdot \frac{M_y \cdot z_{\text{deck}}}{I_{yy}}, \tag{7.3}$$

where S_{cons} is the stress concentration factor, z_{deck} the distance between the neutral axis and the deck, and I_{yy} the section modulus. The stress in the deck can also be obtained by using the modal participation factors calculated for the stress at a point using a 3D-FEM, when available.

7.1.2 Maximum expected bending moment

The maximum expected bending moment is obtained by extrapolating the realisation of extremes using a Weibull extrapolation [24, 21]. The Weibull extrapolation is commonly used to obtain the extreme values in a seakeeping analysis, although there is no solid theoretical foundation to do so. The use of the Weibull method may be more questionable in this case as the bending moment contains both the wave frequency and whipping response which cause the resulting stress spectra to be wide banded where the stress signal of linear seakeeping is narrow banded. For this thesis, it is assumed that the Weibull extrapolation still holds, even with the presence of whipping response. Further

research on which extrapolation method can be used best for a ship experiencing whipping is definitely needed.

The probability that the bending moment M_y will be larger than M is, according to the Weibull distribution, equal to

$$P(M_y > M) = 1 - \exp\left\{\left(-\frac{M - M_0}{M_c - M_0}\right)^{k_w}\right\}, \tag{7.4}$$

where M_c is the scale parameter, k_w the shape parameter and M_0 is the mean value. When the mean value is subtracted from the bending moment signal, M_0 will be zero and the Weibull distribution will be a straight line on Weibull paper ($\ln(-\ln(P(x > M_y)))$ vs $\ln(M_y)$). Be aware that the mean value is generally not the still water bending moment due to the non-linear loads and response of the ship. For all analysis presented here, the mean value will be subtracted from the signal before making the Weibull extrapolation and M_0 will be set to zero. The subtracted mean value is added to the result of the Weibull extrapolation. For a linear small banded process the bending moment probability will have a Rayleigh distribution, which is a Weibull distribution with a shape parameter k_w equal to 2.

The peaks in the bending moment signal obtained for a rigid ship are usually counted by identifying one peaks per crossing of the mean value. This is illustrated in the signal shown in Figure 7.2. Counting the peaks of a signal obtained from a ship modelled with both rigid and flexible modes, which contains whipping and/or springing responses can be done in several ways[1]:

mean-crossing The same approach as used for the rigid ship can be used, counting one peak per mean crossing. One could argue that this is not a good count, as some whipping oscillations are counted because they cross the mean value and others, which do not cross the mean value are not counted.

rigid-body Another counting method is to count one peak of the flexible body signal between the mean crossings of the rigid-body signal. This is the rigid-body count as shown in Figure 7.2. To apply this method of counting an additional calculation run for a rigid ship has to be done using the same wave-train. The signal for the rigid-body ship can also be obtained by applying a low-pass filter on the signal of the flexible ship as long as the whipping frequency is much higher than the wave frequency.

full count The last counting method which is investigated is counting all positive maxima and negative minima.

[1]Even more counting methods are possible. For example counting the "out crossing rate" is another approach. These other counting methods are not investigated in this thesis.

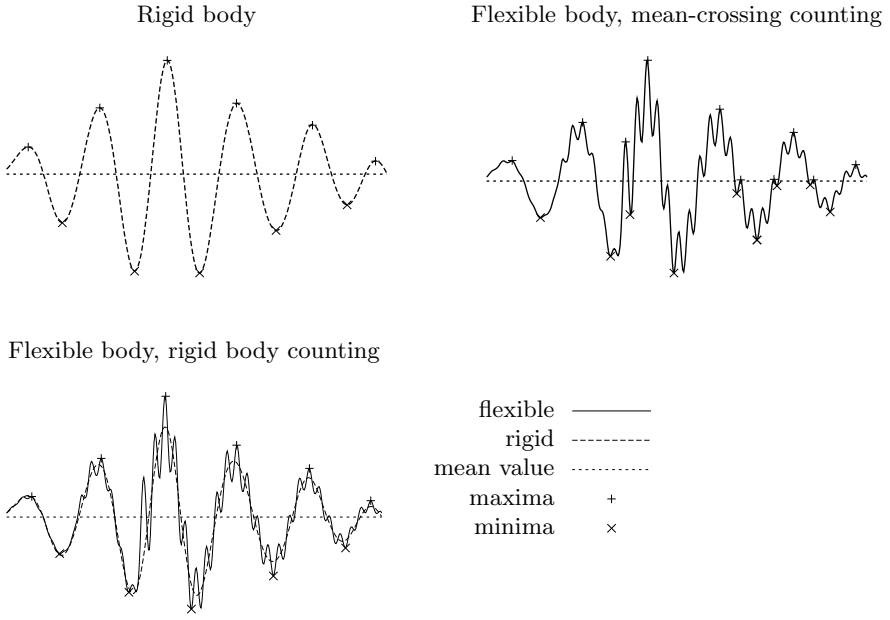

Figure 7.2: Counting methods for extremes.

To compare the counting methods both the rigid-body and flexible body signal are calculated for a container ship in a severe sea state for more than 50 hours. The rigid-body signal has more than 18,000 extremes. The probability of exceeding a bending moment and the fitted Weibull distribution are shown in Figure 7.3 both on Weibull paper and in a normal log graph. The Weibull extrapolation is based on the highest $\frac{1}{3}$-th values, as the lower extremes clearly have a different distribution. The mean-crossing count and the full count show a two-segmented line. The two segments are caused by counting a broad banded spectrum signal. The rigid-body count results in a small banded spectrum signal and the distribution is closer to a Rayleigh distribution which results in a one-segmented line. The distributions obtained by the different counting methods are almost equal for the higher extremes, only the associated probabilities differ.

The maximum sagging moment, which has a probability to occur once every ten hours, is calculated using the different counting methods. Each of the counting methods count a different number of extremes, which results in a different average period of the extremes, which gives a different probability to be used for the Weibull extrapolation. The parameters and resulting ten hour extreme bending moments are presented in Table 7.1.

Although the counting methods are quite different, the resulting maximum bending moments are quite close. The most suitable counting method can be

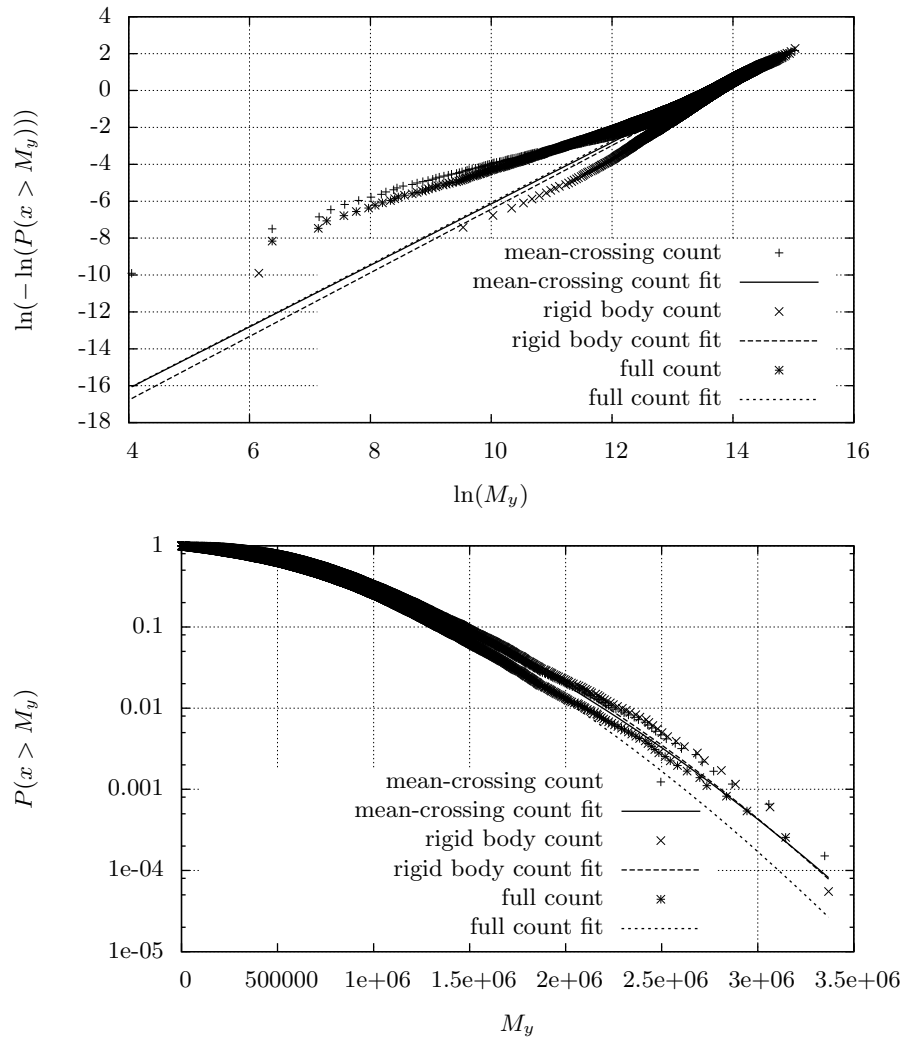

Figure 7.3: Weibull extrapolation of bending moment probability presented on Weibull paper (top) and normal log graph (bottom).

chosen as there is little difference in the results when the 10 hours extreme is considered. The goal in this thesis is to examine the influence of whipping response on the maximum expected bending moment. The rigid-body count will ensure that the same number of extremes are counted both for the signals with and without the presence of whipping response. This ensures that the differences in the results are only due to the whipping contribution and not due

Count method	average period	10 hour probability	wb shape	wb scale	10 hour extreme
mean-crossing	9.87 s	$2.74 \cdot 10^{-4}$	1.67	$8.77 \cdot 10^5$	3101 $[MNm]$
rigid-body	10.75 s	$2.97 \cdot 10^{-4}$	1.72	$9.16 \cdot 10^5$	3083 $[MNm]$
full count	5.55 s	$1.54 \cdot 10^{-4}$	1.68	$8.26 \cdot 10^5$	3021 $[MNm]$

Table 7.1: Resulting Weibull extrapolation using different counting methods.

to the differences in the counting of extremes. Therefore, the rigid-body count method will be used. Another advantage is that this counting method results in a one segmented line for the Weibull fit. This makes the fitting less sensitive to the threshold value above which data points are included in the Weibull fit.

7.1.3 Creating signals

There will be some initialisation effects at the start of the time domain calculation. Sixty seconds are added to the total calculation time and the first sixty seconds of the signal is ignored in the analysis to ensure that the analysed signals do not contain any initialisation effects.

The uncertainty in the results can be reduced by combining different runs for the same sea state. One time trace is created from the different runs and that single time trace is analysed. The different calculation results are combined using the following approach:

1. Calculate the mean value of the signal of the first calculation run.
2. Identify the last mean crossing at the right-hand side and remove the remaining signal from this point.
3. The first mean crossing of the signal of the next calculation with the same direction as the last mean crossing found in 2 is identified and the signal up until this point is removed.
4. The signals are combined and steps 2, 3 and 4 are repeated for all calculation results.

Note that only the mean value of the first calculation is used for combining the signals to ensure a continuous signal. The mean value of the total, combined signal is used for the Weibull extrapolation.

7.2 Calculation approach

The goal is to minimise the computational effort required for the time domain seakeeping calculations in order to obtain results within a reasonable uncertainty range. The variables that are investigated are: the number of wave

components; the length of one calculation; and the number of calculations that are combined.

To be able to investigate the uncertainty in the results of the fatigue and extreme bending moment analysis, many seakeeping calculations have been performed to create a database of time traces of the bending moment. This database is used to analyse the effect of different approaches to compute the design values.

The presented investigation is basically a variation around the already found optimum. This starting point has been found through analyses of the wave-trains and frequency reconstructed signals. Neither the computations nor the results for obtaining this starting point are presented in this thesis. These initial computations did show a faster convergence using equidistant wave components to represent the spectrum rather than using non-equidistant wave components. The Weibull fit on Weibull paper showed less scatter than using the significant values of the bending moment. At the end of this section, these conclusions will be confirmed with analyses performed using the bending moment database.

7.2.1 Bending moment database

A large database of bending moment signals is created to be able to calculate the uncertainty in the computation of the design values. Calculations are performed for two container ships with zero speed in head waves. These are the same ships that will be presented in Chapter 8. For both ships, twelve sea states are considered. A JONSWAP spectrum is used with $T_p = [6, 8, 10, 12][s]$ and $H_{1/3} = [6, 8, 10][m]$. Calculations are made for the ships with flexible modes (with slamming loading) and for the ships considered to be rigid (without slamming). The same wave-trains are used for both calculations to allow for the rigid-body count method.

The spectrum is represented by equidistant wave components. This allows one to calculate the return period of the wave using equation (4.2). The total calculation time of a single calculation is set to three return periods. The wave and the resulting response should repeat after one return period. Therefore, computing more than the wave return period more than once should not provide additional information. The computations for the database are done for three return periods to be able to show if this is indeed the case. New calculations for the same sea state are made until 18 hours of bending moment signal is available for that sea state. For every calculation, a new wave realisation is created using different random phase angles for the wave components and a random offset for all wave frequencies. The range of the random offset is $[-\frac{1}{2}\Delta\omega, \frac{1}{2}\Delta\omega]$.

To be able to investigate the effect of the number of wave components, all calculations are performed using 60, 75, 100, 125, 150, 175, 200 and 250 wave components. This gives a database with 2 (ships) $\times$ 12 (sea states) $\times$ 8 (wave components) $\times$ 18 hours = 3456 hours of bending moment signal for

both a flexible ship with slamming and a rigid ship without slamming. The wave excitation and hydrostatics are kept linear in the calculations to save on computation time.

It is assumed that the whipping response will result in more scatter in the computed design values than the non-linear wave excitation and hydrostatics will cause. Therefore, these computations using linear wave excitation and hydrostatics can be used to find the optimum way of computing the design values. The results found in this chapter will be verified for computations using non-linear wave excitation and hydrostatics in Section 8.4.

Additional calculations are performed in order to obtain a converged value. These calculations are performed for both ships, all sea sates and using 500 wave components. In total, 10 hour time traces are created using one wave return period as calculation time. It should be noted that it is not verified if this calculation really results in converged values. However, as the results will show that using less wave components and less time already results in quite well converged values, these results are assumed to be converged.

The 125, 200 and 250 wave component calculations are also redone using non-equidistant wave components. In this case the distance between the wave components is also randomly chosen. Due to the non-equidistant wave components there will be no well defined wave return period. The return period calculated for equidistant wave components is used in order to have comparable results. The findings of these calculations will determine whether equal or non-equal distance wave components give the best results.

7.2.2 Analysis

The uncertainty in the results of the calculated design values is investigated by analysing as many unique bending moment signals from the database as possible.

The extreme bending moment which is expected to occur every 10 hours at amidships is computed using equation (7.4). The fatigue damage of the deck structure at amidships is computed using (7.1). Both the fatigue damage and extreme bending moments are normalised by dividing by the converged design values from the 500 wave components computation. The mean value and the standard deviation is calculated based on all normalized values.

The variation of these two design values are computed for the different number of wave components, computation times, etc., using the bending moment database, in order to find the most optimum way of computing the design values. The approach used to compute the variation, or uncertainty in the results, is explained next.

For every condition all calculations that are available in the database are analysed. Be aware that the number of calculations for a single sea state will vary for the different sea states as the width of the spectrum differs and thereby

the return time of the waves. For every calculation, only the first part up until the required return time is analysed. The remaining part is neglected. For example, when computing the variation over a single wave return time, the second and third part of every computation is neglected. A separate analyse could be done on the second and third part of a single calculation, but this is not done as the signal will be very comparable to the first part.

The number of normalised values available for calculating the variation in the computed design values reduces significantly when multiple calculations are combined. When, for example, six computations are available and the variation for combining three computations is investigated only two fully unique time traces can be created. This is not enough to compute the variation in the results. In order to obtain enough points for the statistics, calculations 1, 2 and 3 are combined and 2, 3 and 4, etc. which gives five normalized values for the six available calculations.

The normalisation of the fatigue damage and extreme bending moment, using the 500 wave component results, allows one to compute a single value for the variation and bias for the two ships and the twelve sea states, which are 24 conditions. These results are given for every number of the wave components separately as the number of wave components is a variable to find the optimum way of computing the design values.

7.2.3 Calculation time and number of wave components

The number of wave components is an important parameter. The more wave components, the longer the wave return period will be. However, on the other hand, as more components have to be evaluated in the seakeeping program, the computation time needed for the same simulated time will increase.

The effect of the wave return period is investigated first. The bending moment database is analysed using different lengths of each calculation. The results are shown in Figure 7.4. Note that not all numbers of wave components are shown in the graph, as the graph will be very difficult to interpret if they would all been shown. The design values are not calculated for the short signals with a small number of wave components because these signals do not have enough peaks.

The standard deviation only reduces significantly up until the calculation time is equal to the wave return period. After the wave return period is reached, the variation of the extrapolated extreme bending is stationary but the variation of the calculated fatigue damage increases again. The variation of the fatigue damage has a clear minima at a calculation time equal to the wave return period. After the wave return period the wave signal repeats itself. By analysing a signal which is a bit larger than one wave return period the first part of the signal is counted twice and the remaining signal only once. These first peaks are weighed twice in the analysis but without any justification to do so. It is not surprising

that the result of the analysis does not improve when signals of more than one wave return period are used when this unequal weighing is considered.

The standard deviation of the results are also shown in Figure 7.5, but in this case with respect to the average simulation time. An average simulation time is used because due to the difference in spectrum width, the wave return period differs slightly when using the same number of wave components for different sea states. The variation of the extreme bending moment is comparable for the different number of wave components used, until the wave return period has been reached. The differences in variation after one wave return period between the different wave components is smaller for the fatigue results. Due to this small difference, there are only local minima for calculations with a number of wave components that give a n-times return period at the time step for the fatigue results.

The result of a single calculation shows clearly that the best result can be obtained by a calculation over exactly one wave return period. Calculating over two or three times the wave return period hardly decreases the variation in the results, as could be expected.

The variation of the results can also be reduced by combining multiple calculations for one sea state. Figure 7.6 shows the mean value and the standard deviation of the results when multiple calculations of exactly one wave return period are combined. The plots are with respect to the average number of positive peaks of the rigid-body signal. The number of peaks are more important for the accuracy of the calculated extreme bending moment and fatigue damage, rather than the total simulation time. As for this zero speed condition the average zero crossing time is about ten seconds, the plot with respect to the total simulation time will be about the same only with the x-values multiplied by ten. When doing calculations with forward velocity, the average zero crossing period will change and it is better to keep the number of extremes constant rather than the simulation time in order to obtain the same accuracy in the results. Therefore, the presented plots are with respect to the average number of positive peaks of the rigid-body signal.

The first points at the left side of Figure 7.6 are the results when two calculations are combined, for the second point three calculations are combined. More calculations are added until the average number of positive peaks is equal to 1200 (about a 3.3 hour simulation time).

The results now show a bias when less wave components are used. The results for the single calculations did not show this bias. An explanation could be that using a smaller number of wave components does indeed give a bias to the results, but using very short time traces also results in a bias. Consequently, the extreme bending moment and fatigue damage are reduced when less wave components are used, but these values are increased when the analysed time trace is very short. For the single calculation, the analysed time traces are shorter for the calculations with less wave components, so both effects can

cancel each other out and no bias is visible. The bias visible in the combined calculations is still small: the mean value obtained using sixty wave components is still 95 percent of the values for the converged calculation.

The variation of the results does not show much difference for the number of wave components used when the calculations are combined and the same amount of time is analysed. Therefore, the number of wave components should be selected based only on the cpu time needed for the calculation. This will not have a large influence on the accuracy of the calculation. The standard deviation is about five percent of the mean value after 750 extremes for the analysis, which equals about two hours of simulation for this case. This is considered accurate enough for the computation of the design values. Also, the variation of the results hardly decreases when more than 750 extremes are used to estimate the design values.

The duration of one hour of seakeeping calculations, including slamming, for two flexible container ships using a different number of wave components are measured. These measurements are indicated with points in Figure 7.7. There is a clear linear correlation between the cpu time and the number of wave components used. The solid lines are "linear fits" through the measurements using $f(nwc) = 3600 \cdot wt \cdot nwc + 3600 \cdot ct$. Where nwc are the number of wave components, wt the wave component depending time and ct the remaining calculation time.

For each wave component the wave return period is increased by about 3 seconds. The number of calculations needed to obtain one hour of simulation time using calculations of one wave return period is equal to

$$ncal = \text{int}(3600/(3 \cdot nwc)) + 1. \tag{7.5}$$

The total calculation time needed for one hour of simulation using multiple runs is the time for the one hour calculation itself plus the time needed to start the multiple calculations. For every calculation an additional 60 seconds seakeeping is computed to avoid a initialisation effect. For the startup of the program and the additional post processing 30 seconds are estimated. This results in a total cpu-time of

$$t_{cpu} = (wt \cdot nwc + ct) \cdot 3600 + (30 + 60 \cdot (wt \cdot nwc + ct)) \cdot ncal. \tag{7.6}$$

The number of computations and the total computation time needed for a one hour simulation using multiple computations are also shown in Figure 7.7. Note that the resulting calculation time will differ for other spectra and ships, however, changing some constants in formula (7.6) shows that the minimum computation time required is quite stable. The minimum calculation time is obtained if 80 wave components are used. To remove some bias in the results, and to be more on the "safe side", 125 wave components will be used for the calculations. Moving from 80 to 125 wave components gives only a small increase in computation time.

7.2.4 Wave components

The wave spectrum is represented by a number of wave components for the time domain calculation. These wave components can be chosen such that the (encountered) frequency has an equidistant distribution. In that case, the waves will have a clearly defined return period. To avoid this repetition of the wave-train, a random frequency distance between the wave components is often used.

Figure 7.8 compares the variation of the calculated design values of a single calculation using either equally or non-equally distanced wave components. The variation of the extreme sagging moment is equal until the wave return period of the equidistant calculation. After one return period the variation of the non-equidistant calculation is less. The variation in the fatigue damage results shows another trend. The variation using equidistant wave components has a clear minimum for exactly one time the wave return period.

By using exactly one time the wave return time, and equidistant wave components, there is clearly less variation in the fatigue damage. At that point there is no difference between the variation in the extreme bending moment. Figure 7.9 shows the difference in variation between equally and non-equidistant wave components when multiple calculations of one wave return period are combined. Again the variation for the extreme bending moment is almost equal, but the variation of the calculated fatigue damage is less when using equidistant waves. On the other hand, using non-equidistant waves reduces the bias in the results a little. As the bias is small compared to the variation in the results, equidistant waves will be used for the calculations.

Figure 7.8 shows that the variation of the extreme bending moment still reduces after the wave return period when using non-equidistant wave components. It is investigated if less variation in the results could be obtained by combining calculations with a different length rather than a single wave return period. Figure 7.10 shows that the total variation in the results when combining multiple calculations using non-equidistant wave components with a calculation time of 0.8 until 1.5 times the wave return period does show almost no difference. The variation in the results by using equidistant wave components is a little less than for all non-equidistant wave component results.

7.2.5 Weibull extrapolation

The distribution of extremes in the bending moment can be fitted using the Weibull distribution in several ways. The first way is fitting a line on Weibull paper as shown in Figure 7.3. The lower extremes have a different distribution than the higher extremes. To obtain a better distribution for the higher extremes, the lower extremes should be excluded from the fit. The standard deviation and the mean value of the 10 hour sagging extreme calculated when

a different percentage of the highest extremes is taken into account are shown in Figure 7.11.

The highest variation in the results is found when all extremes are included in the fit. The smallest variation is obtained when including 90 percent of the extremes, but this will give a larger bias in the results. When including 70 percent of the highest extremes, the variation is a little higher but the bias is about half of the bias when 90 percent of the extremes are included in the fit. The variation in the results increases significantly when a smaller percentage of the highest extremes are included in the fit.

Another way of obtaining the Weibull distribution is by calculating the Weibull coefficients from the $A_{\frac{1}{2}}$ and $A_{\frac{1}{3}}$ or $A_{\frac{1}{3}}$ and $A_{\frac{1}{10}}$ values of the bending moment. These results are also shown in Figure 7.11. Both the mean value and the standard deviation is worse than using a fit with 70 percent of the extremes. Therefore, a fit with 70 percent of the extremes is used to obtain the Weibull distribution.

7.2.6 Implementation

As shown in the previous sections, the non-linear calculation for the design values can best be computed using calculations with 125 equidistant wave components. Calculations of one wave return period for the same condition are repeated until at least 750 extremes are counted and the signal is combined into one signal. This signal is analysed using a rainflow count and the SN-cure to compute the fatigue damage. The maximum expected bending moment is computed using the Weibull distribution which is obtained by a fit on Weibull paper using 70 percent of the highest extremes.

The calculations of the design values for a complete scatter diagram have been fully automated. This automatisation required some changes to the procedure. As the calculations are distributed over several cpu's, starting of a new calculation takes more time. Therefore, the number of wave components is increased to 150 to reduce the number of calculations by increasing the wave return period. The second change is the number of calculated cycles. The total number of cycles is only known after the different calculation for a single sea state is combined. Some cycles will be lost when combining the signals. Although it is very rare, sometimes the calculation crashes and the results contain less cycles than expected. The automated procedure starts for every single sea state enough calculations such that the summation of the frequency domain cycles is at least 1000. This ensures that the final, combined, signal contains at least 750 cycles.

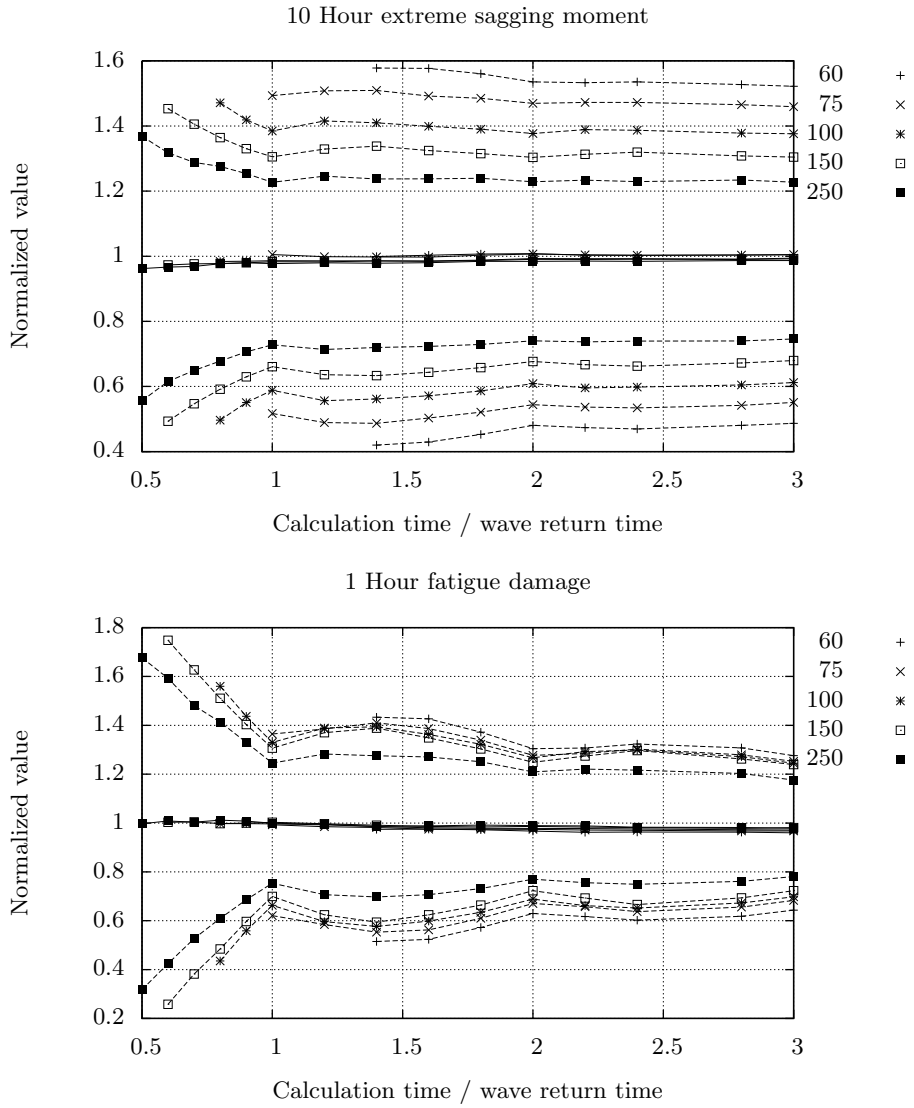

Figure 7.4: Mean and the mean plus/minus two times the standard deviation for single calculations with different run times for different number of wave components.

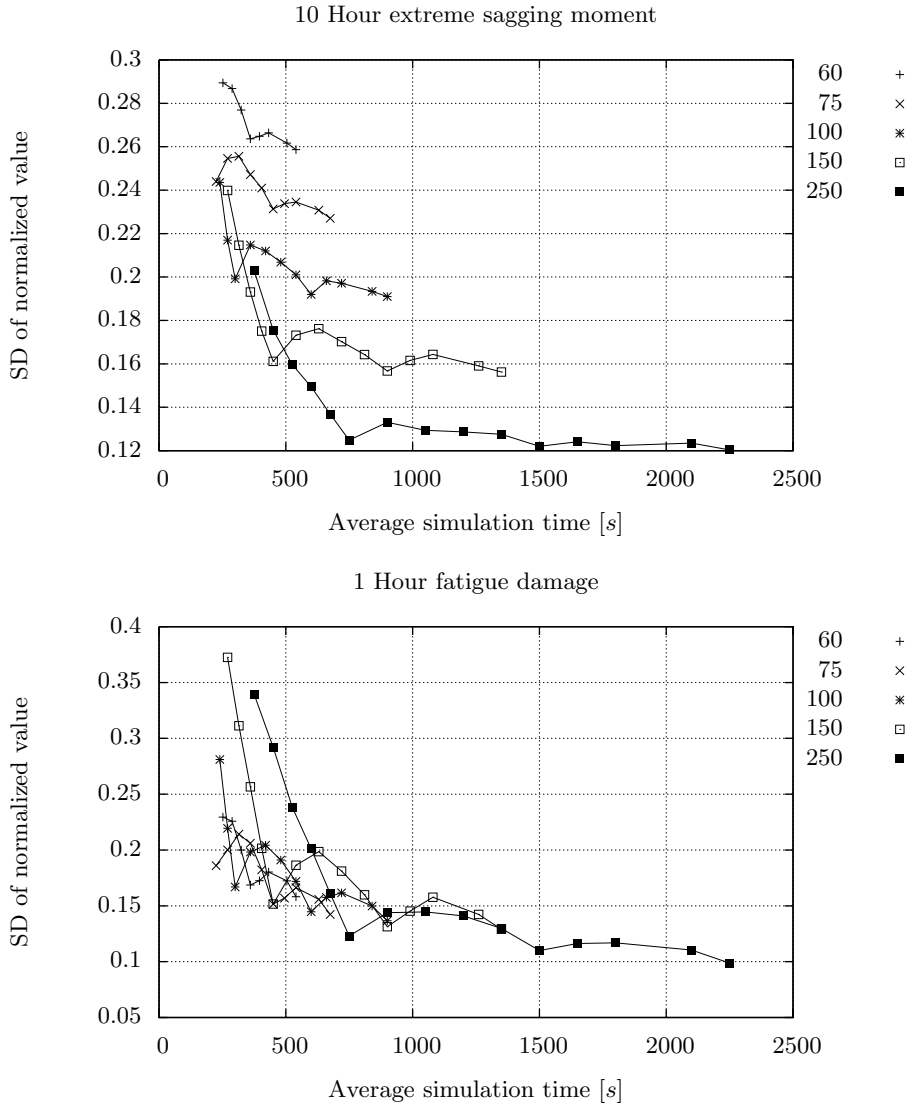

Figure 7.5: Standard deviation for single calculations with different run times for a different number of wave components.

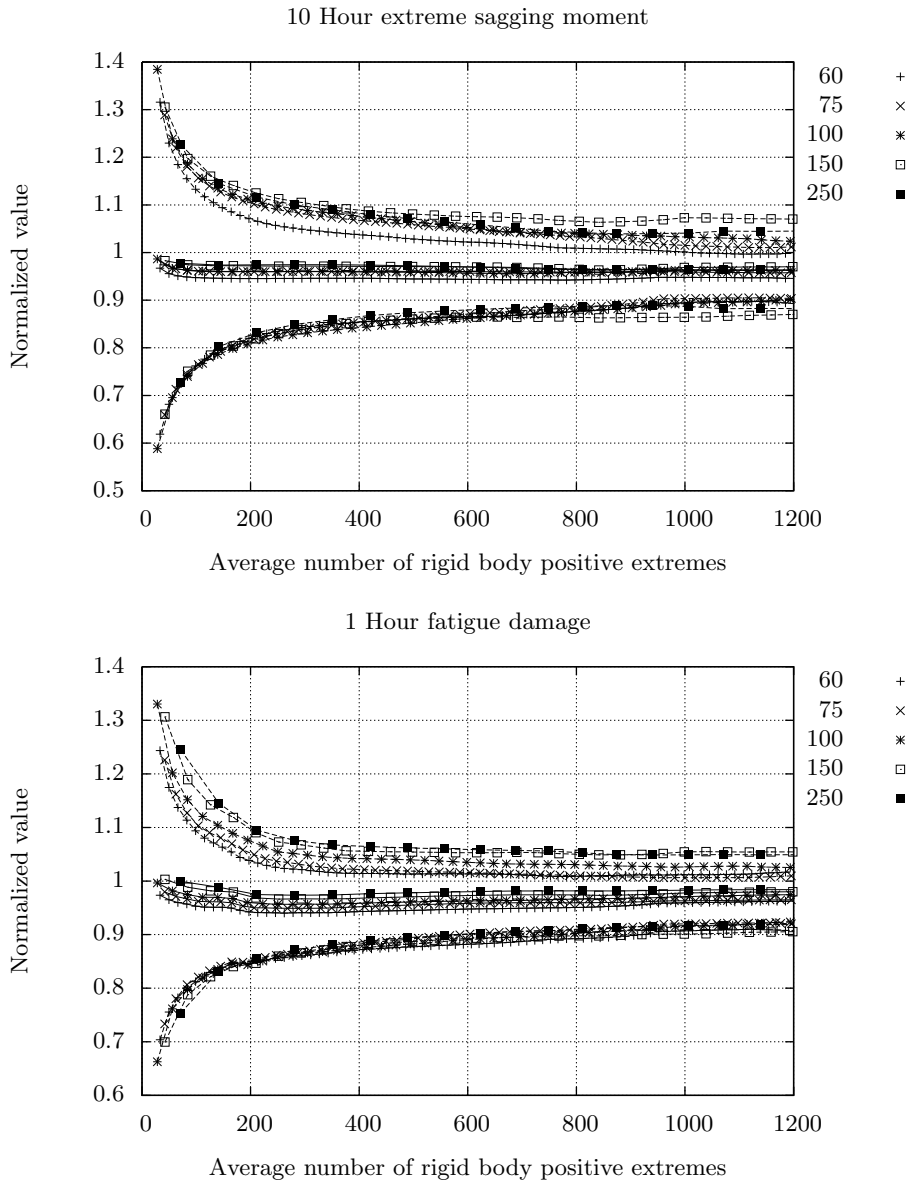

Figure 7.6: Mean and the mean plus/minus two times the standard deviation for multiple calculations with a run time of the wave return period.

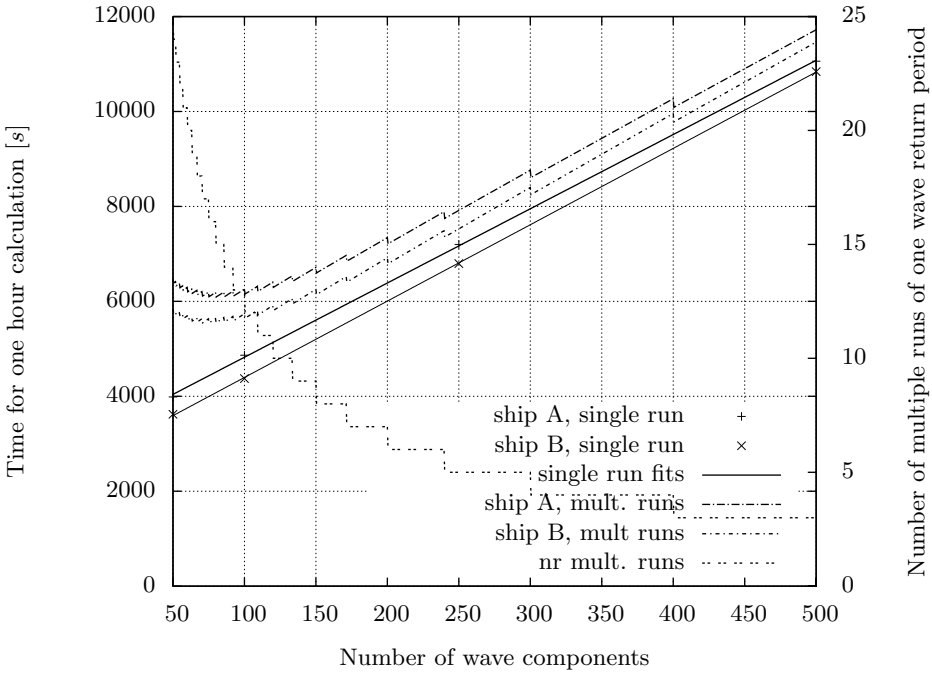

Figure 7.7: Specific computer time needed for calculations.

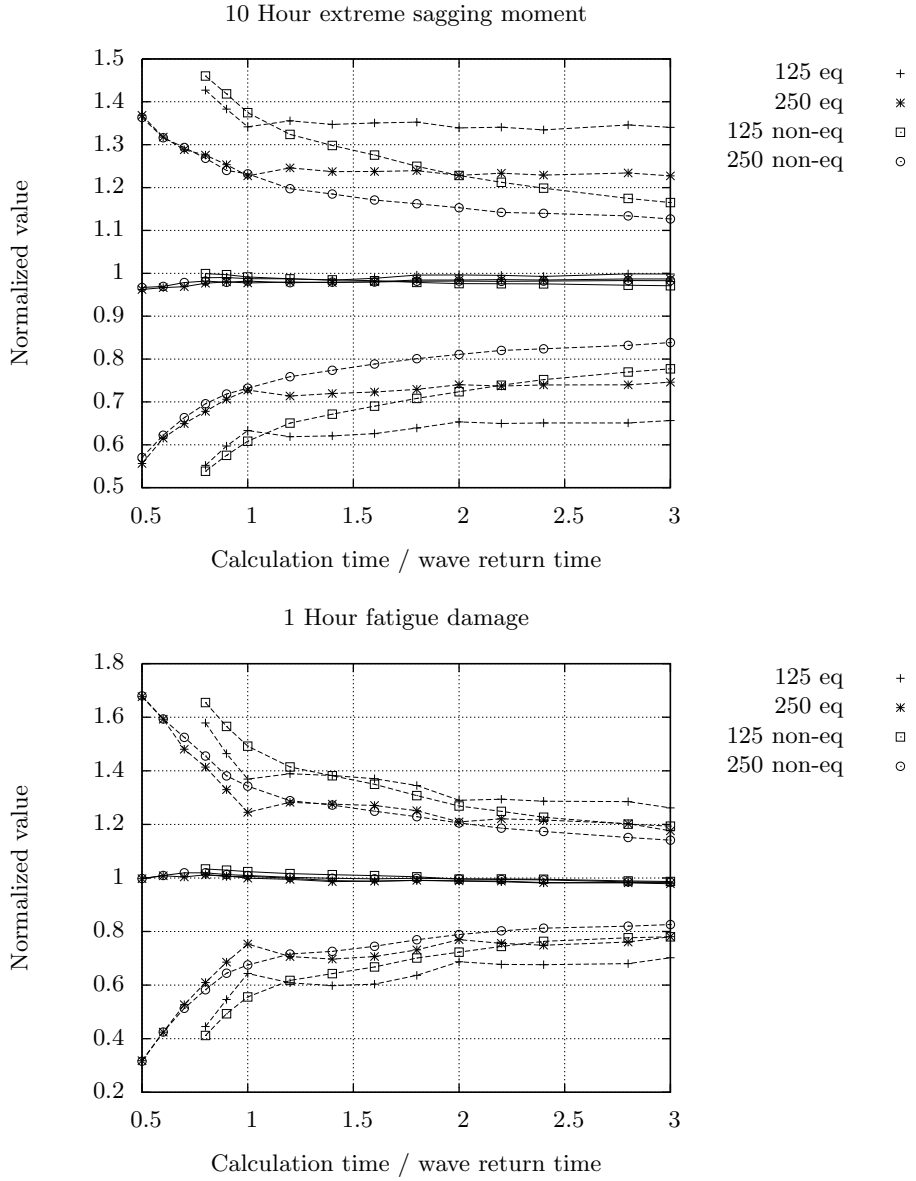

Figure 7.8: Mean and the mean plus/minus two times the standard deviation for single calculations with different run times for two different number of wave components using both equally and non-equally distanced wave components.

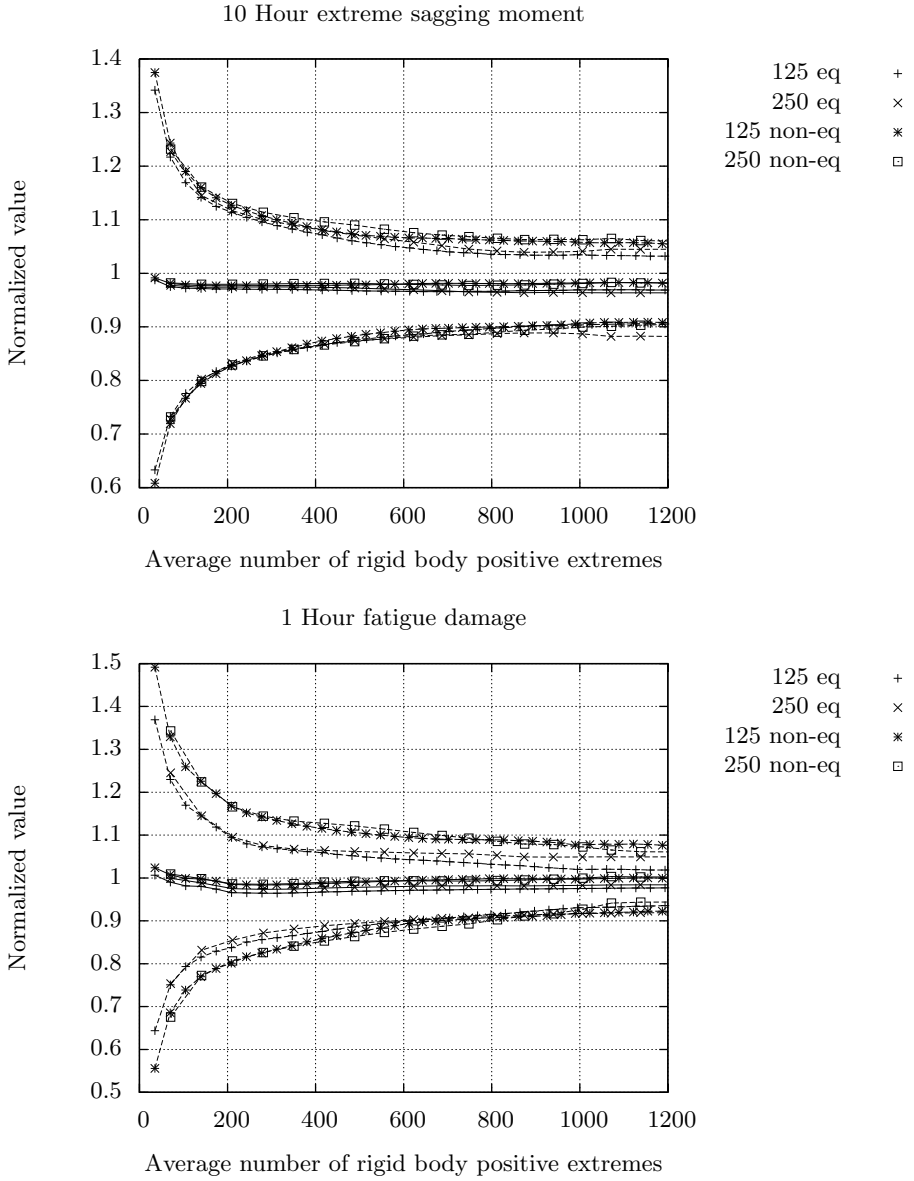

Figure 7.9: Mean and the mean plus/minus two times the standard deviation for multiple calculations with a run time of the wave return period using both equally and non-equally distanced wave components.

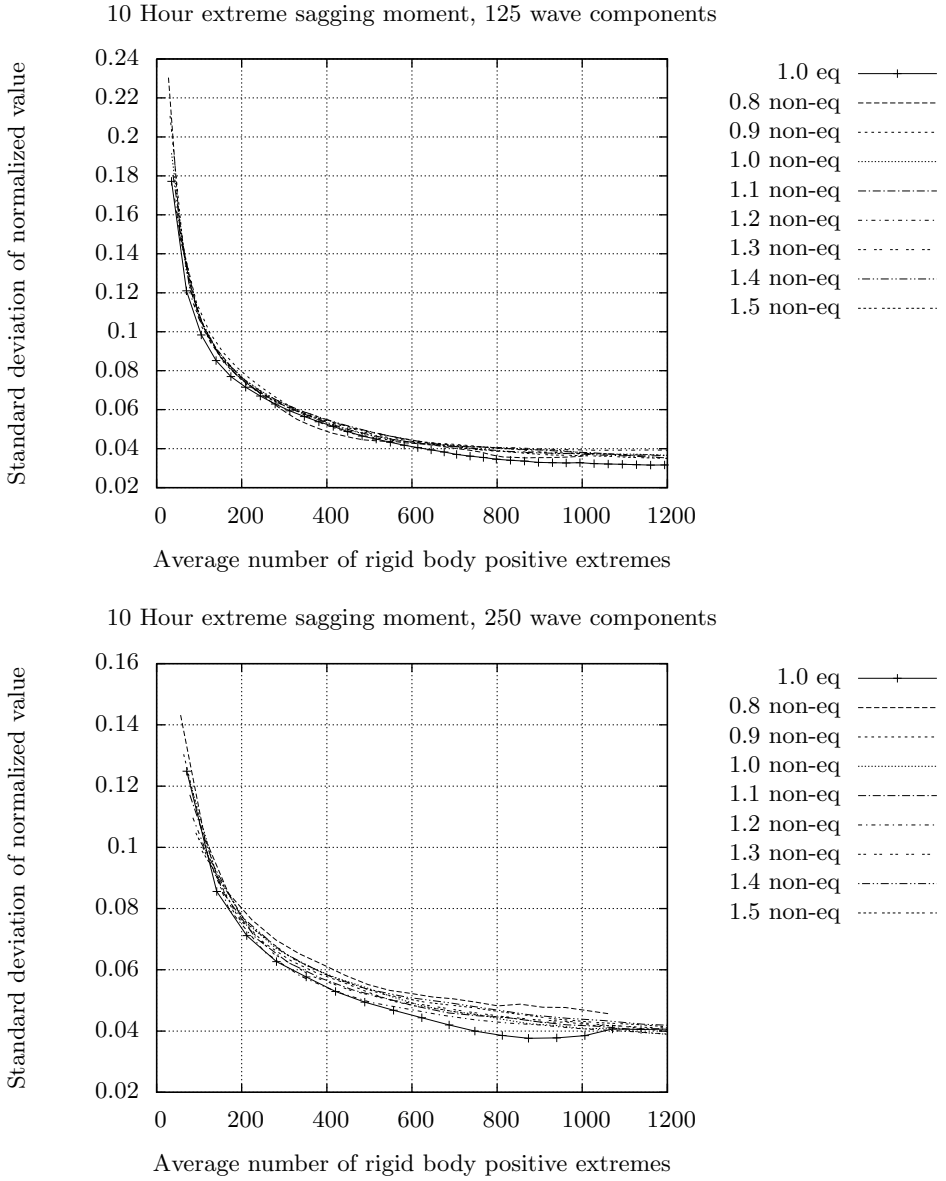

Figure 7.10: Comparison of the standard deviation using multiple calculations with non-equally distanced waves with a different run time compared to calculations with equally distanced wave components.

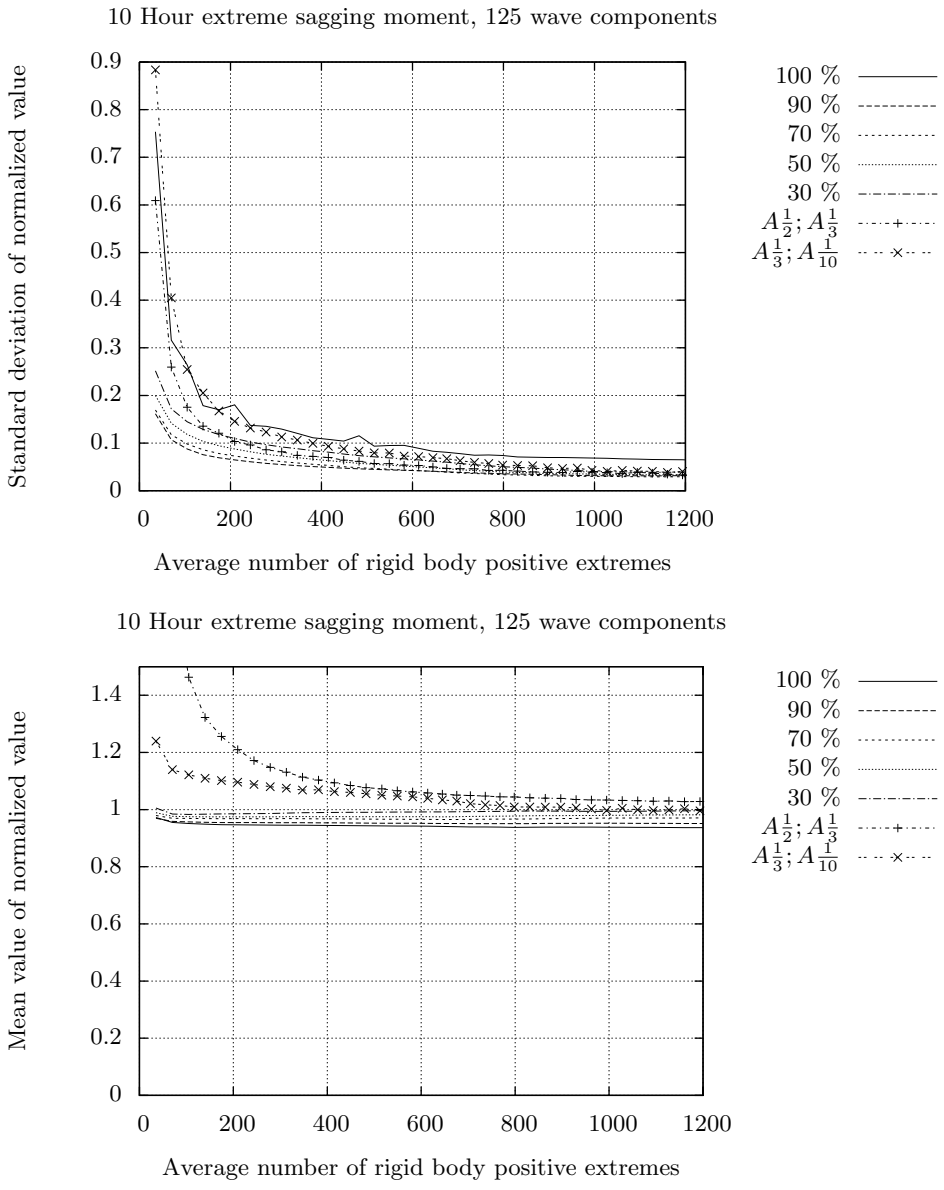

Figure 7.11: Standard deviation and mean value obtained using different approaches for Weibull extrapolation.

Part II

Verifications, validations and case studies

Chapter 8

Container ships

This is the first of five chapters presenting verifications, validations and case studies of the theory presented in the previous chapters.

In this chapter two (ultra) large container ships with respective lengths of 270 and 360 metre are used to verify and to illustrate the presented theory. The first section of this chapter presents the modeling of the ships and the approach used for the seakeeping calculations. Verification runs using the largest container vessel are discussed in the second section. A case study where the design values are computed for both ships, for a full scatter diagram, is presented in the last section of this chapter.

8.1 Ships and calculation approach

The data of the two ships used is confidential, therefore it is not possible to provide information like cross sections, table of main particulars, structural details, etc.

The dry structural modes are calculated using beam models of the ship structures. The first five vertical flexible modes are used. The computed mode shapes for the largest ship are shown in Figure 8.1. The structural damping is estimated to be $2\%, 3\%, 4\%, 5\%$ and 5% of the wet critical damping for the first to the fifth flexible mode, respectively. This structural damping is added using matrix $\mathbf{B}_u$ of equation (4.47).

The slamming sections with the scaled normals created for the largest ship are shown in Figure 8.2. Note that the scaled normals are reversed to make them visible.

The slamming and Froude-Krylov forces will slow down the ships, these forces are a part of the added wave resistance. These resistance forces should be compensated to avoid drift. A possibility is to model the propulsion system, or use springs and dampers, to keep the ship at the desired velocity and location.

A few of the calculations presented in this chapter have been performed by Niels Mallon.

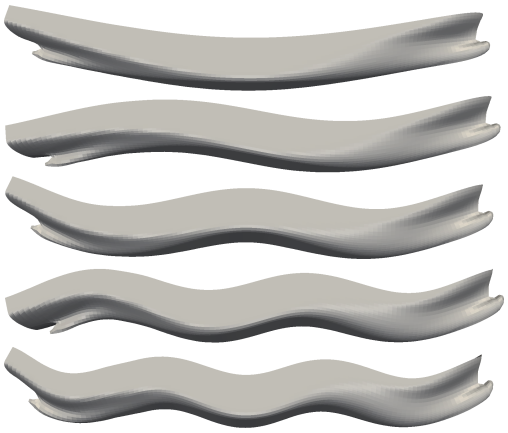

Figure 8.1: Elastic mode shapes.

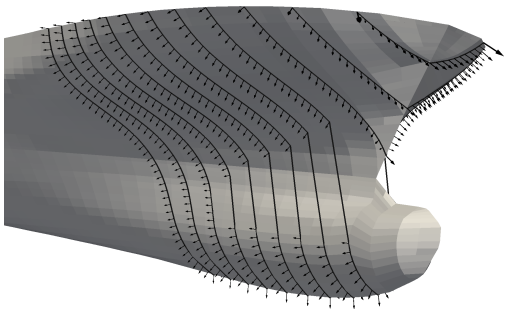

Figure 8.2: Slamming sections and scaled normal.

Both methods require tuning and may not be stable for all sea states. Therefore, kinematic constraints are imposed on the surge, sway and yaw motion, see Appendix B. The linear motion, computed in the frequency domain, is imposed. There is no drift in the linear theory and imposing the linear surge, sway and yaw motions will hardly influence the calculated bending moment, as the linear surge, sway and yaw motions are close to the non-linear motions. Imposing the linear motions is always stable.

8.2 Verifications

The container ship with a length of 360 $[m]$ is used to verify the consistency of the presented theory. The calculated seakeeping response, slamming loading and whipping response for various variations of the computational parameters, e.g. slam section orientation and time step, are presented in this section. In

addition, the hydro-elastic effects on the computed slamming loads is illustrated in this section.

The verifications that include slamming loads are done for the ship sailing at 15 knots in head waves with a significant wave height of 8 metres.

8.2.1 Retardation functions

The frequency dependent part of the radiation force is calculated using retardation functions in the time domain, see Section 4.4.1.

The frequency domain added mass and damping curves can be derived from the retardation functions using

$$B(\omega_e) = B(\infty) + \int_0^\infty K(\tau)\cos(\omega_e\tau)d\tau, \tag{8.1}$$

$$A(\omega_e) = A(\infty) - \frac{1}{\omega_e}\int_0^\infty K(\tau)\sin(\omega_e\tau)d\tau. \tag{8.2}$$

These curves should be close to the original frequency domain results if the retardation functions are calculated correctly. The hydrodynamic coefficients should also be consistent, that is, they should comply to the Kramers-Kronig relations. The retardation functions are created based on the damping curves only, because it is assumed that the Kramers-Kronig relation holds. If the Kramers-Kronig relation between the added mass and damping does not hold, it would be impossible to compute the correct added mass curves from the retardation functions.

The comparison between the original main diagonal added mass and damping curves and the same curves obtained from the retardation function are shown in Figure 8.3 for the heave and the first flexible mode. The original values are indicated by "frequency" and the results of the retardation function by "time". The hydrodynamic panels used for solving the BVP are too large to solve the problem accurately for encounter frequencies higher then 2.5 $[rad/s]$. The damping curves are extrapolated beyond this frequency before computing the retardation functions, see Appendix C. This high frequency problem causes the oscillations in the original results, the extrapolation avoids these oscillations in the retardation functions and therefore in the "time" results. All curves show a good correspondence for the encounter frequencies up until 2.5 $[rad/s]$. This verifies that the retardation functions are correctly calculated and the frequency domain added mass and damping curves are consistent.

8.2.2 Motions

The seakeeping motion of the container ship is calculated using both a frequency domain and time domain calculation. The results of these two approaches are compared in Figure 8.4 for small waves and in Figure 8.5 for large waves.

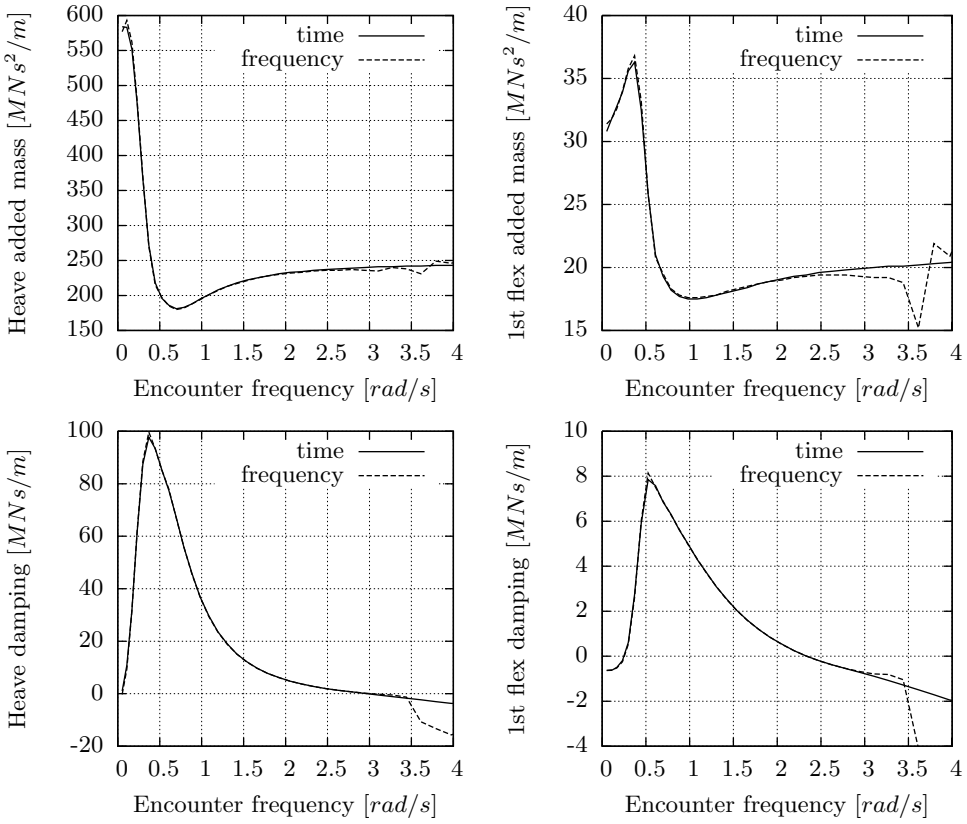

Figure 8.3: Comparison between original hydrodynamic coefficients and the coefficients calculated from retardation functions.

The frequency domain calculation is fully linear. The time domain approach includes the non-linear Froude-Krylov and non-linear hydrostatic forces, see Chapter 4. Note that the slamming loading is not included to ensure a good comparison between the frequency domain and time domain results. The sea-keeping loads by small waves are close to the prediction of the linear theory. Therefore, the resulting response to the small waves is very comparable between calculations using the frequency domain approach and the time domain approach for the small waves. This indicates the consistency between the two different methods.

The non-linearities cause differences between the calculated motion for large waves. Small differences are visible in the rigid-body motions but the motion of the first flexible mode is changed significantly by these non-linearities. Due to the flare of both the bow and the stern, the excitation forces due to the incoming wave and hydrostatics becomes non-linear. These non-linearities af-

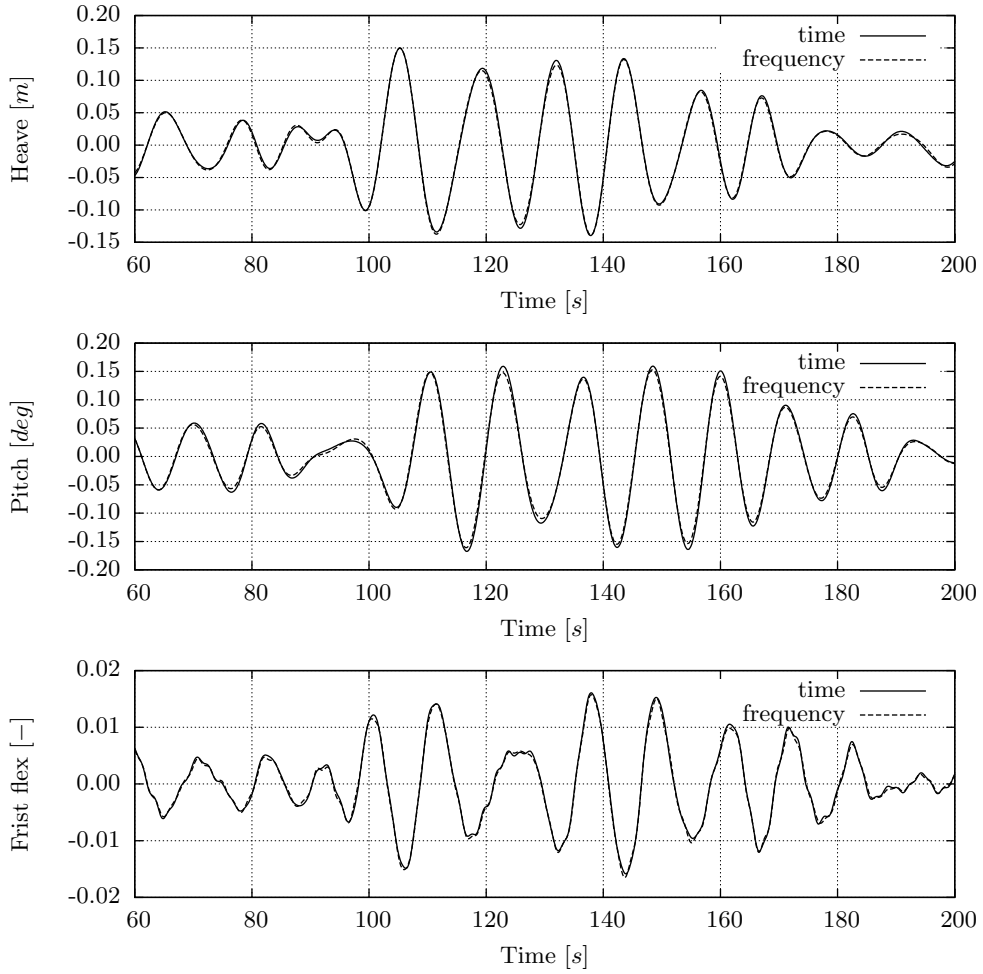

Figure 8.4: Motion comparison for small irregular waves, $H_{1/3} = 0.5$ $[m]$.

fect the heave motion not much, as forces on the bow and stern provide only a small part of the total heave force. The pitch motion is hardly affected by the non-linearities as the effect at the bow will partly cancel the effect at the stern. However, the first flexible mode sensitive to this non-linear effect as the loading at the bow and stern are the main contributions to the modal excitation of this mode. The linear theory clearly underestimates the response of the first mode for this severe sea state.

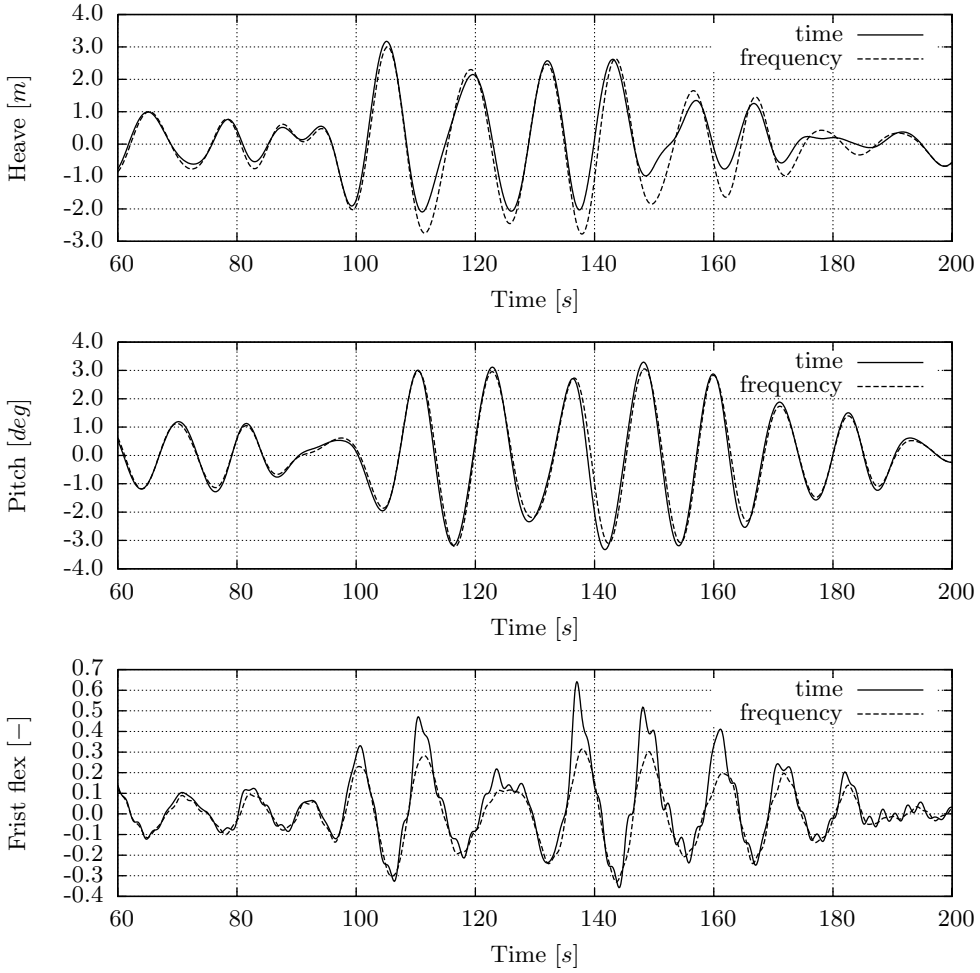

Figure 8.5: Motion comparison for large irregular waves, $H_{1/3} = 10$ $[m]$.

8.2.3 Internal loads

The internal loads can be calculated using direct integration or superposition of the response of the elastic modes, see Section 4.4.8. The superposition result should converge to the result of the direct integration if enough elastic modes are included in the calculation. The bending moment at amidships, between both methods, is compared in Figure 8.6. The internal loads can be integrated from the bow to the midship or from the stern to the midship, these two approaches are denoted by numbers 1 and 2 in Figure 8.6, respectively.

The direction of the direct integration hardly changes the calculated internal load. The result obtained by using superposition is close to the results of the

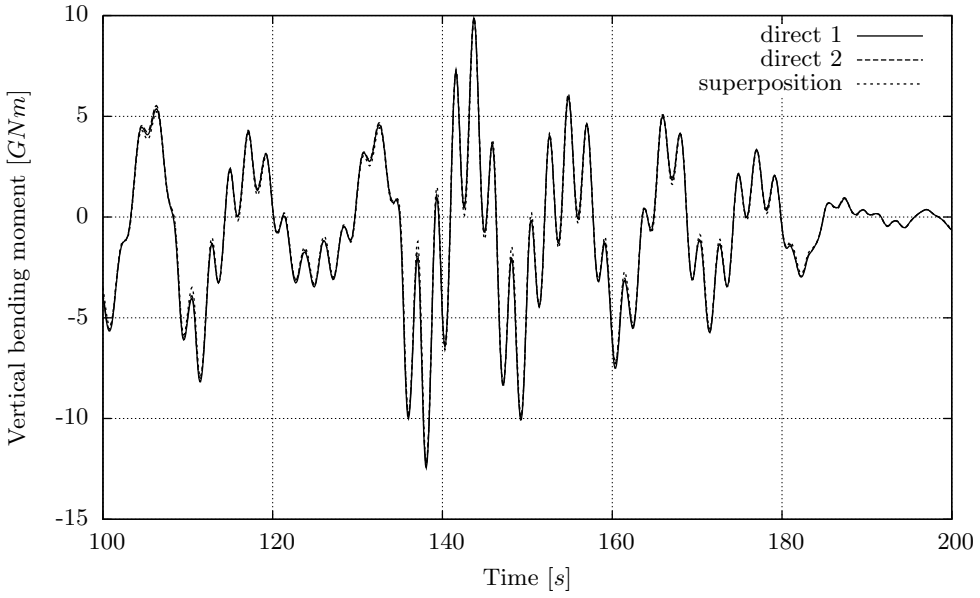

Figure 8.6: Bending moment calculated using direct integration and modal superposition.

direct integration. This difference can be expected as only five elastic modes are included in the calculation. Obtaining almost the same internal load using both the direct integration method and the superposition method indicates the consistency of the method.

8.2.4 3D slamming pressure integration

The 3D slamming pressure integration method is presented in Section 5.2.2. This method should make the calculated slamming force less dependent, or sensitive, to the tilting angle in the pitch direction selected by the user. It is investigated if this method indeed reduces the sensitivity on the tilting angle compared to the classical method where a single slamming force in the plane of the slamming section is assumed.

This is investigated by calculating the total force in heave and surge directions at the bow of the container ship for a severe slamming impact using different tilting angles. The orientation of the 2D sections is varied from 90 degrees (vertical sections) to 40 degrees. The calculated slamming forces using both methods are compared in Figure 8.7. The sensitivity of the calculated slamming force is clearly less for the presented pressure integration method than found for the classical method. A strong sensitivity to the chosen slamming section tilt angle is an undesired property and would raise doubts about

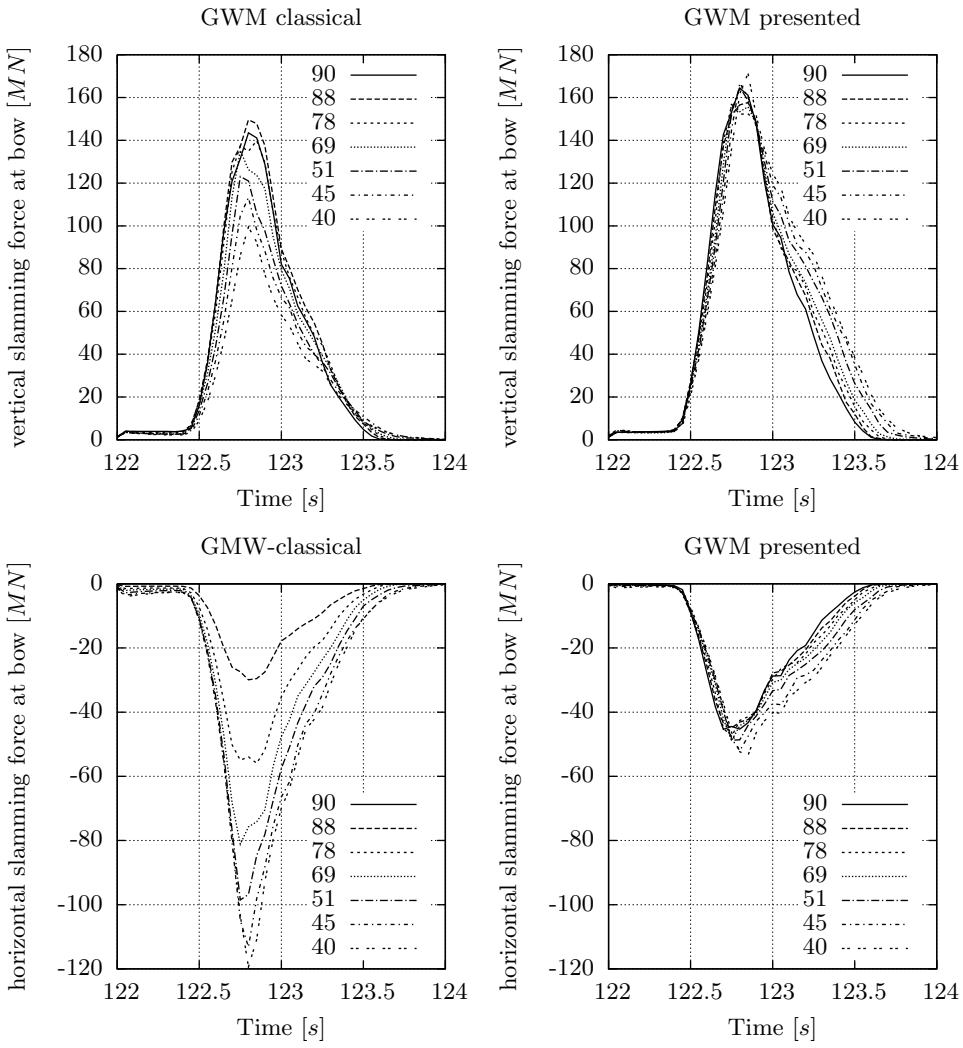

Figure 8.7: Resulting slamming force using the presented and a classical method.

the application of the 2D methods for slamming computations. As shown, the strong sensitivity with respect to the tilting angle is significantly reduced by using the pressure integration method.

8.2.5 Time step

The coupling between the seakeeping and slamming program should ensure that the slamming impulse is correctly transfered regardless of the time step used. Figure 8.8 shows the calculated vertical slamming force and resulting bending

moment at amidships using different time steps. Only the first two flexible modes are considered in these calculations to allow for large time steps in the numerical integration for the seakeeping calculation.

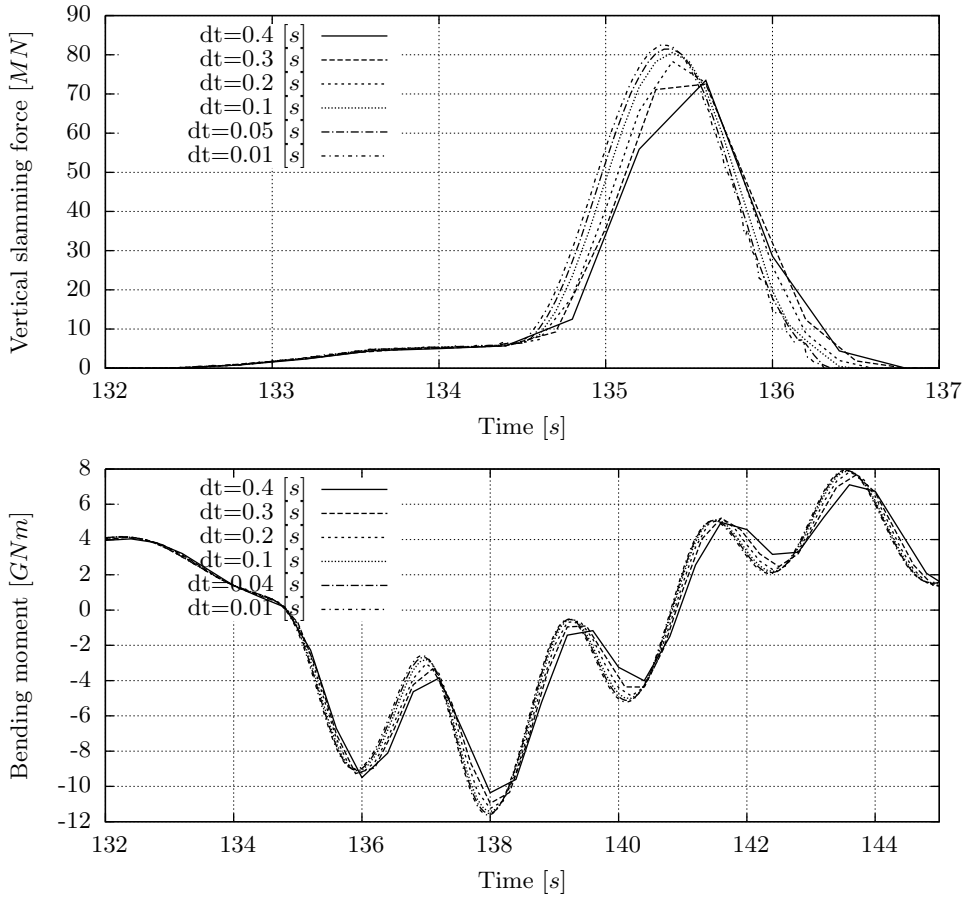

Figure 8.8: Effect of calculation time step.

The amplitude of the whipping is a measure of the total slamming impulse transfered to the seakeeping program. This amplitude hardly changes for time steps smaller than 0.2 seconds. The calculated whipping response is underestimated when using time steps of 0.3 seconds or larger. Likely, this is because the peak in the relative velocity is missed when using these large time steps. The time step used for the other calculations presented in this chapter is 0.1 seconds. This is the maximum stable time step for the explicit numerical integration when all five flexible modes are included. The slamming excitation is accurately integrated using this time step.

8.2.6 Hydroelasticity

The typical duration of a slamming event is about one second for this ship in the investigated condition. The first wet frequency has a period of 1.6 seconds which makes a hydro-elastic analysis necessary according to [2]. If one takes ship flexibility into account, it is expected that the slamming force will reduce due to the global elastic structural response.

Figure 8.9 shows the vertical slamming force calculated when different numbers of flexible modes are included in the calculation. The slamming force is about twenty percent higher if a rigid-body model is used, indicated by 'no flex' in Figure 8.9. The result converged in this case when using two or more elastic modes.

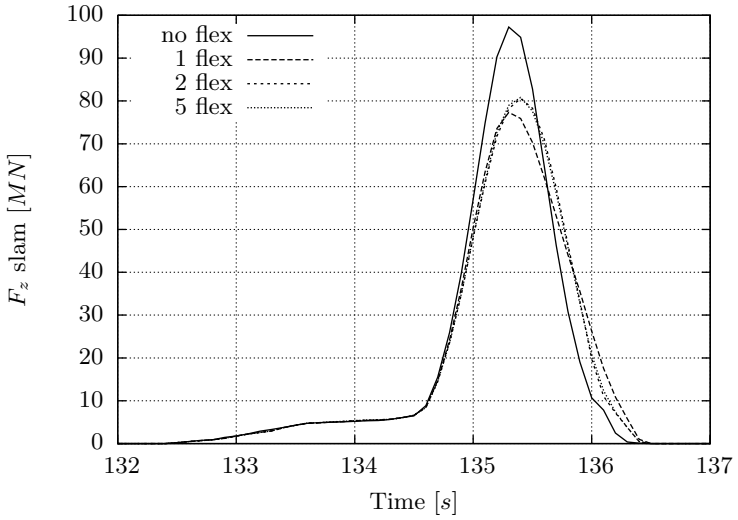

Figure 8.9: Influence of hydroelasticity (1).

The seakeeping and slamming calculation were directly coupled in the previous calculations. Figure 8.10 shows the effect of decoupling the seakeeping and slamming calculation. The decoupled approach is to first calculate the seakeeping response without slamming and then compute the slamming forces based on the calculated relative motions. Even for the rigid-body model the slamming loading is reduced significantly when the direct coupling method is applied. This reduction is caused by the change of the rigid-body motions due to the slamming loading. Although these changes are small they have a significant effect on the slamming forces as this forces scales with about the square of the relative velocity. The difference in the slamming force computed with the decoupled and coupled approach is even more for the flexible ship which indicates the effect of hydroelasticity.

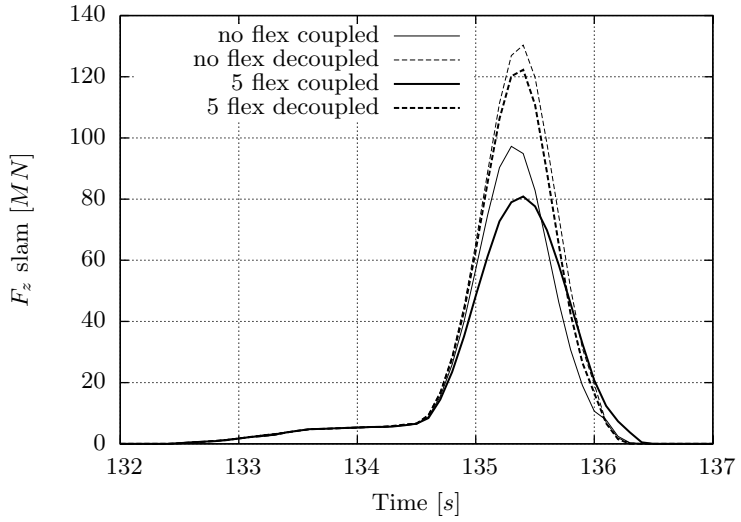

Figure 8.10: Influence of hydroelasticity (2).

8.2.7 Slamming calculation method

Two methods are implemented to calculate the slamming force, GWM and MLM, see Chapter 5. Figure 8.11 shows that the total slamming force acting on the ship calculated by both methods is significantly different. This difference can be explained by the shape of the slamming sections. The ship has a bulbous bow which causes the slamming sections that includes the bulb to be relatively slender, see Figure 8.2. The shape of these sections violates the MLM assumption that the slamming sections can be considered blunt. This effect is shown in Figure 8.12. This figure shows the total vertical slamming force at two individual slamming sections. The first section includes the bulb, the slamming force is quite different between GWM and MLM. The second section is at the bow and does not include the bulb. The calculated slamming force is very comparable between both methods. This shows that the much faster MLM method can only be used as long as the slamming sections shapes are reasonably blunt.

8.3 Case studies

In this section, both container ships are used to illustrate the procedure for the calculation of the design values as discussed in Chapter 7. The ultimate bending moment and fatigue damage is calculated for the whole North Atlantic scatter diagram [57]. The calculations are limited to head waves and a single loading condition. A simplified operational profile is used, this profile is presented in

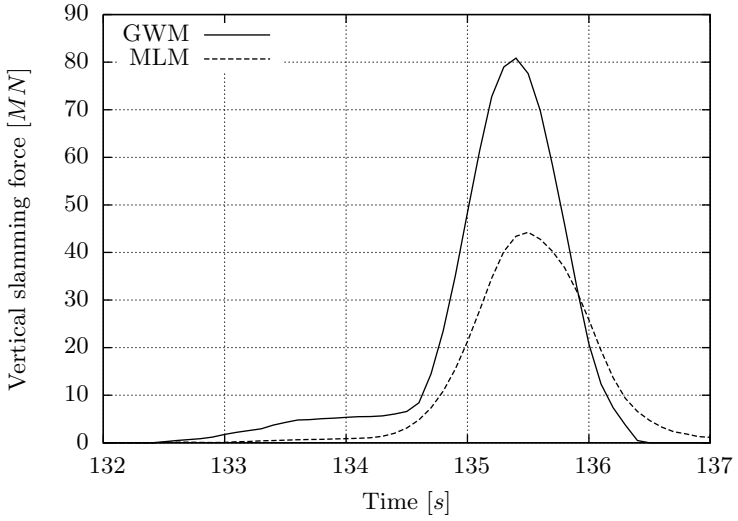

Figure 8.11: Calculated total slamming force at ship using GWM and MLM.

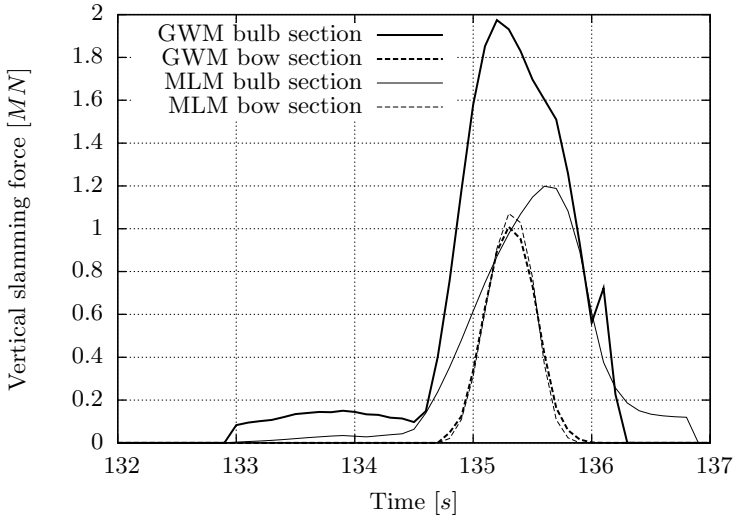

Figure 8.12: Calculated total slamming force at section using GWM and MLM.

Table 8.1.

The influence of the non-linear loading and the whipping and springing response is investigated by performing three calculations for the same wave-trains. First, a linear seakeeping calculation using only the rigid-body modes is performed. The non-linear Froude-Krylov and hydrostatic forces are taken

Significant wave height $[m]$	Operational speed [knots]
$0 \leq H_{1/3} < 5$	20
$5 \leq H_{1/3} < 7.5$	15
$7.5 \leq H_{1/3} < 10$	10
$H_{1/3} \geq 10$	5

Table 8.1: Simplified operational profile.

into account in the second calculation. The flexible modes and the slamming loading are added for the last calculation. It should be noted that in the last calculation not only the whipping response is computed,, but the signals for some sea states also contain some springing response. It is expected that the theory used will underpredict the springing response as most of the springing is likely to be due to non-linearities in load components which are not included in the present theory. However, the resulting bending moment will be slightly increased by the calculated springing response. The still water bending moment is added to the bending moment of the linear calculation to make it comparable to the non-linear calculations.

The ultimate bending moment, occurring once in the 100 hours, and resulting fatigue damage are presented in Figure 8.13 for the 270 metre ship and in Figure 8.14 for the 360 metre ship. The results for the different cells of the scatter diagram are connected by lines in the zero crossing period direction for visualisation purpose. The lines above zero in the figures at the top are the hogging moment found using the three calculation approaches and the lower part are the sagging moments.

The still water bending moment at amidships, which is 2.7 $[GNm]$ hogging for the 270 $[m]$ ship and 6.1 $[GNm]$ hogging for the 360 $[m]$ ship, causes the ultimate sagging moment to be pure hogging for significant wave heights up to 4 metre. The increase of the sagging moment due to the non-linearities in the wave loading is clearly visible. The hogging moment is slightly reduced by the non-linear loading for the 270 $[m]$ ship. The slamming induced whipping and springing increases both the expected hogging and sagging moment.

The lower part of Figures 8.13 and 8.14 shows the fatigue damage of a deck detail caused by one hour in the sea state. The non-linear Froude-Krylov and hydrostatic forces increase the calculated fatigue loading significantly. The increase due to the whipping and springing response is even more. The speed is reduced between 9 and 10 metres significant wave height from 10 knots to 5 knots. This causes the fatigue loading found for 10 metres to be less than that found for a 9 metre significant wave height. The ultimate bending moment is also reduced by this speed reduction.

The probability of the occurrence of a sea state has to be taken into account when computing of the design values. It is assumed that the ships will sail during their lifetime in total 25 years at sea. The total fatigue lifetime of the

deck structure is computed by summing the fatigue damage occurring at the individual cells of the scatter diagram and dividing this with the total time at sea. The fatigue damage for a single sea state is the computed fatigue damage per hour times the total time the ship is likely to be in that sea state. The total ultimate bending moment is computed differently. For every sea state, a Weibull extrapolation of the bending moment is made using the total time the ship will be in the sea state according to the wave scatter diagram. The highest resulting bending moment is taken as the ultimate bending moment. Note that this is the bending moment that the ship is likely to encounter just once during the total life of the ship. However, this method does not give insight into the probability of exceeding the computed ultimate bending moment. It would be better to agree on an acceptable probability of exceeding and to compute the ultimate bending using that value.

Figure 8.15 shows the number of days the ship will be in a certain sea state during the 25 years using both the North Atlantic and the World wide trade scatter diagrams. The ultimate bending moment and the contribution to the total fatigue damage for the different sea states are shown in Figure 8.16 for the 270 $[m]$ ship and in Figure 8.17 for the 360 $[m]$ ship. The computed ultimate bending moment and fatigue lifetime are presented in Table 8.2. The design bending moment according to the Classification Societies rules is also presented in this table. It should be noted that for the calculation for the World wide trade scatter diagram, only the available sea states from the North Atlantic scatter diagram are used. A few sea states which only occur in the World wide trade scatter diagram are neglected. The contribution of these cells are negligible due to their low wave height and probability of occurrence.

The results in Figures 8.16 and 8.17 show that the highest sea states still determine the expected ultimate bending moment even if the ship is expected to be less then a day in one of those sea states during its life. The low probability causes the contribution of the highest sea states to the total fatigue damage to be negligible. The fatigue damage is mainly caused for the sea states with a significant wave height between four and eight metres.

Table 8.2 show that the computations predict a higher ultimate bending moment that the design bending moment prescribed by the Classification Societies rules. The rules do not account for the actual flare of the bow and stern and therefore underestimate the hog/sag ratio. The rules [38] prescribe a design hogging and sagging moment of

$$\begin{cases} M_{WV,H} = 190 F_M n C L^2 B C_B 10^{-3} \\ M_{WV,S} = -110 F_M n C L^2 B (C_B + 0.7) 10^{-3} \end{cases}, \tag{8.3}$$

which result in a wave induced hog/sag ratio of

$$\frac{M_{WV,H}}{M_{WV,S}} = \frac{190 C_B}{110 C_B + 77}. \tag{8.4}$$

		270 $[m]$ ship			360 $[m]$ ship		
		Hogging Total $[GNm]$	Sagging Total $[GNm]$	Fatigue life [years]	Hogging Total $[GNm]$	Sagging Total $[GNm]$	Fatigue life [years]
Rule moment [38]		6.2	0.76	-	14.56	1.74	-
NA	Linear	6.83	1.78	32.0	17.1	5.03	47.2
	Non-linear	6.10	9.72	18.2	16.8	12.3	30.6
	Slamming	7.39	11.9	10.6	19.1	15.8	21.6
WW	Linear	6.30	1.24	66.3	15.8	3.71	117
	Non-linear	5.79	7.02	40.6	15.6	9.42	77.9
	Slamming	7.10	8.84	23.4	17.7	12.4	52.3
		Hogging Wave $[GNm]$	Sagging Wave $[GNm]$		Hogging Wave $[GNm]$	Sagging Total $[GNm]$	
Rule moment [38]		3.5	3.46		8.4	7.84	
NA	Linear	4.13	4.48		11.1	11.1	
	Non-linear	3.40	12.42		10.7	18.4	
	Slamming	4.69	14.60		13.0	21.9	
WW	Linear	3.60	3.94		9.7	9.8	
	Non-linear	3.09	9.72		9.5	15.5	
	Slamming	4.40	11.54		11.6	18.5	

Table 8.2: Rule bending moment, 25 years ultimate bending moment and fatigue lifetime for both the North Atlantic (AN) and World Wide trade (WW) scatter diagram for the two ships. Both the total bending moment and the wave induced bending moment are presented.

These container ships have a block coefficient C_B of about 0.6 which results in an rule hog/sag ratio of 0.8. The calculations shows a hog/sag ratio of the wave bending moment of 0.6 for the largest ship and 0.32 for the 270 $[m]$ ship for the most severe seas of the North Atlantic scatter diagram. The hogging moment is still the largest moment due to the hogging SWBM for the 360 $[m]$ ship. However, the sagging moment is the largest moment for the 270 $[m]$ ship.

The computed ultimate sagging moment is about two times the rule bending moment for the 270 $[m]$ ship. The computed values must be incorrect, otherwise ships built according to these rules are likely to break in very severe sea states. The sea state with a significant wave height of 15 metres and a zero crossing period of 11 seconds resulted in the highest sagging moment. The bending moment signal resulting from this computation is presented in Figures 8.18 and 8.19 for both the non-linear and the slamming computation. The ship is expected to be 2.2 hours in this condition during its lifetime when sailing in the North Atlantic. The bending moment signal is computed for about 3 hours. One large peak is visible in the signal. The computed bending moment is about 11.4 $[GNm]$ when slamming is included and 9.3 $[GNm]$ when only using the non-linear Froude-Krylov forces and hydrostatics. As this peak is much larger

than the other peaks, such a peak is likely to be encountered less than once in the three hours.

The one occurrence in the 2.2 hour extreme should be the design value, but this is estimated to be even higher than the very large peak in the 3 hour computed signal. The Weibull extrapolations are shown in Figure 8.20 for the non-linear case and in Figure 8.21 for the slamming case using both Weibull paper and a normal logarithmic scale. Especially, the plot on the normal logarithmic scale shows that the highest extremes have another distribution than that predicted by the Weibull extrapolation. This is due to waves reaching the deck. The green water pressure acting on the deck compensates the wave bending moment. Note that the green water is only modeled by applying the pressure of the undisturbed incoming wave at the deck. This is insufficient in order to model the real forces acting at the deck by the green water. However, it gives an indication of the trend. When making a fit using only the highest extremes, the ultimate sagging bending moment will be 9.3 $[GNm]$ for the slamming case and 7.3 $[GNm]$ for the non-linear case. These values seem much more realistic. The Weibull extrapolation as used is clearly not valid when significant green water loading occurs.

Even with the corrections for the incorrect Weibull extrapolations, the computed ultimate moment is still larger than the rule bending moment. This does not indicate that the class rules underestimate the ultimate hogging bending moment. As explained below, the computations will give conservative results, the capacity of the structure is larger then the rule moment and the accuracy of the computations is not clear for these very high sea states.

The calculations are done for only head waves using unidirectional waves. There will always be some wave spreading which will reduce the resulting bending moment as the same amount of wave energy is distributed in different headings. The ultimate bending moment will also be reduced by accounting for a different heading instead of only head seas. However, it may also be argued that it is likely that the master steers the ship into the waves if such severe seas are encountered. For the computation it is assumed that the ship sails at a speed of 5 knots in the most severe sea states. The master will probably retain some speed to be able to steer the ship, but this may be less than 5 knots.

The rule bending moment is a design value. The rules contain a number of safety factors which mean that the ship structure can withstand a large bending moment without any yield or buckling. Local yield may be even acceptable for a few occasions during the lifetime of the ship. It would be better to compare the ultimate bending moment computed using these direct calculations with the ultimate bending moment which the structure can withstand but this information is not available.

The accuracy of the computations for the very high seas is not clear. The validation using the full scale measurements of the M-frigate, which is presented in Chapter 12, shows that the structural response is well predicted for a sea

state with a significant wave height of 5 metres. However, it is not validated if this is also the case for a significant wave height of 15 metres. Most likely, the accuracy of the computations will reduce for increasing wave height. One can also question the accuracy of the wave condition and the probability value used. The probability of the severe sea state where the ultimate bending moment is found is 1/100000 which is equal to 2.2 hours during the 25 years of lifetime. However, if the real probability would be 0.7/100000 or 1.3/100000 the computed ultimate bending moment would be different. The Bretschneider spectrum is used to describe the waves. It is not clear if this spectrum is still valid for these very severe sea states. It is possible that some of the computed waves can physically not exist and may break in reality.

The ultimate bending moment as presented in Table 8.2 cannot be used as a substitute for the rule values. However, as the Figures 8.13 and 8.14 show similar trends for higher sea states, some conclusions can be drawn. The actual wave sagging moment is higher than the design sagging moment prescribed by the Classification Societies rules for these container ships. Slamming induced whipping and springing increases both the hogging and sagging moment. The ultimate bending moments are increased with about twenty percent for the 270 $[m]$ ship. The ultimate hogging moment is increased by about ten percent and the ultimate sagging moment by about thirty percent for the largest ship. The fatigue damage is mainly caused by the less severe sea states. This gives more confidence in the accuracy of the computed fatigue damage. The reduction of the lifetime due to the slamming induced whipping and springing is about fifty percent for the 270 $[m]$ vessel and thirty percent for the 360 $[m]$ ship.

8.4 Calculation of design values

The ultimate bending moment and fatigue damage is calculated in the previous section using the theory described in Chapter 7. These values are calculated using a limited number of computed extrema. The variation of the predicted ultimate bending moment and fatigue damage is investigated for the non-linear calculation where slamming and whipping are included. This should provide verification if the method described in Chapter 7 may be used to calculated design values. The results which include whipping are used as it is expected that these will result in the largest variation. It should be noted that this investigation only verifies the method to compute the design values from the bending moment signal. It does not verify if the calculated bending moment is correct.

The lines in Figures 8.13 and 8.14 are reasonably smooth which is a first indication that the calculation procedure as used gives converged values. To have more insight into the scatter of the results, the calculation of the design values for the 270 $[m]$ ship is repeated twenty times, including the seakeeping

calculation, using different wave realisations. The computations for the 360 $[m]$ is repeated eighteen times. The mean values and two times the standard deviation based on these samples are plotted in Figures 8.22 and 8.23. Assuming the results to be normally distributed, 95 percent of the results will be within the two times the standard deviation lines. The figures show that this 95 percent band is small which indicates that the scatter in the calculations is small. This gives confidence in using the proposed procedure to obtain design values, provided that the calculated bending moment is correct.

8.5 Conclusions

An ultra large container ship of 360 $[m]$ has been used in this chapter to verify the presented theory. It has been shown that the computed retardation function is consistent with the frequency domain added mass and damping. These coefficients comply also to the Kramers-Kronig relations. The computed response using the time domain approach was shown to be close to the results when using the frequency domain approach, when the ship is sailing in a mild sea. The difference between results of a linear frequency domain calculation and a non-linear time domain calculation increases for a more severe sea state, which is expected.

The computed internal loads are verified by comparing the internal loads computed using the direct integration method and the modal approach. The direct integration was also applied to both the forward and the backward direction. All three results showed very good correspondence which indicates the consistency of the presented method.

An investigation into the sensitivity of the computed whipping response to the time step used showed that converged results are obtained when using a time step of 0.2 $[s]$ or less. As the maximum stable time step for the explicit numerical integration scheme, when including the first five flexible modes in the calculation, is smaller, the found converged time step for the whipping computation was deemed acceptable.

The effect of hydroelasticity was also investigated. First, the slamming force computed for a ship modelled with only rigid-body modes and for the same ship including flexible modes were compared. The flexibility of the ship was shown to decrease the computed slamming forces significantly, as could be expected. The second investigation was comparing the computed slamming forces when using the direct calculation as presented in this thesis and using a separated approach where the slamming forces are computed afterwards, using the computed motions obtained from a seakeeping computation without slamming. This showed that using the direct, hydro-elastic coupling, also reduced the computed slamming loads. This illustrated the importance of performing a hydro-elastic analyses for such large flexible ships.

In the last verification run it was shown that with the approach of integrating the slamming pressure over the 3D geometry the sensitivity of the resulting slamming force with respect to the tilting angle of the 2D slamming sections is significantly decreased compared to the classical method where the slamming loading is applied as a single force.

The presented method was used for the computation of the fatigue lifetime and the ultimate bending moment for two ships. The 360 metre container ship and a 270 metre container ship were used for this case study. The ultimate bending moment which is expected to occur once during the 25 years of lifetime of both ships and the fatigue lifetime were calculated for both the North Atlantic and World Wide trade scatter diagram.

These computations showed that the design wave sagging moment is underestimated by the Classification Societies rules. It is also shown that the computation of the extreme bending moment using the Weibull extrapolation is incorrect as soon as there is a significant green water loading. The accuracy of the results for the very extreme seas is not clear because the theory used is not validated for these conditions. Also, the wave probability, the actual spectra, course and speed of the vessel for the most extreme conditions are uncertain.

The slamming induced whipping and springing causes the ultimate bending moment to be about twenty percent higher for the 270 $[m]$ vessel, about ten percent for the hogging moment and about 30 percent for the sagging moment for the 360 $[m]$ ship. The fatigue lifetime was reduced by about fifty percent by the slamming induced whipping and springing for the 270 $[m]$, and thirty percent for the 360 $[m]$ ship. This showed the importance of accounting for slamming, whipping and springing when computing the design values for such flexible ships. Provided that the computed bending moment is correct.

At the end of this chapter the accuracy of the method for calculating the design values, which was presented in Chapter 7, was investigated by recomputing the design values for the ships using different wave realisations. It was shown that the variation in the computed design values remained small, which showed that the method used was accurate.

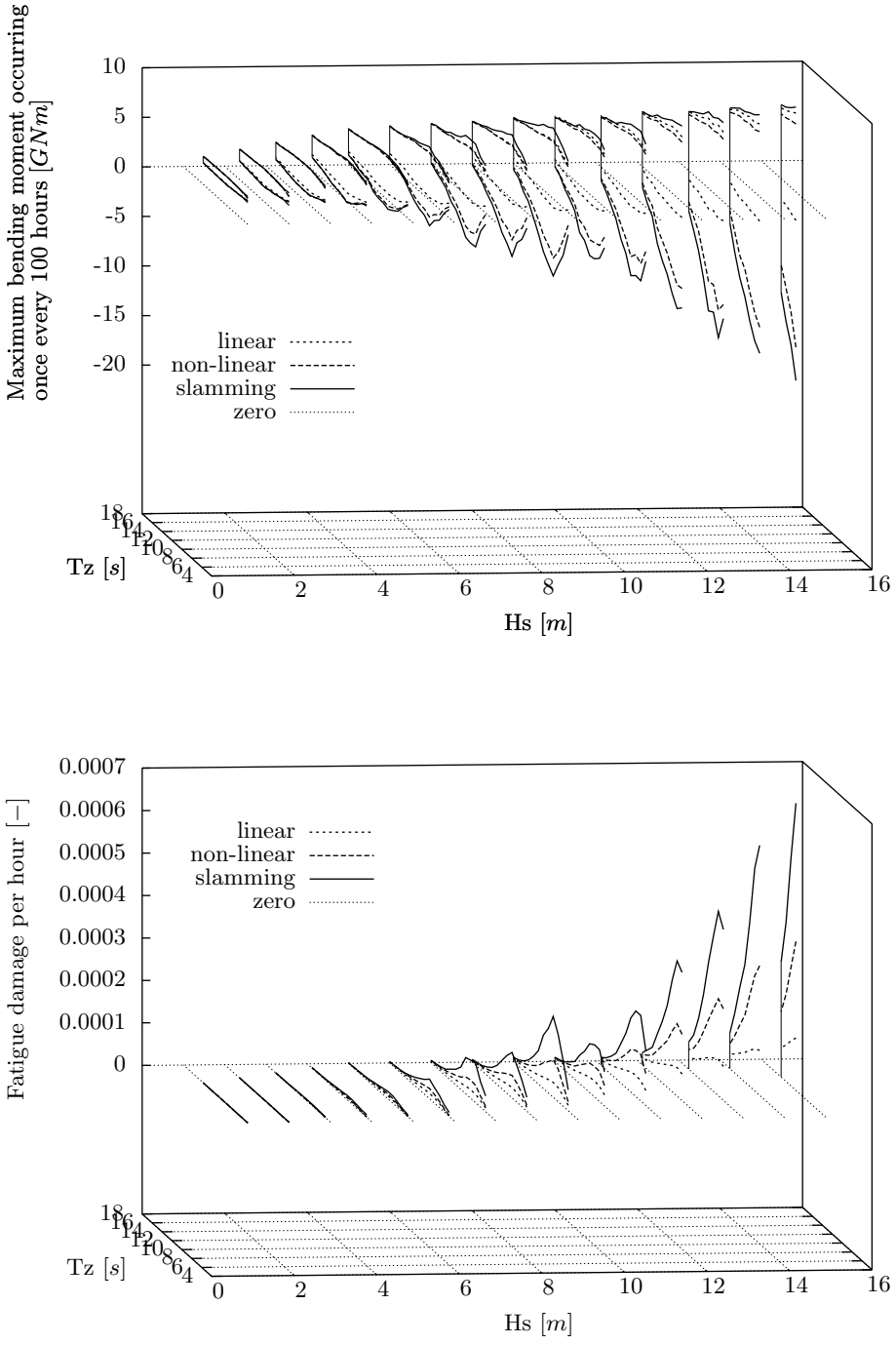

Figure 8.13: Design values for the 270 [m] container ship.

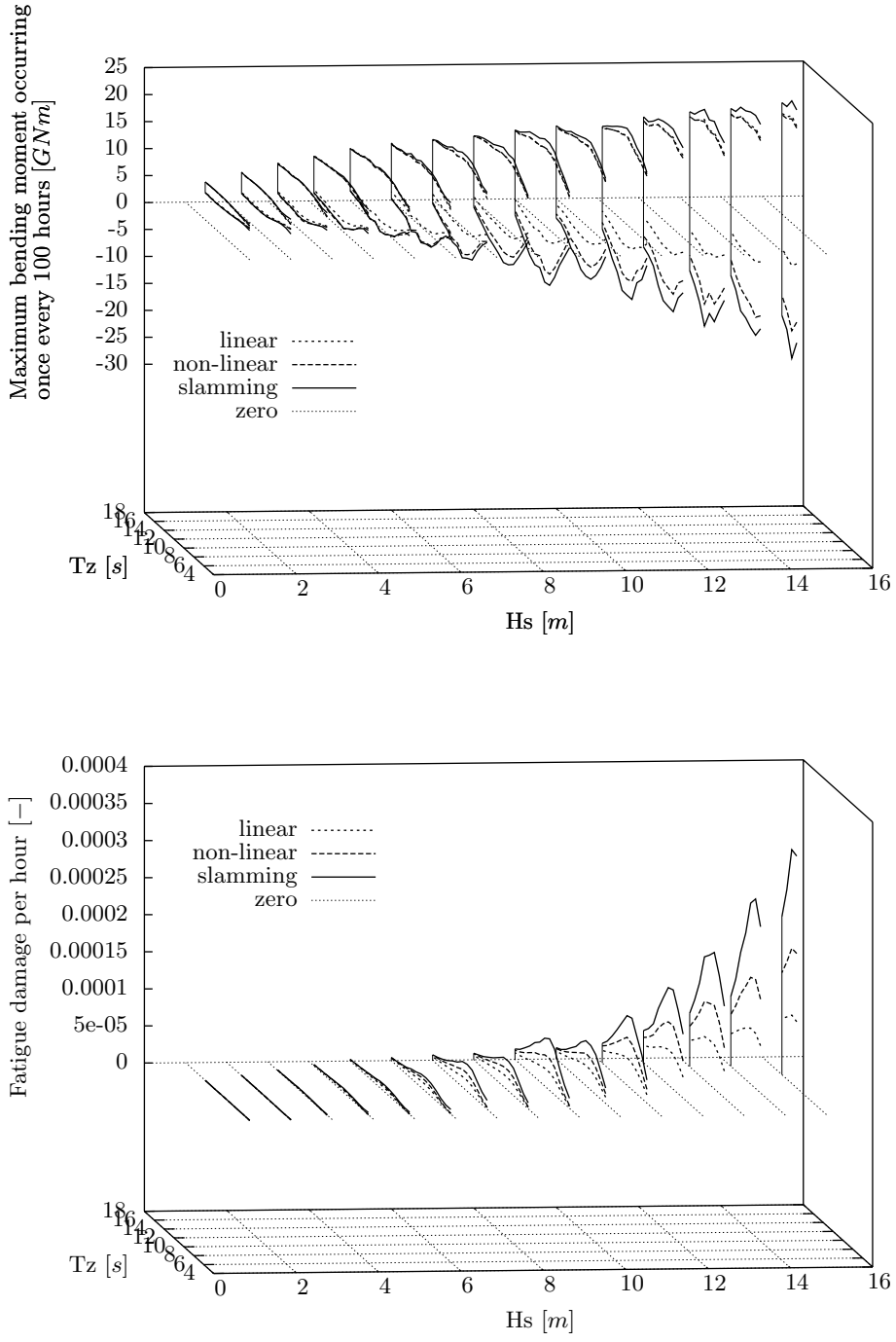

Figure 8.14: Design values for the 360 $[m]$ container ship.

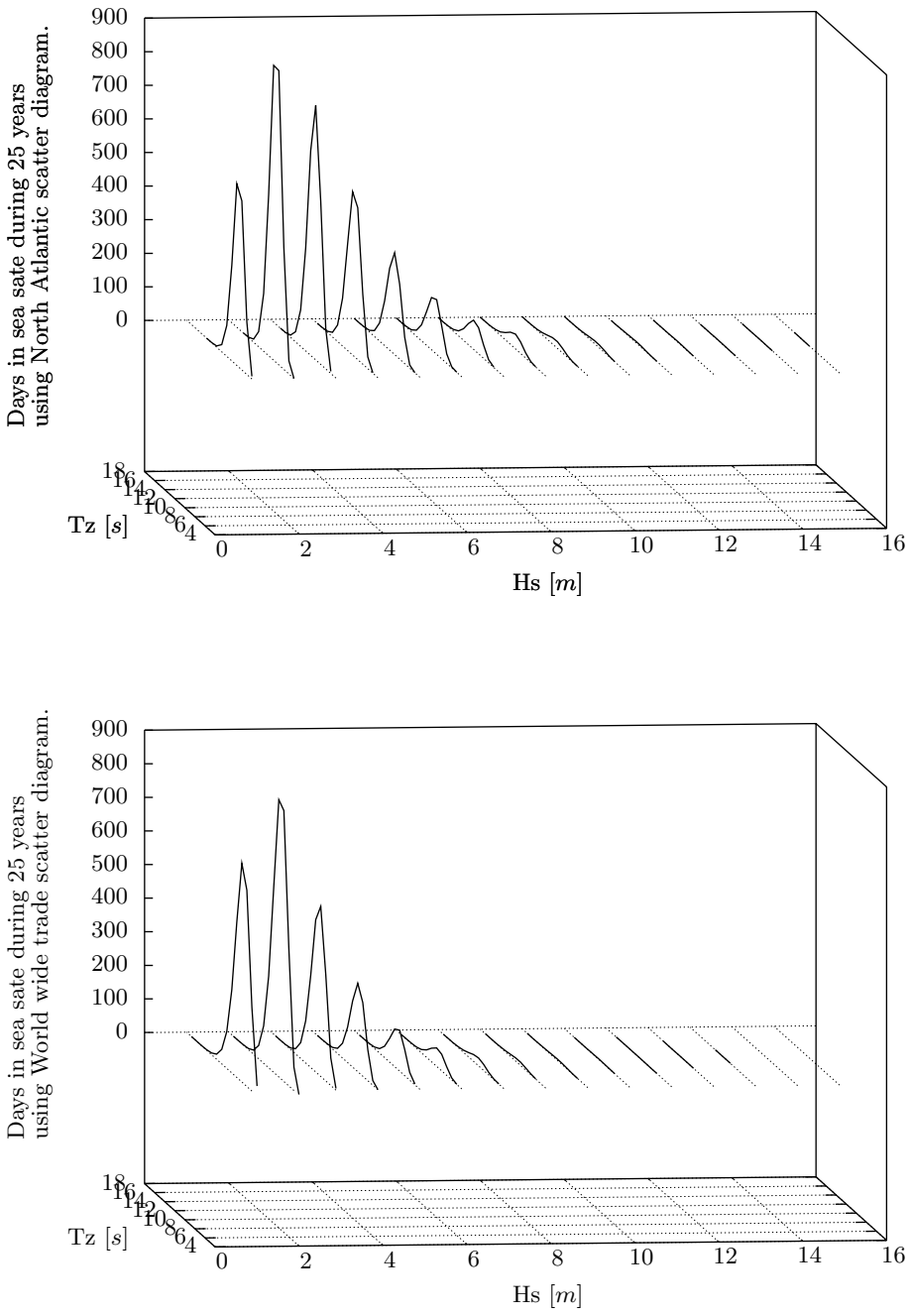

Figure 8.15: Total time in sea state using different scatter diagrams.

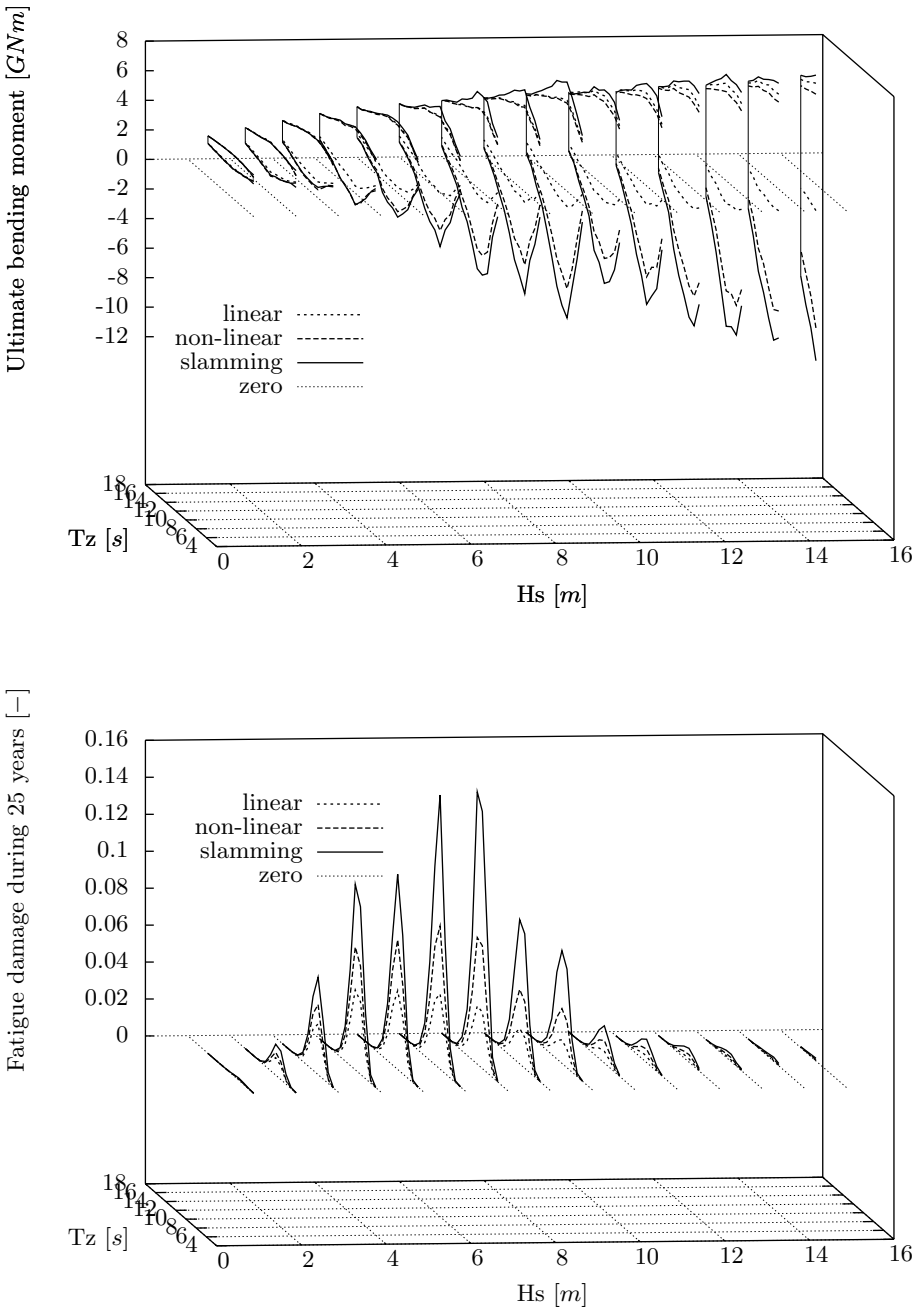

Figure 8.16: Design values for the 270 $[m]$ container ship for 30 years in the North Atlantic.

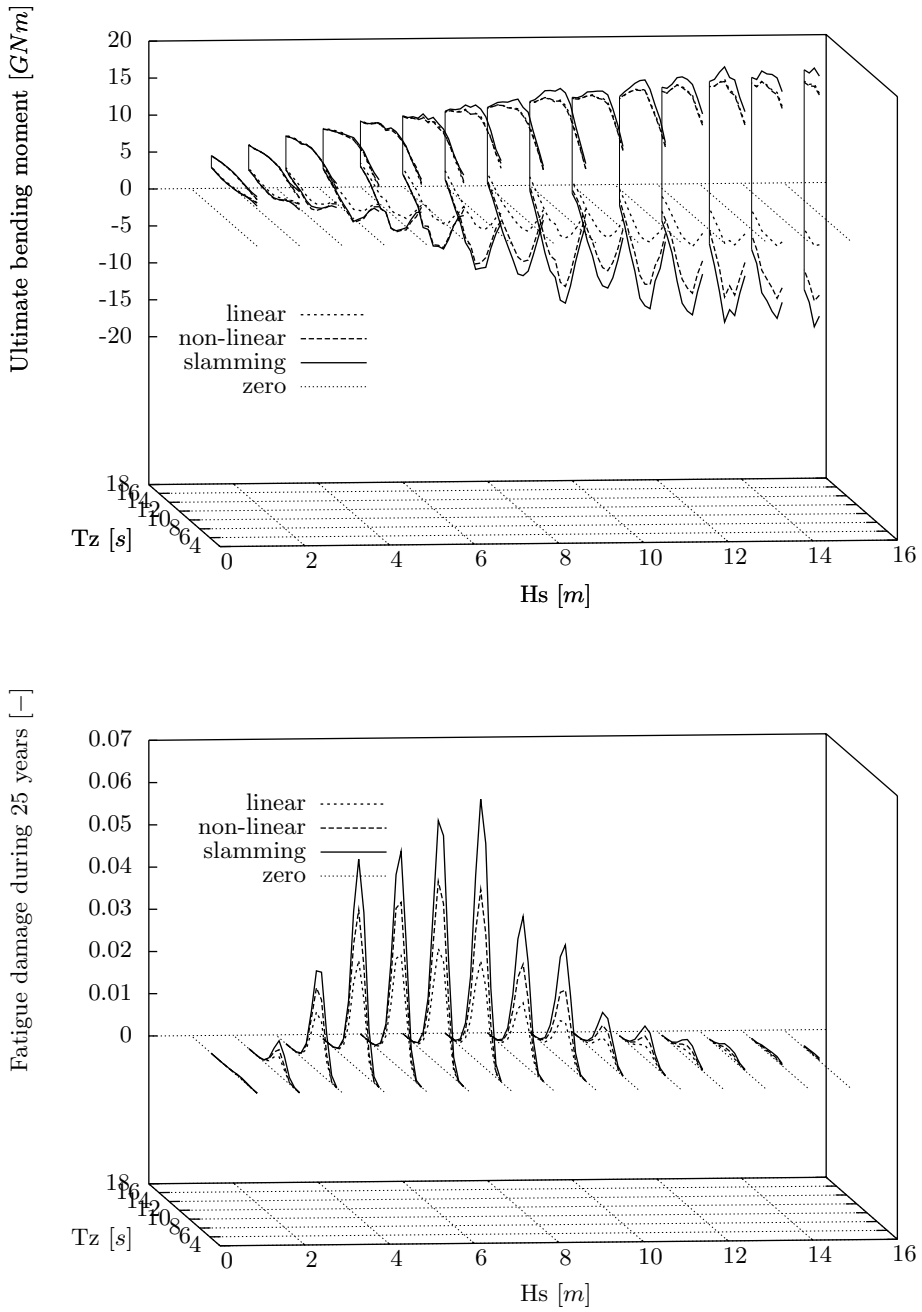

Figure 8.17: Design values for the 360 [m] container ship for 30 years in the North Atlantic.

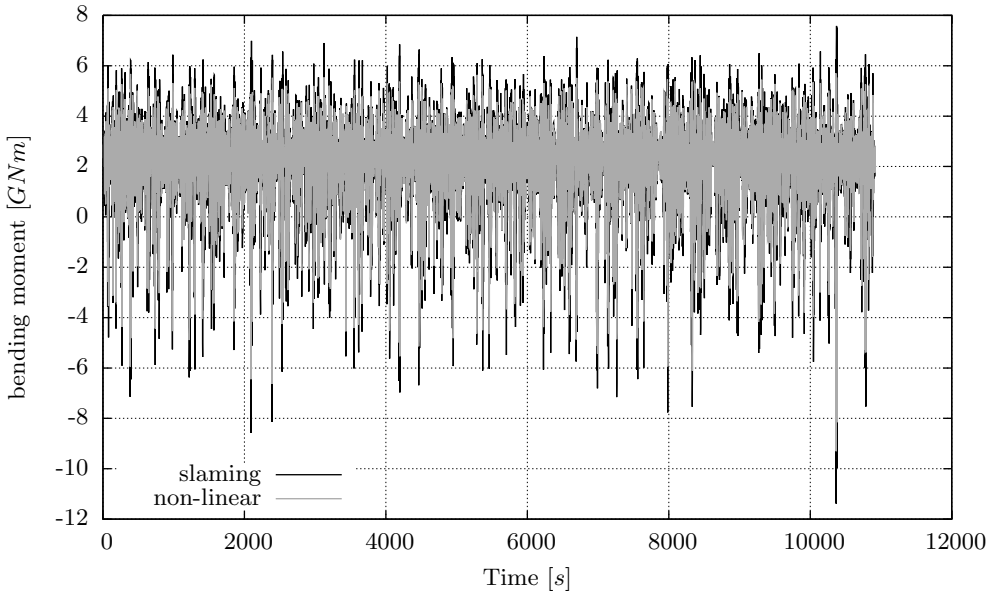

Figure 8.18: Bending moment signal for the 270 $[m]$ vessel in $H_s = 15[m]$ and $T_z = 11[s]$.

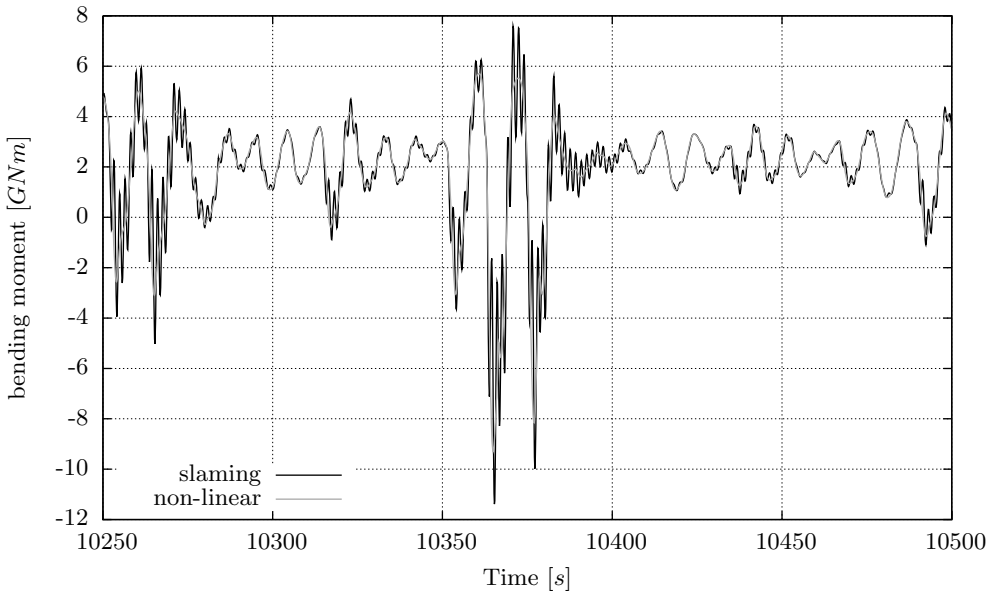

Figure 8.19: Bending moment signal for the 270 $[m]$ vessel in $H_s = 15[m]$ and $T_z = 11[s]$, zoomed.

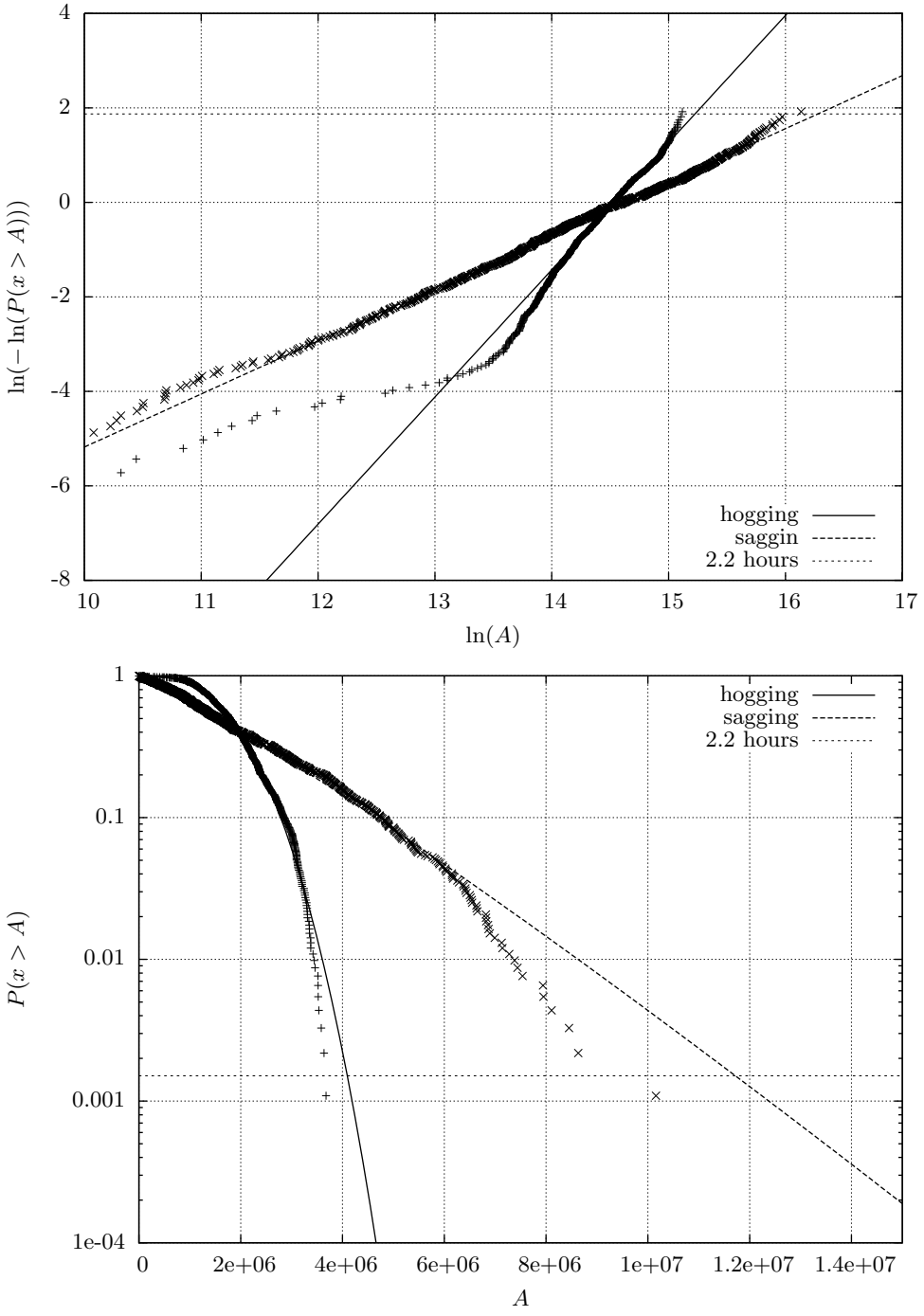

Figure 8.20: Weibull fit of extremes of bending moment for the 270 $[m]$ vessel in $H_s = 15[m]$ and $T_z = 11[s]$ when including non-linear loads.

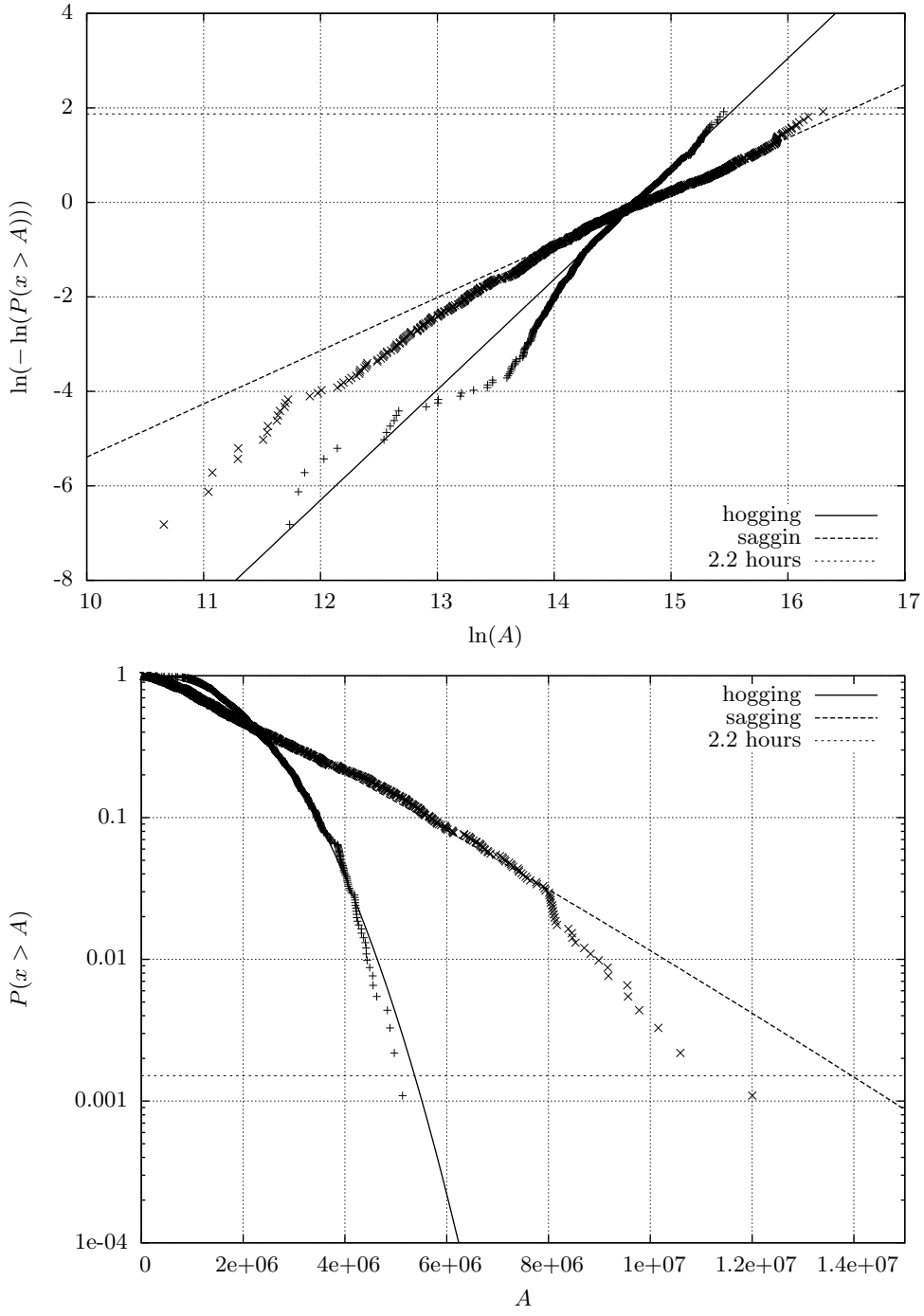

Figure 8.21: Weibull fit of extremes of bending moment for the 270 $[m]$ vessel in $H_s = 15[m]$ and $T_z = 11[s]$ when including slamming.

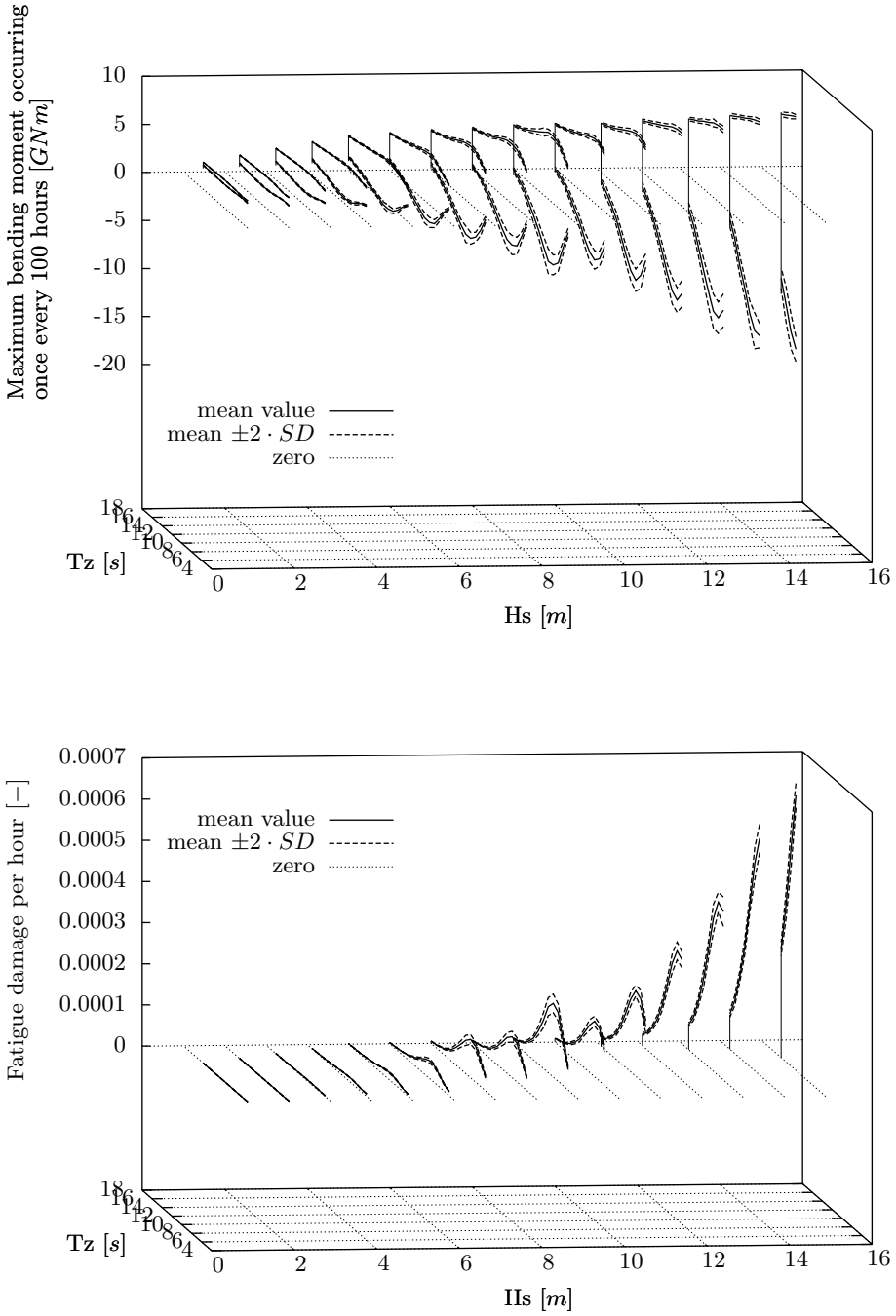

Figure 8.22: Variation in calculation of the design values for the 270 [m] container ship.

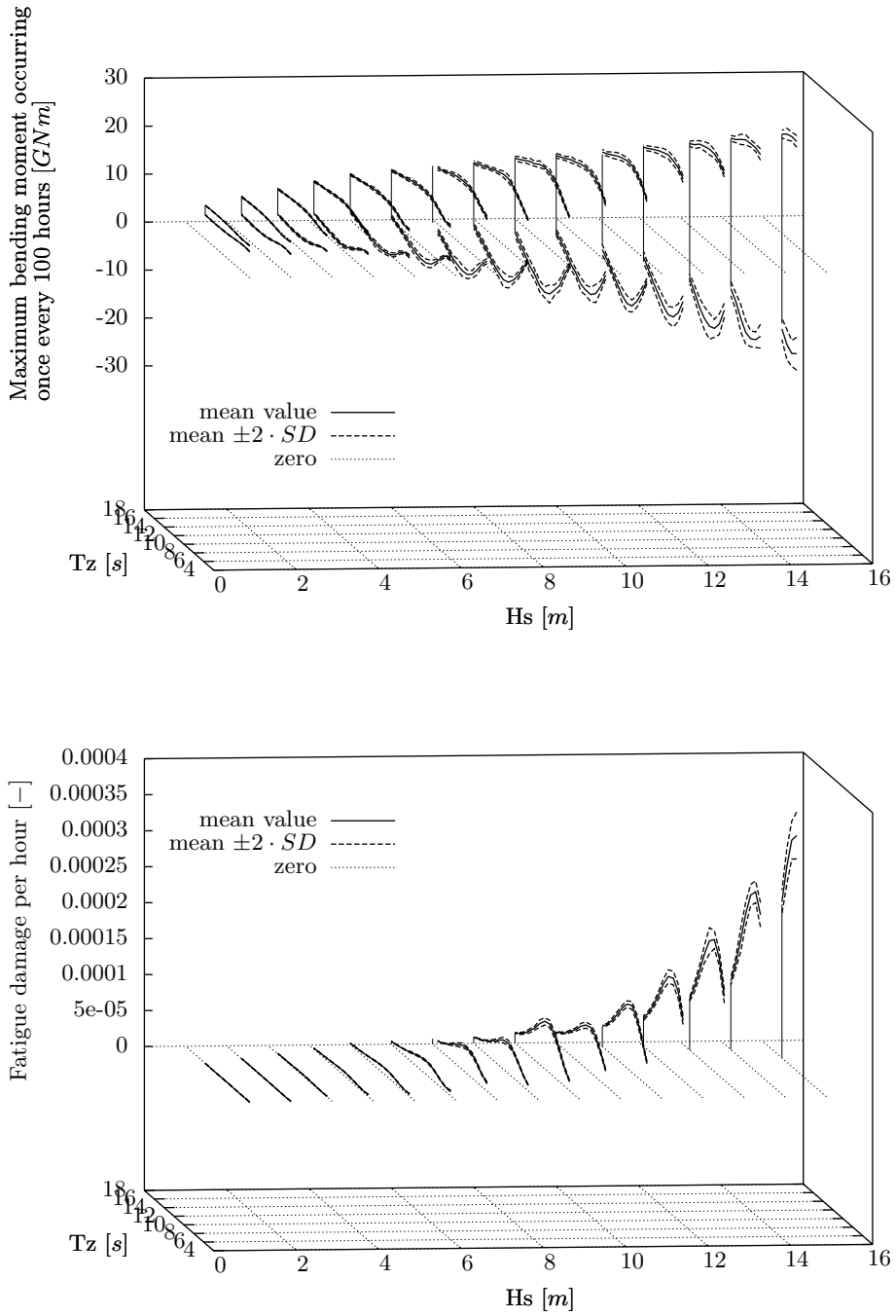

Figure 8.23: Variation in calculation of the design values for the 360 [m] container ship.

Chapter 9

Flexible barges

Barges or floaters mutually connected by flexible connections are considered in this chapter for the verification and the validation of the multi-body and hydro-elastic capabilities of the presented theory. Two barges connected by a hinge are used for verification in the first part of this chapter. The calculated response of a barge with twelve flexible connected floaters is compared with experimental results in the second part of this chapter. The time domain seakeeping theory is used for the computations presented in this chapter because the coupling between different bodies is not implemented in the frequency domain theory as presented in this thesis.

9.1 Barges connected by hinge

The two barges shown in Figure 9.1 are connected by a hinge which allow only for pitch rotation. A similar problem was presented in [37] using a frequency domain approach. An example of two barges connected by a spring can be found in [51]. There are two possible approaches to calculate the response of the coupled barges using the generalised modes:

Single body The two barges are modeled as one body. This body has the basic six rigid-body modes and one additional flexible mode which describes the motion around the hinge. This "hinge" mode is a rotation of one radian in pitch direction of the barge at the left-hand side and minus one radian of the barge at the right-hand side.

Two body Both barges are modeled as a single body. This results in a total of twelve rigid-body degrees of freedom. The hinge is taken into account by kinematic constraints. Relative translations are constrained by the 'spherical'-constraint. Two 'first form dot' or 'd1'-constraints restrict the relative roll and yaw motions. The different constraints are explained in Appendix B.

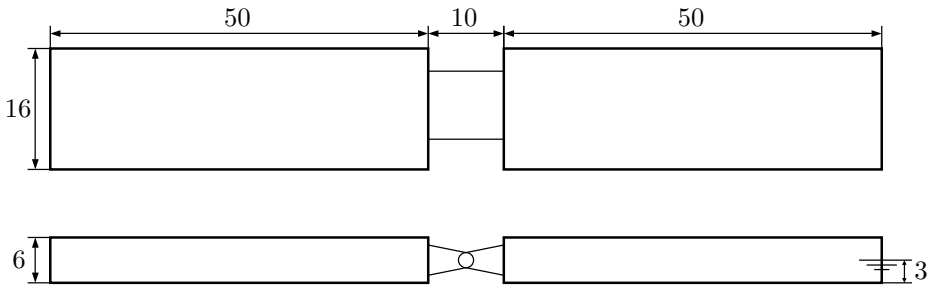

Figure 9.1: Dimensions in metres of the connected barges.

The first approach is clearly the most simple and shows the advantage of using the generalised modes approach in the seakeeping calculation. This approach is also used in [37] to solve the motions of a comparable problem in the frequency domain. However, it will be shown in this verification that the single body approach is not fully correct as, for the time domain seakeeping calculations, it is assumed that the amplitudes of the motions of elastic modes remain small, which may not be the case for this 'hinge' mode.

The problem is first slightly changed to allow one to use this two body configuration for additional verifications of the presented theory. The hinge connection is changed to a rigid connection by removing the "hinged" mode for the single body model. The two body model is adapted similarly by adding a 'first form dot'-constraint in the pitch direction.

The motions are calculated for irregular head seas with a significant wave height of 9 metres. Drift in the surge direction is avoided by adding weak springs to the barges. Figure 9.2 shows the heave and pitch motion at the location of the hinge. The resulting motion is the same, even if the approaches used are quite different. A major part of the theory used for the computation has to be consistent to obtain comparable results. These are mainly the calculation of excitation forces, the different reference frames for the bodies, the dynamics and the kinematic constraints.

The hinge is restored and a stiff spring is added between the barges in the pitch direction for the next verification case. Both the heave at the location of the hinge and the relative pitch angle between the two barges are shown in Figure 9.3. The relative pitch shows some springing response. Again, both approaches give the same results. Even the springing response is exactly the same for both approaches. This illustrates again the consistency of the presented theory.

The original problem, with only the hinge and no spring, is considered next. The resulting motions are presented in Figure 9.4. There are differences between the results obtained with both approaches in this case. These differences could be expected as the deformations of the flexible modes are assumed to

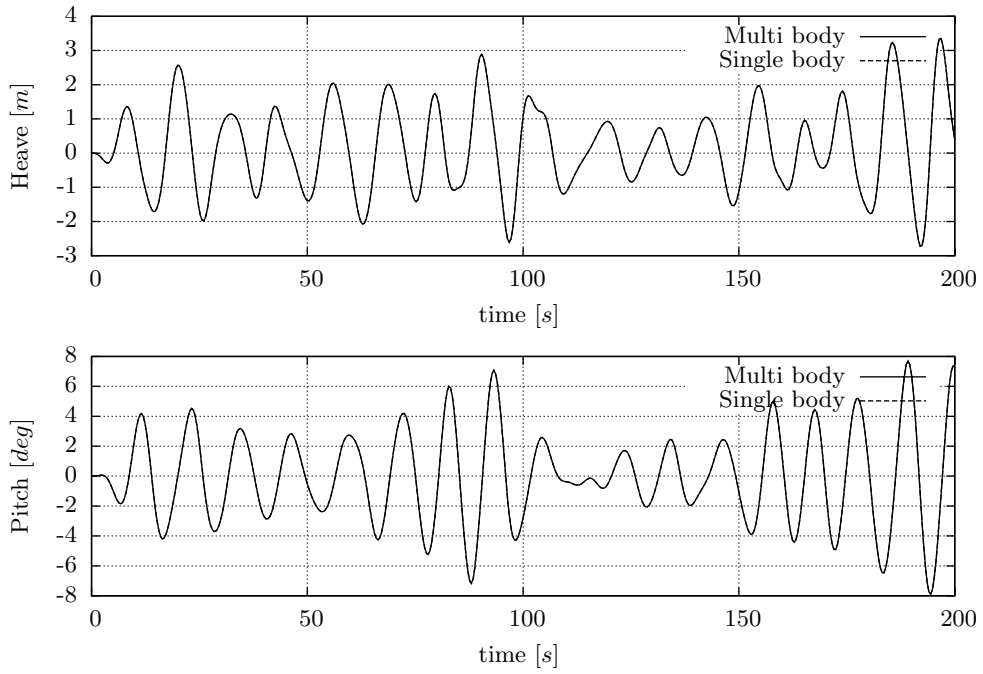

Figure 9.2: Motions with a rigid connection.

be small in the seakeeping calculation. The "hinge" mode of the single body is a flexible mode and the deformation should remain small. The stiff spring used in the previous calculation ensured that the displacement of the "hinge" mode remained small enough for an accurate prediction of the motions using the single body approach. Without the spring, the motion of the "hinge" mode is too large in this severe sea state to use the single body approach. The linear transformations for this flexible mode are not valid anymore in this case. However, the flexible body response is still close to the two body approach and will give a reasonable estimation for the motions even for this severe sea state.

9.2 Flexible barge

Experimental results of the seakeeping response of a flexible barge are used to validate the presented theory. These experiments where carried out at the BGO FIRST offshore and seakeeping tank at Océanide in France [43]. The flexible

The calculations presented in this section have been performed by Jasper van den Broek, see [54].

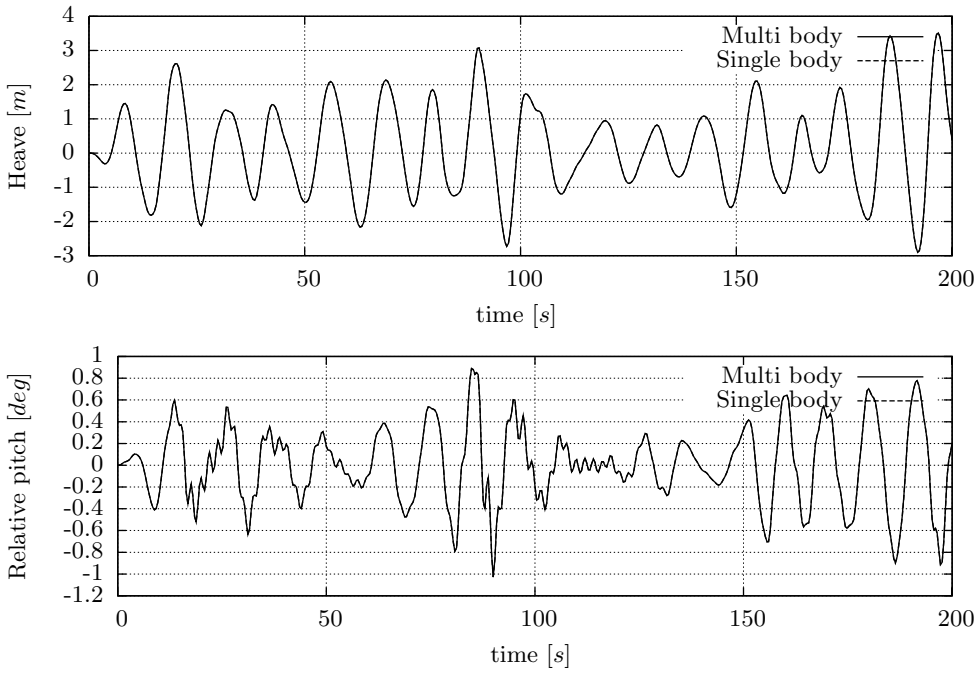

Figure 9.3: Motions with a stiff spring and hinge.

barge consisted of twelve floaters mutually connected at the top by two steel strips. Figures 9.5 and 9.6 are a technical drawings of this flexible barge. Figure 9.7 shows a photograph of the model.

Multiple configurations have been tested and are used in various papers for validation of hydro-elastic theories. The results of the experiments of configuration "C1" are used in this thesis. This configuration and the "C2" and "C3" configurations were tested during the first series of the experiments. Only head sea conditions are considered in these tests. Oblique conditions were considered in the second test series. The two steel strips were replaced by a single steel rod to allow for torsional deformation in this second test series.

"C1" is the most flexible configuration of the first series of tests. The steel strips have a thickness of 4 $[mm]$ for this configuration. The steel strips have a thickness of 6 $[mm]$ for configuration "C2", and "C3" is a rigid model. All configurations except "C1" have a modified floater at the front. This modified floater makes the barge more ship-like.

The motions of six floaters of the barge are measured using an optical tracking system known as the Krypton system. The crosses in Figure 9.5 indicate

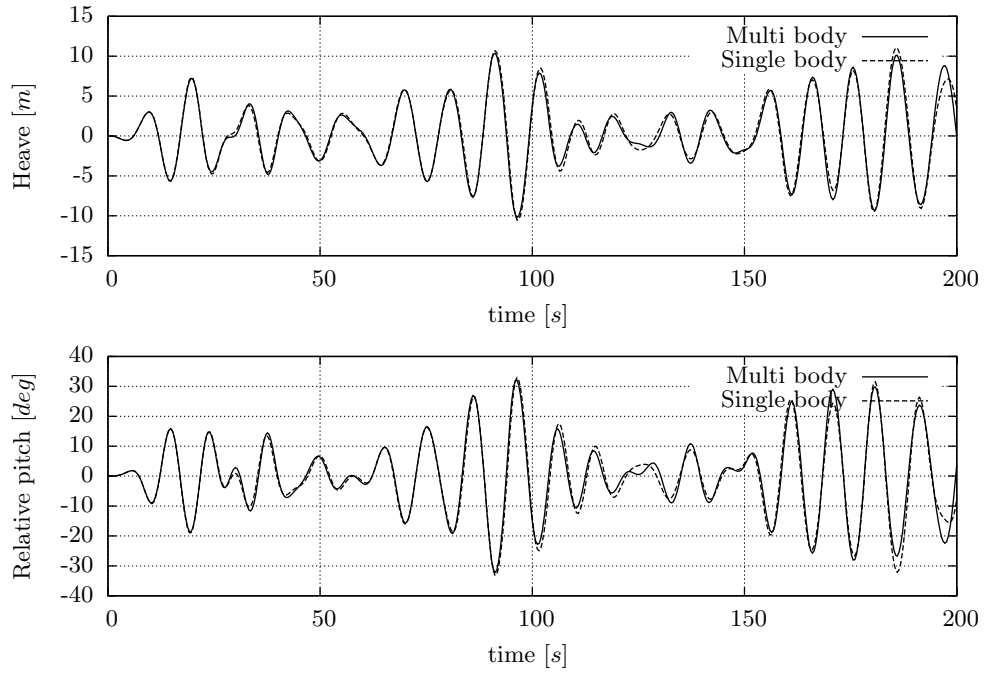

Figure 9.4: Motions with only the hinge.

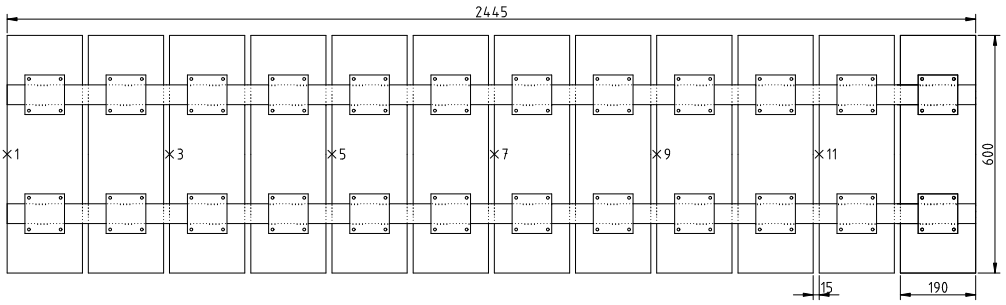

Figure 9.5: Flexible barge, top view; dimensions in $[mm]$.

the locations where the motions were measured.

Both the seakeeping and a decay test are used for the validation. The seakeeping experiments where done for both regular and irregular seas. The experimental results published in this thesis may differ from results published elsewhere, e.g. [42, 28], as the raw experimental data has been reanalysed. The

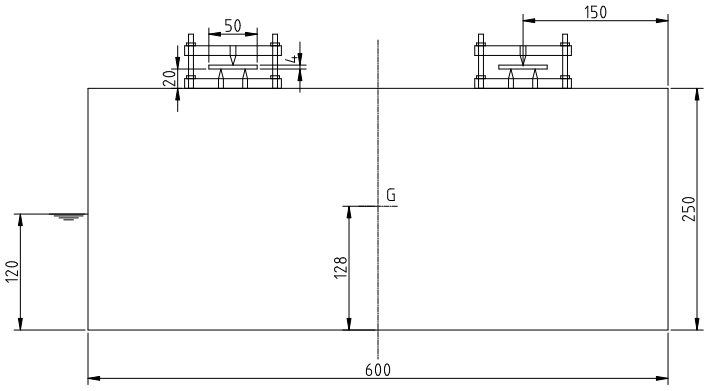

Figure 9.6: Flexible barge, front view; dimensions in $[mm]$.

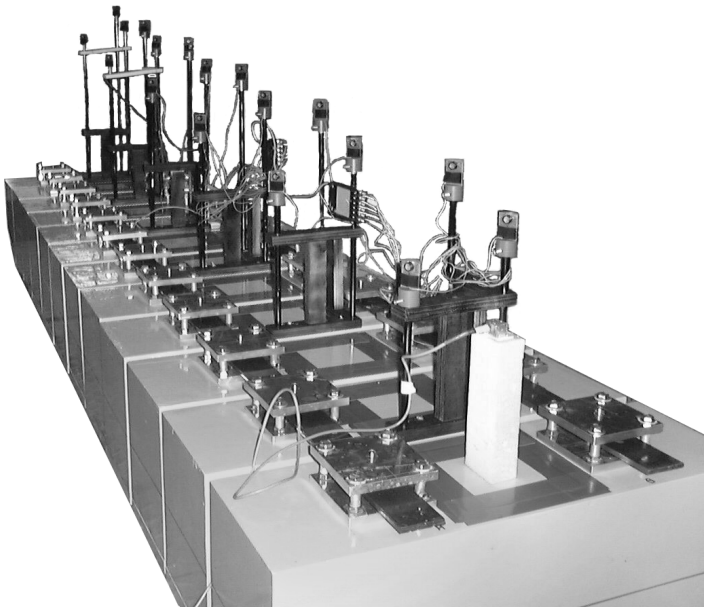

Figure 9.7: Flexible barge, photograph.

decay test has been carried out by lifting the forward floater and releasing it. All experiments are performed with zero speed. Weak springs were used to keep the model in a horizontal position.

The two numerical models used to compute the response of the flexible barge are discussed in the first part of this section. The second part shows the comparisons with the decay test. The seakeeping results are compared in the last part of this section.

9.2.1 Numerical models

This flexible barge can be modeled as one flexible body or multiple rigid bodies connected by a beam element. The results of both approaches are compared with the experimental results. Although multiple bodies are used in the actual experiment, the results of the single flexible body approach are quite interesting. This is the only available experiment where the measured motions of the flexible modes have the same frequency range as the incoming waves. This allows to validate the hydro-elastic coupling for the frequency dependent parts of the theory.

The first approach is using one flexible body. A uniform mass and stiffness is assumed for the calculation of the first ten dry mode shapes for this flexible body using a beam model. Figure 9.8 shows the hydrodynamic mesh used and the first two mode shapes projected onto this mesh. This mesh is also used as the integration mesh. Note that the part of the mesh above the still water line is omitted in the figures to visualise the mode shapes better. The gaps between the floaters are not modeled to avoid resonance problems in the frequency domain BVP calculation. Neglecting these gaps causes an overestimation of the internal load due to the hydrostatic force at the bow and stern. The model is so flexible that the model will actually deform significantly in the calculation due to this still water loading. This is compensated by subtracting the still water bending moment in the time domain calculation using equations (2.39) and (4.47).

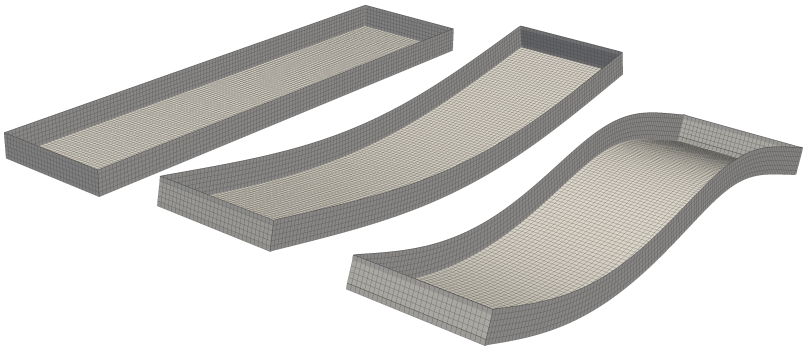

Figure 9.8: Mesh with elastic modes.

The second approach uses twelve rigid bodies to model the barge. The corresponding mesh used in the time domain calculation is shown in Figure 9.9. The bodies are connected by beam elements which represent the steel strips shown in Figure 9.7. The axial stiffness of the steel strips is not modeled using the beam elements as these are very stiff and will reduce the stable time step for the explicit integration scheme to almost zero. Kinematic constraints are used to impose that the length of the steel strip cannot change. This makes the

steel strips infinitely stiff in the axial direction without influencing the stable time step.

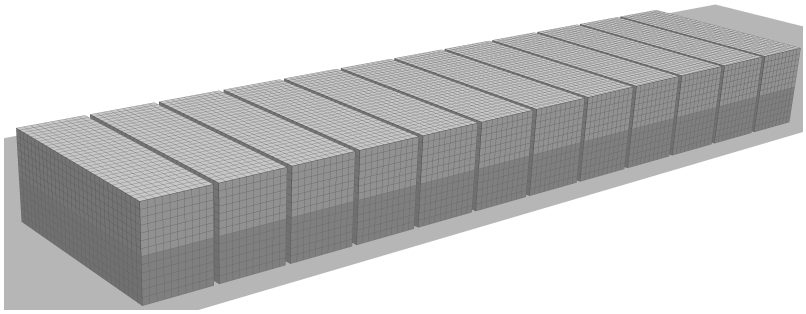

Figure 9.9: Multi-body mesh for time domain calculation.

The time domain mesh shown in Figure 9.9 cannot be used to solve the BVP in the frequency domain. The sides of the floaters which are facing each other will cause resonance and negatively affect the solution of the BVP. Figure 9.10 shows the mesh and a mode shape used to solve the multi-body problem in the frequency domain. The gaps between the floaters are modeled by panels but the modal displacements of these panels are always zero. One of these "joints" is indicated by the thick lines in Figure 9.10. The mode shape shown in Figure 9.10 is the heave of the third body.

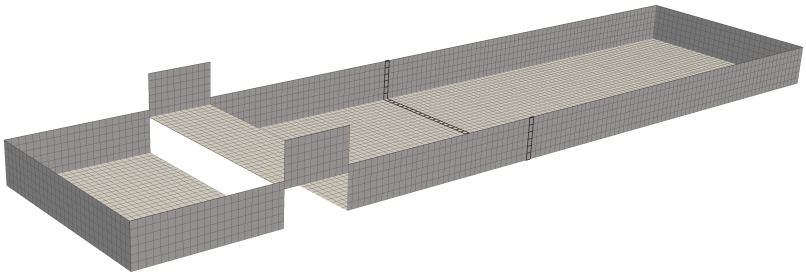

Figure 9.10: Multi-body mesh for frequency domain calculation.

Springs were used to keep the model in position during the experiments. The same spring stiffness was added to the surge, sway and yaw motions of the flexible body. Springs to all surge and sway modes of the multi-body model are added such that the same total stiffness is obtained. The calculation will not predict the correct surge motions as the second-order drift forces are not calculated accurately by the theory used.

The two approaches to model the flexible barge are not equivalent as illustrated for the two barges connected by the hinge presented in Figure 9.1. A

uniform distribution of mass, stiffness and buoyancy is assumed in the flexible body approach. The multi-body approach takes into account the rigid parts and localised masses. Therefore, it is expected that the multi-body approach should give a better representation of the real model. The calculated responses will not be the same using both models, however, the models should give comparable results.

9.2.2 Decay experiment

A comparison of the heave motion of the first floater between the experimental results and the calculations is presented in Figure 9.11. The calculations using both the flexible body and the multi-body approach are performed with and without additional viscous damping. The amount of damping has been tuned to obtain similar amplitudes of motion as found for the first two peaks in the experiments. The additional damping for the flexible body is 2.5 percent of the wet critical damping for the heave and pitch mode, and 5 percent for the flexible modes. The damping for the multi-body approach is defined for the individual floaters 7.5 percent of the critical damping is added to the heave modes and 5 percent to the pitch modes. The critical damping is based on a single wet floater without any connection to the other floaters. Note that the applied damping is not equivalent between the models, it is very difficult to apply equivalent damping using the different models.

The amount of additional damping is quite high. The calculated response is changed significantly by this additional damping. There is a physical explanation for the source of this additional viscous damping. The relative motion of the floaters will pump water in and out of the gaps between the floaters. This will cause viscous damping, however, it is very difficult to model this phenomena accurately. Therefore, the simple damping models are used and are tuned through the decay test. Adding additional viscous damping is also done by other authors, for example [45] uses 6 percent of the critical heave and pitch damping, and 7.5 percent for the flexible modes for the configuration with the rod.

The results in Figure 9.11 show that the calculations with the additional viscous damping are reasonably close to the experiments for the first two peaks. The result shows that the calculated natural frequencies are accurate, as the timing of the first peaks compare well with the experimental results.

The calculated motion using the flexible body and multi-body approach is very comparable despite the large differences between these methods. This illustrates the consistency of the presented methodology.

The wet natural frequencies are calculated in the frequency domain using the flexible body approach. The multi-body approach cannot be used to compute the natural frequencies in the frequency domain as the beam elements are not implemented for that. These results are compared to other analytical and

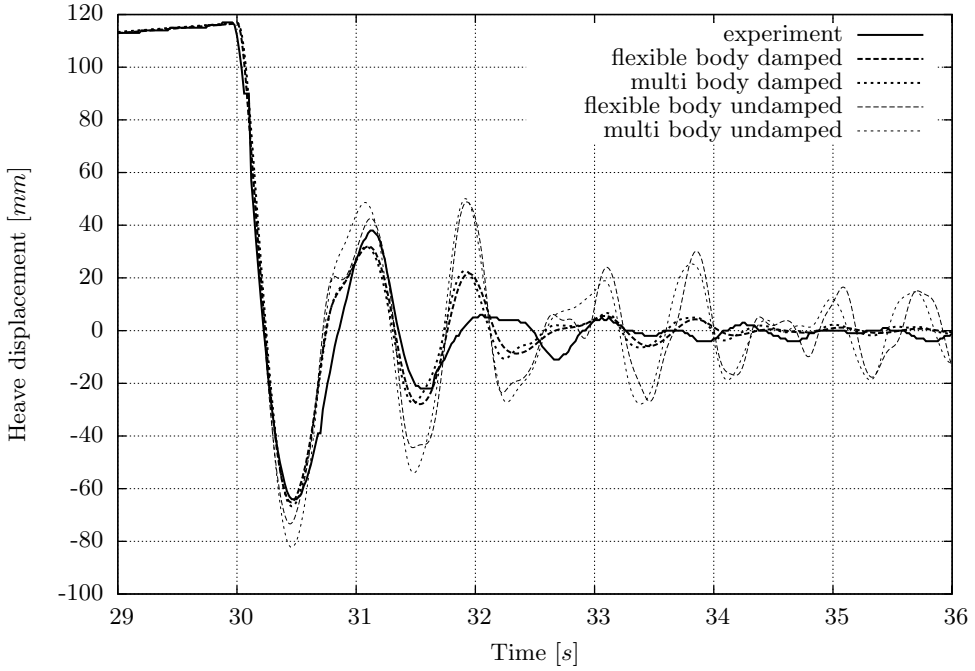

Figure 9.11: Heave displacement of the first floater during decay test.

Mode	Analytical [42]	Numerical [28]	Current method
Heave	5.50	5.50	5.45
Pitch	5.50	5.71	5.68
Flexible mode 1	6.17	6.45	6.27
Flexible mode 2	9.43	9.56	9.68

Table 9.1: Wet natural frequencies (in $[rad/s]$) of the heave, pitch and the first two flexible modes of the barge.

numerical results in Table 9.1. The results of the presented method compare well with the other results. There are no experimental values as the high damping makes the time trace of the decay test too short to accurately calculate the natural frequencies from the motion signal of the decay test.

The names of the mode shapes in Table 9.1 refer to the most pronounced dry mode shape contributing to the wet mode shape. Due to the hydrodynamic coupling, all dry mode shapes contribute to the wet mode shapes. Therefore, there is no real wet heave or pitch mode shape. Examples of the wet mode shapes are presented in [28].

condition	$H_{1/3}[mm]$	$T_z[s]$	condition	$H_{1/3}[mm]$	$T_z[s]$
Irr 1	37	1.19	Irr 4	96	1.60
Irr 2	55	1.19	Irr 5	94	2.00
Irr 3	66	1.60	Irr 6	141	2.00

Table 9.2: Parameters for the irregular waves using JONSWAP spectrum.

9.2.3 Seakeeping experiments

The seakeeping response is measured in both regular and irregular waves. Table 9.2 presents the parameters used for the JONSWAP spectrum for the irregular seas. The calculations are only performed for irregular waves. The same wave-train as was measured during the experiment is used in the calculation. Spectral analysis of the time traces of the motions are used to calculate the RAOs.

Figure 9.12 shows the heave response of the first floater and Figure 9.13 the heave response of the seventh floater. The experimental results for irregular seas show significant variation in heave response of the first floater for the different sea states close to the natural frequency of 6 $[rad/s]$. The lowest experimental RAO value corresponds with the highest waves. This difference is caused by non-linearities in the seakeeping loads, most likely the viscous damping.

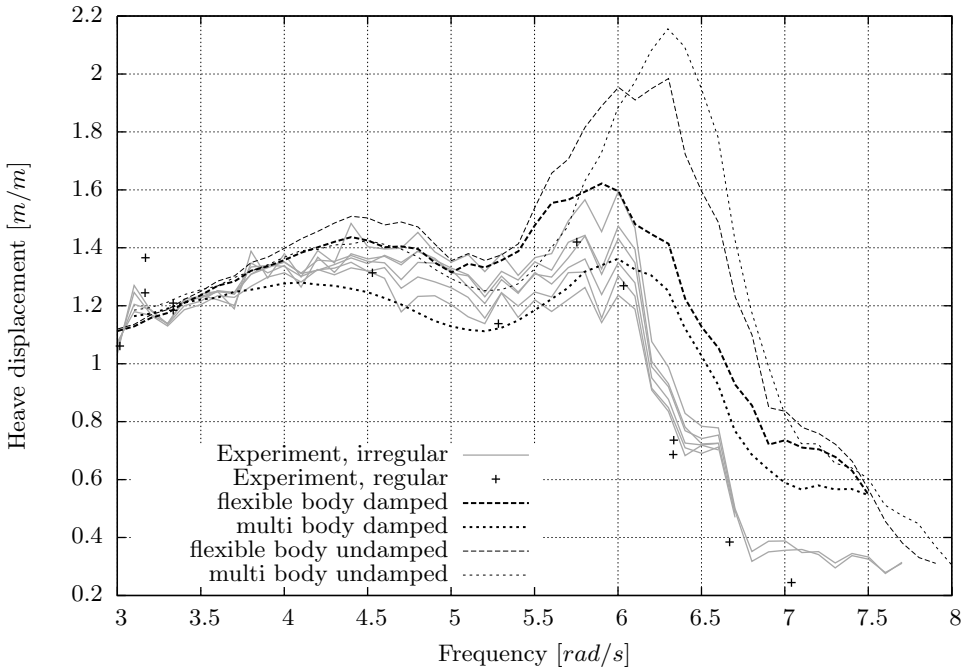

Figure 9.12: RAO heave of the first floater.

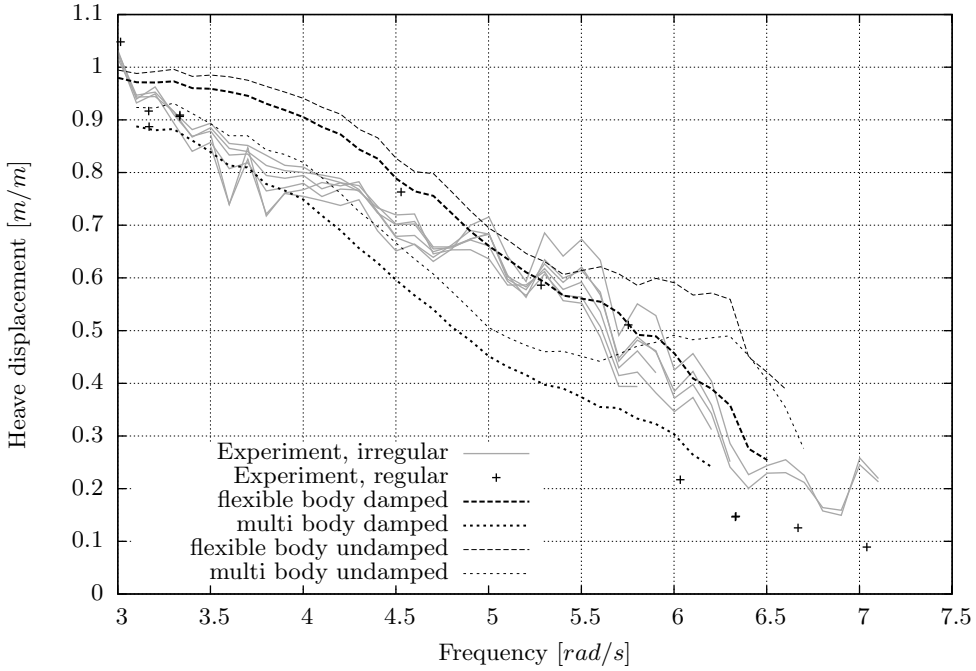

Figure 9.13: RAO heave of the seventh floater.

Only the results of the calculations with wave Irr 3 are presented in the Figures 9.12 and 9.13 as the calculation results show less dependency to the wave height as found in the experiments. This is probably because a linear viscous damping model is used in the calculations. The motion calculated using the two approaches is quite different in magnitude. This difference can be explained by three things: the large flexible deformations which are not allowed for the flexible body approach; the difference between the modeling; and the difference in the computation of the viscous damping between the two models. The damping has a large impact on the calculated motion. It is likely that better results could be obtained when a more accurate damping model is used. Nevertheless, the results obtained using the two approaches with the additional damping show a fair correspondence with the experimental results.

Predicting the viscous damping is not an objective of this thesis. The objective is to predict the hydro-elastic response accurately for problems where the wave radiation or structural damping is dominant. It is difficult to judge if the presented theory correctly predicts the hydro-elastic response of this flexible barge, except for the viscous damping. These comparisons only validate that the presented method computes the measured trends in the RAO well. Similar differences between the measurements and the predictions are also found in the validations presented in [28] and [45].

Chapter 10

Experiments with an aluminium model

Experiments with an aluminium model are used in this chapter to validate the calculated hydro-elastic response. Figure 10.1 shows a photograph of the aluminium model. The experiments were carried out in towing tank of the Delft University of Technology in the summer of 2006. The goal of these experiments was to measure the wet natural frequencies and the response to slamming loading. Using an aluminium model allows one to create an accurate numerical model of the structure as the material parameters are well known for aluminium in contrast to materials which are often employed for ship models. A detailed description of the experiments can be found in [52].

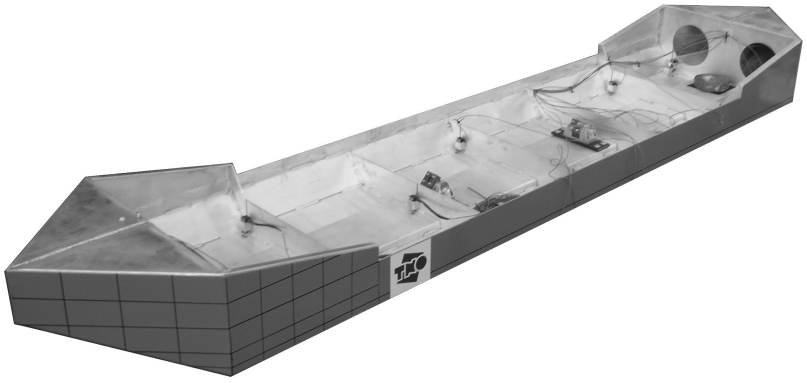

Figure 10.1: Photograph of the aluminium model.

The model and the experimental setup is explained in the first section of

A number of the calculations presented in this chapter have been performed by Kirk Green, see [13].

this chapter. The validation of the wet natural frequencies is presented in the second section. To be able to validate the slamming forces, a method which estimates the slamming forces using the measured response is presented in the third section. The last section presents a validation of the calculated slamming forces and the whipping response.

10.1 Model and experimental setup

The model used in the experiments is described in the first part of this section. The second part describes the experimental setup and data acquisition procedure.

10.1.1 Model

The hydrostatics of the model are presented in Table 10.1. The hydrodynamic cross sections are presented in Figure 10.2.

Length over all	3.8	$[m]$
Length at waterline	3.32	$[m]$
Length of parallel body	3.0	$[m]$
Beam	0.75	$[m]$
Draught	0.08	$[m]$
Depth	0.20	$[m]$
Volume of displacement	0.130	$[m^3]$
Displacement of mass	130	$[kg]$
Area of water-plane	2.38	$[m^2]$

Table 10.1: Hydrostatics.

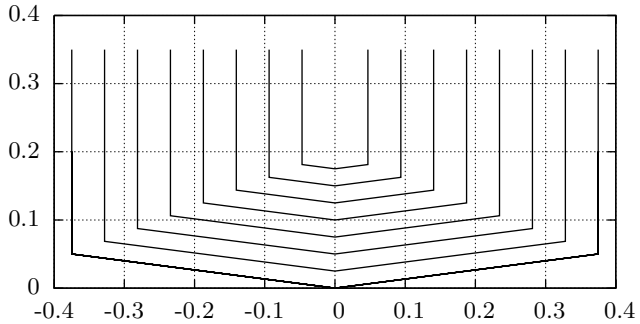

Figure 10.2: Cross sections.

The structural drawings of the model can be found in Appendix D. The model is made from aluminium plates with a thickness of 5 $[mm]$. The structural design is such that the local modes have a high frequency compared to the frequency of the first few global modes. This allows one to accurately measure the response of the global modes. It also helps to compute the first few global modes relatively easily using a FEM method, as this method will solve the natural modes starting from the lowest frequency.

The model has a relatively large width to draught ratio to ensure a significant influence of the added mass on the natural frequencies. Otherwise, it would be difficult to validate the computed added mass by comparing the wet natural frequencies with the experimental values. The bow of the model has been designed to optimise slamming impact. This should ensure significant slamming impacts and consequently a significant whipping responses. The bottom has a small dead-rise angle to avoid entrapment of air during the slamming events.

The hull, excluding paint, has a mass of 95.4 $[kg]$. The total mass of the paint is estimated at 1 $[kg]$. During the experiments with waves, a plastic cover was placed on the model with a mass of 0.8 $[kg]$. The masses of the ballast and the items to connect the model to the towing carriage can be found in Appendix D.

The finite element model of the structure is shown in Figure 10.3. The small mesh size is chosen to make the meshing of the small geometrical details possible. The density of the aluminium is scaled slightly to obtain the same mass as the real model. This accounts for the weight of cables, accelerometers, paint, etc.

10.1.2 Experimental setup

As stated before, the experiments were performed in the large towing tank of the Delft University of Technology. This tank is 142 metres long, more than 4 metres wide and 2.5 metres deep. The tank is equipped with a wave generator which can produce regular and irregular head waves.

The model is attached to the towing carriage in such way that the sway, roll and yaw motions are constrained. Springs in the surge direction prevent drifting of the model. The model can move freely in the heave and pitch direction. A sketch of the constraints can be found in Figure 10.4. Figure 10.5 is a photograph of the actual experimental setup. Hinges supported by steel plates are attached to the model. Steel pipes are connected to the hinges. These pipes are connected to a small carriage by bearings. The small carriages run over a rail on the towing carriage and can only move in surge direction. The small carriage at the front is connected to the two springs. The small carriage at the back runs freely.

The rigid-body motions are measured by an optical tracking system called the Krypton system. The structural response is measured using twenty ac-

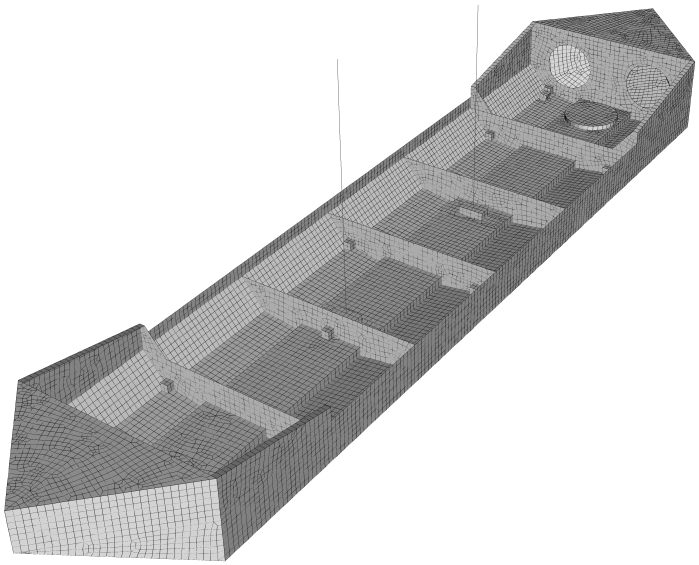

Figure 10.3: FE model of structure.

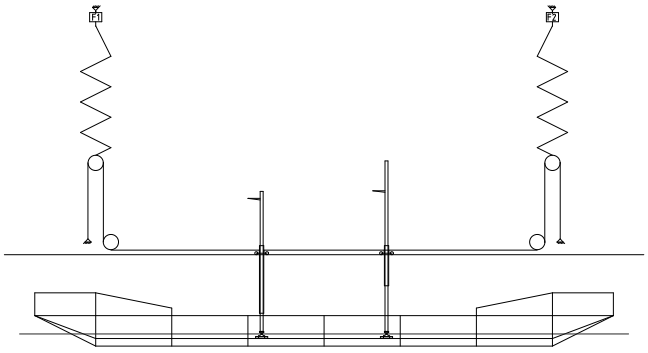

Figure 10.4: Model constraints, sketch.

celerometers. The location of these accelerometers can be found in Appendix D. Sixteen accelerometers measure the vertical accelerations and four measure the horizontal accelerations. The wave elevation is measured by a wave probe in front of the towing carriage. The forces in the surge springs are also measured using force transducers `F1` and `F2` shown in Figure 10.5. The data is acquired using a sample rate of 10 $[kHz]$ which is large enough to measure the natural

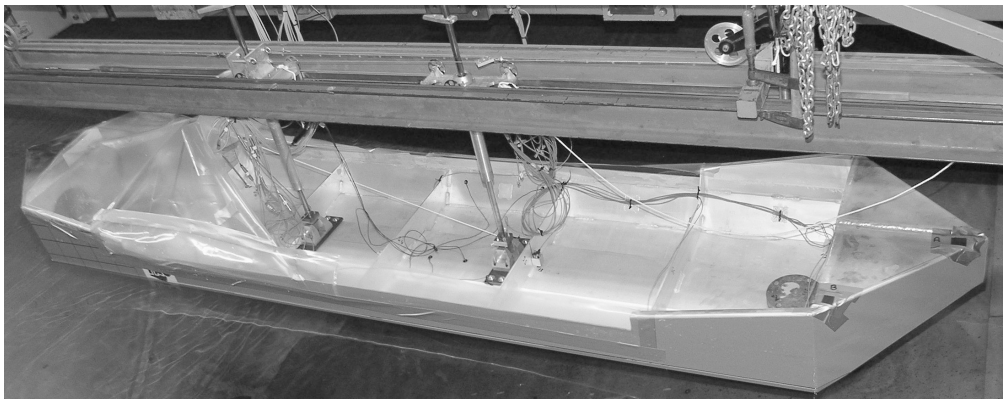

Figure 10.5: Model constraints, experiment.

frequencies of the first few global modes of the structure which have a frequency up to 300 $[Hz]$. It should be noted that the optical tracking system samples the position at a frequency of 60 $[Hz]$.

10.2 Natural frequencies

The natural modes are measured during the first phase of the experiments. The Frequency Response Functions (FRF) are measured at the 14 accelerometers, after a hit with an instrumented hammer. The results of the measurements in still water are shown in Figure 10.6. The amplitude of the FRF indicates the frequencies of the natural modes. The shape of the natural modes is determined using the phase differences found for the different accelerometers in the FRF. This experiment is repeated using other locations along the model for the hammer hit to ensure that all global vibration modes up to 200 $[Hz]$ are found. This experiment is also carried out for different velocities to investigate the velocity dependency of the (infinite frequency) added mass.

The response of the model in air is investigated first. This validates if the numerical model of the structure is accurate. The natural frequencies and mode shapes are measured for the model lifted out of the water by soft springs. The effect of these springs on the natural frequency is negligible. Besides the springs, the connection of the model to the towing carriage is exactly the same as used for the experiments. This ensures that the effect of these connections are included in the measured dry frequencies. These connections are also modelled in the FE model of the structure.

The comparison of the calculated and measured dry frequencies of the first few global modes can be found in Table 10.2. The results obtained by the numerical model are close to the measurements which indicates that the FE

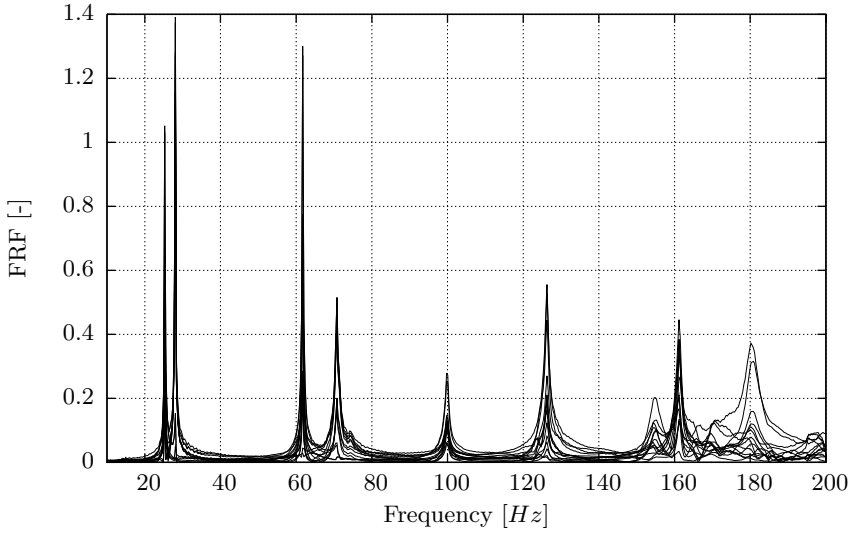

Figure 10.6: FRF between hammer and the 14 vertical accelerometers for the model in still water.

	Frequencies [Hz]	
Mode description	Experiments	FEM calculation
1st Torsional	42.6	45.3
1st Longitudinal	46.9	47.0
2nd Torsional	111.8	112.0
2nd Longitudinal	123.4	125.5

Table 10.2: Dry natural modes.

model is a sufficiently accurate representation of the structure.

The wet natural frequencies are calculated using the frequency domain method described in Section 3.4. The comparison between the calculated and measured wet frequencies is presented in Table 10.3. The calculated natural frequencies are equal for all speeds because the speed is only included in the encounter frequency. The frequencies of the natural modes are relatively high meaning that the frequency dependent part of the added mass is almost zero for these frequencies. This results in an added mass which is the same for all velocities and almost equal to the infinite frequency value. The comparison between the experimental and calculation results shows good agreement. The natural wet frequencies are also calculated in the time domain by giving a mode an initial displacement and calculating the spectra of the resulting motion in still water. The calculated natural frequencies using the time domain were found to be almost equal to the results of the frequency domain computation.

	Frequencies $[Hz]$				
Mode description	Expt. $0ms^{-1}$ Fn 0	Expt. $1ms^{-1}$ Fn 0.18	Expt. $1.5ms^{-1}$ Fn 0.26	Expt. $2ms^{-1}$ Fn 0.35	Calc.
1st Torsional	28.1	28.0	28.9	30.8	30.3
1st Longitudinal	25.3	25.0	25.6	27.3	25.3
2nd Torsional	70.8	70.7	71.3	71.0	74.6
2nd Longitudinal	61.8	61.2	60.3	59.4	62.4

Table 10.3: Wet natural modes.

The wet natural frequencies of the longitudinal modes are about half that of the dry natural frequencies. As the increase of the total stiffness by the hydrostatics is negligible, the total modal mass has to be four times larger for the wet situation compared to the dry situation. This indicates that the added mass for these modes is about three times the structural mass. This large contribution of the added mass to the wet natural frequencies makes the wet natural frequencies a good measure to investigate if the added mass is computed accurately.

In addition, the results show that the contribution of the added mass hardly changes due to the forward velocity. The experiments were carried out with a velocity up to Froude number $Fn = 0.35$, but the measured natural frequencies hardly change. Therefore, calculating the infinite added mass without accounting for forward speeds effect gives reasonable results for this model. The zero speed infinite added mass is normally used when the added mass is included in the FEM calculation.

10.3 Estimation of slamming loads

In the second part of the experimental investigation the response of the model in waves with slamming is measured. The slamming loads are not directly measured, instead the response of the aluminium model is measured using the accelerometers in combination with the optical tracking system which measures the rigid-body motions. The Optimal State Estimation method (OSE) is used to estimate the slamming loads using the measured response. The theoretical background of the OSE method can be found in Appendix E. This section explains the preparations to utilise the OSE method. In addition, to validate the OSE estimate, the estimated external force is compared with a measured hammer impact.

10.3.1 Preparation for the OSE

The first forty natural modes are calculated using the FE package TRIDENT [34]. The FE mesh used is shown in Figure 10.3. The FE model also contains the small blocks which are used to support the accelerometers. These blocks are added to the FE model to obtain the eigenvectors for the locations of the accelerometers as accurately as possible

Boundary elements are placed on all wetted elements for the calculation of the infinite frequency zero speed added mass in still water using the BEM solver within the FE program. Hydrostatic springs are added to obtain the correct heave and pitch frequencies. Note that this approach results in different mode shapes compared to the dry mode shapes which are used in the seakeeping calculations.

The accelerations, velocities and displacements are estimated by the OSE method. The errors in the velocities and displacements cannot be estimated if only the measured accelerations are used as input for the OSE estimation. The rigid-body displacements have been measured using an optical tracking system. These measurements cannot directly be used because the motions were measured with a frequency of 60 $[Hz]$. The signal does also not include the small displacements given by the flexible deformations.

A displacement signal can also be obtained by double integration of an acceleration signal. The calculated displacement is shown in Figure 10.7. Line $d(t)$ is the displacement measured by the optical tracking system and line $\iint a(t)$ is the double integration of the acceleration signal. There is a clear difference between the two signals. The difference is mainly due to the fact that the initial velocity and displacement are not known and set to zero for the double integration, but the changing pitch angle with respect to the gravity field and inaccuracies in the accelerometer cause a so-called drift in the signal.

Before the OSE can be used, the error in both the acceleration and displacement signals are minimised using the rigid-body displacement signals from the optical tracking system.

The accelerations are corrected using

$$a_c(t) = a(t) + g(1 - \cos(\theta)) + 2c_2 + 6c_3 t + 12c_4 t^2 + 20c_5 t^3, \tag{10.1}$$

with

$$c_0 + c_1 t + c_2 t^2 + c_3 t^3 + c_4 t^4 + c_5 t^5 \approx d_m(t) - \iint_0^t a(t) + g(1 - \cos(\theta))\ \mathrm{d}t, \tag{10.2}$$

where $d_m(t)$ are the measured displacements from the optical tracking system.

The $g(1-\cos(\theta))$ term accounts for the gravity accelerations due to gravity, due to changes in the pitch angle. Coefficients c_0 to c_5 are obtained by a polynomial fit of the difference between the original double integration and the measured motions. Coefficient c_0 corresponds to the initial displacement of the

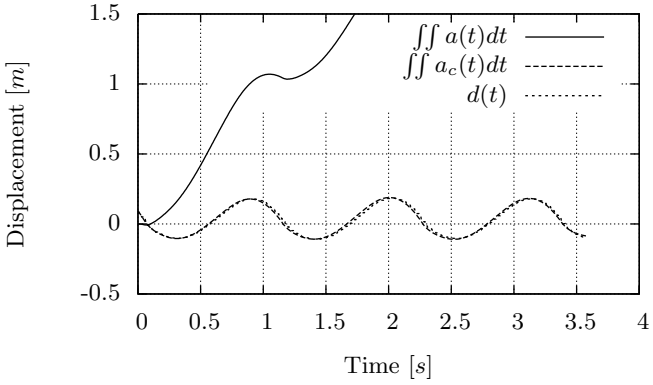

Figure 10.7: Displacements at accelerometer number 1.

point, which cannot be known from the acceleration only. The initial velocities is c_1 and c_2 are the mean offset of the accelerometer. Only c_3 to c_5 are used to remove actual drift in the accelerometer signal. The original and corrected acceleration signals are shown in Figure 10.8. The corrections are very small, but the displacement signals in Figure 10.7 show that the double integration of the corrected signal is very close to the measured motions.

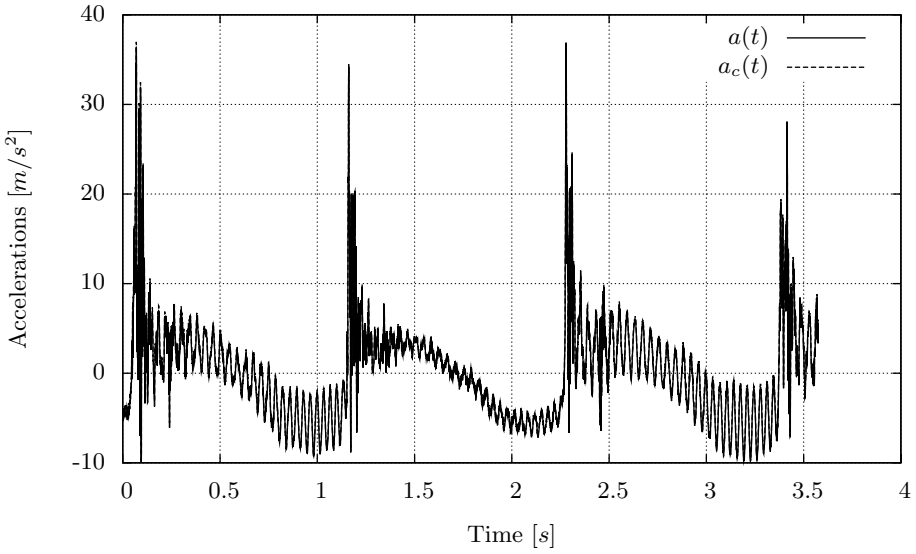

Figure 10.8: Original and corrected acceleration at accelerometer 1.

Only vertical forces are estimated using the OSE method. The OSE esti-

mation is based on

- The corrected vertical accelerations of the fourteen accelerometers which where oriented in the vertical direction
- Displacements using double integration of the corrected accelerations at accelerometers 1, 4, 6, 16, 19 and 20, see Figure D.4.
- The first fifteen mode shapes which have a significant contribution to the vertical accelerations. These are the longitudinal and torsional mode shapes. The damping for all modes of the wet model is estimated to be one percent of the critical damping.

The input signals are down-sampled to 5 $[kHz]$ before the OSE estimation is made. Otherwise, computing a estimation for a time trace of twenty seconds would require more computer memory than was available (32 Gb). The user selects locations where the external forces are estimated. Four forces are distributed over the ship. One at the bow, one at the aft, one in the middle and one at the side. The OSE estimation becomes inaccurate if more force locations are added for the estimation. The measurements and the mode shapes do not contain enough information to estimate the contribution of more than four external forces. The total heave force, which is the sum of the four predicted forces is presented as the result of the OSE estimation.

10.3.2 Validation of the OSE estimation

For validation purposes, the aluminium model is hit with a large hammer in still water. Rubber sheets where placed between the hammer and the model to obtain a comparable response as was measured during the slamming induced whipping responses. The hammer force is measured using an accelerometer, such that $f = m \cdot a$. This will result in a non-zero force before and after the impact because the hammer also accelerates during these time spans.

The measured and the estimated force are shown in Figure 10.9. An unknown force at the location of the hammer impact is used for the OSE calculation. The estimated force by the OSE during the actual hit is very close to the measurement. The OSE estimation shows some oscillations after the hit because the actual damping of the modes is not known. The OSE uses the external force to compensate for the differences between the real damping and the user defined damping.

10.4 Validation of computed slamming impact and whipping response

Regular head waves are used to investigate the slamming impact and resulting whipping response of the aluminium model. The experiments were carried out

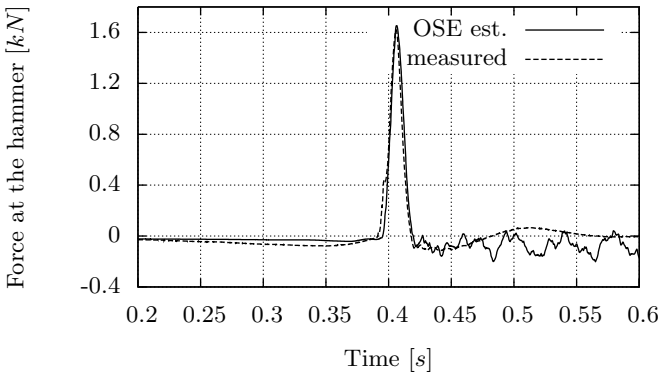

Figure 10.9: Comparison hammer force.

Run	U $[m/s]$	H $[m]$	ω $[Hz]$	Figure	Run	U $[m/s]$	H $[m]$	ω $[Hz]$	Figure
1	0.0	0.23	0.56	10.11	9	1.0	0.15	0.68	10.15
2	0.0	0.23	0.60	10.11	10	1.0	0.16	0.72	10.15
3	0.0	0.24	0.64	10.12	11	1.5	0.16	0.54	10.16
4	0.0	0.19	0.68	10.12	12	1.5	0.15	0.56	10.16
5	0.0	0.28	0.72	10.13	13	1.5	0.14	0.60	10.17
6	1.0	0.15	0.56	10.13	14	1.5	0.14	0.64	10.17
7	1.0	0.16	0.60	10.14	15	1.5	0.14	0.68	10.18
8	1.0	0.15	0.64	10.14	16	1.5	0.12	0.72	10.18

Table 10.4: Conditions for whipping experiments.

with velocities of 0, 1 and 1.5 $[m/s]$ and wave frequencies of 0.56, 0.60, 0.64, 0.68 and 0.72 $[Hz]$ resulting in wavelengths ranging from 5 $[m]$ to 3 $[m]$. An additional run using a wave frequency of 0.54 $[Hz]$ was done for 1.5 $[m/s]$. The wave height used is the maximum wave height which was shown to be possible during the experiments. Higher waves would likely result in green water, waves over-topping the towing tank and/or larger displacements of the model than the setup could handle. An overview of the experiments is given in Table 10.4.

Next to the estimation of the slamming forces, the slamming loads and the whipping responses are also computed for all measured conditions. The hydrodynamic mesh and the slamming sections used for the calculations are shown in Figure 10.10. It was found that the prediction of the rigid-body seakeeping motions are quite inaccurate. This could be expected as the video recording of the experiments shows that the model was, at some time steps, more than fifty percent out of the water. The linear assumption for the diffraction and radiation forces do not hold in such conditions. Another problem is the surge

motions which cannot be correctly computed without correct computation of resistant and drift forces. Both are not included in the theory used.

The measured rigid-body motions are, therefore, imposed in the calculations using kinematic constraints. This should ensure the correct relative velocity and it still allows to validate the whipping response as only the rigid-body motions are imposed. The wave elevation measured by the wave probe is used to generate the wave-train for the seakeeping calculations assuming that the diffraction from the model is negligible at the location of the probe.

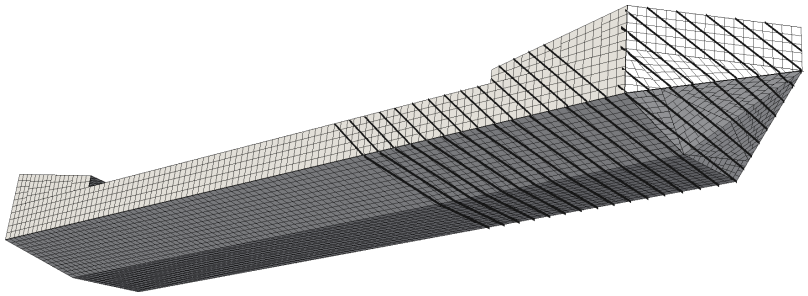

Figure 10.10: Hydrodynamic mesh and slamming sections.

Figures 10.11 to 10.18 shows the comparison between the estimated and calculated total force in the heave direction. The figures show also the comparison between measured and calculated accelerations at the bow, accelerometer 1, see Figure D.4. Both the forces and accelerations are measured in the body reference frame. Note that the corrected accelerations are presented as the measured accelerations.

It should be kept in mind that the given heave force is really an estimation. The OSE is developed to predict impulsive loading at a structure. The prediction of the slamming load will be accurate but the prediction of the non-impulsive loading will be less accurate. Hydrostatic springs were used to solve the wet natural modes, which are used by the OSE. The forces from these hydrostatics springs are not included in the OSE estimate which will result in a difference in the non-impulsive loading. There are also whipping oscillations visible in the heave force. This is caused by the OSE using the external forces to create the correct structural damping.

10.4.1 Zero speed cases

The prediction of the slamming force and the resulting whipping response is not so good for the zero speed conditions. This is probably caused by a difference in wave realisation between the experiment and calculation. The experiments were carried out in a relatively small towing tank. The radiated waves will reflect on the tank wall and influence the wave elevation at the model. The tank

walls are not modelled in the computations and the wave realisation is based on the measured wave elevation at the probe. This probe will also measure the radiated waves, but they travel in a different direction which means that they are incorrectly taken into account for the calculation where only head waves are assumed. Another reason for the poor prediction is that the magnitude of the slamming impacts are relatively small for this condition. A small variation in relative velocity will have a large effect on the total slamming force.

The computation does not predict any slamming between 5 and 10 seconds for run 1 presented in Figure 10.11(top) where small slamming impacts are measured. The computed whipping is a result of a slamming event that occurred at an earlier time step. Due to the very low structural damping, the whipping response is still present in the acceleration signal. The amplitude of the whipping is still very comparable between the measurement and calculation.

The slamming impact and whipping response is overestimated for the $0.60[Hz]$ wave, see Figure 10.11(bottom). The computed whipping signal shows that the slamming impact at 8 seconds actually reduces the whipping response. This is caused by the fact that the present whipping response has an opposite phase with respect to the slamming loading. This effect is also visible in some measurements. As there is a small difference in measured and computed natural frequency, the phase between the present whipping response and slamming impact will not be correctly computed.

The slamming and resulting whipping is also overpredicted for the 0.64 $[Hz]$ wave and for the 0.68 $[Hz]$ wave, see Figure 10.12. However the resulting whipping response is quite close to the measurements for the 0.68 $[Hz]$ wave. The comparison of the total heave force of the shortest wave, 0.72 $[Hz]$, in Figure 10.13(top) really gives doubts about the coherence between the actual wave elevation and the wave elevation used in the computation for this case. The wave signal should have been measured without the model for this zero speed case.

10.4.2 Forward speed cases

The prediction of the slamming force and the resulting whipping response is much better for forward speed. The results for 1 $[m/s]$ are shown in Figures 10.13(bottom), 10.14 and 10.15. The computed slamming force compares very well with the estimation from the experiments. The computed whipping response is in very good agreement with the measurements for the 0.56, 0.60 and 0.68 $[Hz]$ waves and is slightly underpredicted for the 0.64 and 0.72 $[Hz]$ waves.

The slamming impacts are underpredicted for the longer waves up to 0.64 $[Hz]$ for the highest velocity of 1.5 $[m/s]$, see Figures 10.16, 10.17 and 10.18. The resulting whipping response is quite close to the measurements. The measured slamming impacts last for a time which is approximately the period of the first natural frequency of the model. This causes the last part of the slam-

ming impact to reducing the whipping response as the modal velocity is then opposite to the slamming loading. This explains why the computed whipping response is still close to the measurements even if the slamming impact is underestimated. The underestimation of the slamming impact is visible in the acceleration signals of the 0.60, 0.64, 0.68 $[Hz]$ waves. The acceleration peaks during the impact are underestimated for these waves. An explanation of the underprediction of the slamming force at this high velocity could be the planing forces which are not computed in the 2D theory used to compute the slamming forces.

10.5 Conclusions

The presented theory has been validated for the added mass, the slamming impact and whipping response using experiments with an aluminium model. The advantage of using the aluminium model is that the structural properties are well known. The computed and measured dry natural frequencies compare very well. The computed wet natural frequencies also compare well with the measured wet frequencies. This shows that the influence of the added mass is captured well by the computations. The wet natural frequencies were measured for different speeds and it was shown that the wet natural frequency, and thereby the infinite frequency added mass, is quite independent of the velocity. This indicates that it is possible to use the zero speed infinite added mass even for ships at forward speed. This assumption is often used when including the added mass in FEM computations.

Slamming induced whipping experiments are also performed using the aluminium model. The computed heave forces and accelerations at the bow were compared to the experimental values. The results for the zero speed cases are not so good. Likely, this is mainly due to the diffracted waves reflecting at the tank walls. The predictions for the forward speed conditions show good agreement with the measurements. The slamming forces at the highest velocity are slightly underpredicted. A possible explanation could be the contribution of the planing forces which are not included in the theory used.

It can be concluded that this validation shows that the presented theory is capable of accurately predicting the wet natural frequencies, slamming impact and resulting whipping response. However, it should be noted that it was necessary to impose the measured rigid-body motions to obtain these good results. The computed rigid-body seakeeping motion proved to be inaccurate for this model for very severe wave conditions.

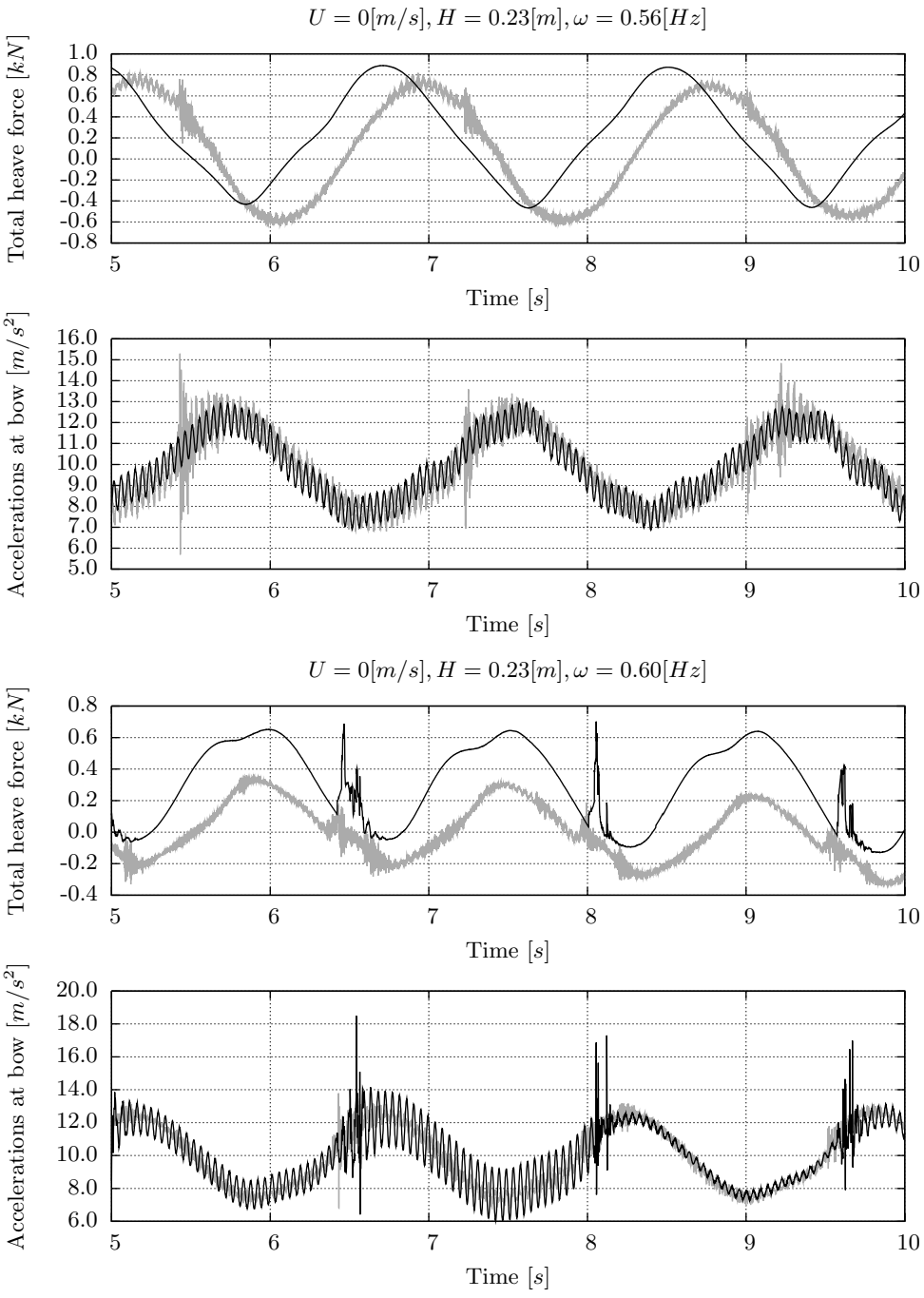

Figure 10.11: Comparison between calculated (black lines) and estimated (gray lines) heave force and comparison between calculated (black lines) and measured (gray lines) bow accelerations (a).

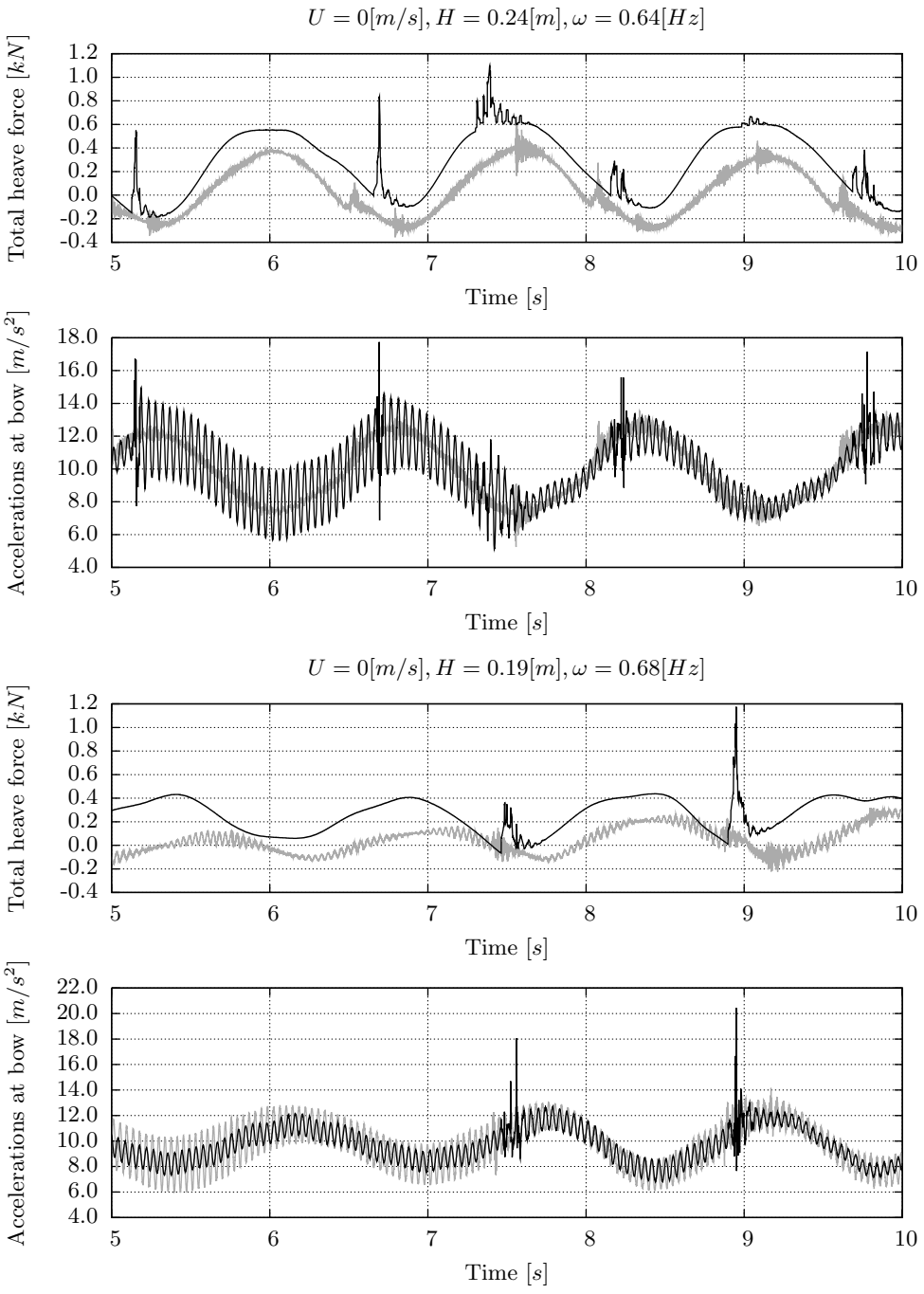

Figure 10.12: Comparison between calculated (black lines) and estimated (gray lines) heave force and comparison between calculated (black lines) and measured (gray lines) bow accelerations (b).

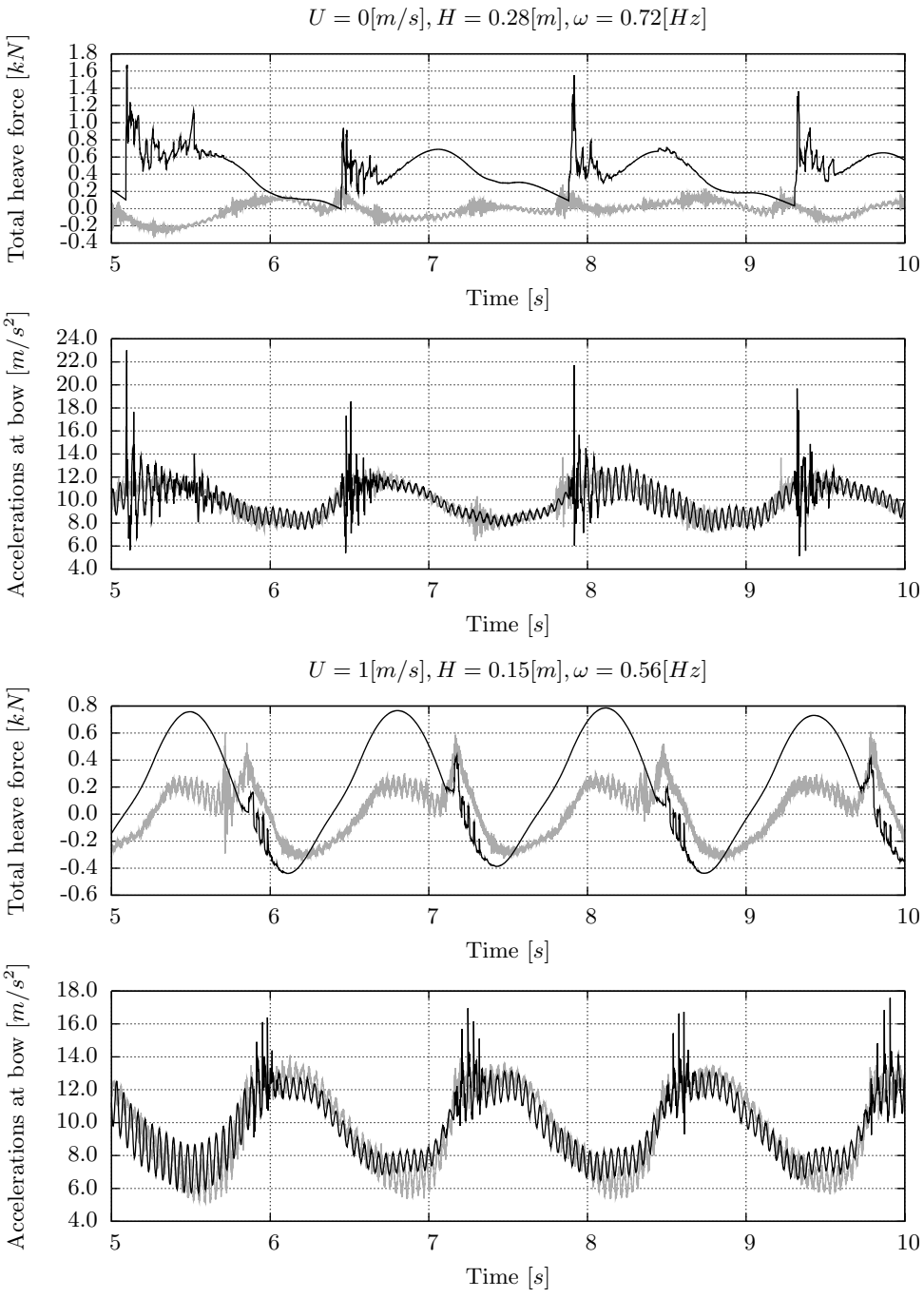

Figure 10.13: Comparison between calculated (black lines) and estimated (gray lines) heave force and comparison between calculated (black lines) and measured (gray lines) bow accelerations (c).

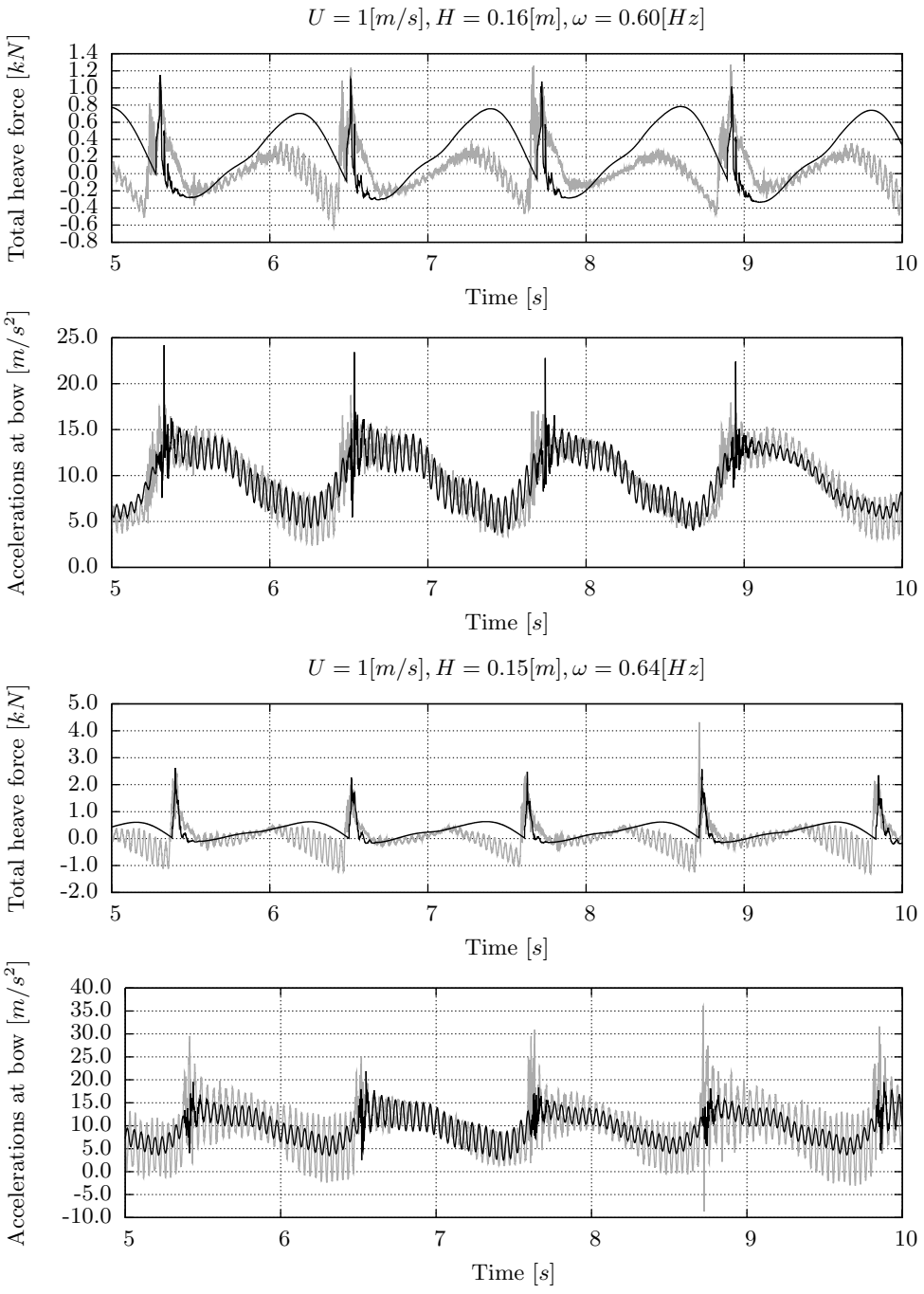

Figure 10.14: Comparison between calculated (black lines) and estimated (gray lines) heave force and comparison between calculated (black lines) and measured (gray lines) bow accelerations (d).

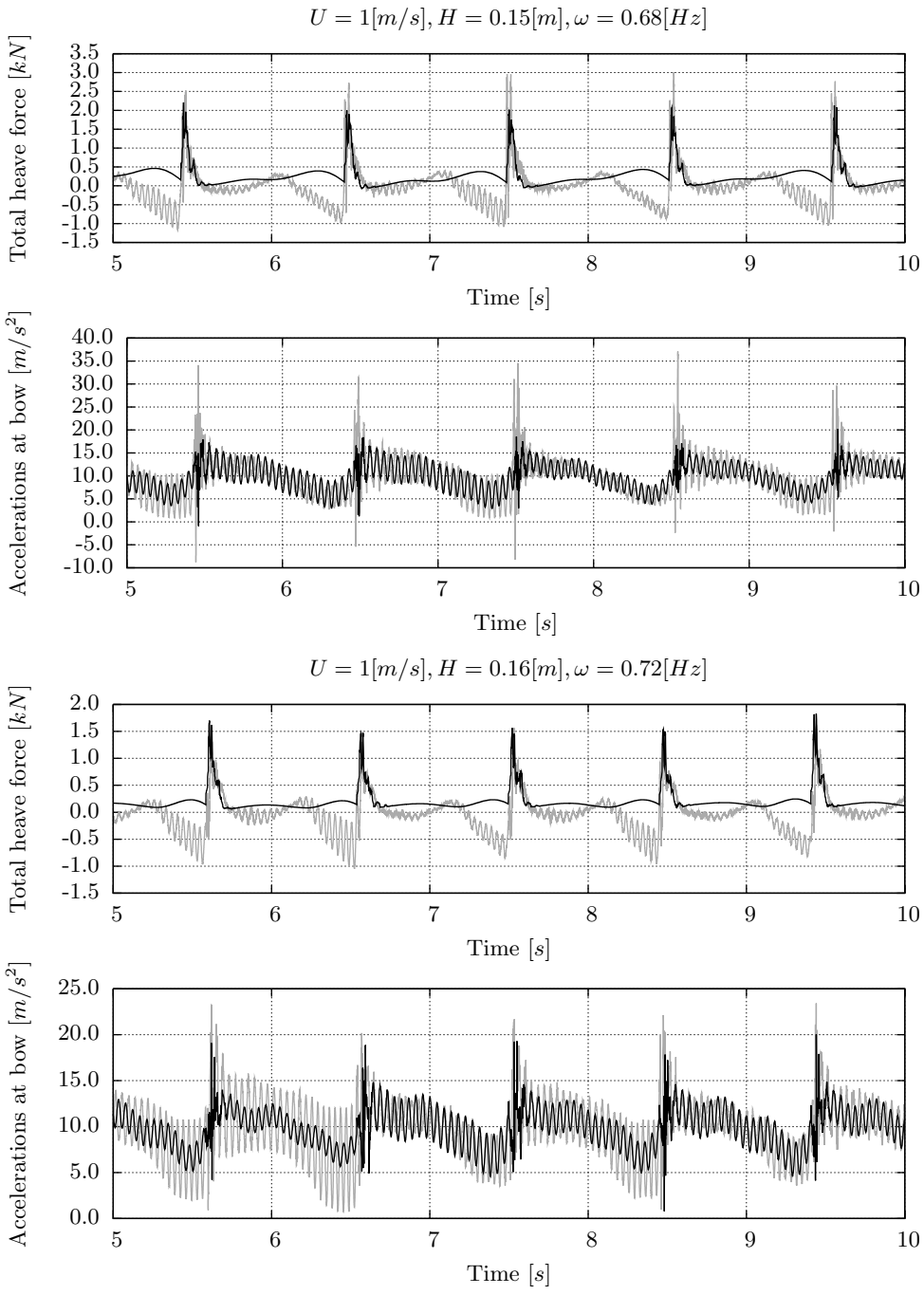

Figure 10.15: Comparison between calculated (black lines) and estimated (gray lines) heave force and comparison between calculated (black lines) and measured (gray lines) bow accelerations (e).

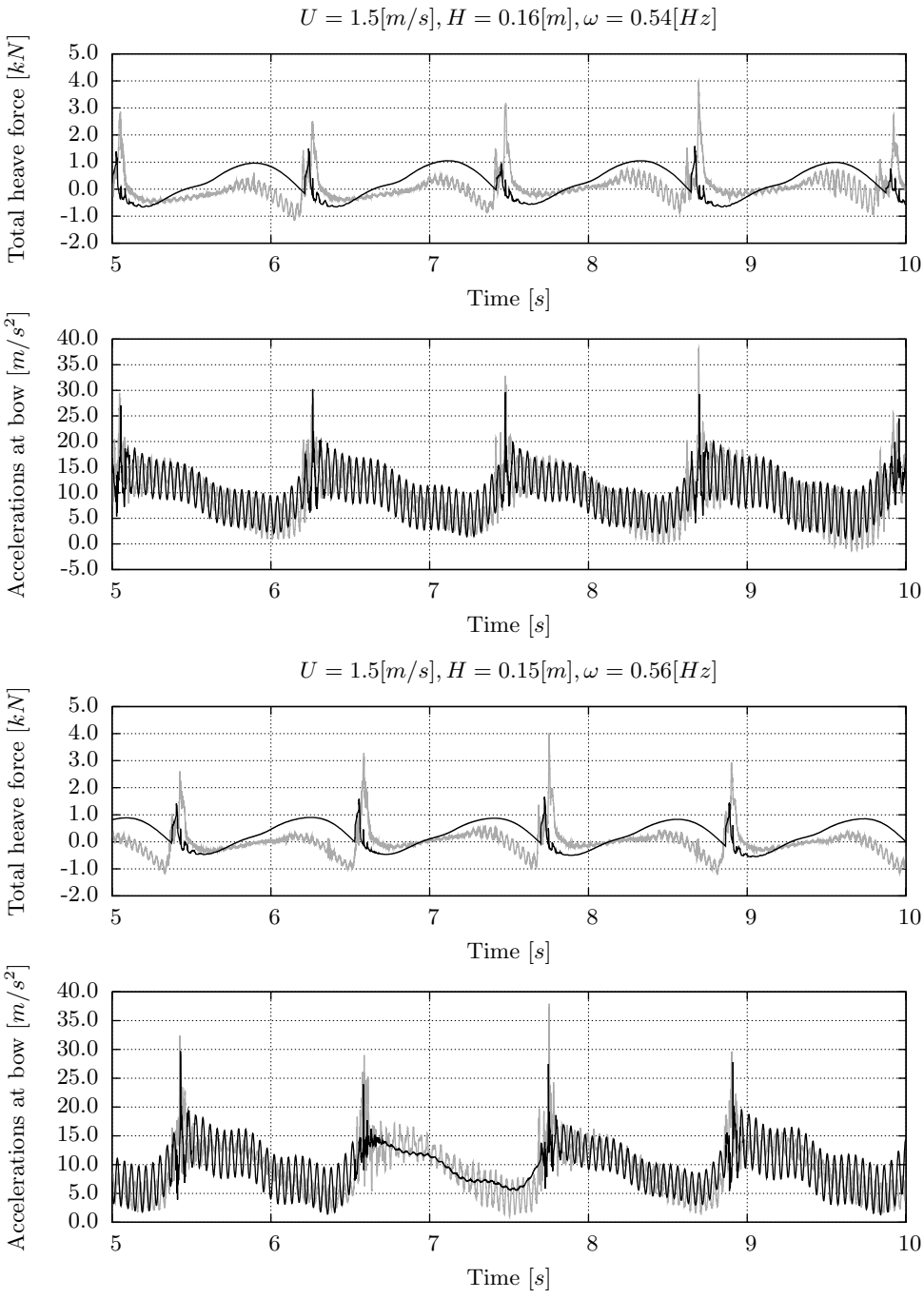

Figure 10.16: Comparison between calculated (black lines) and estimated (gray lines) heave force and comparison between calculated (black lines) and measured (gray lines) bow accelerations (f).

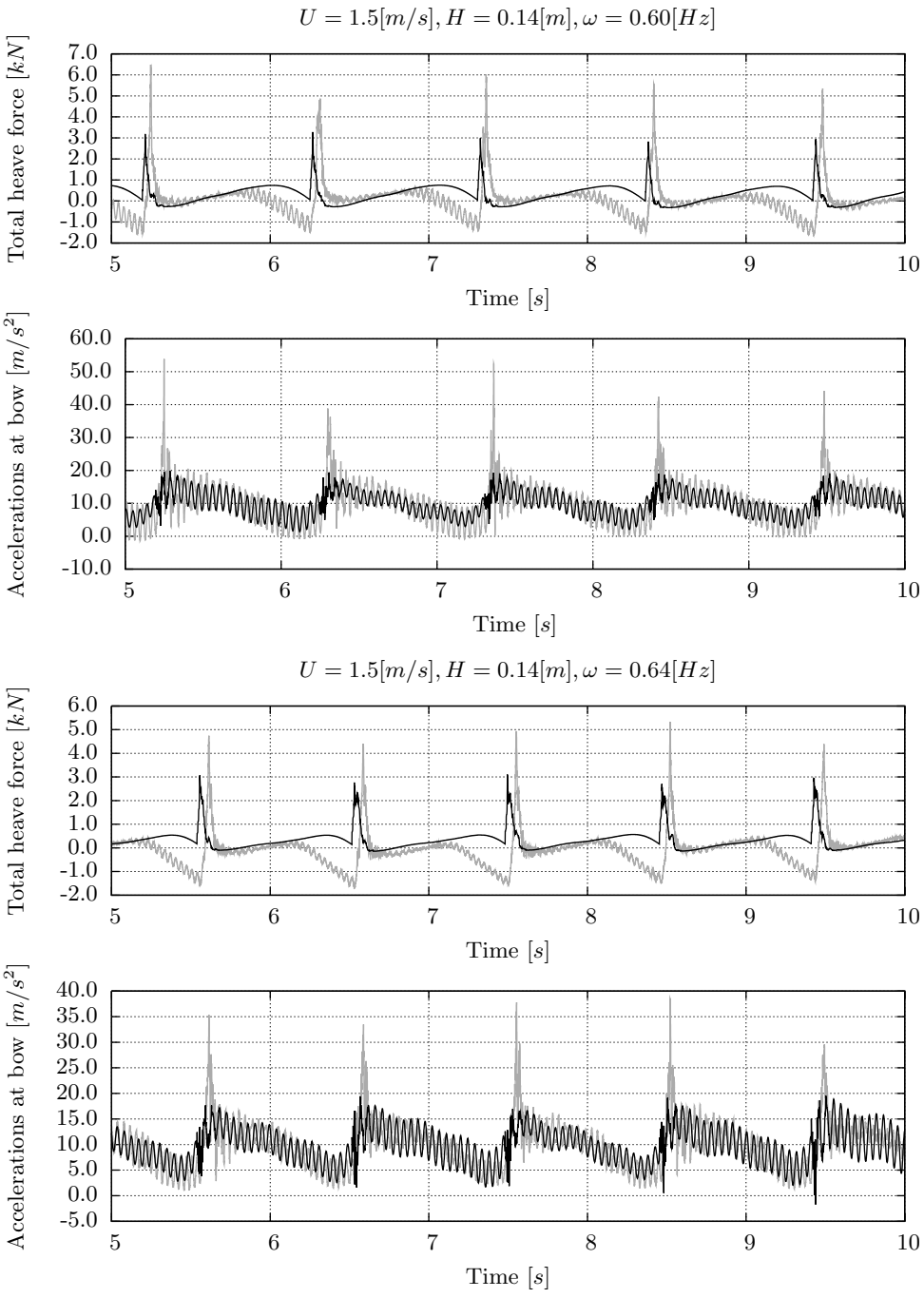

Figure 10.17: Comparison between calculated (black lines) and estimated (gray lines) heave force and comparison between calculated (black lines) and measured (gray lines) bow accelerations (g).

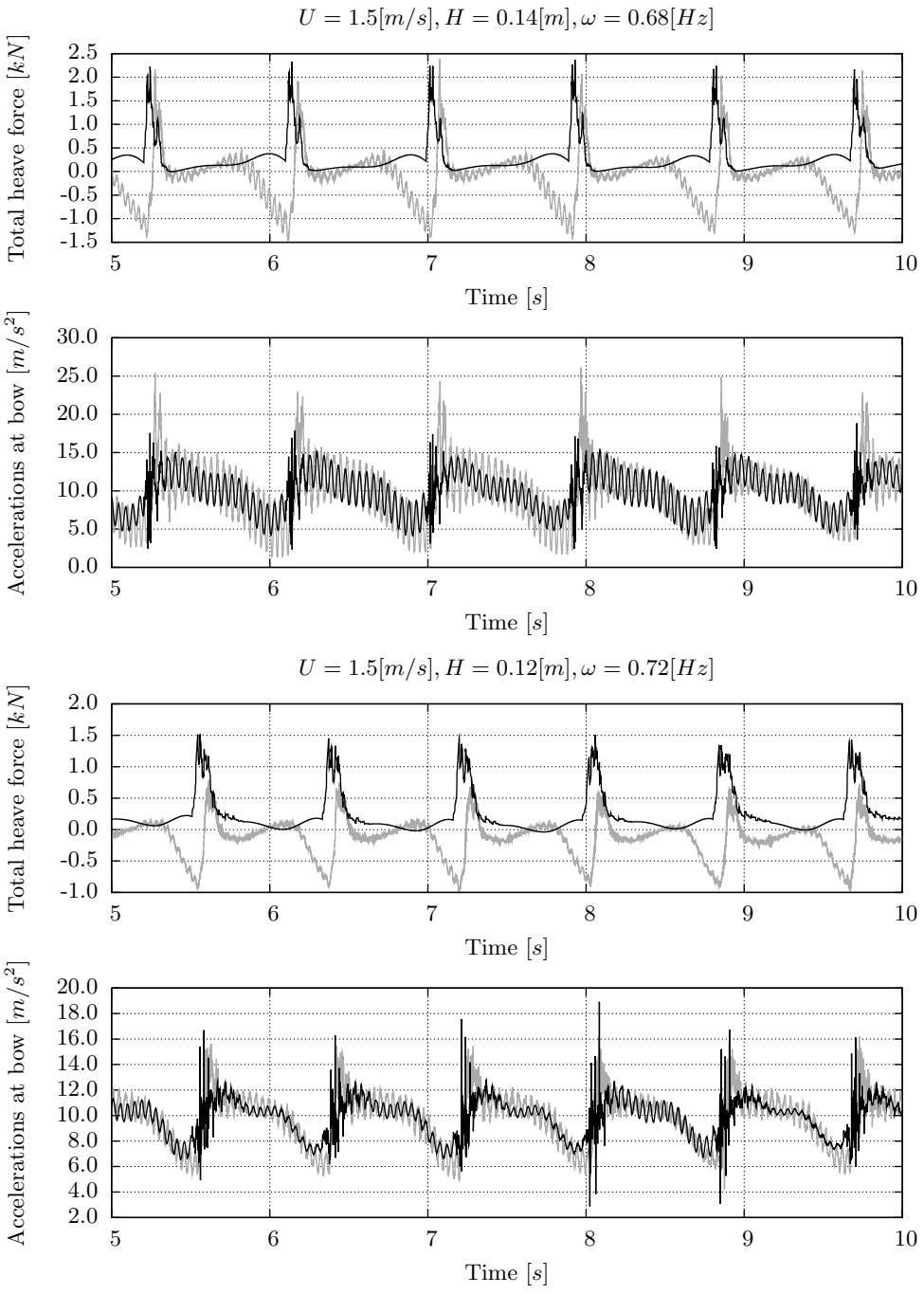

Figure 10.18: Comparison between calculated (black lines) and estimated (gray lines) heave force and comparison between calculated (black lines) and measured (gray lines) bow accelerations (h).

Chapter 11

Slamming measurements on a container vessel

The slamming loads on the bow of a container vessel have been measured during model experiments for regular and irregular head waves. The presented theory is validated using these experimental results. Also some verification is carried out using this ship which is much smaller than the two container ships presented in Chapter 8.

A full description of the model experiments can be found in [15]. The characteristics of the model and the real ship are given in Table 11.1. The experimental setup is shown in Figure 11.1. The model is free in heave and pitch direction but constrained in the other four directions. The upper bow section, dashed in Figure 11.1, is connected by a force transducer to the model. This allows to measure the total force on the bow section. The accelerations of the bow section are also measured and the inertial forces are subtracted from the measured forces to obtain the external force solely on the bow section. The external force is also measured at section 18, which is the other dashed section in Figure 11.1, using the same approach.

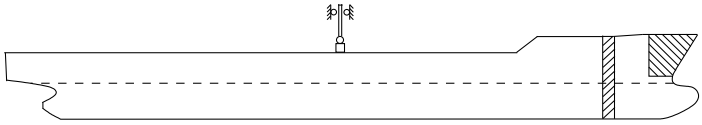

Figure 11.1: Experimental setup.

The integration mesh, which is based on the hydrodynamic mesh, of the ship is shown in Figure 11.2. The different gray scales indicate the sections as

Most calculations presented in this chapter have been performed by Niels Mallon. A more detailed validation report can be found in [32].

		Model	Ship at full scale
Nominal displacement	∇	1200 $[kg]$	21618 $[t]$
Length between perpendiculars	L_{pp}	5.84 $[m]$	151.9 $[m]$
Beam	B	1.069 $[m]$	27.8 $[m]$
Draught	T	0.317 $[m]$	8.25 $[m]$
Vertical distance of the centre of gravity from OH (baseline)	VCG	0.3 $[m]$	-
Longitudinal distance of the centre of gravity from AP	LCG	2.836 $[m]$	73.76 $[m]$
Inertia	K_{yy}/L_{pp}	0.25 $[-]$	0.25 $[-]$

Table 11.1: Characteristics of the model.

defined in the ship model. The cut planes used to create the sections are located at the boundaries of the sections used to measure the slamming forces during the experiments. As only planes can be used to create sections, the forces at the two small sections have to be added to obtain the total force at the section 18. The 2D slamming sections and scaled normals are shown in Figure 11.3. The ship is modelled as rigid-body.

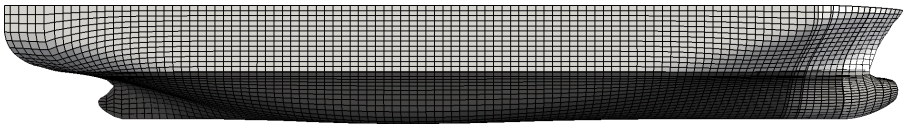

Figure 11.2: Integration mesh for container ship.

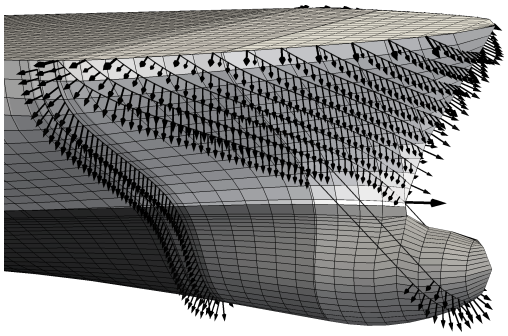

Figure 11.3: Slamming sections and scaled normals.

A few verifications of the calculated slamming force are presented in the first part of this chapter. The calculated slamming forces are validated using

the experimental results from the model in the second part of this chapter.

11.1 Verification of calculated slamming loading

This section presents verifications of the calculated slamming forces. The same kind of verification is also presented for the two large container ships in Chapter 8.

The slamming force at the whole bow starting from section 18 is compared for all verifications. As this part of the bow is not fully covered by the 2D slamming sections presented in Figure 11.3, additional 2D slamming sections are added for these verifications.

11.1.1 Tilting angle of slamming sections

The first verification considers the sensitivity of the computed slamming forces with respect to the chosen tilting angle of the 2D slamming sections. Figure 11.4 shows the slamming force calculated for different tilting angles.

When using the GWM the calculated slamming force is reasonably independent of the tilting angle used. It seems best to avoid using vertical sections of 90 degrees. The MLM method is much more sensitive to the tilting angle compared to the GWM method. This sensitivity can be explained by the bulbous bow which violates the MLM assumptions. By tilting the sections, more sections will include the bulb part. The sensitivity of the MLM method is also caused by a less accurate pressure description. The MLM uses a flat plate assumption. The pressure at this plate is projected onto the sections, see Section 5.3.5. This results in a less accurate pressure distribution when using the MLM method which results in a less accurate slamming force when using the MLM method.

11.1.2 Time step

The coupling between the seakeeping and slamming program should ensure that the slamming impulse is correctly transfered regardless of the time step used. This was already shown for the large container ship in Section 8.2.5.

The same verification is now repeated for this rigid ship. Using a rigid ship allows for a larger stable time step for the explicit integration scheme. Figure 11.5 shows the calculated vertical slamming force. This force is integrated over time to obtain the corresponding impulse, see Figure 11.6. The total slamming impulse remains about the same for time steps up to 0.4 $[s]$ using the GWM method. The peak of the relative velocity curve is missed when using a large time step which causes the calculated slamming impulse to decrease. The time step of 0.4 $[s]$ is usually larger than the maximum stable time step when the elastic modes are included for a whipping calculation. The slamming calculation

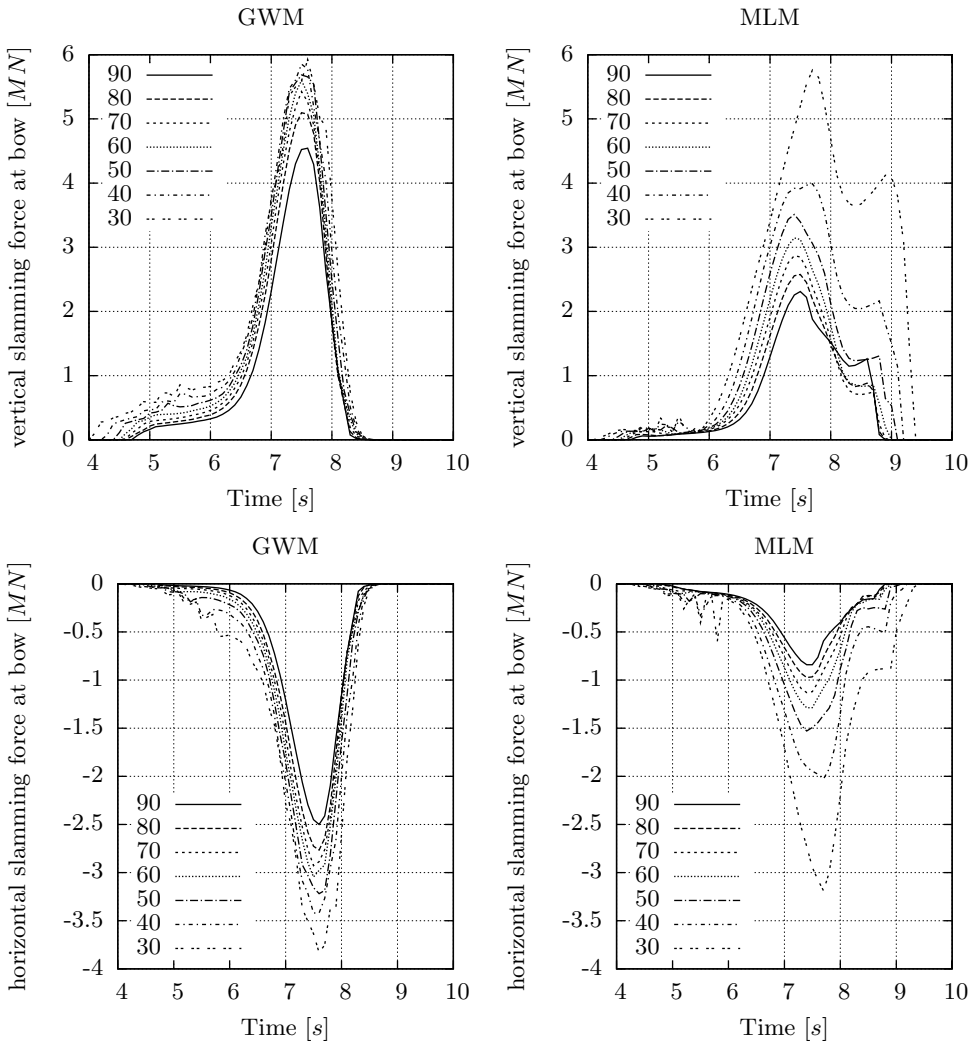

Figure 11.4: Slamming force using different tilting angles for the slamming sections.

using the MLM method converges less well for the small time steps because the calculated force is partly dependent on the accelerations of the previous Runge-Kutta step, see Section 5.3.5. This approach becomes less accurate when increasing the time step.

11.1.3 Sensitivity to relative motion

The sensitivity of the calculated slamming force to small changes in the computed ship motions is now investigated. The slamming loads scales approxi-

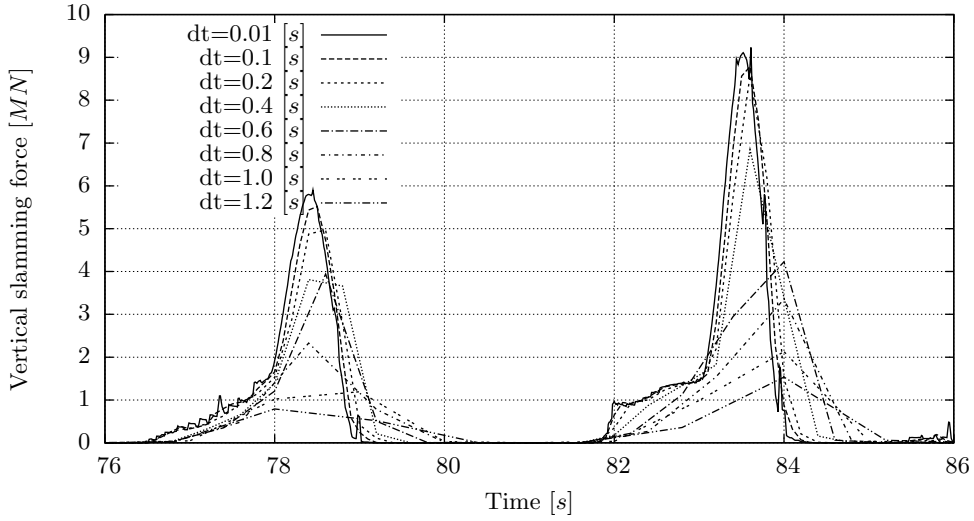

Figure 11.5: Slamming force using different time steps in the seakeeping calculation using the GWM method.

mately with the square of the relative velocity. This should make the slamming force very sensitive to changes in the relative motions.

To get an insight into this sensitivity, the slamming force is computed for the same wave but with small changes in the motions of the ship. The computed ship motions are varied by changing the main diagonal stiffness or damping value for the heave or pitch motion. The resulting heave and pitch motions and the calculated slamming forces are shown in Figure 11.7.

The computed slamming force changes only slightly with the small changes in the heave motion. The small variations in the pitch motions, however, causes significant changes in the computed slamming forces. This difference in sensitivity to the heave and pitch motions is expected as the pitch motions contribute much more to the relative velocity at the bow than the heave motion does. The large sensitivity of the calculated slamming force towards the relative motions shows the importances of an accurate ship motion prediction when calculating the slamming loads.

11.2 Validation of calculated slamming forces

The measured and calculated slamming forces are compared in Figures 11.8 and 11.9 for regular waves and in Figure 11.10 for irregular waves. The slamming forces are computed using the GWM method. The measured motions are imposed in the seakeeping calculation to ensure that the slamming forces are

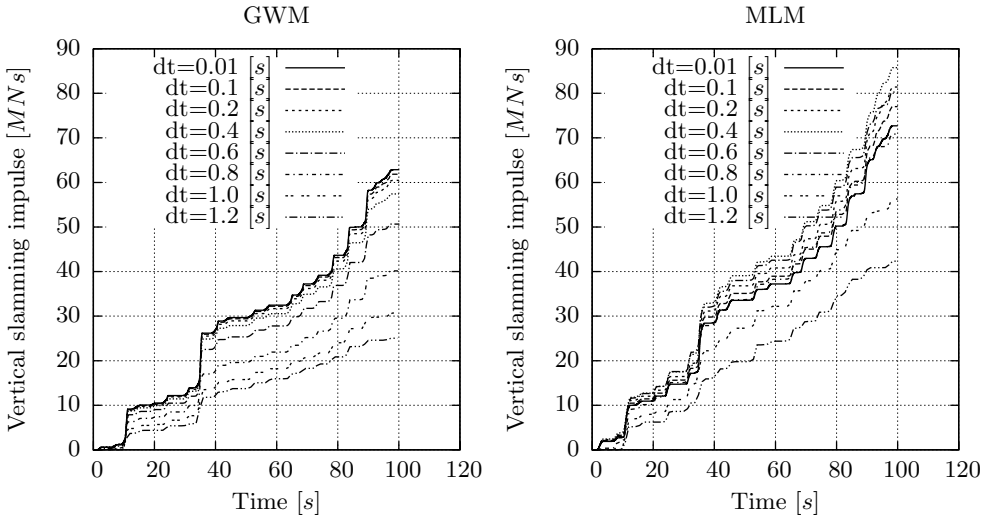

Figure 11.6: Slamming impulse using different time steps in the seakeeping calculation.

calculated using the same relative motions as found during the experiments. Note that the prediction of the rigid-body motions is reasonably accurate for this ship using the presented theory. However, any variation in the relative motion will make the validation of only the slamming force more difficult.

All components of the hydrodynamic forces are present in the total force at the section. The slamming contribution is the sharp small peak seen on top of the broad peak in the calculated force curve. The broad peak is caused by the non-impulsive, wave frequency, hydrodynamic forces.

The slamming forces at the bow section are underpredicted, especially for the 25 knots cases, see Figure 11.9. An explanation for this underprediction could be that there is in reality an additional uprise of the free surface due to the bow wave. The bow of this vessel is quite flared and a significant bow wave will form if the ship would sail in still water at 25 knots with a draught which is equal to the maximum relative displacement during the slamming events. This effect is not included in the slamming calculations as the theory used to calculate the slamming forces is based on drop tests without forward velocity.

An engineering approach is used to investigate if the missing bow wave could explain the underprediction of the slamming forces. MARIN has kindly calculated the static bow wave for five different draughts with their program RAPID. The wave height for the relative motion calculation is changed using this static bow wave. The relative displacement based on the original wave height is calculated first. The equivalent "draught" is computed and linear interpolation is used to obtain the height of the static bow wave for the current

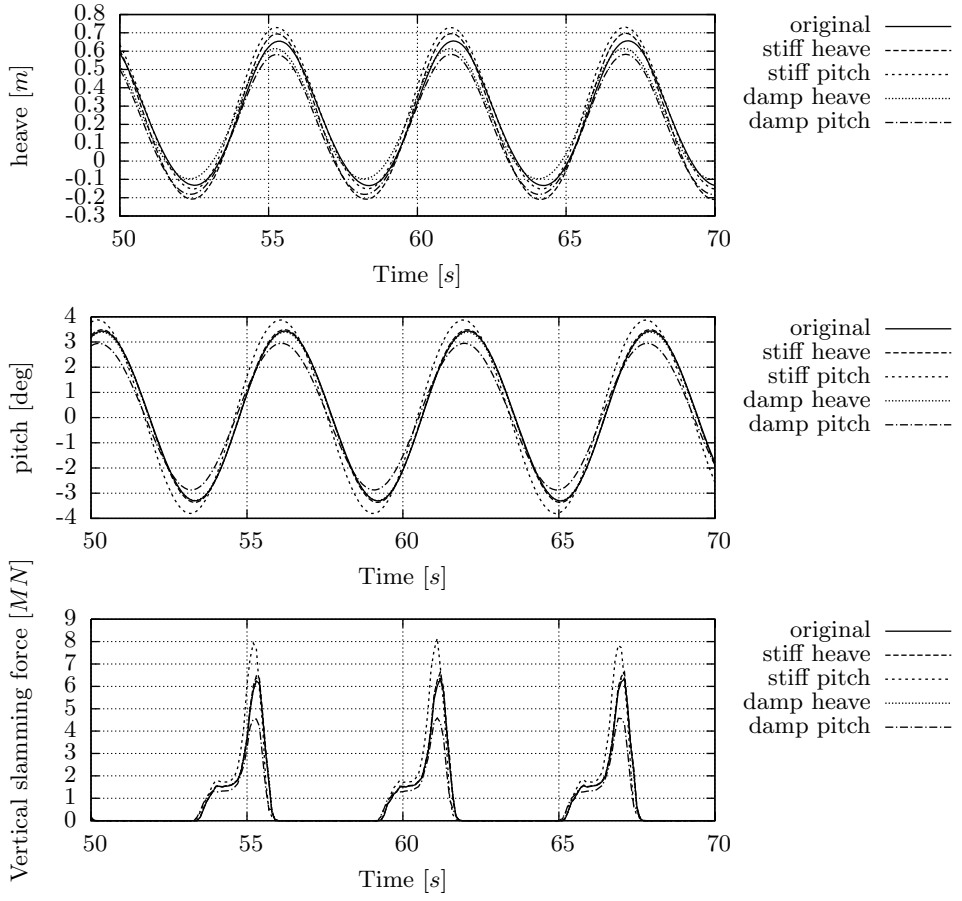

Figure 11.7: Slamming force with small differences in relative motion. Slamming computed using the GWM method.

relative displacement at that location where the slamming forces are computed. This static bow wave elevation is added to the original wave height and is used for the calculation of relative motion used for computing the slamming forces. The results of this approach are also presented in Figures 11.8, 11.9 and 11.10. This approach turned out to be unstable for the forces at section 18 for the 25 knots case. This is due to the fact that the static bow wave height is actually decreasing for increasing draughts at section 18. The unstable results are not shown in the Figures. Note that this static bow wave was not an issue in the validation using the aluminium model presented in the previous chapter as these impacts were more bottom slamming instead of bow flare slamming as is the case for this ship.

The comparison with the experiments, which are presented in Figures 11.8,

11.9 and 11.10, show that the inclusion of the static bow wave improves the prediction of the slamming force at the bow significantly. However, the predicted slamming forces at the bow section are still lower than found in the experiments. The prediction using the bow wave is reasonable but the total impulse of the slamming event is still too low. A possible explanation are the missing planing forces from 2D approach used for computing the slamming loads.

The force at the bow is overestimated after the slamming event. This is probably due to the so-called exit phase of the slamming. The slamming computation presented in this thesis does not account for this exit phase.

The non-impulse hydrodynamic forces are overestimated for section 18. The measurements show no impulsive loading for the zero speed case where the calculation predicts some slamming force. The prediction of the slamming loading for the 25 knot cases seems quite good while the slamming loading is overestimated at 15 knots.

11.3 Conclusions

The verification using this 152 $[m]$ container ship shows good results. The slamming forces computed with the GWM were shown to be quite independent on the tilting angle of the 2D slamming section as selected by the user. The slamming force computed by the GWM method is converged for the time steps normally used for the seakeeping calculations. The performance of the MLM method is less good for both the sensitivity towards the tilting angle of the 2D slamming sections and the time step used in the seakeeping calculation.

The last verification showed that the computed slamming force is very sensitive with changes in the calculated seakeeping motions, especially the pitch. This sensitivity was expected, but it illustrates the importance of an accurate seakeeping computation.

The calculated slamming forces at the bow are compared with experimental results for both regular and irregular waves. The comparison showed that the slamming forces are significantly underpredicted at forward speed. An explanation of this effect may be the static bow wave due to the velocity. Including the static bow wave improved the calculation results significant. However, the slamming forces at the bow section are still underpredicted slightly which could be explained by the missing planing forces.

It can be concluded that the verification showed that the GWM slamming computation performs better than the MLM method. The validations show that the slamming forces are computed with reasonable accuracy when the relative velocity input is correct. The static bow wave needs to be taken into account for this ship to obtain an accurate relative velocity prediction used for the slamming computation.

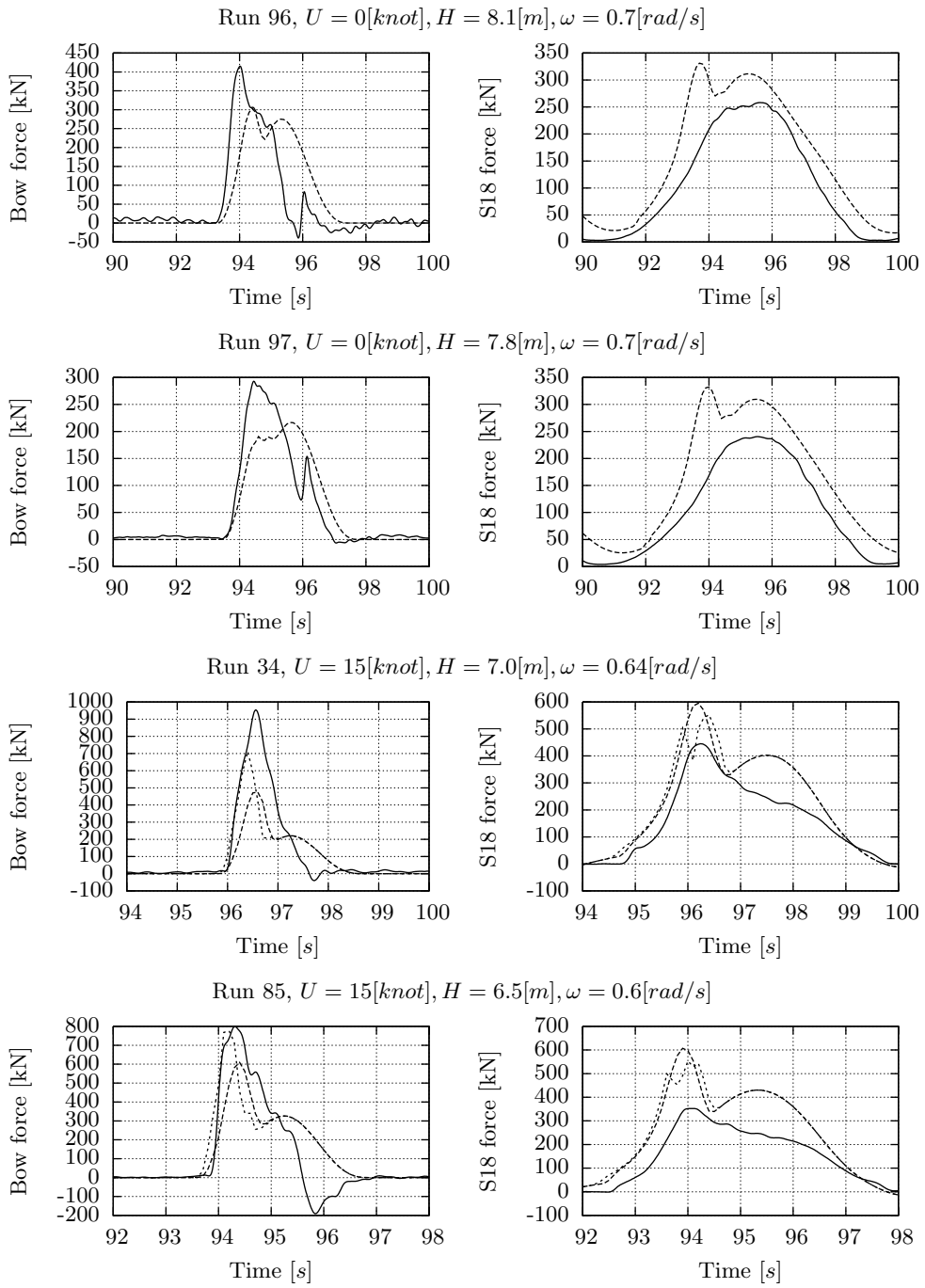

Figure 11.8: Comparison between measured and calculated slamming force in regular waves (a). Measurements are solid lines, calculations long dashed lines and calculations with additional static bow wave short dashed lines.

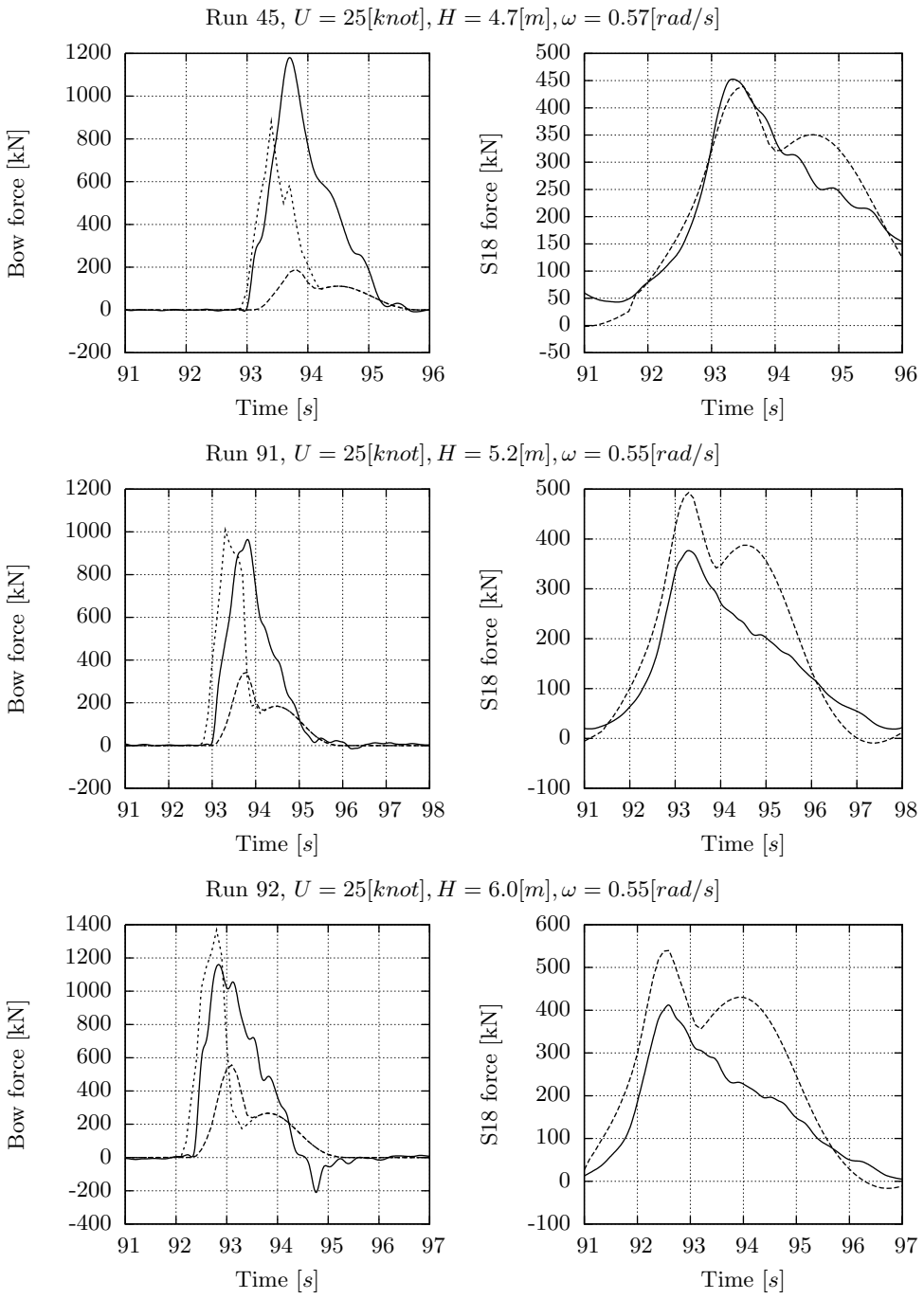

Figure 11.9: Comparison between measured and calculated slamming force in regular waves (b). Measurements are solid lines, calculations long dashed lines and calculations with additional static bow wave short dashed lines.

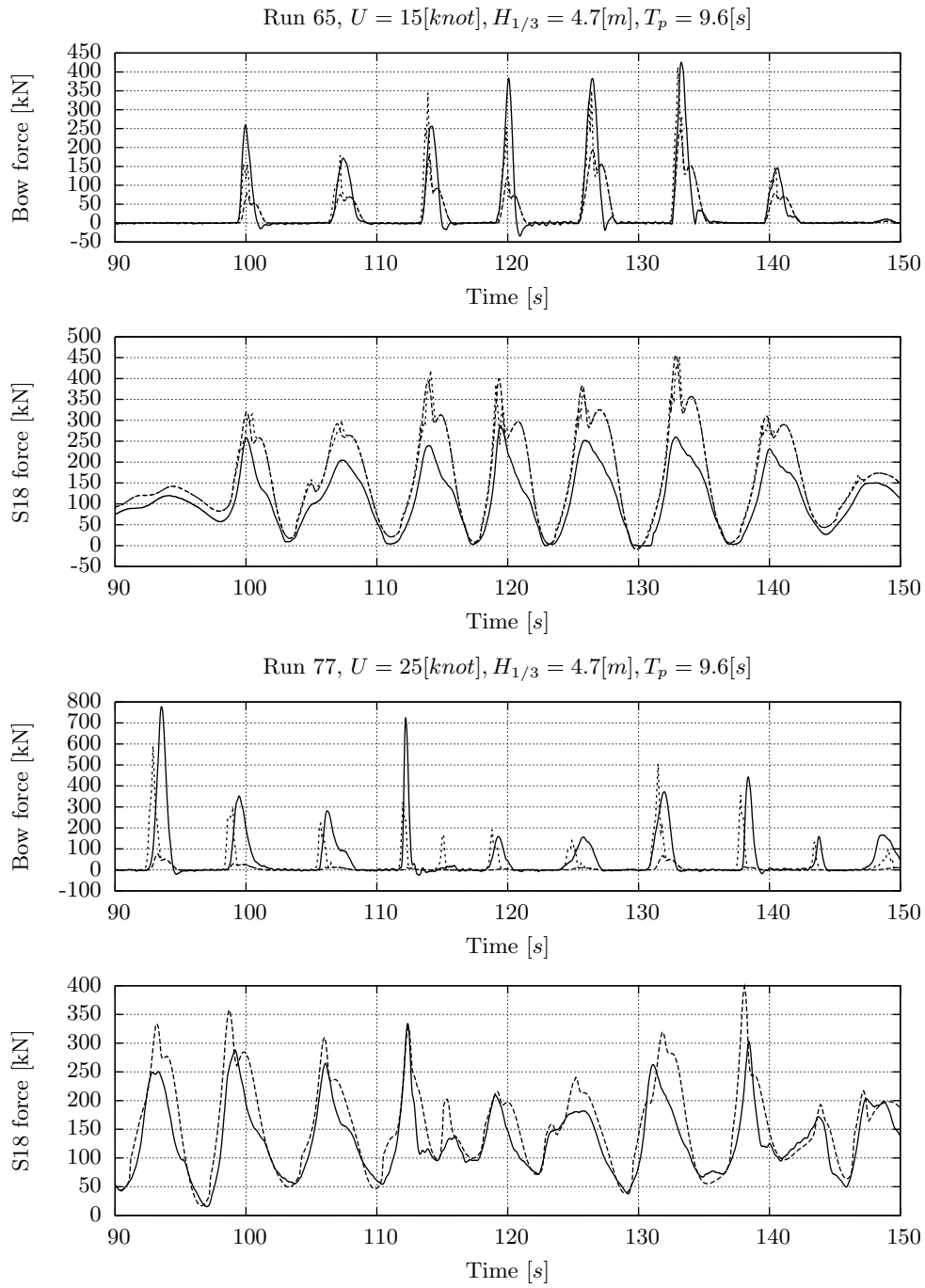

Figure 11.10: Comparison between measured and calculated slamming force in irregular waves (c). Measurements are solid lines, calculations long dashed lines and calculations with additional static bow wave short dashed lines.

Chapter 12

M-frigate

The multi-purpose frigate (M-frigate) of the Royal Netherlands Navy (RNlN) is used in this chapter for verification and validation of the presented theory. The M-frigate has a displacement of about 3300 tons and has a maximum velocity of 29 knots [61]. The length over all is 122 metre and the maximum beam is 14.4 metre. Figure 12.1 shows a photograph of the Hr. Ms. Karel Doorman which is one of the eight M-frigates.

Figure 12.1: M-frigate Hr. Ms. Karel Doorman, (source RNlN).

The structural 3D-FEM model of the M-frigate has been provided by the RNlN. Figure 12.2 shows this structural mesh and also the hydrodynamic mesh used for the presented computations. The program used for creating the hydrodynamic mesh is not able to model the shear of the deck correctly. The deck of the hydrodynamic mesh is a bit too high due to this. This will only affect the seakeeping calculation if the water reaches the deck which will only be the case for very severe seas.

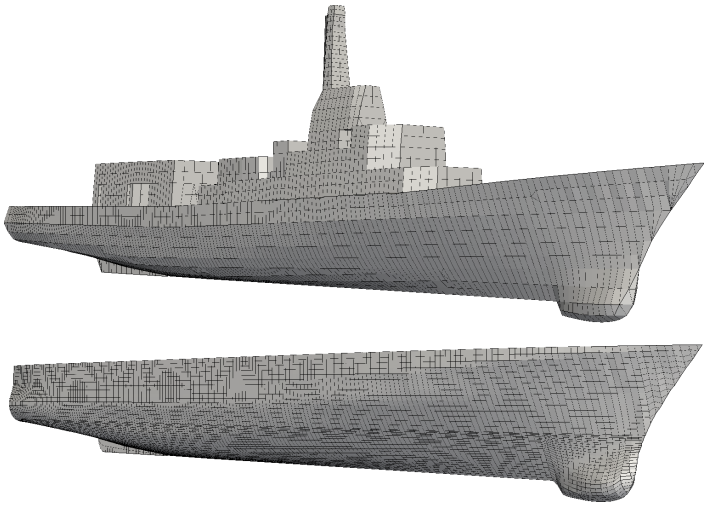

Figure 12.2: Structural and hydrodynamic mesh of M-frigate.

The first eleven elastic mode shapes found in the 3D-FE analysis are included in the seakeeping calculation. The stress at the desired location is obtained by multiplying the calculated modal amplitudes with the participation factors for the stress in the longitudinal direction, computed by the 3D-FE program.

A structural damping of 2% of the wet critical damping is assumed for the first two elastic modes, 3% is assumed for the third and fourth mode and 4% is assumed for the other modes. The time signals of the stress for a measured slamming event[1] and for a calculated slamming event, respectively, are shown in Figure 12.3. Both events are due to a different wave-train, as the encountered wave train during the trial is unknown. The signals cannot be the same due to the difference in wave-trains, but it shows that the damping of the whipping response in the calculation is reasonably close to the experimental trend.

The first part of this chapter presents a verification of the calculation of the load cases for the structural model as is described in Chapter 6. A validation of predicted stress in the deck using the results of a full scale sea trial is presented in the second part of this chapter.

12.1 Seakeeping load case for the structural model

The loading and response of the M-frigate is calculated for an extreme sea state with a significant wave height of 8 metres and a peak period of 8 seconds using

[1]This is a measurement of the full scale trails as described in the second section of this chapter.

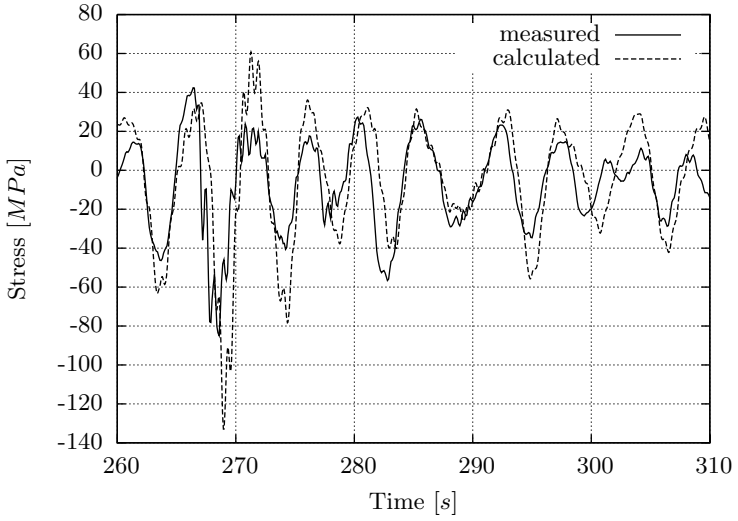

Figure 12.3: Measured and calculated stress signal for different wave-trains for the 12 knots run.

the JONSWAP spectrum. This severe sea-state ensures that the pitch motions are large enough to cause a difference between the reference frames. Otherwise, the transformation between the different reference frames used to compute the loading at the FE model would not be tested. The frigate has a velocity of 12 knots and is heading towards the incoming waves for the computations presented in this chapter. The frequency domain surge, sway and yaw are imposed by using kinematic constraints.

The response will be computed using three approaches. The first approach is the normal seakeeping computation. The second approach is performing the seakeeping computation using the structural mesh. The last approach is transferring the seakeeping loads to the structural model and solving the response within the FE package. The computation of the seakeeping forces using the structural mesh is investigated in the first part of this section. The second part presents the seakeeping calculations. The last part of this section presents the results of the structural response calculation.

12.1.1 Hydrodynamic coefficients at structural mesh

When computing the seakeeping loads at the structural mesh, to solve the response within the FE-solver, it is also used as the integration mesh in all computations. The hydrodynamic pressure at the structural mesh and the resulting coefficients are computed using the translated dummy Gauss points, see Section 2.8.1. It is first investigated if this approach, which avoids interpola-

tion of pressures between the hydrodynamic and structural mesh, is consistent before computing the loading at the structural mesh.

The dummy Gauss points are translated such that they are located just outside of the hydrodynamic mesh. The distance between the hydrodynamic mesh and the dummy Gauss points are normally set to $0.001\sqrt{A_a}$, with A_a the average area of the hydrodynamic panels. Figure 12.4 shows the translation of the dummy Gauss points at the sonar dome of the frigate. The distance between the hydrodynamic panels and the Gauss points is increased by a factor of ten for a better visualisation. The figure clearly shows that all Gauss points are translated in the correct direction and the translations remain small. This indicates the correctness of the translations procedure as described in Section 2.8.1.

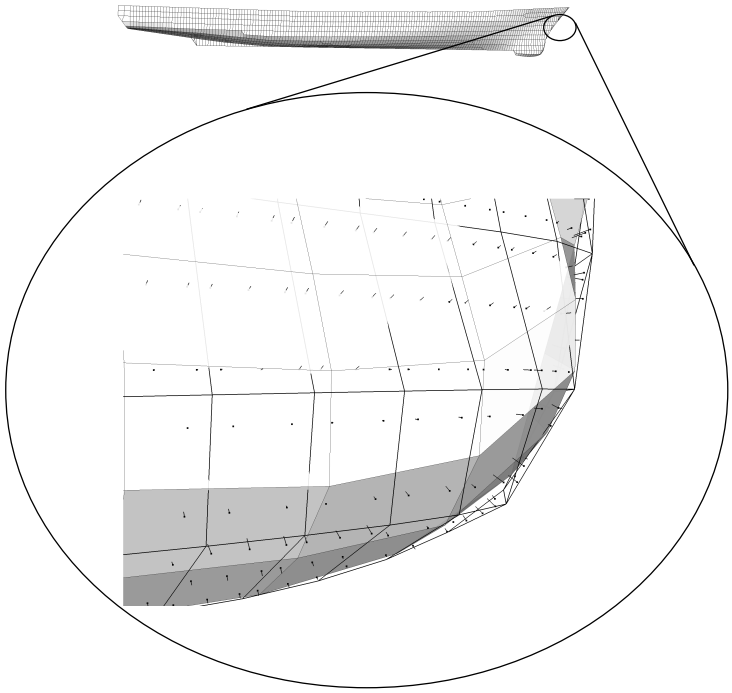

Figure 12.4: Translation of dummy gauss points. Gray coloured mesh is the hydrodynamic mesh and the wire frame indicates the structural mesh. The dots are the original Gauss points and the lines indicate the translation.

The approach used for computing the pressures at the structural mesh assumes that the pressure can be computed at every location as long as it is outside the hydrodynamic mesh. One could argue that the potential, and thereby the resulting pressures, is not continuous very close to the hydrodynamic panels since a constant source strength is defined at the hydrodynamic panels.

This is investigated by computing the pressures at many locations over the hydrodynamic mesh. Sixteen Gauss points are used for every structural panel in order to obtain a large number of points where the pressures is evaluated. The surge radiation pressure at the sonar dome is presented in Figure 12.5. This pressure component has a large gradient at the sonar dome which should help reveal any discontinuities in the pressure distribution due to the hydrodynamic mesh. The pressure for 1 $[rad/s]$ at 5 $[m/s]$ forward velocity is presented. The results shows a smooth distribution of the pressure. This shows that the pressure can indeed be computed everywhere as long it is outside of the hydrodynamic mesh.

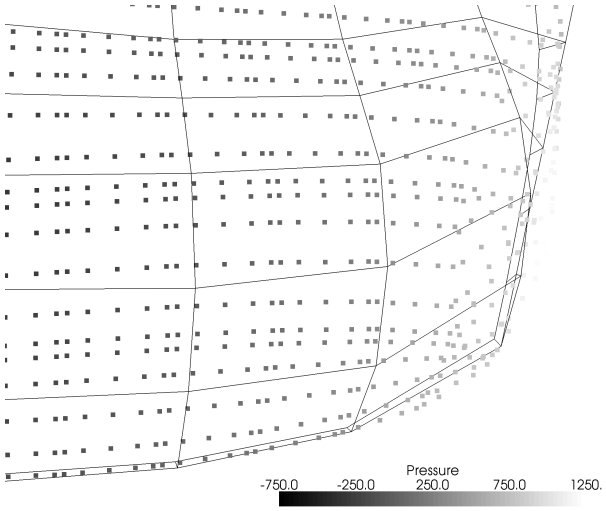

Figure 12.5: Surge radiation pressure computed at Gauss points of the structural mesh. The wire frame is the hydrodynamic mesh, the structural mesh is not shown here.

The dummy Gauss points cannot be translated such that they are exactly at the hydrodynamic mesh as that is the location of discontinuity of the gradient of the potential. However, evaluating the pressures at some distance from the hydrodynamic mesh will change the resulting pressure and hydrodynamic coefficients. This sensitivity is investigated by computing the hydrodynamic coefficients when evaluating the pressure at different distances from the hydrodynamic mesh. The results computed for 1 $[rad/s]$ and 5 $[m/s]$ forward velocity are presented in Figure 12.6. The resulting coefficients are divided by the coefficients computed using only the hydrodynamic mesh and not the structural mesh. The results show that the computed coefficients decrease slightly when the pressures are evaluated at larger distance from the hydrodynamic mesh. A decrease could be expected, but the results shows that the decrease is not significant. The results also shows that the lines are smooth, so there is no

numerical problem at any of the investigated distances. Using a distance of $0.001\sqrt{A_a}$ will result in about $0.005[m]$ in this case. The results are nearly converged at this distance.

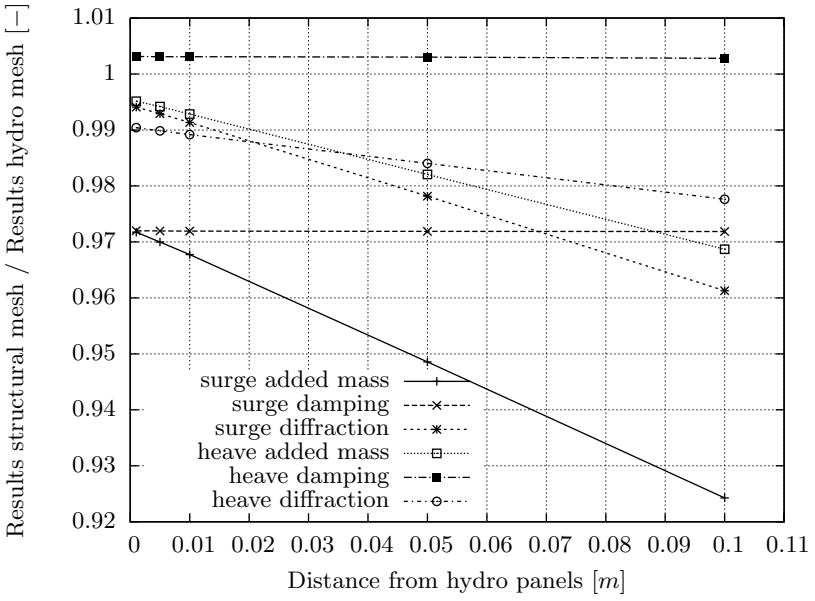

Figure 12.6: Sensitivity of computed hydrodynamic coefficients with respect to variation in distance of the pressure evaluation.

12.1.2 Seakeeping calculation

The seakeeping loading and response is calculated for the same wave-train using three different methods:

Hydro seakeeping This is the normal, or classical approach, to calculate the time domain non-linear seakeeping response of the ship. The hydro mesh is used in all steps of the seakeeping calculation. The structural mesh is not used in this case except for projection of the mode shapes onto the hydrodynamic mesh.

Struct seakeeping The hydro mesh is used to solve the BVP and the structural mesh is used for integrating the hydrodynamic coefficients and for calculating the non-linear terms in the time domain calculation for this seakeeping calculation.

Struct FEM This is the calculation or reconstruction of the nodal forces at the structural mesh. These nodal forces are used as load cases to compute

the structural response using the FE method. The summation of these nodal forces are presented as result of this calculation. There are no motion results for this calculation because it is a post-processing of the motions of the structural seakeeping calculation. The structural forces should be almost identical to the forces found in a structural seakeeping calculation.

The mass distribution of the structural (FEM) model is used for all calculation methods. This ensures that any difference in response can only be caused by differences in the calculated loading.

The different force components in the heave direction can be found in Figure 12.7. Figure 12.8 shows the total loading for the heave and pitch modes. The resulting heave and pitch motions are shown in Figure 12.9. The accelerations are not shown as the mass distribution used is the same for all methods, the difference in acceleration is identical to the differences in total force.

The hydrodynamic loading and resulting motion calculated using the different methods are very comparable. The diffraction force, equation (6.7), is identical for all methods. This force depends only on the location of the ship, which is the same for all methods as the frequency domain surge, sway and yaw are imposed. Obtaining the same diffraction force proves that integration of the hydrodynamic coefficients over different meshes gives consistent results.

There are small differences in the calculated motion between the seakeeping calculation with the hydro and structural meshes. These differences are caused by differences in one or more force components. However, as soon there is a difference in the resulting motion, there will occur a difference in the slamming, Froude-Krylov, hydrostatic, gravity and radiation loading as these depend on the computed motion. The gravity loading depends only on the mass distribution and the orientation of the ship, so this component will not cause the differences in motion. The linear hydrodynamic coefficients are almost identical for all methods, as already shown for the diffraction force. The radiation force is also based on the linear hydrodynamic coefficients and will result in an almost equal force if the motions would be equal. The most likely cause of the difference in motions are the Froude-Krylov and hydrostatic loading. Due to the difference in geometry of the deck, see Figure 12.2, the calculated loads will show small differences. Note that in this severe sea-state the deck is sometimes wetted.

A Fourier transform, equation (6.4), together with a frequency reconstruction, equation (6.5), is used to calculate the nodal retardation force. This approach avoids the calculation and evaluation of the retardation functions for every node, which saves a lot of computation effort. The retardation functions are used to compute the modal forces in the time domain seakeeping calculations. Figure 12.7 shows that there is a large difference in the computed nodal structural and seakeeping radiation forces at the start of the calculation. The

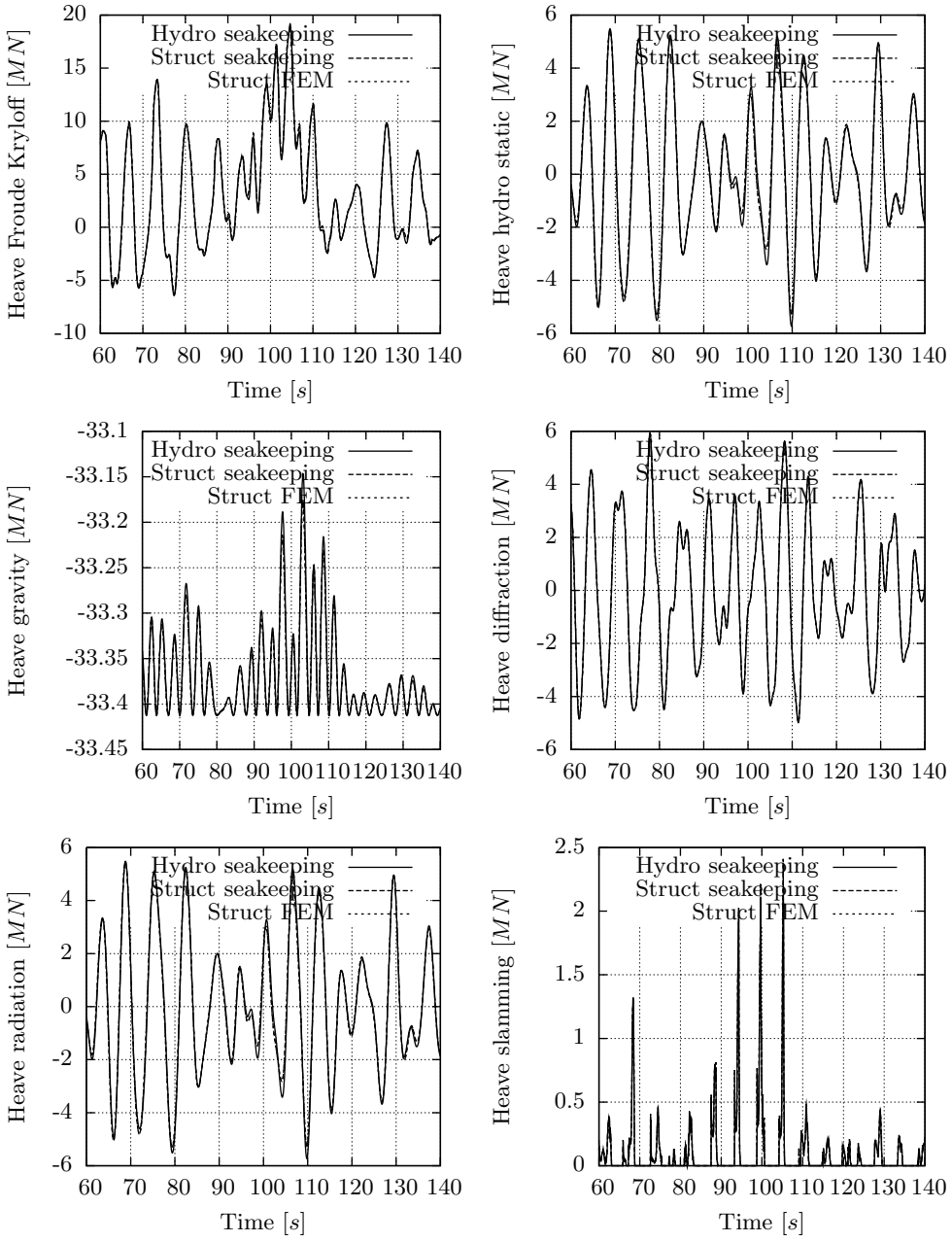

Figure 12.7: Force components.

seakeeping radiation force is incorrect at the start of the calculation because the evaluation of the retardation function needs the velocity history which is lacking at the start of the calculation. As soon as there is enough history,

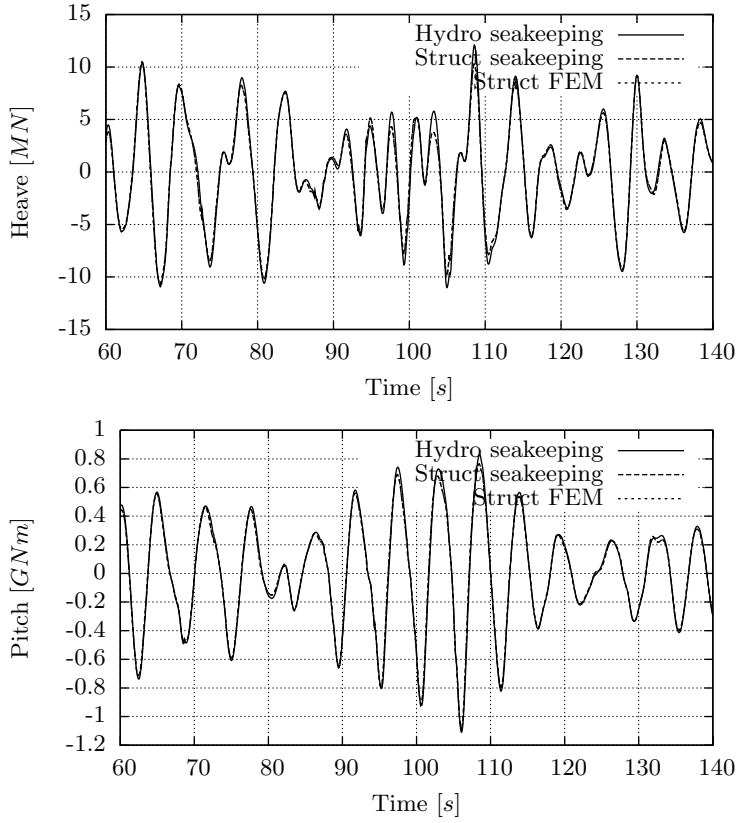

Figure 12.8: Total loading.

the radiation force is almost the same for the structural seakeeping and the nodal forces. Note that this problem of lack of history does not occur for the computation of the nodal diffraction forces as these are based on the Fourier results which contain the full history of the motions. There are some minor differences in the remaining signal, but they are hardly visible in the graph. This results shows the consistency of using the Fourier results to compute the nodal diffraction forces.

It is found that after 10 seconds there are almost no differences between the total loading calculated during the structural seakeeping and for the nodal loads at the FEM model. This indicates that the nodal hydrodynamic and acceleration loading at the structural model represent the seakeeping loading and accelerations very well. The good agreement between the seakeeping calculations with the hydrodynamic mesh and structural mesh shows that the structural mesh can be used to perform seakeeping calculations.

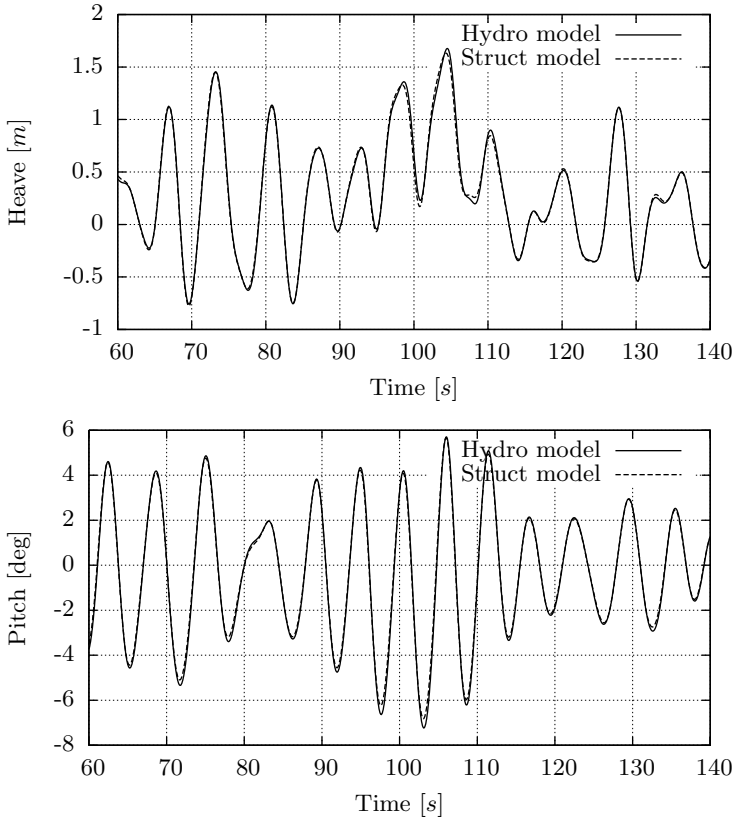

Figure 12.9: Motions using structural and hydro models.

12.1.3 FEM results

The structural response is calculated using a quasi-static FEM approach. Some nodes are constrained to be able to solve the quasi-static problem. These nodal constraints are placed such that they suppress the rigid-body motions but will not cause any additional loading due to constrained lateral contraction.

The structural response is calculated between 85 $[s]$ and 115 $[s]$ of the seekeeping calculation using the FE method. The resulting forces at the constrained nodes indicate how well the hydrodynamic and acceleration forces balance each other. The maximum force at the constrained nodes is below $60[N]$ for all time steps. This force is negligible compared to the total loading at the model which shows that the model is well balanced. The reaction force found is on the order of 10^{-6} of the total loading at the ship which can be explained by the numerical accuracy of the FEM program.

The stress in the deck between the superstructure and hangar is evaluated in Figure 12.10. The stress computed using the direct FEM calculation and

using the modal superposition within the seakeeping program are presented in the figure. The stress at this location should be well described using modal analysis. The good agreement between the direct FEM results and the modal analysis result shows the consistency of the transfer of the seakeeping load to the FEM. It also shows that using nodal acceleration forces allows one to account for whipping induced stress.

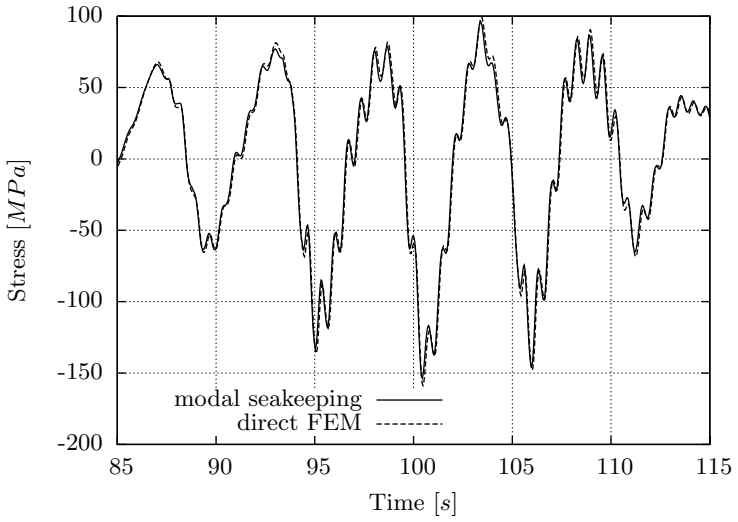

Figure 12.10: Stress in deck.

A direct FEM analysis is only necessary when evaluating the stress at a location where local response contributes to the resulting stress. Figure 12.11 shows the stress in the foremost bulkhead. The figure clearly shows the increase of the maximum stress due to the slamming loading. The whipping response hardly contributes to the stress at this location as can be expected. It would be very difficult to obtain this stress history when using only a modal analysis.

12.2 Full scale measurements

A full scale sea trial has been carried out on the Hr. Ms. Karel Doorman in January 1992 at the Northern part of the North Sea. The strains were measured at thirty locations by the MEOB[2], and MARIN[3] measured the motions of the ship. Detailed documentation of these measurements can be found in [5] and [18].

All calculations presented in this section have been performed by Mirre Janssen. A detailed description of this validation can be found in [19]

[2]Former electronic and optic services of RNlN

[3]Maritime Research Institute Netherlands

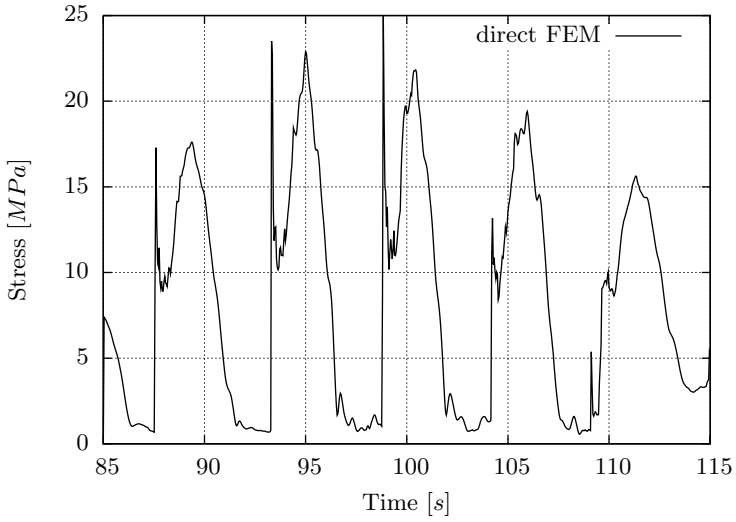

Figure 12.11: Stress in the most forward bulkhead.

The measured stress on the weather deck, somewhere near amidships, is used for the validation. This location is chosen because the stress here will be mainly induced by the deformations of the global modes and should be well described using the modal approach for calculation of the stress, which was shown for a comparable location in the previous section. The measured and calculated seakeeping motions are not presented in this thesis as the measured seakeeping motion is restricted information.

The sea trail has been carried out for different headings and two speeds. The two speeds are 12 and 17.5 knots. Only the head wave conditions are considered for this validation as the slamming loading cannot be calculated accurately for oblique seas. Two runs of approximately 24 minutes were measured for both velocities in head seas. The significant wave height was about 5 metre during the sea trial which resulted in significant slamming impacts, especially for the highest velocity.

12.2.1 Sea state

It was planned to measure the sea state using a wave buoy during the sea trial. However, this buoy could not be deployed due to the heavy weather. Fortunately, the sea spectra were also recorded at a nearby offshore platform. The three hour spectra measured at this platform are used to create the wave-trains used in the calculations.

The measurements while sailing with a speed of 17.5 knots were done between 6:30 and 7:30 and are simulated using a wave-train based on the spectra

from 6:00 and 9:00. The measurements while sailing with a speed of 12 knots were done between 14:10 and 15:10 and are simulated using a wave-train based on the measured spectra from 12:00 and 15:00 hours. This also gives an idea of the sensitivity of the results to the wave spectra used. The different measured sea spectra are shown in Figure 12.12.

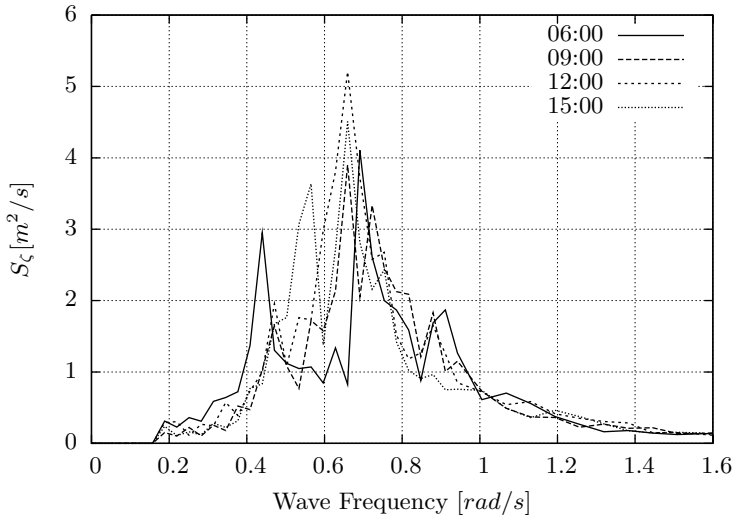

Figure 12.12: Measured wave spectra.

The actual sea was short-crested due to the directional spreading between the different wave components. This spreading has been measured and is shown in Figure 12.13 for the 09:00 hour spectra. The average spreading angle is about forty degrees. The spectra is slightly doubled peaked and the difference in mean direction of the two peaks is about thirty degrees. The "head wave" direction is visually determined at 06:00 hours and is used for all measurements of the sea trial. This makes it likely that the actual heading is not exactly head waves.

The wave spreading, or short-crested seas, cannot be taken into account in the calculation. Therefore, all wave energy is assumed to be directed at exactly the head wave condition in the calculations. Using these long-crested seas will overestimate the resulting bending moment and the stresses for this sea state.

12.2.2 Creating signals

The duration of the measurements was approximately 24 minutes and the same duration is used for the simulations. The uncertainty in the results is reduced by combining the two different runs for the condition considered. The different runs are combined using the approach described in Section 7.1.3. The mean stress is subtracted from both the measured and the calculated stress signals

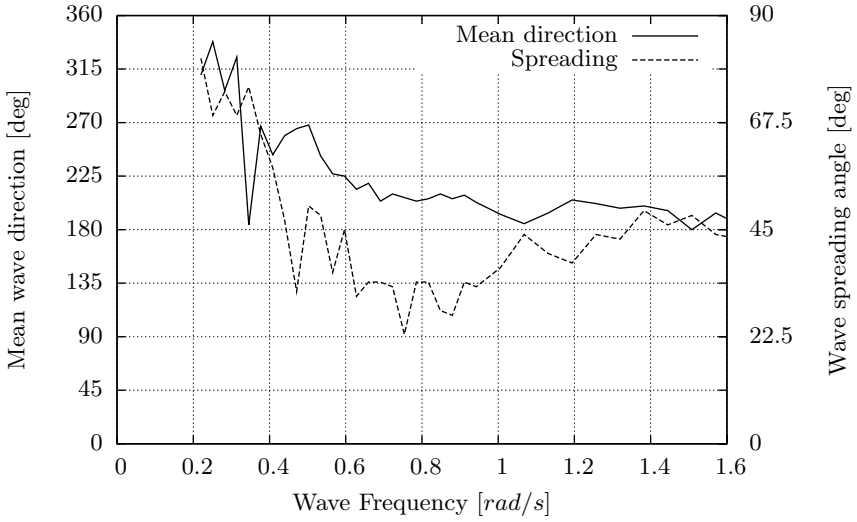

Figure 12.13: Spreading of the 09:00 hour waves.

because the stress signals of the measurements do not include the contribution of the SWBM.

The zero crossing period of the wave-train is about 9.9 [s]. When sailing at 12 and 17.5 knots, the average encounter periods are 5.7 and 4.8 [s] respectively. During the 48 minutes the vessel encounters approximately 484 wave peaks when sailing with 12 knots and 575 wave peaks when sailing with a speed of 17.5 knots. The amount of encountered peaks is an important parameter for the accuracy of the Weibull extrapolation and the calculated fatigue damage. The number of wave peaks present in the measurement is about seventy percent of the 750 extremes needed for an accurate prediction as demonstrated in Chapter 7. This will result in some additional uncertainty in the calculated Weibull extrapolations and fatigue damage.

The stress signals are low-pass filtered to remove the contribution of the slamming induced whipping in the stress signals. This allows the determination of the effect of the whipping response. The stress signals are filtered using a 5th order low-pass Butterworth filter with a cut-off frequency of 1.91 [Hz]. The effect of this filter on a time trace is shown in Figure 12.14.

12.2.3 Response spectra

Figures 12.15 and 12.16 show the power spectral density of the measured and calculated time traces of the stress on the deck. These power spectral densities are calculated using Welch's method. The left-hand side of the figure shows the wave frequency response and the energy of the whipping response is shown

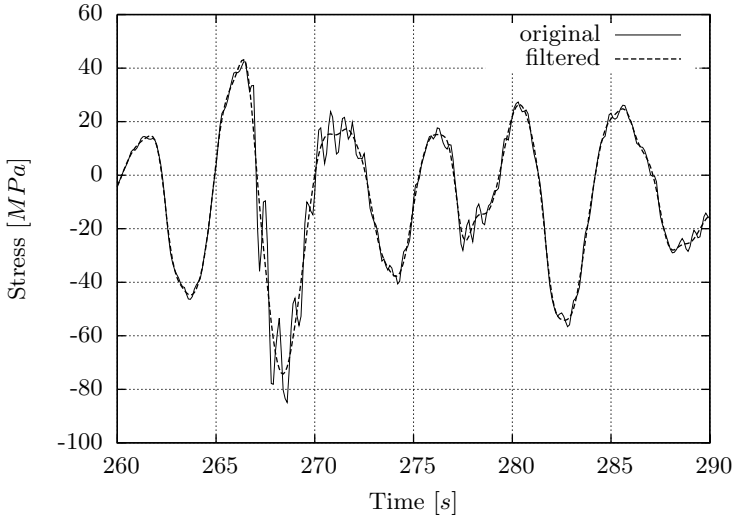

Figure 12.14: Original and filtered stress signal.

in the right-hand side figure. Note the difference in scale between the figures. The statistical values of the response spectra are presented in Table 12.1.

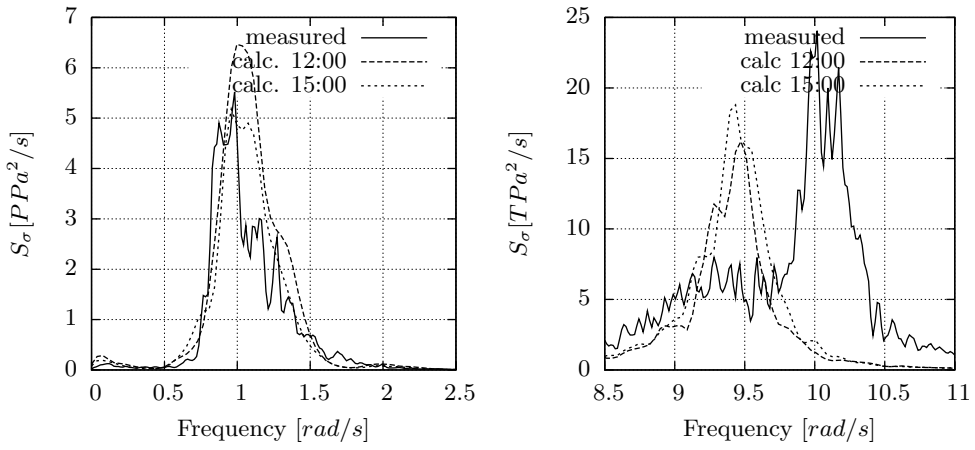

Figure 12.15: Spectra of deck stress for 12 knots.

The wave frequency response is overestimated for both speeds but especially for the 17.5 knots case. This overestimation can partly be explained by using a long-crested sea in the calculation where the real sea was short-crested. However, one would expect the same amount of overestimation for both speeds if this was the only source of error. The overestimation is probably also caused by

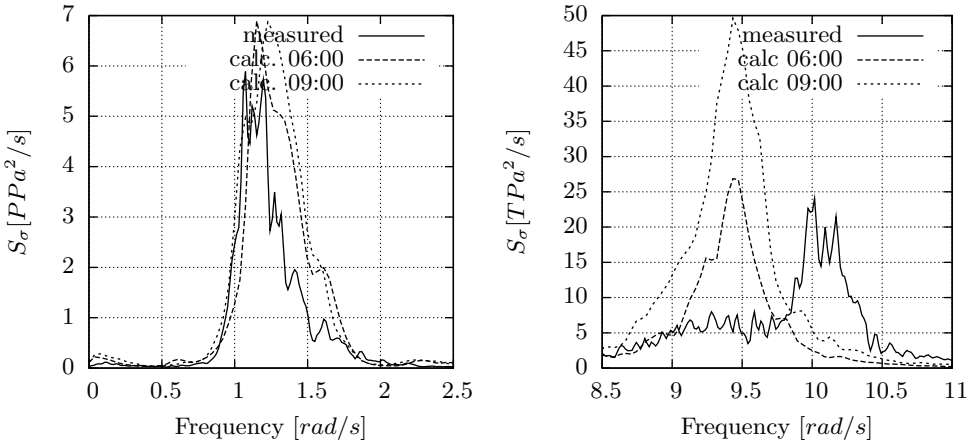

Figure 12.16: Spectra of deck stress for 17.5 knots.

	V [knts]	$M_0 < 0.5Hz$	$M_0 > 0.5Hz$	M_0	$T_1[s]$
measurement	12	3.35×10^{14}	3.02×10^{12}	3.38×10^{14}	5.56
simulation 12:00	12	4.43×10^{14}	2.19×10^{12}	4.45×10^{14}	5.63
simulation 15:00	12	3.78×10^{14}	3.16×10^{12}	3.81×10^{14}	5.58
measurement	17.5	3.33×10^{14}	6.97×10^{12}	3.40×10^{14}	4.58
simulation 06:00	17.5	4.74×10^{14}	4.88×10^{12}	4.79×10^{14}	4.66
simulation 09:00	17.5	5.46×10^{14}	8.64×10^{12}	5.54×10^{14}	4.60

Table 12.1: Response spectra properties for stress.

using a seakeeping theory which does not fully correctly account for the forward speed and all non-linearities occurring in this heavy sea.

The calculated first wet hull natural frequency is a bit lower than found in the measurements. It was shown in Section 10.2 that the natural frequencies can be predicted accurately using the presented theory if an accurate FE model of the structure is available. It is almost impossible to model a real ship with the same level of accuracy as was done for the aluminium model. It is likely that the difference in measured and calculated natural frequency is caused by differences between the modelled FE structure and the real structure of the ship.

The amount of energy of the whipping response in the stress signal is well predicted for the 12 knots case. The whipping is overestimated when using the 09:00 spectra for the calculation of the 17.5 knots case. It could be argued that calculating the same whipping energy as found in the experimental results is in fact an underestimation of the whipping response because long-crested seas are used as input for the calculations. However, it is difficult to quantify the effect of short-crested seas on the whipping response since short-crested seas cannot

be used in the calculations.

12.2.4 Weibull extrapolation

Weibull plots and extrapolations are created for the stress signal using the approach described in Section 7.1.2. Figures 12.17 and 12.18 are the Weibull plots for the two velocities. All counted peaks of the measured signal and from the combined simulation are plotted in the figures. The Weibull fits are shown using lines. The line indicated by "lin $k_w = 2$" is a line with a shape parameter of two which is a Rayleigh distribution that would be obtained if linear theory was used. Note that the scale parameter of these linear lines is just estimated because these lines are only intended to show that the Weibull fits for the stress signals have different shape parameters.

The slope of the Weibull fits of both the measured and calculated response compare very well. This is the shape parameter of the Weibull fit. This shape parameter is clearly different from 2, the linear line, for the higher extremes, which indicates non-linearity in the seakeeping loading. This seems to be well predicted by the presented theory. The scale parameter of the calculated extremes is just a bit higher than found for the measured extremes of the 12 knots case. The difference is bigger for the 17.5 knots case. This is due to the overestimation of the seakeeping response as explained in the previous section.

The one hour extrapolations of the extremes in the stress signal are presented in Table 12.2. The slamming hardly increases the extreme stress for the 12 knots case. This increase is well predicted by the calculations. The increase is more significant for the 17 knots case, about 8 percent for the sagging extreme. The calculations seems to underpredict this increase but that is likely due to the overestimated wave frequency response.

Both the measured and calculated stress signals contain only 70 percent of the required number of extremes for an accurate Weibull fit. The calculation for the 12 knot case, including slamming, is repeated ten times using different wave realisations to get an insight into the uncertainty in the Weibull extrapolation. The results are presented in Table 12.3. These results show that the Weibull extrapolation is quite accurate for this case. Note that the variation of the presented difference between the resulting extreme stresses with and without slamming will be less because the same but filtered time trace is used for both Weibull extrapolations.

	V [knots]	hogging incl. slam $[MPa]$	hogging excl. slam $[MPa]$	influence slamming $[MPa]$
measurement	12	53.8	51.9	1.9
calculation 12:00	12	60.5	59.0	1.5
calculation 15:00	12	56.3	55.3	1.0
measurement	17.5	55.7	53.6	2.2
calculation 06:00	17.5	63.0	61.4	1.6
calculation 09:00	17.5	62.6	60.0	2.5

	V [knots]	sagging incl. slam $[MPa]$	sagging excl. slam $[MPa]$	influence slamming $[MPa]$
measurement	12	83.2	79.7	3.5
calculation 12:00	12	102.0	98.3	3.8
calculation 15:00	12	84.3	82.5	1.9
measurement	17.5	86.4	80.0	6.4
calculation 06:00	17.5	108.9	105.7	3.2
calculation 09:00	17.5	118.7	113.2	5.5

Table 12.2: One hour extremes.

run	sagging incl. slam $[MPa]$	hogging incl. slam $[MPa]$
1	84.3	56.3
2	93.2	56.8
3	88.1	56.6
4	88.9	55.5
5	98.5	61.0
6	94.3	58.2
7	87.2	54.0
8	89.7	56.6
9	94.6	58.7
10	97.3	58.1
mean	91.6	57.2
stdv	4.65	1.91

Table 12.3: 1 hour extreme stresses for 12 knots with slamming for the 15:00 hour spectrum.

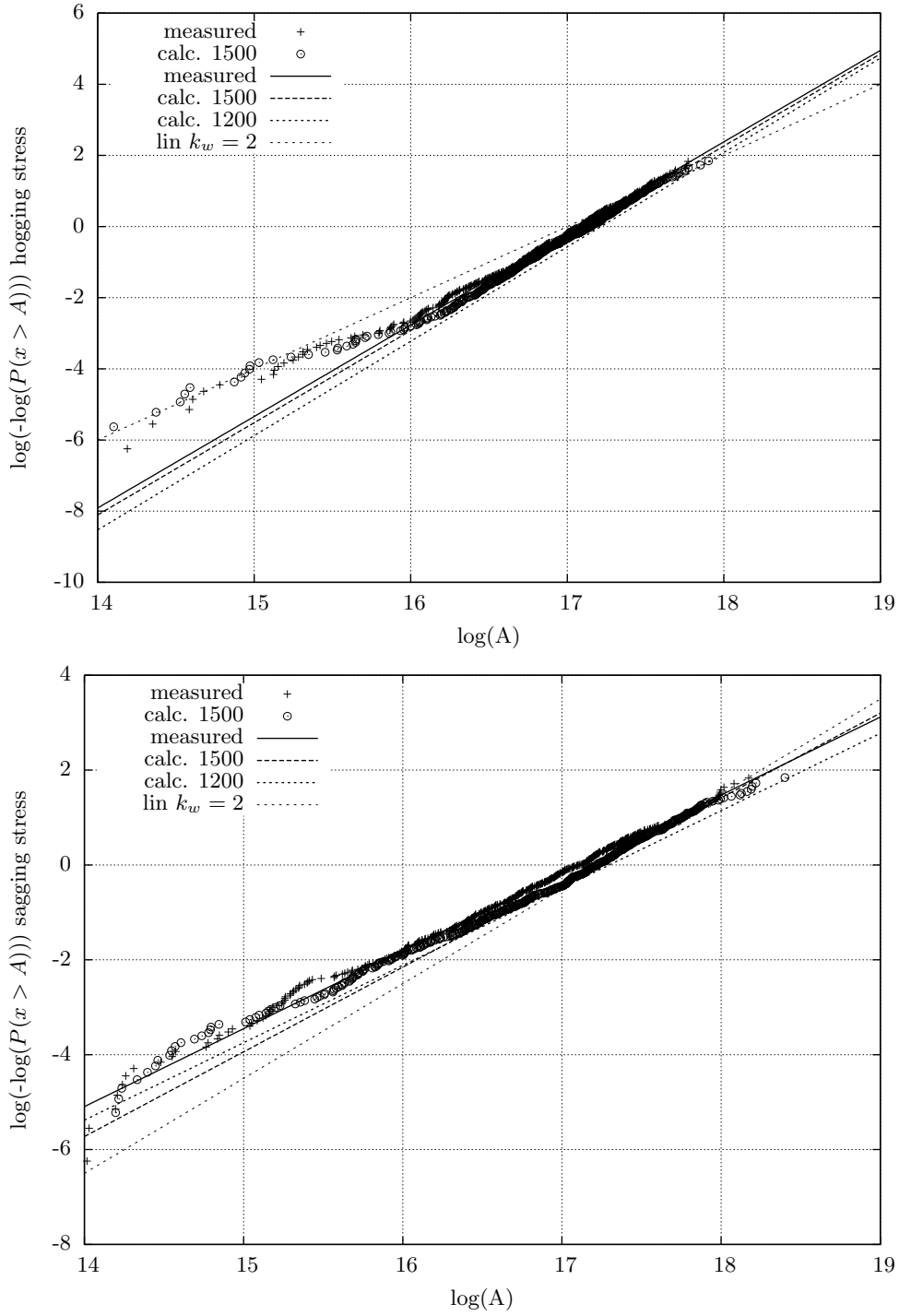

Figure 12.17: Weibull plots for 12 knots including whipping response.

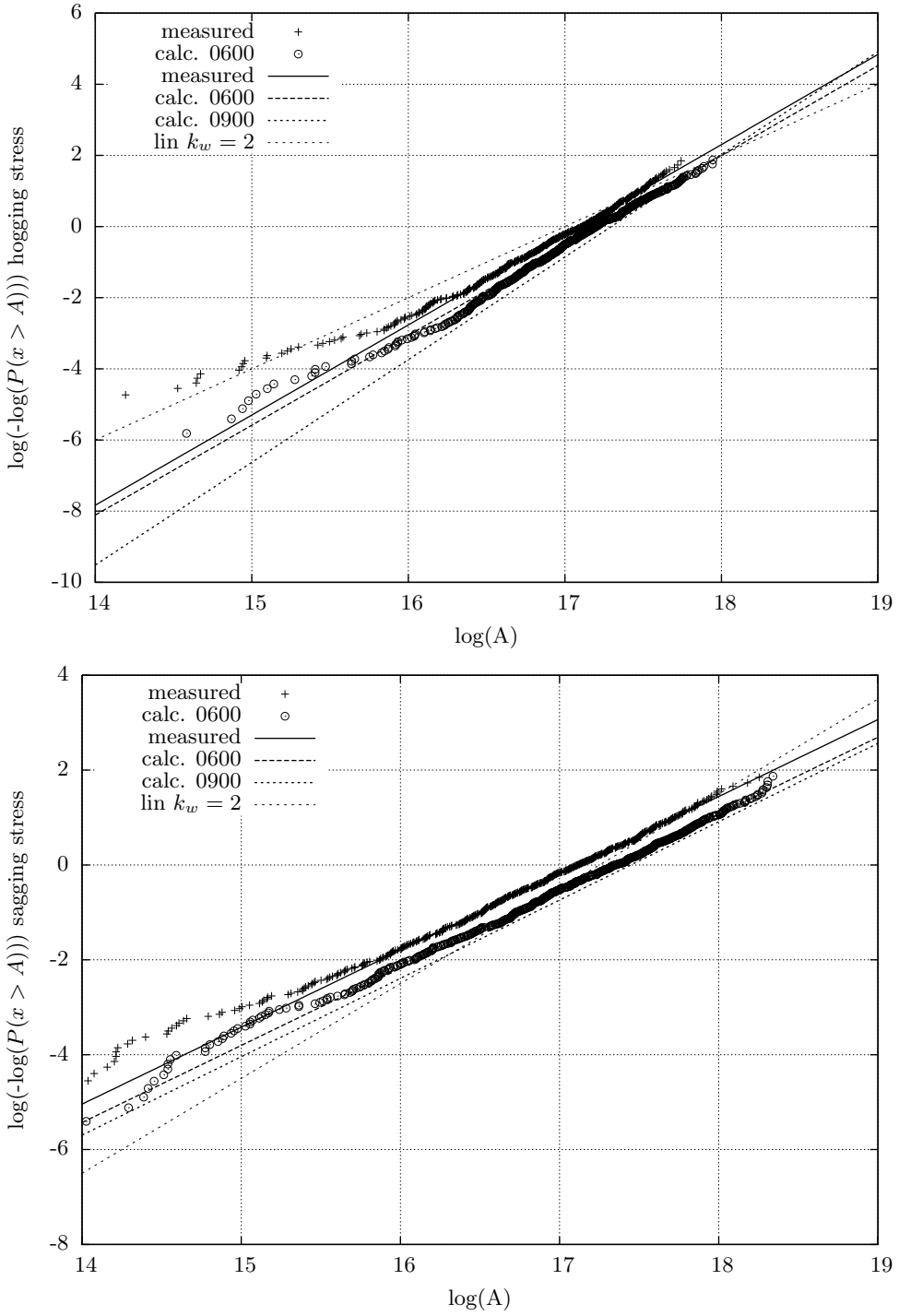

Figure 12.18: Weibull plots for 17.5 knots including whipping response.

12.2.5 Fatigue damage

The number of fatigue cycles are counted using the rainflow count method explained in Section 7.1.1. The damage is calculated using the FAT 160 [17] SN-curve. Both the number of cycles and resulting damage per hour seakeeping are shown in Figures 12.19 and 12.20. The same trend as observed in the previous sections is visible. The calculated seakeeping response is slightly overpredicted for the 12 knots case and the overprediction is larger for the 17 knots case when looking at the number of fatigue cycles. The SN-curve causes the differences between the computation and measurements to be amplified in the resulting fatigue damage. The predicted damage for the 12 knots case is reasonable but the damage is really overpredicted for the 17 knots case.

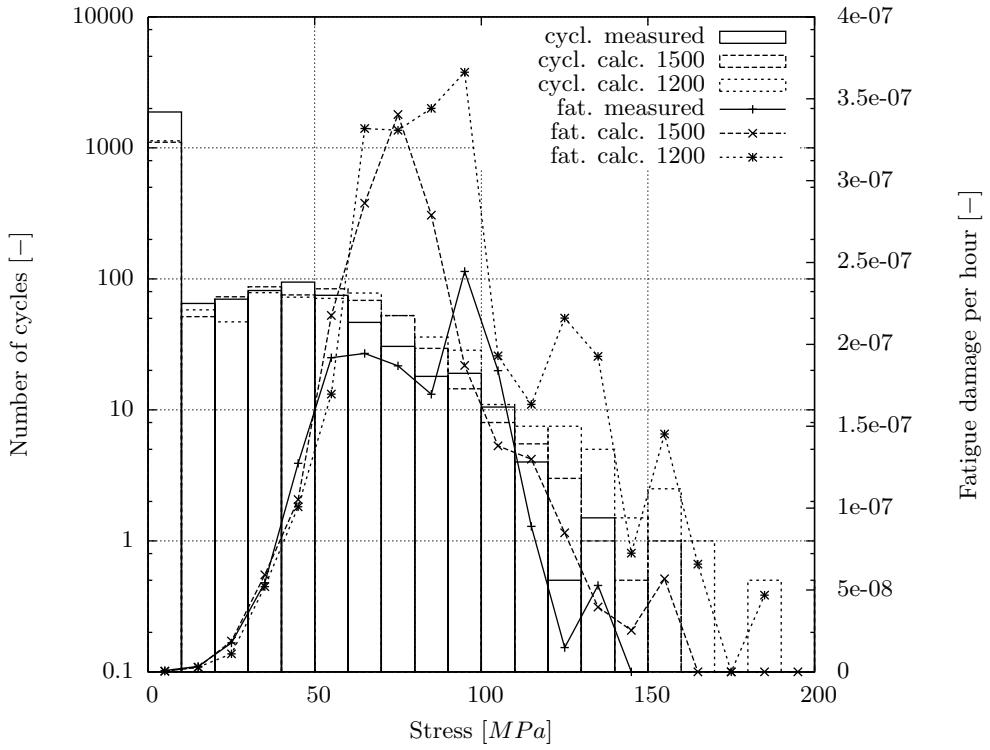

Figure 12.19: Rainflow count and fatigue damage for 12 knots including whipping response.

The hourly fatigue damage and the lifetime extrapolation for the sea states are presented in Table 12.4. The whipping response causes a reduction of 10 percent of the lifetime for the 12 knot case and 16 percent for the 17.5 knot case when looking at the measurements. These reductions are not predicted by the calculations because the wave frequency response is overpredicted.

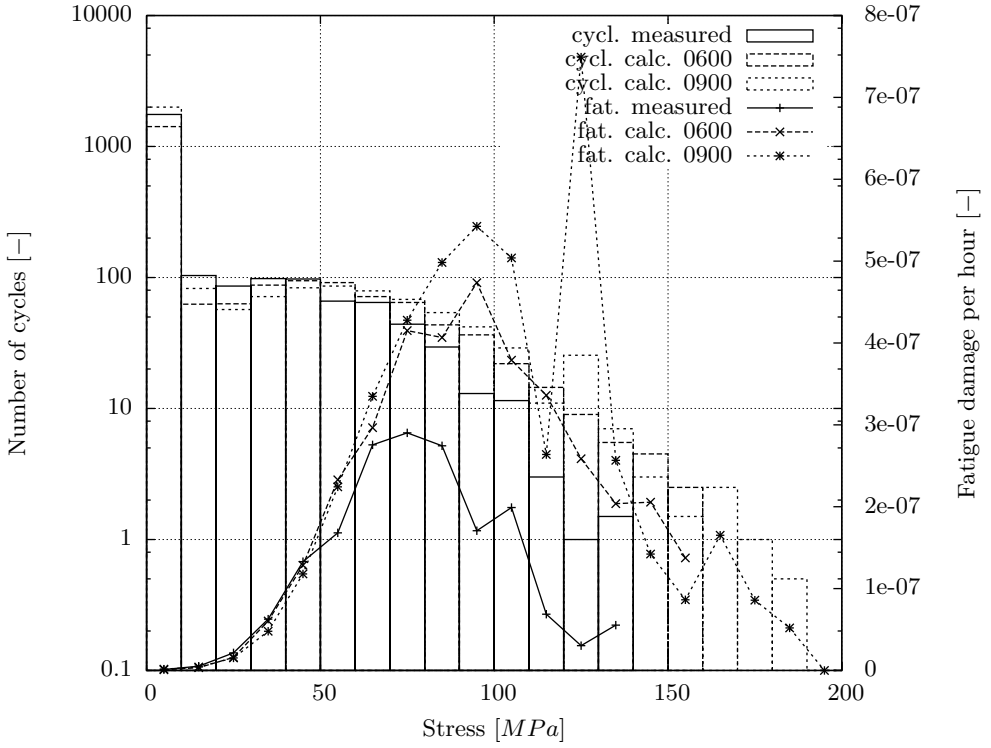

Figure 12.20: Rainflow count and fatigue damage for 17.5 knots including whipping response.

	V [knts]	fatigue/hour excl. slam [-]	lifetime in years	fatigue/hour incl. slam [-]	lifetime in years	Δ life-time
measurem.	12	0.1662E-05	68.7	0.1889E-05	60.4	8.3
calc. 12:00	12	0.2854E-05	40.0	0.3166E-05	36.1	3.9
calc. 15:00	12	0.2088E-05	54.7	0.2306E-05	49.5	5.2
measurem.	17.5	0.1904E-05	60.0	0.2285E-05	50.0	10.0
calc. 06:00	17.5	0.3561E-05	32.1	0.4006E-05	28.5	3.7
calc. 09:00	17.5	0.4277E-05	26.7	0.5112E-05	22.3	4.4

Table 12.4: Overview of the fatigue damage results.

12.3 Conclusions

The approach presented in this thesis avoids interpolation of pressures between the hydrodynamic and structural mesh by using the structural mesh to perform the seakeeping computations when the seakeeping forces are used for a FE computation. This approach requires the computation of the hydrodynamic pres-

sures at the structural mesh while the BVP is solved using the hydrodynamic mesh. The pressure is evaluated at translated dummy Gauss points, which are located outside the hydrodynamic mesh, to obtain the hydrodynamic coefficients. In the first section of this chapter it is shown that the dummy Gauss points are indeed located outside the hydrodynamic mesh and still close to the structural mesh. It was also shown that the pressure distribution is continuous near the hydrodynamic mesh which is necessary for the approach used. The last verification for the use of the dummy Gauss points was an investigation of the effect of the distance between the hydrodynamic mesh and the dummy Gauss points. This investigation showed that converged values for the hydrodynamic coefficients are obtained with the distance used.

The verification of the computed loading for a structural FEM computation showed good results. First, the forces and motions were compared between a seakeeping calculation using the normal approach with a hydrodynamic mesh, a seakeeping calculation using the structural mesh and the computed loading for the FE computation. The computed forces and motions compared very well between the different methods which indicated the consistency of the approach for computing the structural loading. The structural response was solved using the FE method. Negligible reaction forces were found at the constrained nodes which indicated that the seakeeping and acceleration forces were well balanced. The computed stress signal for the deck near amidships agreed very well with the modal solution from the seakeeping computation. This indicated not only the consistency of the approach of computing the FE loads, but also showed that stress induced by the whipping response can be taken into account by applying nodal acceleration forces.

It can be concluded that the method described in chapter 6 is consistent and can be used to compute the FE load cases for computing the local structural response.

A validation using the data of a full scale sea trail of the M-frigate was presented in the second section of this chapter. The measured stresses at the weather deck for the head seas conditions were used to validate the presented theory. The wave frequency response was slightly overestimated for the 12 knots case and a bit more for the 17.5 knots case. The whipping response was well predicted when sailing at 12 knots and overestimated for the 17.5 knots condition. The Weibull extrapolation showed that the computations predict the measured non-linearities well. Good results were also found for the computed fatigue damage, although the SN-curve amplified the overestimation of the seakeeping response. The overestimation can partly be explained by using unidirectional waves when the actual sea trail was performed in short-crested seas.

This validation shows that the presented theory can be used for predicting the structural response of this ship in head sea condition with the occurrence of slamming induced whipping.

Chapter 13

Conclusions and recommendations

The main conclusions about the work presented in this thesis are presented in the first section of this chapter. Recommendations for future research are given in the second section.

13.1 Conclusions

The goal set for this thesis is to develop a practical method to calculate the global and local response of a ship structure due to the seakeeping loading including the slamming loading. The method should contain the full hydro-elastic coupling. The previous chapters are first summarised and conclusions are drawn to judge whether the goals set for this thesis are accomplished.

The hydro-elastic seakeeping problem is formulated in the second chapter. The seakeeping problem is formulated using generalised modes. All degrees of freedom are described by this approach using mode shapes, even the rigid-body modes. The number of degrees of freedom is arbitrary. The generalised mode approach not only allows to solve hydro-elastic seakeeping problems but it also allows to solve multi-body problems. The elastic mode shapes are obtained from either a 3D-FEM calculation or an 1D-beam model of the ship structure. All degrees of freedom of the ship are balanced in still water to avoid transient response at the start of the time domain calculation.

The boundary value problem, the seakeeping response including the calculation of internal loads and the wet natural frequencies are solved in the frequency domain in the third chapter. The resulting linear coefficients for the added mass, damping and diffraction force are used for the time domain seakeeping calculation. The effect of hydroelasticity is investigated by separating the contribution of the rigid-body modes and elastic modes and investigating the consequential effect on the internal loads for an ultra large container ship.

It is shown that the ship has a significant springing response which would be excluded when using a rigid-body approach. However, including the elastic modes in the seakeeping calculation changes also slightly the predicted internal loads for the lower frequencies which shows the importance of performing a hydro-elastic analysis for such large flexible ships.

The fourth chapter presents the theory for computation of the seakeeping motions and internal loads in the time domain. The time domain allows to account, with relative ease, for non-linear load components and transient responses. As the time domain also allows for large amplitudes of motion, the concept of generalised modes is extended to account for these motions. The Froude-Krylov and hydrostatic loads are computed non-linearly to improve the seakeeping and internal load predictions. The diffraction and radiation loads are kept linear to allow for reasonably fast computation times. Spring-damper and beam elements can be used to connect bodies to the Earth and to each other. Kinematic constraints can be used to connect bodies and to impose or constrain motions.

The computation of the slamming force using two different 2D methods is presented in the fifth chapter. The first method is the Generalised Wagner Model (GWM) and the second method is the Modified Logvinovich Model (MLM). The GWM is the most accurate method and has a wider range of validity compared to the MLM method. The MLM is much faster and a bit more robust compared to the GWM. The computation of the slamming loads is integrated into the time domain seakeeping calculation. The slamming loads are calculated based on the relative motion provided by the seakeeping calculation and the resulting loads are included in the calculation of the seakeeping response. The modal excitation by the slamming pressure is calculated using an integration over the 3D geometry of the bow. This includes some 3D effects and makes the calculation of the slamming pressure less sensitive to the user selected tilting angle of the 2D sections.

The modal approach used for the seakeeping calculation gives insight into the global response of the ship structure. However, it is difficult to compute the local structural response using the modal approach. The local structural response is computed by transferring the seakeeping loads to a 3D-FE model of the structure and computing the response within the FEM method. This approach is explained in the sixth chapter. A method which ensures perfect balance between the seakeeping and acceleration loads is used.

The seventh chapter explains how design values such as the maximum expected bending moment and fatigue damage can be calculated from results of the non-linear time domain calculations. It is investigated how an accurate estimation of the design values can be obtained while minimising the computational effort. It is shown that it is best to merge the results of different computations until in total 750 linear extrema are present in the combined signal.

The eighth chapter is the first of five chapters presenting verifications, val-

idations and case studies of the developed theory. Two ultra large container ships are used for verification and case studies in this chapter. It is shown that the computed retardation functions are consistent with the added mass and damping. Another verification shows that the linear motions computed in the frequency domain are close to the non-linear motion computed in the time domain for small waves. The computed internal loads are verified by comparing the results from the direct integration method for both the forward and aft direction and the modal superposition method. It is shown that these three results are very close to each other. Another verification is the sensitivity of the calculated whipping response to the selected time step in the seakeeping calculation. Using a time step of 0.2 seconds results in convergence of results for this ship. This time step is acceptable as it is larger than the stable time step for the explicit time integration scheme when including the first five flexible modes. The effect of hydroelasticity is also investigated. It is shown that the hydro-elastic effects reduce the computed slamming forces significantly for the large ship. This again shows the importance of performing a hydro-elastic analyses for large flexible ships. The last verification investigates if the approach of integrating the slamming pressure over the 3D geometry indeed adds some 3D effect and reduces the sensitivity towards the chosen tilting angle of the 2D slamming sections. It is shown that this is the case. A case study is presented in the last part of the chapter. The ultimate bending moment and fatigue damage are calculated for both the North Atlantic and the World wide trade scatter diagrams. It is shown that including the flexible modes and slamming loading reduces the fatigue lifetime by about forty percent. The maximum bending moment computed for 25 years sailing is increased by about twenty percent by the slamming induced whipping and springing. Unfortunately, it was shown that the method used to extrapolate the ultimate bending moment fails as soon as significant green water loading occurs. The computation of the design values is repeated using different wave realisations in order to investigate the accuracy of the computation of these design values. It is shown that the variation of the results is small, so the proposed method for computation of the design values is accurate.

Flexibly connected barges are used for the verification and validation presented in the ninth chapter. The flexibly connected barges can be modeled using a multi-body approach where the connection between the bodies is modeled, or a single body approach where the elastic modes provide the flexibility between the barges. The presented theory is verified by comparing the computed seakeeping motions of two barges connected by a hinge, modeled by both the multi-body approach and the single flexible-body approach. Very comparable motions are found when the hinge connection is made stiff by either a spring or rigid connection. The computed motions using the single flexible model are unreliable when no stiffness is applied in the hinge direction as the deformations of the flexible body become too large. It is assumed in the the-

ory used that the deformation of the elastic modes remain small. Experiments with twelve flexible connected floaters are used to validate the hydro-elastic theory. Good agreement between a multi-body and a flexible-body approach is found. The calculation results also compare reasonably well with the experimental results. This shows the ability to compute hydro-elastic effects and the multi-body response. However, the viscous damping seems to play a major role in the resulting motions, the good agreement could only be obtained by tuning the damping values.

The tenth chapter presents validation of the wet natural frequencies, slamming impact and whipping response using an aluminium model. The calculated wet natural frequencies correspond very well with the measurements. This shows that the contribution of the added mass to the flexible motions is well captured by the theory. The computed slamming forces are reasonably close to the slamming forces estimated from the measurements. The calculated whipping response is close to the measured whipping response. These results could only be obtained by imposing the measured rigid-body motion in the seakeeping calculation.

The measured slamming forces at the bow of a container ship model are used for validation in the eleventh chapter. Verification of the sensitivity with respect to the tilting angle of the 2D slamming sections and the time step shows the same good results as were found for the other container ships presented in chapter eight. The sensitivity of the predicted slamming loads to changes in predicted seakeeping motions is also investigated. This sensitivity showed to be very high for the predicted pitch motion. This could be expected as the slamming loads scale with approximately the square of the relative velocity. These results show the importance of an accurate seakeeping prediction when calculating the slamming loads. The measured rigid-body motions are imposed to the seakeeping calculation in order to validate the computed slamming force with the experimental results. The estimation of the slamming impacts compare reasonably well with the experimental results for low speeds. However, the slamming loads are significantly underestimated at high speeds. This is probably due to a static bow wave for which the calculations do not account. The bow of this container vessel has much flare which results in a significant static bow wave. The predicted slamming loads are much closer to the measured loads when the wave elevation by the static bow wave is added to the calculation.

Results of a full scale trial with the M-frigate of the Royal Netherlands Navy are used for the validation presented in chapter twelve. Predicted and measured stresses in the weather deck near amidships are compared. The stress due to the seakeeping are slightly overestimated, especially for the highest velocity. This can partly be explained by the use of unidirectional waves in the calculation where the actual sea was short crested. The whipping contribution is well predicted. It could be argued that it is actually underestimated as the slamming

loads are also computed using the unidirectional waves. The Weibull fits of the hogging and the sagging stresses show a very good agreement between the calculations and measurements. The hog/sag ratio is well captured by the computation. The Weibull fits shows a slight overestimation for the highest velocity. The fatigue calculation shows good results for the low velocity and an overestimation for the highest velocity. The addition of a static bow wave is not necessary for the M-frigate as the bow is much less blunt than the bow of the container ship. The M-frigate is also used to verify the correctness of the computation of the seakeeping loads evaluated using a 3D-FEM model. It is shown that the FEM model is indeed perfectly balanced. It is also shown that the total seakeeping loads and response of both the original seakeeping calculation and the 3D-FEM are very close which indicates the consistency of the method.

It is shown that the presented theory allows the computation of the structural response of the ship due to the seakeeping loading, including the slamming loading. The full hydro-elastic coupling is implemented. The modal seakeeping approach solves for the global structural response, the local structural response can be obtained by transferring the seakeeping loads to 3D-FEM. All verifications show that the presented methodology is consistent. The validation shows that the slamming loads, whipping response and the stresses in the structure can be predicted with reasonable accuracy provided that the rigid-body seakeeping prediction is accurate. The case studies show that the methodology can be used to compute the design values. This includes the contribution of slamming induced whipping for all cells of a scatter diagram. This shows that the developed method is practical to apply in terms of computational effort. It also illustrates the importance for an hydro-elastic analysis for large flexible ships, especially when computing the fatigue loading.

While, it can be concluded that the goals set for this thesis are accomplished, there are some limitations and points for improvement of the presented method. First of all, the slamming loads can only be predicted for (near) head sea conditions because of the 2D approach used for the computation of the slamming loads. Another drawback is the accuracy of the seakeeping and slamming predictions. It has been shown that these are predicted quite accurately for low speeds but the prediction is not as good for higher velocities. The predicted rigid-body seakeeping response is also less accurate in very severe condition when large parts of the ship emerges. Not all load components are currently included for the internal load calculations and the transfer to 3D-FEM, this is another limitation of the presented theory. The forces due to the roll damping and station-keeping should be included for computations in oblique seas.

Even with the current limitations, the presented methodology proves to be a good framework to define a hydro-elastic problem and to compute the resulting motions and loads. As the methodology combines different modules such as the formulation of the hydro-elastic problem, solving the seakeeping response,

slamming calculation, etc, it is possible to make changes in order to extend the range of validity of the methodology. One could, for example, change the 2D slamming prediction method by a 3D method to be able to compute the slamming in oblique seas without changing other components.

13.2 Recommendations

Recommendations for further research are given in this section. The first are improvements to the presented theory. The others are recommendations on specific, and more general, topics arising from the research presented in this thesis.

The improvement of the seakeeping and slamming prediction is an important topic for further research. The slamming load prediction method should be able to handle oblique conditions. It appears not to be feasible to utilise a 2D method in real oblique conditions where large relative roll motion can be expected. A fast and accurate 3D method has to be developed. The method should also better account for forward speed effects. It has been shown that the static bow wave can have a significant effect on the predicted slamming forces. Another effect of forward speed is the planing force which is not accounted for in the presented 2D method. An improved method should also account for the exit phase of the slamming events and not only the entry phase.

The computation of the seakeeping response at forward speeds and in very severe seas should be improved. It should not only improve the predictions of the internal loads by the non-impulsive hydrodynamic loading, but it should also provide a better relative motion prediction which is used to compute the slamming forces. The seakeeping prediction can be improved by solving the forward speed boundary value problem instead of using a modified zero speed solution. The seakeeping prediction can also be improved by accounting better for the non-linearities in the loading. The diffraction and radiation force are computed using linear theory in the presented method. Not only will the seakeeping prediction become more accurate if the non-linearity of these force components would be included in the computations, but the non-linear radiation computation will also account for the 3D slamming loading for both the entry and exit phases. This would make an additional slamming module superfluous. However, the method should still be fast and robust enough to compute the design values for a complete scatter diagram. It seems to be quite a challenge to develop such a method in the near future.

Another topic for future research is the inclusion of the roll damping and station-keeping forces in the internal loads computation and the transfer of seakeeping forces to the 3D-FEM model. The roll damping is now only included as a linear damping term. This gives a roll moment, but it should be known how the force causing this moment is distributed over the hull. The same holds

for station keeping. In the presented method the ship is kept at its position by imposing the linear motions using kinematic constraints. These corrections could also be seen as a single force and the distribution of this force over the hull should be known. The best solution would be to compute the roll damping, manoeuvring, resistance, rudder and propeller force at the 3D FE-model of the ship. This would be the only way to obtain an accurate distribution of forces and also an accurate computation of their contributions. The computation of the roll damping should also be improved. Using a linear model is considered by many authors to be inadequate to predict the damping of the roll motion during seakeeping.

The validation of the hydro-elastic theories should also be improved. There is currently only a very limited set of model and full scale experiments available to validate the computational results. Most of the available experimental results also contain some uncertainly, for example, actual wave realisation and viscous damping, which makes validation difficult. The first step is to acquire more experimental results which can be used for validation purpose. The next step is to improve the validation itself. Instead of reporting comparisons between measurements and computation results as "reasonable agreement was found" and "it follows the trends well", an error estimation should be sought such that the level error of a hydro-elastic computation would be known in advance. Note that the latter is currently not the case even for rigid-body seakeeping predictions.

The design values are obtained using brute force computation and post processing using a rainflow count, SN-curves and Weibull extrapolation. There are many aspects to improve the computation of the design values. The first is the use of the Weibull extrapolation. It should be investigated if this is the best probability distribution to be used for extrapolating the expected maximum bending moment using signals which includes whipping response and possible green water loading. The approach to compute the design values using the brute force method was chosen such that the computational effort is minimised while having reasonable accuracy in all cells of the scatter diagram. The presented approach can be changed if only the lifetime values are of interest. Only a few cells in the scatter diagram are likely to result in the maximum expected bending moment. About half of the cells contribute significantly to the total fatigue damage. The computational approach could be to only compute the design values for the cells of the scatter diagram that contribute significantly to the fatigue damage or are likely to set the maximum bending moment. Not using the brute force approach but other methods like response conditioned waves is another way of reducing the computational effort for calculating the design values.

The case study with the container ships and the comparison with the data of the full scale trial of the M-frigate indicated that the bending moment prediction can be improved by allowing for short-crested seas. Except for the slamming

computation, it is not difficult to change the theory presented in this thesis to allow for short-crested seas, this is mostly additional book keeping. However, to describe short-crested seas accurate, many more wave components will be necessary which will increase computation times significantly.

The case study presented in Chapter 8 showed that the maximum expected bending moment is encountered in very severe sea states, which the ship is expected to encounter for only a few hours during its life. The accuracy of the computed ultimate bending moment for these very severe conditions can be questioned. The actual probability of encountering such conditions, which waves can be expected and at which course and speed the master will sail in these conditions should be investigated. The computational results should also be validated using model or full scale test results for those very severe conditions.

The approach used to solve the boundary value problem in the frequency domain cannot be used to compute the hydrodynamic damping for the first few natural modes. This would require more computer memory than is available. It has been shown in Appendix C that the used extrapolation method for the damping curve gives good results for a ferry. A better test case for the used extrapolation method would be using an ultra large container ship at high speed such that linear springing will be present in the results. A better solution would be to change the method to solve the boundary value problem such that the hydrodynamic damping could actually be computed for the very high frequencies.

Appendix A

Gauss quadrature

The Gauss quadrature is used for numerical integration of the pressure over the body surface. The Gauss quadrature is the most accurate numerical integration scheme available. This appendix briefly explains the Gauss quadrature by summarising the explanation found in [7] and [60].

The Gauss quadrature is explained first for a one-dimensional problem. The second section of this appendix generalises the theory for the two-dimensional problems. The integration of pressure to modal and nodal forces is discussed in the last section.

A.1 One-dimensional

$f(x)$ is the function that is to be integrated between x_1 and x_2. The limits for this integral are first rescaled to $\xi = -1$ and $\xi = 1$

$$I = \int_{x_1}^{x_2} f(x)\,\mathrm{d}x = \int_{-1}^{1} J(\xi) f(\xi)\,\mathrm{d}\xi, \tag{A.1}$$

with $J(\xi) = \frac{\mathrm{d}x}{\mathrm{d}\xi}$ the Jacobian of the transformation. The integral is approximated by evaluating the function at a limited number of points and multiplying the results with a weighting factor

$$\int_{-1}^{1} J(\xi) f(\xi)\,\mathrm{d}\xi \approx W_1 J(\xi_1) f(\xi_1) + W_2 J(\xi_2) f(\xi_2) + \cdots + W_n J(\xi_n) f(\xi_n). \tag{A.2}$$

The locations for the function evaluations and the weight factors are chosen such that the highest possible accuracy is obtained. The locations and weighting factors for different numbers of function evaluations can be found in Table A.1.

Figure A.1 illustrates the Gauss quadrature approach. The top figure at the left hand side is the original function. The other figures is the integration of this function use 1, 2 or 3 Gauss points.

Number n	location ξ_i	Weight factor W_i
1	0	2
2	$\pm\sqrt{1/3}$	1
3	$\pm\sqrt{3/5}$ 0	$5/9$ $8/9$
4	$\pm\sqrt{\left(3-2\sqrt{6/7}\right)/7}$ $\pm\sqrt{\left(3+2\sqrt{6/7}\right)/7}$	$\frac{18+\sqrt{30}}{36}$ $\frac{18-\sqrt{30}}{36}$
5	0 $\pm\frac{1}{3}\sqrt{\left(5-2\sqrt{10/7}\right)}$ $\pm\frac{1}{3}\sqrt{\left(5+2\sqrt{10/7}\right)}$	$128/225$ $\frac{322+13\sqrt{70}}{900}$ $\frac{322-13\sqrt{70}}{900}$

Table A.1: Location and weight factor for Gauss quadrature.

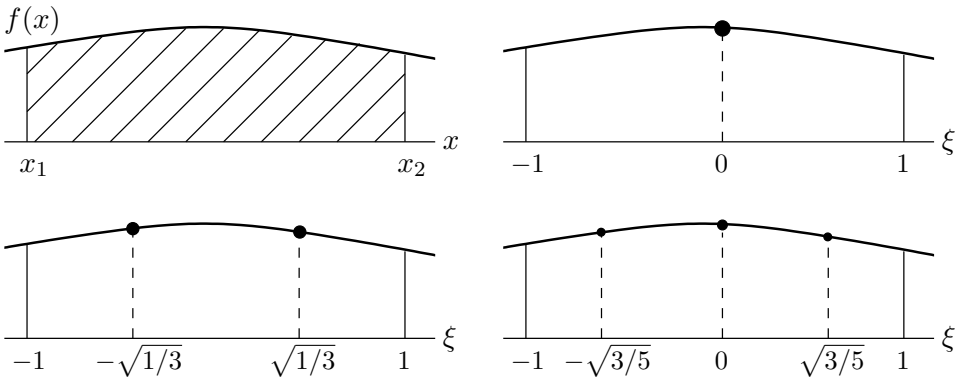

Figure A.1: Integration using Gauss quadrature with 1, 2 and 3 Gauss points.

A.2 Two-dimensional

The pressure over the body surface is integrated using the integration mesh. This mesh consists of four-node quadrilateral and three-node triangular panels. A comparable approach is used to integrate the pressure for both element types. Therefore, only the integration using the quadrilateral element is explained in this section.

Figure A.2 shows the local coordinates for a quadrilateral panel. Both local coordinates have limits -1 and 1. This allows one to write

$$I = \iint_s f(x,y)\,\mathrm{d}s = \int_{-1}^{1}\int_{-1}^{1} J(\xi,\eta) f(\xi,\eta)\,\mathrm{d}\xi\,\mathrm{d}\eta. \tag{A.3}$$

The Gauss quadrature is used in both directions, which results in an approximation for the integral of

$$I \approx \sum_i \sum_j W_i W_j J(\xi_i, \eta_j) f(\xi_i, \eta_j). \tag{A.4}$$

This integration is illustrated in Figure A.3 for different number of Gauss points. The weighting is the same as that given in Table A.1.

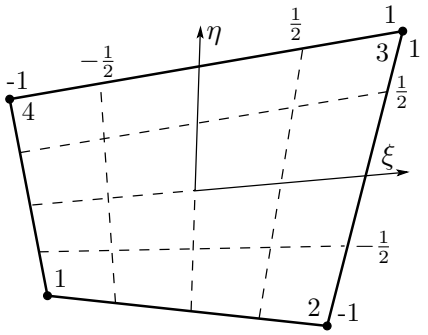

Figure A.2: Local coordinates of quadrilateral panel.

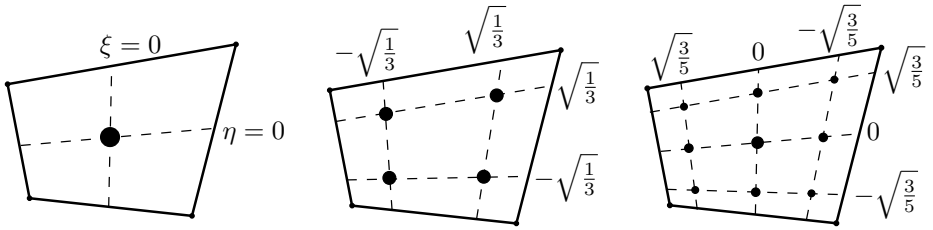

Figure A.3: Integration at quadrilateral panel using Gauss quadrature with 1, 2 and 3 points.

A.3 Pressure integration

In this thesis the Gauss quadrature is only used for pressure integration. The pressures are integrated to modal forces for the body or sections in order to solve the seakeeping problem. Nodal forces are necessary to calculate the loading at the structural model.

The mode shapes and normals are calculated for every Gauss point in the pre-processing phase, see Chapter 2. Note that the four-node panel may be warped which results in a different normal vector for all Gauss points at a panel.

The contribution of a single Gauss point to the total force vector working on the element is equal to

$$f^k \approx p(\xi_i, \eta_j) W_i W_j J(\xi_i, \eta_j) \vec{h}_{ij}^k \vec{n}_{ij}. \tag{A.5}$$

The contribution of all Gauss points attached to the body or sections is summed to obtain the total force vector.

Shape functions are used to calculate the nodal force. The linear quadrilateral panel has four linear shape functions

$$h_1(\xi, \eta) = \frac{1}{4}(1-\xi)(1-\eta), \tag{A.6}$$

$$h_2(\xi, \eta) = \frac{1}{4}(1+\xi)(1-\eta), \tag{A.7}$$

$$h_3(\xi, \eta) = \frac{1}{4}(1+\xi)(1+\eta), \tag{A.8}$$

$$h_4(\xi, \eta) = \frac{1}{4}(1-\xi)(1+\eta). \tag{A.9}$$

The contribution to the nodal force at node l by a single panel is

$$\vec{f}_l^k \approx \sum_i \sum_j h_l(\xi_i, \eta_j) W_i W_j J(\xi_i, \eta_j) p(\xi_i, \eta_j) \vec{n}(\xi_i, \eta_j). \tag{A.10}$$

The total nodal force is the summation of the contributions over all attached panels.

Appendix B

Kinematic constraints

Kinematic constraints are implemented by adding Lagrange multipliers to the system of Newton equations and by correcting the velocity and displacement for the kinematic constraints. The Lagrange multipliers do not affect the stable time step. They are also more accurate than using penalty functions.

The theory presented in [16] is used to implement the kinematic constraints. The theory is extended for the use of generalised modes. A different approach is used to correct the velocity and displacement for the constraints. The notation as used in [16] is partly adopted, this differs from what has been used in this thesis.

For the kinematic constraints one or more constraint equations are created in the form

$$\vec{\Phi}(\vec{\xi}) = \vec{0}. \tag{B.1}$$

Differentiating this constraint equation with respect to time gives

$$\dot{\vec{\Phi}} = 0 \rightarrow \mathbf{\Phi}_\xi \cdot \dot{\vec{\xi}} = -\vec{\Phi}_t \equiv \vec{\nu}, \tag{B.2}$$

$$\ddot{\vec{\Phi}} = 0 \rightarrow \mathbf{\Phi}_\xi \cdot \ddot{\vec{\xi}} = -\left(\mathbf{\Phi}_\xi \cdot \dot{\vec{\xi}}\right)_\xi \cdot \dot{\vec{\xi}} - 2 \cdot \mathbf{\Phi}_{\xi t} \cdot \dot{\vec{\xi}} - \vec{\Phi}_{tt} \equiv \vec{\gamma}, \tag{B.3}$$

where the subscript ξ indicates the partial derivative with respect to the coordinates ξ, and t the partial derivative with respect to time.

The equations for one constraint are derived first. The matrices and vectors of the different constraints are combined at the end to obtain one set of constraint equations.

A number of the constraints used are defined between two bodies. The other constraints are defined for a single body. A single constraint may consider more than one degree of freedom. Figure B.1 illustrates the different vectors used for the constraints. Vector $\vec{s}^\star$ is a vector from the center of gravity to the location of the selected node for the constraint. Vector $\vec{a}^\star$ is a user defined vector which is used for the orientation.

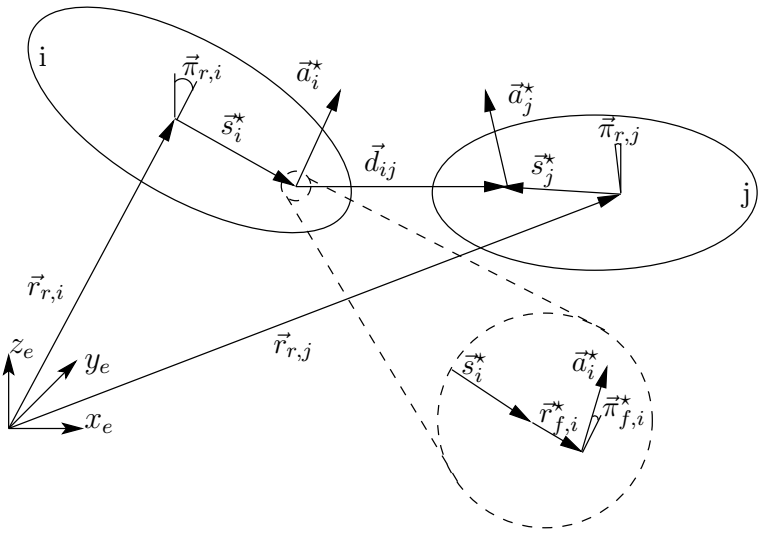

Figure B.1: Vectors for constraint equations.

B.1 Coordinate system

A fixed set of degrees of freedom is used to calculate the values of a single constraint equation. This set is $\vec{\xi}^* = [\vec{r}_{r,i}, \vec{\pi}^\star_{r,i}, \vec{r}^\star_{f,i}, \vec{\pi}^\star_{f,i}, \vec{r}_{r,j}, \vec{\pi}^\star_{r,j}, \vec{r}^\star_{f,j}, \vec{\pi}^\star_{f,j}]$, where $\vec{r}_r$ is rigid-body displacement, $\vec{\pi}^\star_r$ the rigid-body rotation, $\vec{r}^\star_f$ the displacement due to flexible modes and $\vec{\pi}^\star_f$ the rotation due to flexible modes. Figure B.1 shows these degrees of freedom The index i indicates the first body and j the second (if any). Please note the mixed reference system of $\vec{\xi}^*$, some components are defined in the Earth reference system and others in the body system. It is easier to derive the derivatives of the constraint equations using this mixed system.

The different components of the $\vec{\xi}^*$-vector can be calculated using the approach described in Section 4.3.3. The transformation matrices derived in Section 4.2.1 are also used. The flexible deformation will cause that point on a body have a different orientation than the rigid-body itself. The transformation matrix between the body and the point orientation is

$$\mathbf{T}_{bf,\mathbb{R}3,i} = \mathbf{I} + \tilde{\vec{\pi}}_{f,i}. \tag{B.4}$$

A tilde above a vector indicates the skew-symmetric matrix of the vector

$$\tilde{\vec{n}} = \begin{bmatrix} 0 & -n_z & n_y \\ n_z & 0 & -n_x \\ -n_y & n_x & 0 \end{bmatrix}. \tag{B.5}$$

The transformation from the point orientation to the body is

$$\mathbf{T}_{ef,\mathbb{R}3,i} = \mathbf{T}_{bf,\mathbb{R}3,i}^{-1}. \tag{B.6}$$

These linear transformations can be used because the deformations by the flexible modes are assumed to remain small.

All of the constraints used have only dependency on the coordinates and not on time. This makes it possible to simplify the acceleration equation, (B.3), to

$$\vec{\gamma} = -\vec{\Phi}_{tt} + \sum_{i=1}^{2} \Big\{ -\dot{\vec{\Phi}}_{r_r,i} \cdot \dot{\vec{r}}_{r,i} - \dot{\vec{\Phi}}^{\star}_{r_f,i} \cdot \dot{\vec{r}}^{\star}_{f,i} - \dot{\vec{\Phi}}^{\star}_{\pi_r,i} \cdot \dot{\vec{\pi}}^{\star}_{r,i} - \dot{\vec{\Phi}}^{\star}_{\pi_f,i} \cdot \dot{\vec{\pi}}^{\star}_{f,i} \Big\}. \tag{B.7}$$

Some of the constraints have a time-dependent driver, for example a prescribed motion. The time dependency of these driver functions has to be added to vectors $\vec{\nu}$ and $\vec{\gamma}$.

B.2 Basic equations

The constraints may be based on the actual location of a point, the distance between two points or the orientation of a vector at the body. The equations and their derivatives are first derived for these three basic constraint equations.

B.2.1 Location of a point

The equation for the location of point $s^{\star}$, see Figure B.1, in the Earth reference frame is equal to

$$\vec{\Phi}^{lp} = \vec{r}_r + \mathbf{T}_{e,\mathbb{R}3} \cdot \vec{s} + \mathbf{T}_{e,\mathbb{R}3} \cdot \vec{r}_f. \tag{B.8}$$

The derivatives with respect to the different mode groups are

$$\mathbf{\Phi}^{lp}_{r_r} = \mathbf{I}, \tag{B.9}$$

$$\mathbf{\Phi}^{lp}_{\pi^{\star}_r} = -\mathbf{T}_{e,\mathbb{R}3} \cdot \tilde{\vec{s}} - \mathbf{T}_{e,\mathbb{R}3} \cdot \tilde{\vec{r}}_f, \tag{B.10}$$

$$\mathbf{\Phi}^{lp}_{r^{\star}_f} = \mathbf{T}_{e,\mathbb{R}3}, \tag{B.11}$$

$$\mathbf{\Phi}^{lp}_{\pi^{\star}_f} = \mathbf{0}. \tag{B.12}$$

The derivative with respect to time is equal to

$$\dot{\vec{\Phi}}^{lp} = \dot{\vec{r}}_r + \mathbf{T}_{e,\mathbb{R}3} \cdot \tilde{\vec{\omega}}_r \left(\vec{s} + \vec{r}_f \right) + \mathbf{T}_{e,\mathbb{R}3} \cdot \dot{\vec{r}}_f. \tag{B.13}$$

B.2.2 Distance between two points

The distances between the two points $s_i^\star$ and $s_j^\star$ in the Earth reference frame is equal to

$$\bar{\Phi}^{dp} = \vec{\Phi}_j^{lp} - \vec{\Phi}_i^{lp}. \tag{B.14}$$

The time derivative is

$$\dot{\bar{\Phi}}^{dp} = \dot{\vec{\Phi}}_j^{lp} - \dot{\vec{\Phi}}_i^{lp}. \tag{B.15}$$

Because the two bodies are associated with different modes, the derivatives with respect to the coordinates for the location of the points, derived in the previous section, can simply be added.

B.2.3 Orientation of a vector

The orientation of a vector at a body in the earth reference frame is equal to

$$\vec{\Phi}^{vo} = \mathbf{T}_{e,\mathbb{R}3} \cdot \mathbf{T}_{f,e,\mathbb{R}3} \cdot \vec{a}. \tag{B.16}$$

The derivatives with respect to the different mode groups are

$$\mathbf{\Phi}_{r_r}^{vo} = \mathbf{0}, \tag{B.17}$$

$$\mathbf{\Phi}_{\pi_r^\star}^{vo} = -\mathbf{T}_e \cdot (\widetilde{\mathbf{T}_{f,\mathbb{R}3} \cdot \vec{a}}), \tag{B.18}$$

$$\mathbf{\Phi}_{r_f^\star}^{vo} = \mathbf{0}, \tag{B.19}$$

$$\mathbf{\Phi}_{\pi_f^\star}^{vo} = -\mathbf{T}_{e,\mathbb{R}3} \cdot \mathbf{T}_{f,\mathbb{R}3} \cdot \tilde{\vec{a}}. \tag{B.20}$$

$$\tag{B.21}$$

The relevant second order derivatives with respect to time are equal to

$$\dot{\mathbf{\Phi}}_{r_r}^{vo} = \mathbf{0}, \tag{B.22}$$

$$\dot{\mathbf{\Phi}}_{\pi_r^\star}^{vo} = -\mathbf{T}_{e,\mathbb{R}3} \cdot \tilde{\omega}_r \cdot (\widetilde{\mathbf{T}_{f,\mathbb{R}3} \cdot \vec{a}}) - \mathbf{T}_{e,\mathbb{R}3} \cdot (\widetilde{\mathbf{T}_{f,\mathbb{R}3} \cdot \dot{\tilde{\vec{\pi}}}_f \cdot \vec{a}}), \tag{B.23}$$

$$\dot{\mathbf{\Phi}}_{r_f^\star}^{vo} = \mathbf{0}, \tag{B.24}$$

$$\dot{\mathbf{\Phi}}_{\pi_f^\star}^{vo} = -\mathbf{T}_{e,\mathbb{R}3} \cdot \tilde{\omega}_r \cdot \mathbf{T}_{f,\mathbb{R}3} \cdot \tilde{\vec{a}} - \mathbf{T}_{e,\mathbb{R}3} \cdot \mathbf{T}_{f,\mathbb{R}3} \cdot \dot{\tilde{\vec{\pi}}}_f \cdot \tilde{\vec{a}}. \tag{B.25}$$

The time derivative is equal to

$$\dot{\vec{\Phi}}^{vo} = \mathbf{T}_{e,\mathbb{R}3} \cdot \tilde{\omega}_r \cdot \mathbf{T}_{f,\mathbb{R}3} \cdot \vec{a} + \mathbf{T}_{e,\mathbb{R}3} \cdot \mathbf{T}_{f,\mathbb{R}3} \cdot \dot{\tilde{\vec{\pi}}}_f \cdot \vec{a}. \tag{B.26}$$

B.3 Constraint equations

A formulation for $\mathbf{\Phi}, \mathbf{\Phi}_\xi$ and $\vec{\gamma}$ is derived in [16] for every constraint. By adding the flexible modes, these formulations will be quite lengthy due to the number

of derivatives. Therefore, another approach is followed. Most constraints can be formulated using two basic constraint equations from the previous section. The values of $\mathbf{\Phi}_\xi$ and $\vec{\gamma}$ are calculated by combining the derivatives of the basic constraint equations.

The following constraint equations are defined:

d1 The first form of the dot constraint keeps two vectors orthogonal

$$\Phi_{ij}^{d1} = \vec{\Phi}_i^{voT} \cdot \vec{\Phi}_j^{vo} = 0. \tag{B.27}$$

d2 The second form of the dot constraint keeps a vector and the line between the points orthogonal

$$\Phi_{ij}^{d2} = \vec{\Phi}_i^{voT} \cdot \vec{\Phi}_{ij}^{dp} = 0. \tag{B.28}$$

s The spherical constraint keeps two points together

$$\vec{\Phi}_{ij}^{s} = \vec{\Phi}_{ij}^{dp} = \vec{0}. \tag{B.29}$$

This constraint results in three constraint equations.

ss The spherical-spherical constraint keeps two points at a fixed distance

$$\Phi_{ij}^{ss} = \vec{\Phi}_{ij}^{dpT} \cdot \vec{\Phi}_{ij}^{dp} - C^2 = 0. \tag{B.30}$$

x The location constraint keeps a point at a body at a fixed location in the moving Earth reference frame. Three constraint equations are used for this constraint

$$\vec{\Phi}_i^{x} = \vec{\Phi}_i^{lp} - \vec{x}_0^{e} = 0. \tag{B.31}$$

$\bar{x}_0^e$ is the user defined location at which the point should be constrained. It is possible to delete some components of this constraint equation to fix the body point along only one or two dimensions of the Earth fixed point.

1 Only one degree of freedom is constrained with this constraint. This is the only constraint that does not use the basic equations. This constraint is equal to

$$\Phi^1(\xi_i, d(t)) = \vec{\xi_i} - d(t) = 0, \tag{B.32}$$

where $d(t)$ is the driver function, which can be the displacements as calculated in the frequency domain or a measured motion. For this constraint $\nu = \dot{d}(t)$ and $\gamma = \ddot{d}(t)$.

Both the d1, d2 and the ss constraints are expressed in the form $\vec{\Phi}^{aT} \cdot \vec{\Phi}^b = 0$ The $\vec{\Phi}_{\xi^*}$ and γ values for these constraints are

$$\vec{\Phi}_{\xi^*} = \vec{\Phi}^{aT} \cdot \mathbf{\Phi}_{\xi^*}^b + \vec{\Phi}^{bT} \cdot \mathbf{\Phi}_{\xi^*}^a, \tag{B.33}$$

$$\gamma = \sum_{i=1}^{2} \sum_{\xi^* = [\vec{r}_{r,i}, \vec{\pi}_{r,i}^\star, \vec{r}_{f,i}^\star, \vec{\pi}_{f,i}^\star]} \left(\vec{\Phi}^{aT} \cdot \dot{\mathbf{\Phi}}_{\xi^*}^b + \dot{\vec{\Phi}}^{aT} \cdot \mathbf{\Phi}_{\xi^*}^b + \vec{\Phi}^{bT} \cdot \dot{\mathbf{\Phi}}_{\xi^*}^a + \dot{\vec{\Phi}}^{bT} \cdot \mathbf{\Phi}_{\xi^*}^a \right) \cdot \dot{\vec{\xi}}^*. \tag{B.34}$$

B.3.1 Correction force

The velocity and displacement are corrected for the applied constraints by using a correction force or moment. The direction of the correction force should be representative for the constraint. A unit force vector $\vec{f}^{\star}_{\text{corr}}$ is created for every constraint. Because the mass matrix in the body reference frame will be used for the correction, the force vector should also be in the body reference frame. Only the unit vector for force or moment in the Cartesian system acting on the point is calculated, the modal excitation will be calculated later.

The force vector of the 1-constraint is the only vector that is created directly in the generalised coordinates. It is a vector that is one in the degree of freedom which is constrained and zero for all other degrees of freedoms.

The s- and the x-constraints fix the displacement of a point in three directions. Three unit vectors in the x, y and z-directions of the Earth reference frame are used. The vectors in the body reference frame are given by

$$\mathbf{f}^{\star}_{\text{corr},i,\mathbb{R}3} = \mathbf{T}^{T}_{e,\mathbb{R}3,i} \cdot \mathbf{I}. \tag{B.35}$$

The ss-constraint keeps a fixed distance between two points. The unit force has the same direction as the vector between the two points $\vec{d}_{ij}$

$$\vec{f}^{\star}_{\text{corr},i,(x,y,z),\mathbb{R}3} = \mathbf{T}^{T}_{e,\mathbb{R}3,i} \cdot \frac{\vec{d}_{ij}}{|\vec{d}_{ij}|}. \tag{B.36}$$

Both the d1 and d2-constraints keep two vectors orthogonal. A unit moment around the vector of the cross product of the two vectors is used for the correction

$$\vec{f}^{\star}_{\text{corr},i,(\phi,\theta,\psi),\mathbb{R}3} = \mathbf{T}^{T}_{e,\mathbb{R}3,i} \cdot \frac{\vec{v}_i \times \vec{v}_j}{|\vec{v}_i \times \vec{v}_j|}. \tag{B.37}$$

B.4 Combining constraints

The different constraints are collected to obtain the system of constraint equations. The vectors $\vec{\Phi}, \vec{\gamma}$ and $\vec{\nu}$ are simply a collection of the values of the different constraints

$$\vec{\Phi} = [\Phi_1, \Phi_2, \ldots, \Phi_n]^T, \tag{B.38}$$

$$\vec{\gamma} = [\gamma_1, \gamma_2, \ldots, \gamma_n]^T, \tag{B.39}$$

$$\vec{\nu} = [\nu_1, \nu_2, \ldots, \nu_n]^T. \tag{B.40}$$

Note that ν will be zero except for the 1-constraint.

Before the global $\mathbf{\Phi}_{\xi}$ and $\mathbf{\Phi}^{\star}_{\xi}$ can be derived, the $\vec{\Phi}_{\xi^*}$ vectors have to be transfered to the modal coordinates and their values transformed to the Earth and body reference frame. The Earth frame values are obtained by $\mathbf{T}_{e,\mathbb{R}3,i} \cdot \vec{\Phi}_{\pi_r,i}$ and $\mathbf{T}_{b,\mathbb{R}3,i} \cdot \vec{\Phi}_{r_r,i}$ will give the body frame values.

Equation (2.48) is used to put the rigid-body values in the correct location of the generalised mode vectors. The contributions for the flexible modes is equal to

$$\vec{\Phi}^i_{\xi,n} = \vec{h}^i_{(x,y,z)} \cdot \vec{\Phi}^i_{r_f,n} + \vec{h}^i_{(\phi,\theta,\psi)} \cdot \vec{\Phi}^i_{\pi_f,n}, \tag{B.41}$$

where n indicates the constraint number.

The unit force vector for the correction of the velocities and displacements is in the modal coordinates

$$\vec{f}^{i\star}_{\text{corr},n} = \mathbf{h}^i \cdot \vec{f}^{i\star}_{\text{corr},n,\mathbb{R}3}. \tag{B.42}$$

The matrices for all constraint equations in the generalised coordinates can now be created as

$$\mathbf{\Phi}^\star_\xi = [\vec{\Phi}^\star_{\xi,1}, \vec{\Phi}^\star_{\xi,2}, \dots \vec{\Phi}^\star_{\xi,n}], \tag{B.43}$$

$$\mathbf{\Phi}_\xi = [\vec{\Phi}_{\xi,1}, \vec{\Phi}_{\xi,2}, \dots \vec{\Phi}_{\xi,n}], \tag{B.44}$$

$$\mathbf{f}^\star_{\text{corr}} = [\vec{f}^\star_{\text{corr},1}, \vec{f}^\star_{\text{corr},2}, \dots \vec{f}^\star_{\text{corr},n}]. \tag{B.45}$$

B.5 Velocity and displacement correction

Since the kinematics are non-linear, the velocity and displacements still have to be corrected when Lagrange multipliers are included in the calculation of accelerations.

A virtual force $\delta\vec{f}_{dv}$ is introduced for correction of the displacements

$$\Delta\vec{\xi} = \mathbf{T}_e \cdot (\mathbf{A}^\star(\infty) + \mathbf{m}^\star)^{-1} \cdot \mathbf{f}^\star_{\text{corr}} \cdot \delta\vec{f}_{dv}. \tag{B.46}$$

The values for the virtual force can be solved using the Newton-Raphson method

$$\mathbf{\Phi}_\xi \cdot \mathbf{T}_e \cdot (\mathbf{A}^\star(\infty) + \mathbf{m}^\star)^{-1} \cdot \mathbf{f}^\star_{\text{corr}} \cdot \delta\vec{f}_{dv} = -\vec{\Phi}(\vec{\xi}). \tag{B.47}$$

After calculating the virtual force, equation (B.46) is used to calculate the displacement correction. Normally, the Newton-Raphson method is iterated until the required accuracy is obtained. However, as this displacement correction is carried out at every Runge-Kutta step, only one iteration is required to obtain sufficient accuracy for normal seakeeping problems.

The velocities are corrected by another virtual force $\delta\vec{f}_{vv}$, following from

$$\Delta\dot{\vec{\xi}} = \mathbf{T}_e \cdot (\mathbf{A}^\star(\infty) + \mathbf{m}^\star)^{-1} \cdot \mathbf{f}^\star_{\text{corr}} \cdot \delta\vec{f}_{vv}. \tag{B.48}$$

The constraint equation for the velocities (B.2) is a linear equation and can be directly used to obtain the virtual force needed to correct the velocities

$$\mathbf{\Phi}_\xi \cdot \mathbf{T}_e \cdot (\mathbf{A}^\star(\infty) + \mathbf{m}^\star)^{-1} \cdot \mathbf{f}^\star_{\text{corr}} \cdot \delta\vec{f}_{vv} = \vec{\nu} - \mathbf{\Phi}_\xi \cdot \dot{\vec{\xi}}. \tag{B.49}$$

The correction vector for the velocities is calculated using equation (B.48).

Appendix C

Extrapolation of damping curve

The frequency dependent part of the radiation force is calculated using retardation functions for the time domain calculations. These retardation functions are created by a Fourier transformation of the damping curve. The damping coefficients are calculated in the frequency domain. It is difficult to calculate the damping curve for high frequencies. Therefore, the damping curve is extrapolated above a user defined threshold value. The influence of the starting point and the method for the extrapolation of the damping curve is investigated in this appendix.

C.1 Calculating of hydrodynamic coefficients

The panel size used to solve numerically the hydrodynamic BVP limits the highest frequency that can be calculated accurately in the frequency domain. The stability of the solution of the BVP depends on the wave-length in proportion to the panel size. The relation between the encountered frequency and the wave-length is $\lambda = \frac{2\pi g}{\omega_e^2}$ which decreases quadratically for high frequencies. The total number of panels scales quadratic with the panel size and the computer memory required to solve the BVP also increases quadratic to the total number of panels. Therefore, doubling the available computational memory will only allow for a small increase in the maximum frequency for which the BVP can be solved accurately.

Figure C.1 shows an example of the computed damping curve for a ferry model with a length of about 170 metres and sailing at 12 knots in head waves. The main diagonal damping curve for the first bending mode, index 7-7 of the damping matrix, is shown. The natural frequency for the first flexible mode is 6.7 $[rad/s]$. The oscillations of the damping curve are due to a too coarse mesh and not due to irregular frequencies. Surface lid panels are used to suppress

the occurrence of irregular frequencies for this calculation. If the oscillations were irregular frequencies, the frequency where the oscillations occurs would be identical for all meshes and a "$+\infty \ -\infty$" behaviour of the damping curve is expected for irregular frequencies. Therefore the oscillations are most likely due to using a too coarse mesh.

The arrows in Figure C.1 show the highest frequency for which the solution is correct and the computer memory required for the calculation using the program PRECAL [33]. The damping curve cannot be calculated beyond an encounter frequency of 5.5 $[rad/s]$ using the available computer with 16 $[Gb]$ of memory.

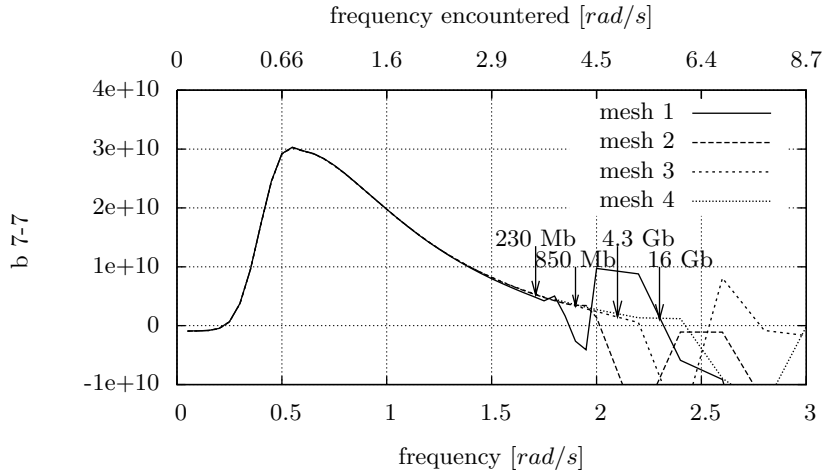

Figure C.1: Damping curve for various panel sizes.

C.2 Extrapolation methods

The damping curve has to be extrapolated to the value at the "infinite" frequency. The value of the damping calculated for the infinite frequency is located at a high frequency.

A possibility is the use of a linear extrapolation. A linear extrapolation between the highest calculated frequency value and the infinite frequency value located at 1.33 times the highest frequency is investigated.

Another extrapolation is also investigated. In this case the infinite frequency value is located at about two times the highest frequency. A function of type $\frac{a}{\omega^b} + c$ is used to extrapolate the damping curve between the highest frequency and the infinite frequency. Values for the b-coefficient for main diagonal rigid-body mode terms for zero speed can be found in [55], however there are no values for the other terms. Because the b value is only known for a few terms,

all curves are calculated by imposing the condition that the slope should be the same for the damping curve and the extrapolation at the highest frequency for which the damping curve can be computed accurately. The variables a and c follow from the required value at the start and the end of the extrapolation.

The damping curves using the different extrapolation methods are shown in Figure C.2.[1] The damping curve is extrapolated from encounter frequencies 2.7 and 4.0 $[rad/s]$. The damping curve ending at 2.7 $[rad/s]$ represents the results of a coarse mesh and the one ending at 4.0 $[rad/s]$ that of a refined mesh. The function extrapolation is almost identical for the different end frequencies for these two damping curves. This is an indication that the $\frac{a}{\omega^b} + c$ function is a good approximation of the damping curve at high frequencies.

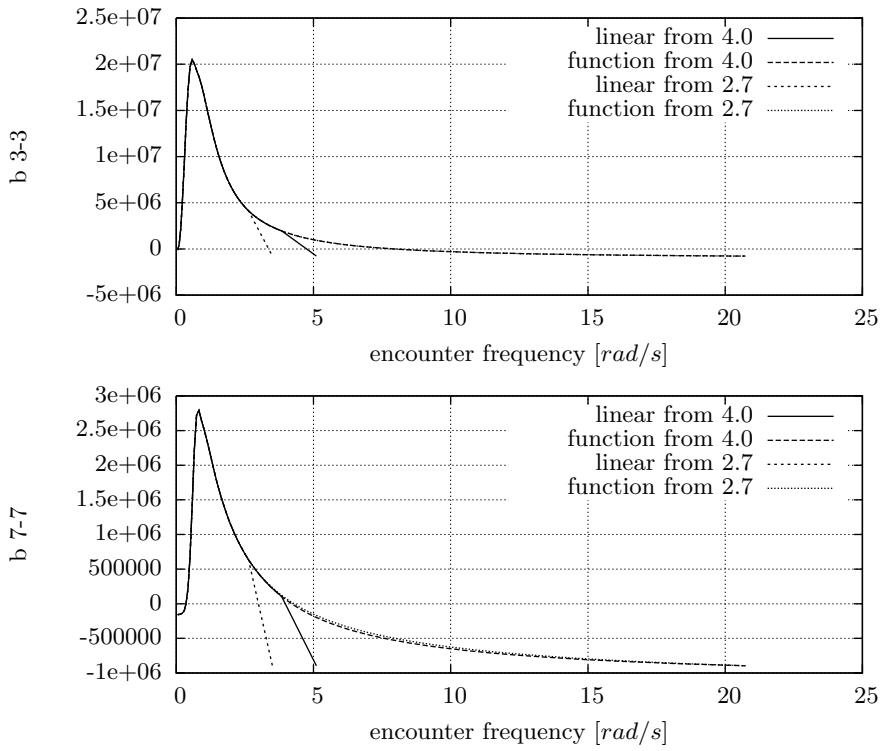

Figure C.2: Different damping extrapolations for the heave mode and the first flexible mode.

The resulting retardation functions using the different damping curves are shown in Figure C.3. The smooth damping curves created by the function extrapolation results in smooth retardation functions. The retardation function

[1]The computed damping is negative at some frequencies. This is an error resulting most likely from using a body boundary condition corrected for forward velocity and a zero speed surface boundary condition.

created using the linear extrapolated damping curves shows some oscillations. The oscillations of the 4.0 $[rad/s]$ curves are less than for the 2.7 $[rad/s]$ curves.

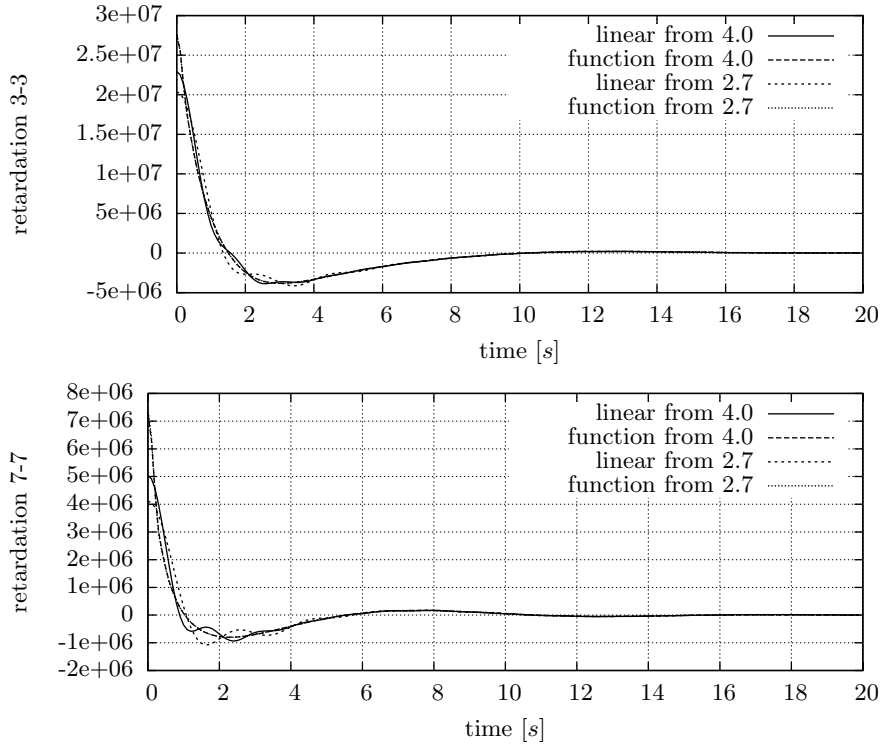

Figure C.3: Retardation functions for various damping curve extrapolations.

C.3 Response

The different damping curves are used for a fully coupled slamming and whipping calculation in the time domain for a 170 $[m]$ ferry model. Because the calculated hydrodynamic damping for the main diagonal terms at infinite frequency for some of the flexible modes is negative, a significant structural damping is added to ensure positive damping for the flexible modes. The frequency reconstructed motion for surge, sway and yaw are imposed during the time domain calculation. The resulting heave motion and the response of the first flexible mode is shown in Figure C.4.

There are almost no differences in motions using the different damping curves. Only the motions calculated using the linear 2.7 $[rad/s]$ damping curve show very small differences. This result can be explained by the frequency of

the wave and slamming excitation. Even with a 12 knot forward speed the wave excitation is still below the frequency at which the damping curve is interpolated. For these frequency ranges the damping curve is the same for all cases and the retardation function should give the same result. The frequency of the slamming excitation and the frequency of the natural modes are at a frequency where the damping is (almost) the infinite damping for all damping curves so no large differences are expected.

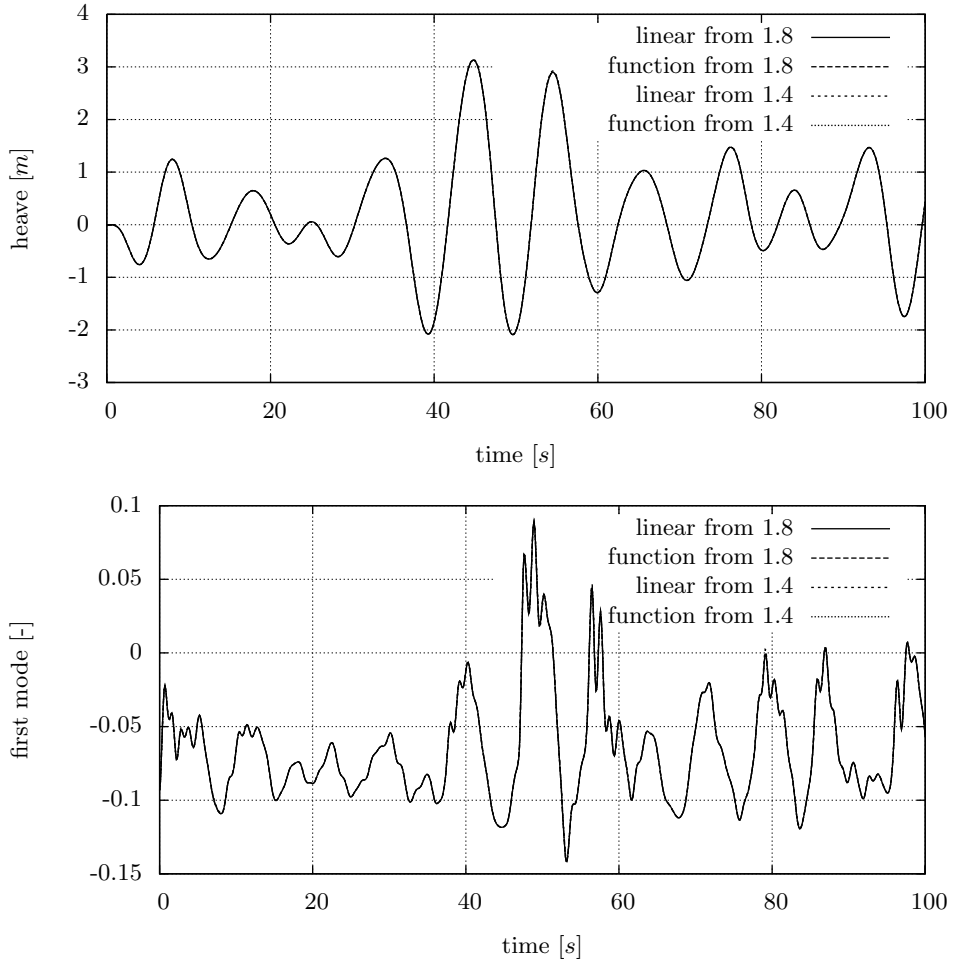

Figure C.4: Motion response for various damping curve extrapolations.

C.4 Conclusion

It is not possible to calculate the complete damping curves up to the frequencies of the first natural modes of the ship in a computationally efficient manner. This is a limitation of the method used. Due to the very rapid increase in computer memory required for accurate solving of the BVP at increasing frequencies, this problem will not be solved by the next generation of computers.

This example shows almost no sensitivity between the results and the chosen extrapolation method of the damping curve. A plausible explanation is that there is no excitation in the frequency range where the extrapolation gives differences in the damping curve. This will not be always the case. With higher forward velocity, or larger ships, the wave excitation will move towards the frequency where the extrapolation starts.

Because it is difficult to judge the sensitivity to the extrapolation method at the start of the calculation, it is advised to do the analysis as well as possible. Using a refined mesh allows to calculate a large part of the tail of the damping curve. This will make extrapolation less important but it will also cause the damping curves to get closer to the infinite frequency value. The extrapolation using the $\frac{a}{\omega^b}+c$ function shows better results than the linear extrapolation. This extrapolation has some theoretical justification [55]. Therefore, this function extrapolation is used for all the results presented in this thesis.

Appendix D

Aluminium model

A few technical drawings of the aluminium model used for the experiments are presented in this appendix. The masses of the additional components are shown in Figure D.1, and Figure D.2 shows the top and side view of the structural design. The cross-sections can be found in Figure D.3. The location of the accelerometers are presented in Figure D.4

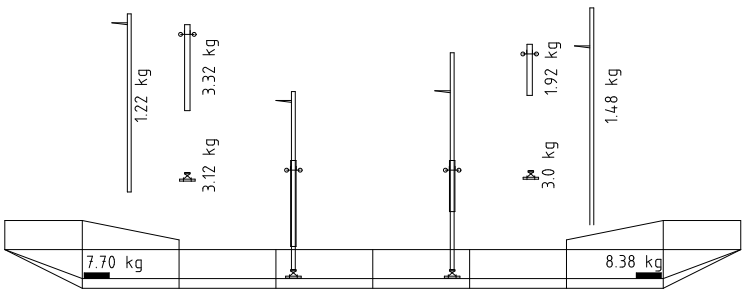

Figure D.1: Mass of additional components.

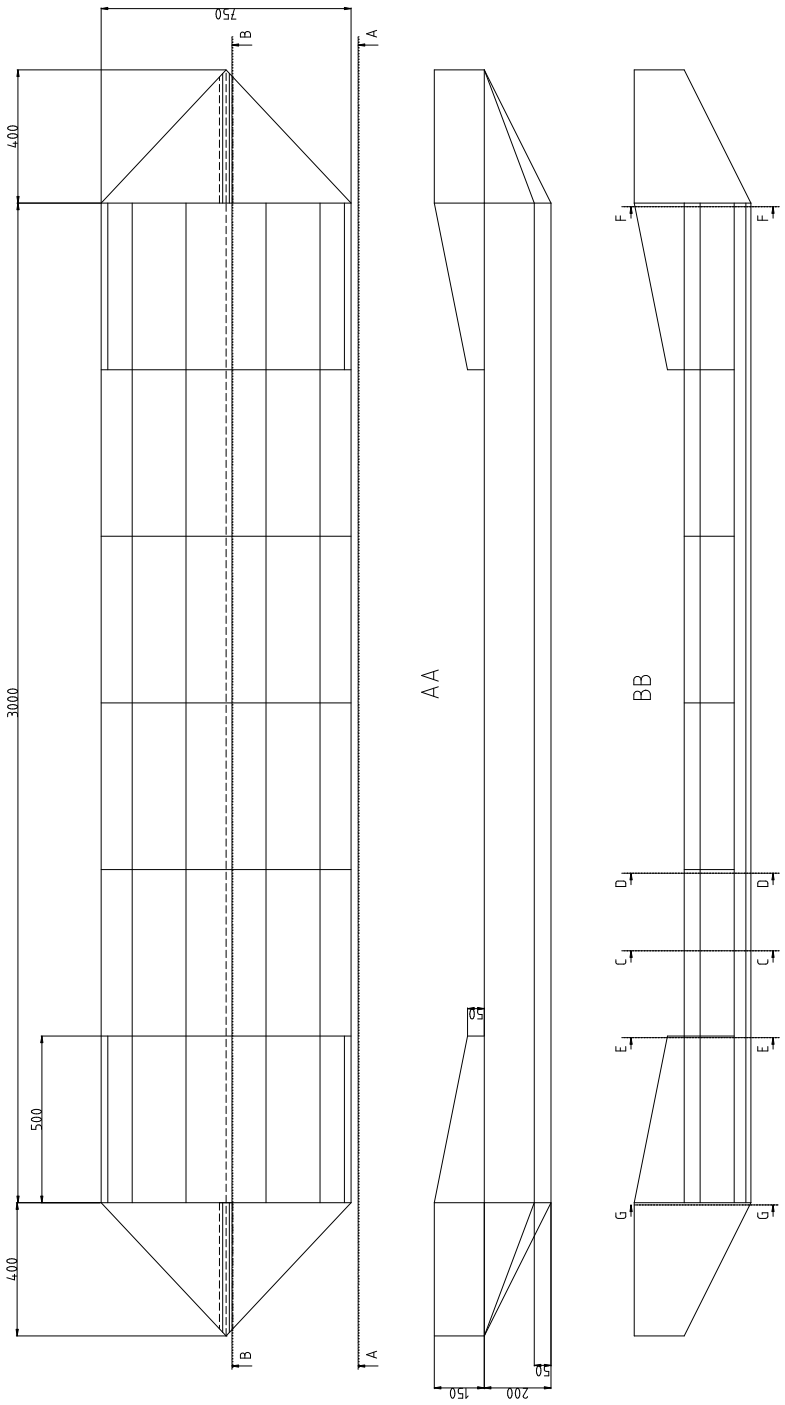

Figure D.2: Top and side view of the aluminium model.

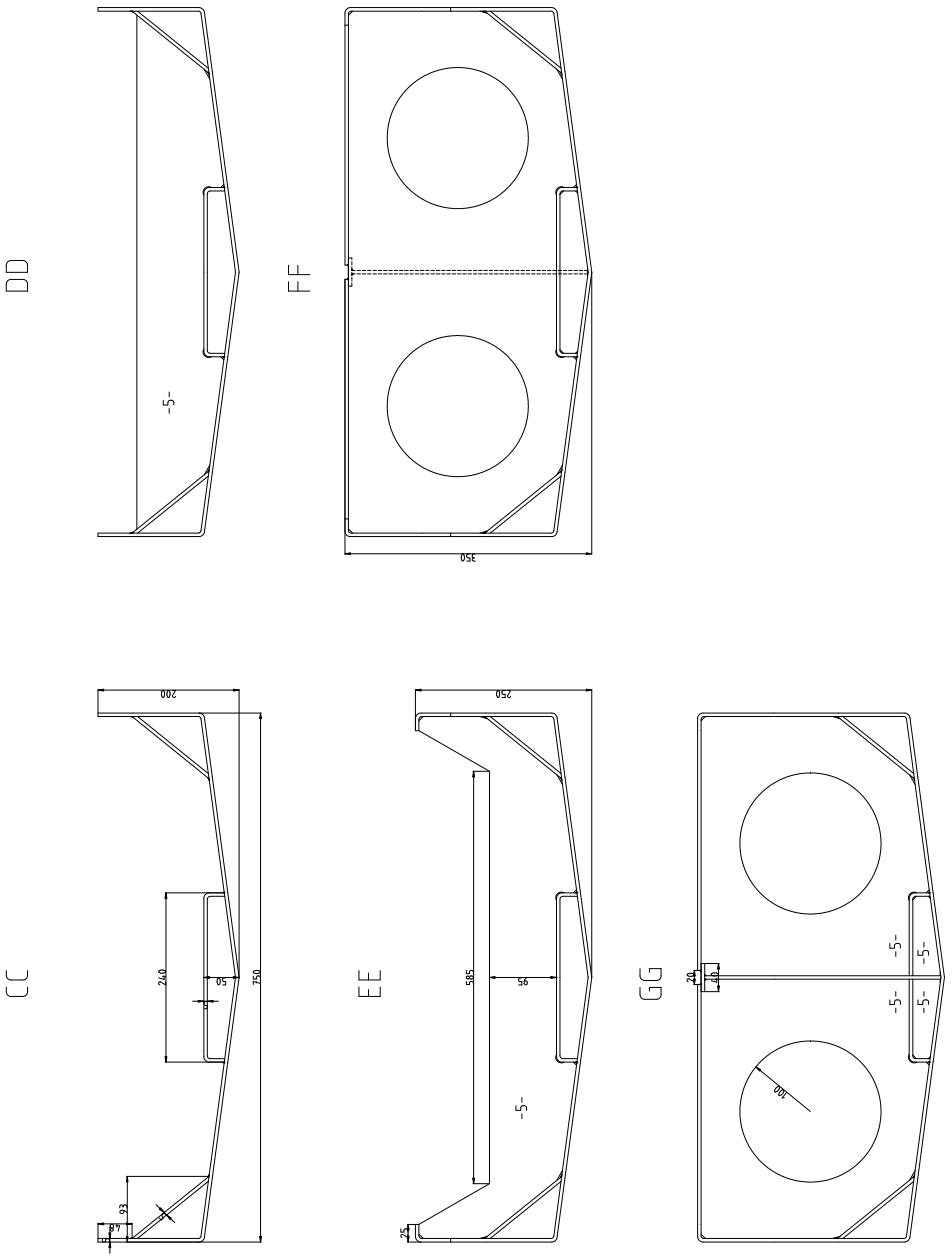

Figure D.3: Cross sections of the aluminium model.

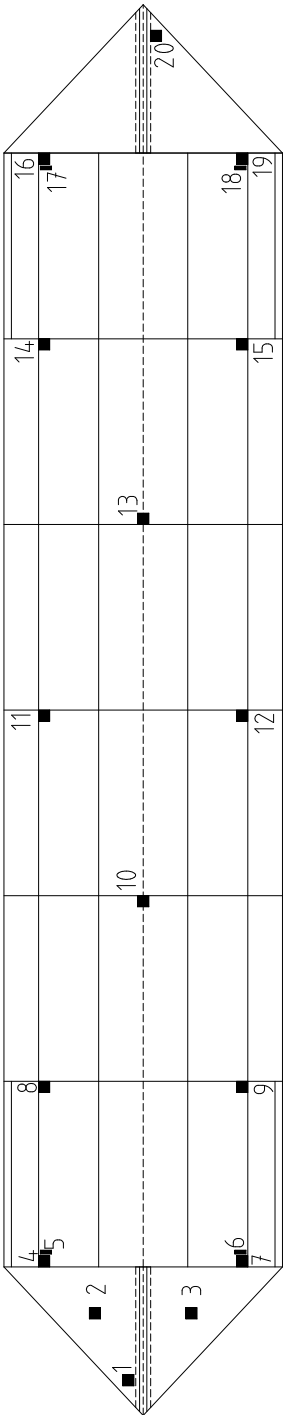

Figure D.4: Location of accelerometers.

Appendix E

The Optimal State Estimation Method

The OSE method makes an estimation of the response of the structure and the external loading at the ship using the modal equations and the measurements.

The theory of the OSE method is briefly discussed in this appendix using the discussion found in [50]. An extensive discussion can be found in [35, 11, 48, 49].

E.1 Modal equations

The standard equations of motion are used as a starting point

$$\mathbf{M}^x \ddot{\vec{x}} + \mathbf{C}^x \dot{\vec{x}} + \mathbf{K}^x x = \vec{f}^x. \tag{E.1}$$

The mass matrix should include the added mass of the fluid. The infinite, frequency independent, added mass can be used because of the high frequency of natural modes of ship structures. The undamped eigenvalue problem is solved using a 3D FE-package

$$\left(-\omega_i^2 \mathbf{M}^x + \mathbf{K}^x\right) \vec{\varphi}_i = 0. \tag{E.2}$$

The results are the eigen-frequencies ω_i and eigenmodes $\vec{\varphi}_i$. The eigenmodes are normalised with respect to the mass matrix

$$\vec{\varphi}_i^T \mathbf{M}^x \vec{\varphi}_i = 1,\ \vec{\varphi}_i^T \mathbf{K}^x \vec{\varphi}_i = \omega^2, \text{ for } i = 1, n. \tag{E.3}$$

The dynamic equation is transformed to modal coordinates using the transformation matrix $\mathbf{T}$ which contains a subset of eigenmodes

$$\mathbf{M}^p \ddot{\vec{p}} + \mathbf{C}^p \dot{\vec{p}} + \mathbf{K}^p p = \vec{f}^p, \tag{E.4}$$

with

$$\begin{aligned} \mathbf{M}^p &= \mathbf{T}^T \mathbf{M}^x \mathbf{T}, \quad \mathbf{C}_p = \mathbf{T}^T C^x \mathbf{T}, \\ \mathbf{K}^p &= \mathbf{T}^T \mathbf{K}^x \mathbf{T}, \quad \vec{f}_p = \mathbf{T}^T \vec{f}^x. \end{aligned} \tag{E.5}$$

The transformation to modal coordinates allows for a significant reduction of the number of degrees of freedom. Only the eigenmodes below a user defined cut-off frequency and with sufficient contribution to the expected response will be used.

E.2 Measurement equations

A vector with measurement signals $\vec{z}^m$ is introduced

$$\vec{z}^m = \mathbf{Z}^s \vec{p} + \mathbf{Z}^v \dot{\vec{p}} + \mathbf{Z}^a \ddot{\vec{p}} + \mathbf{Z}^u \vec{u}, \tag{E.6}$$

with $\vec{p}, \dot{\vec{p}}$ and $\ddot{\vec{p}}$ the modal displacements, velocities and accelerations according to equation (E.4). The matrices $\mathbf{Z}^s, \mathbf{Z}^v$ and $\mathbf{Z}^a$ are the participation matrices for the measured displacements, velocities and accelerations as present in $\vec{z}^m$. In fact, based on the kept eigenmodes, these matrices transform the modal quantities $\vec{p}, \dot{\vec{p}}$ and $\ddot{\vec{p}}$ to physical displacements, velocities and accelerations.

Vector $\vec{u}$ contains the measured external forces, if any. The boolean matrix $\mathbf{Z}^u$ selects which measured forces are used.

E.3 The OSE method

There will always be differences between the measurements and the mathematical model. To account for these differences, residuals are introduced for all equations. The OSE estimates the response and external loads of the model by minimizing these residuals.

Vectors $\vec{\xi}_1$ and $\vec{\xi}_2$ contain the residuals of the time derivative equations for the velocities and the accelerations, respectively. These are defined by

$$\dot{\hat{\vec{s}}} = \hat{\vec{v}} + \vec{\xi}_1, \quad \dot{\hat{\vec{v}}} = \hat{\vec{a}} + \vec{\xi}_2, \tag{E.7}$$

where $\hat{\vec{s}}, \hat{\vec{v}}$ and $\hat{\vec{a}}$ are the estimated displacements, velocities and accelerations respectively, based on the set with modal degrees of freedom.

By replacing $\vec{p}, \dot{\vec{p}}$ and $\ddot{\vec{p}}$ in the modal equation (E.4) by the estimation variables $\hat{\vec{s}}, \hat{\vec{v}}$ and $\hat{\vec{a}}$ the residual $\vec{\zeta}_1$ is introduced

$$\mathbf{M}^p \hat{\vec{a}} + \mathbf{C}^p \hat{\vec{v}} + \mathbf{K}^p \hat{\vec{s}} + \mathbf{H} \hat{\vec{u}} = \vec{\zeta}_1. \tag{E.8}$$

Vector $\hat{\vec{u}}$ contains the unknown external forces which the OSE should estimate. Matrix $\mathbf{H}$ is the participation matrix for the external forces.

The last residual $\vec{\zeta}_2$ is introduced for the measurement equation (E.6)

$$\vec{z}^m = \mathbf{Z}^s \hat{\vec{s}} + \mathbf{Z}^v \hat{\vec{v}} + \mathbf{Z}^a \hat{\vec{a}} + \mathbf{Z}^u \hat{\vec{u}} + \vec{\zeta}_2. \tag{E.9}$$

Equations (E.7) to (E.9) form the so-called identification model, which is the basis for the OSE method. Following [35], the identification model can be formulated more compactly using the augmented state estimator $\hat{\vec{x}}$ and the augmented input estimator $\hat{\vec{p}}$

$$\hat{\vec{x}} = \left(\hat{\vec{s}}^T, \hat{\vec{v}}^T\right)^T, \quad \hat{\vec{p}} = \left(\hat{\vec{u}}^T, \hat{\vec{a}}^T\right)^T. \tag{E.10}$$

Using these estimators, equations (E.7) to (E.9) can be rewritten as

$$\dot{\hat{\vec{x}}} = \mathbf{A}\hat{\vec{x}} + \mathbf{B}\hat{\vec{p}} + \vec{\xi}, \tag{E.11}$$

$$\mathbf{E}\vec{z}^m = \mathbf{F}^x \hat{\vec{x}} + \mathbf{F}^p \hat{\vec{p}} + \vec{\zeta}, \tag{E.12}$$

with

$$\begin{aligned} \mathbf{A} &= \begin{pmatrix} \mathbf{0} & \mathbf{I} \\ \mathbf{0} & \mathbf{0} \end{pmatrix}, \ \mathbf{B} = \begin{pmatrix} \mathbf{0} & \mathbf{0} \\ \mathbf{0} & \mathbf{I} \end{pmatrix}, \ \vec{\xi} = \begin{pmatrix} \vec{\xi}_1 \\ \vec{\xi}_2 \end{pmatrix} \\ \mathbf{E} &= \begin{pmatrix} \mathbf{0} \\ \mathbf{I} \end{pmatrix}, \ \mathbf{F}^x = \begin{pmatrix} \mathbf{K}^p & \mathbf{C}^p \\ \mathbf{Z}^s & \mathbf{Z}^v \end{pmatrix} \\ \mathbf{F}^p &= \begin{pmatrix} \mathbf{H} & \mathbf{M}^p \\ \mathbf{Z}^u & \mathbf{Z}^a \end{pmatrix}, \ \vec{\zeta} = \begin{pmatrix} \vec{\zeta}_1 \\ \vec{\zeta}_2 \end{pmatrix} \end{aligned} \tag{E.13}$$

For an optimal state estimation, $\hat{\vec{x}}$ and $\hat{\vec{p}}$ have to be determined such that the residuals $\vec{\xi}$ and $\vec{\zeta}$ are minimised. For the minimization of the residuals the following penalty function is introduced

$$\begin{aligned} J\left(\hat{x}, \hat{p}\right) = \frac{1}{2} \int_{t_o}^{t_e} \left(\vec{\xi}^T(t)\, \mathbf{W} \vec{\xi}(t) + \vec{\zeta}^T(t)\, \mathbf{V} \vec{\zeta}(t)\right) \mathrm{d}t \\ + \frac{1}{2} \left(\hat{\vec{x}}(t_0) - \vec{q}_0\right)^T \mathbf{R}_0 \left(\hat{\vec{x}}(t_0) - \vec{q}_0\right). \end{aligned} \tag{E.14}$$

This function is minimised using the conditions of equations E.11 and E.12. Vector $\vec{q}_0$ is the initial condition at the starting time t_0 as defined by the user. The term $\left(\hat{\vec{x}}(t_0) - \vec{q}_0\right)$ is a residual on the initial conditions at starting time t_0. The user supplies the weighting matrices $\mathbf{W}, \mathbf{V}$ and $\mathbf{R}_0$ which express the confidence in the time derivative equations, model equations, measurements and initial conditions.

The approach to minimise function (E.14) can be found in [35]. The estimated response and external forces are known after the optimisation.

E.4 Previous use of the OSE method

The OSE method has been used for estimation of the response and external loading for full scale shock trials and slamming events [50]. An example of the analysis of a full scale under-water shock trial is presented as this is a validation of the predictions by the OSE method.

Figure E.1 shows the velocity at a location of a M-Frigate of the Royal Netherlands Navy during a full scale shock trial using explosives located under water. This shock trial is analysed using the OSE method. The accelerations are measurements at the location but they are not included in the input for the OSE estimation of the response. The velocity signal is reconstructed using the estimated response based on measurements at other locations.

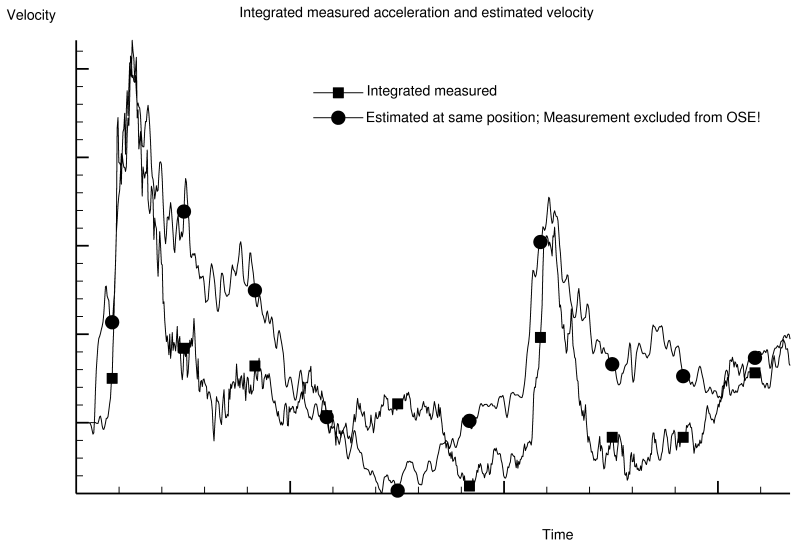

Figure E.1: OSE results for M-frigate.

The shock load excites many high-order modes which are not included in the OSE estimate. Also there will always be some differences between the structural model and the actual ship. Therefore, the estimated velocity response will differ from the measured velocity.

Figure E.1 shows that the estimated response is reasonably close to the measured response at the location. This validates that the OSE method can be used to estimate the global response of the structure.

Bibliography

[1] P.J. Aalberts and M. Nieuwenhuijs. Full scale wave and whipping induced hull girder loads. In *4th. Int. Conf. on Hydroelasticity, Wuxi, China*, 2006.

[2] Alexei Bereznitski. *Local hydroelastic response of the structures under impact loads from water (slamming).* PhD thesis, TU Delft, 2003.

[3] R.E.D. Bishop, J.D. Clarke, and W.G. Price. Comparison of full scale and predicted responses of two frigates in a severe weather trial. *Trans. RINA*, 126:153–166, 1984.

[4] R.E.D. Bishop and W.G. Price. *Hydroelasticity of ships.* Cambridge University Press, 1979.

[5] T.N. Bosman. Rekstrookmeting hr. ms. karel doorman, revisie 1. Technical report, Royal Netherlands Navy, 1992.

[6] Marine Accident Investigation Branch. Report on the investigation of the structural failure of msc napoli english channel on 18 january 2007. Technical report, 2008.

[7] Robert D. Cook. *Concepts and Applications of Finite Element Analysis.* John Wiley & sons, INC., 2001.

[8] W.E. Cummins. The impulse response function and ship motions. *Schiffstechnik*, 47:101–109, 1962.

[9] Gijsbert de Jong. Bow flare impact simulation on a 9000t dwt general cargo vessel, part a; literature study. Master's thesis, Delft University of Technology, 2001.

[10] Pepijn de Jong and Jan Alexander Keuning. 6-dof forced oscillation test for the evaluation of nonlinearities in the superposition of ship motions. *International Shipbulding Progress*, 53:123–143, 2006.

[11] R.H.B. Fey. Shock data reduction, state of the art. Technical Report 94-CMC-R0894, TNO, 1994.

[12] Thor I. Fossen and Øyvind N. Smogeli. Nonlinear time-domain strip theory formulation for low-speed manoeuvring and station-keeping. *Modeling, Identification and Control*, 25:201–221, 2004.

[13] K. Green. Hydrodynamic response of an aluminium ship. Technical Report TNO-034-DTM-2009-03131, TNO, 2009.

[14] The WAFO group. Wafo, a matlab toolbox for analysis of random waves and loads. Technical report, Lund University, 2000.

[15] J.-F. Le Guen. 3d model tests. Technical Report 981481 C, DCE/ETC5/BA/DT/F/S, Affaire E10159 Pice No. 2. Essais CRS Slamming., Bassin D'Essais des Carenes, 1999.

[16] Edward J. Haug. *Computer-Aided Kinematics and Dynamics of Mechanical Systems*, volume I: Basic Methods. Allyn and Bacon, 1989.

[17] A Hobbacher. Fatigue design of welded joints and components. Technical Report XIII-1539-96/XV-845-96, International Institute of Welding, 1996.

[18] A.M. Hubrechtse. Data report of full scale motion measurement with the m-frigate hr. ms. karel doorman. Technical Report S410943-1-SE, MARIN, 1992.

[19] M.M.H.H. Janssen. Hetime analyses of the m-frigate. Technical report, TNO, 2009.

[20] J. Juncher Jensen. Stochastic procedure for extreme wave load predictions - wave bending moment in ships. *Marine Structures*, in press, 2009.

[21] J.M.J. Journée and W.W. Massie. *Offshore Hydromechanics*. Delft University of Technology, 2001.

[22] G.K. Kapsenberg. Cfd comparison for 2d and 3d drop tests. Technical Report 19836-3-RD, MARIN, CRS, restricted acces, 2008.

[23] A.A. Korobkin and Š Malenica. Modified logvinovich model for hydrodynamic loads on asymmetric contours entering water. In *Proceedings International Workshop on Water Waves and Floating Bodies, Norway*, 2005.

[24] Edward M. Lewandowski. *The dynamics of marine craft*. World Scientific, 2004.

[25] Š Malenica. *DYANA, Theory, User's and Example Manual*. Bureau Veritas, 2003.

[26] Š Malenica. *AMG User's and Example Manual*. Bureau Veritas, 2005.

[27] Š Malenica, A.A. Korobkin, and J.T. Tuitman. *MLM_ROC Modified Logvinovich model for 2D sections constant roll angle*. Bureau Veritas, 2007.

[28] Š Malenica., B. Molin, F. Remy, and I. Senjanović. Hydroelastic response of a barge to impulsive and non impulsive wave loads. In *3rd. Int. Conf. on Hydroelasticity, Oxford, UK*, 2003.

[29] Š Malenica, B. Molin, J.T. Tuitman, F. Bigot, and I. Senjanovic. Some aspects of hydrostatic restoring for elastic bodies. In *24th IWWWFB, Saint Petersburg, Russia*, 2009.

[30] Š Malenica, E Stumpf, F.X. Sireta, and X.B. Chen. Consistent hydro-structural interface for evaluation of global structural responses in linear seakeeping. In *26th OMAE Conf., San Diego*, 2008.

[31] Š Malenica and J. T. Tuitman. 3dfem-3dbem model for springing and whipping analyses of ships. In *Int. Conf. design and operation of container ships, London, UK*, 2008.

[32] N. Mallon. Validation of the hydroelastic code hetime: Comparison with crs slam model test results. Technical Report TNO-034-DTM-2009-04586, TNO, 2009.

[33] MARIN. *PRECAL V 6.0 Theory Manual*, 2003.

[34] Martec Limited. *Vibration and Strength Analysis Program (VAST), Version 8.4*, 2003.

[35] M.J.G. Molengraft. *Identification of non-linear mechanical systems*. PhD thesis, Eindhoven University of Technology, 1990.

[36] J.N. Newman. The theory of ship motions. *Advances in Applied Mechanics*, 18:221–284, 1978.

[37] J.N. Newman. Wave effects on deformable bodies. *Applied Ocean Research*, 16:47–59, 1994.

[38] International Association of Classification Societies. Requirements concerning strength of ships, 2007.

[39] T. Francis Ogilvie. Recent progress toward the understanding and prediction of ship motions. In *Proc. 5th Symposium on Naval Hydrodynamics, Wageningen, the Netherlands,*, 1964.

[40] Panel SH-2. Technical and research bulletin 2-30, notes on ship slamming. Technical report, SNAME, 1993.

[41] L.W. Pastoor. *On the Assessment of Nonlinear Ship Motions and Loads*. PhD thesis, TU Delft, 2002.

[42] F. Remy and B. Molin. Essais GIS-Hydro sur une maquette de barge elastique. Analyse des resultats de mesure. Technical report, ESIM, 2002.

[43] T. Rippol, B. Thibault, J-P. Aulanier, and G. Facon. Reponse sur houle d'une barge elastique. Technical report, Océanide, 2002.

[44] I. Senjanović, S. Tomšević, and N. Vladimir. An advanced theory of thin-walled girders with application to ship vibrations. *Marine Structures*, pages MAST–D–08–00056R1, 2009.

[45] I. Senjanović, Š. Malenica, and S. Tomašević. Investigation of ship hydroelasticity. *Ocean Engineering*, 35:523–535, 2008.

[46] G. Skeie, J. Kvålsvold, and A. Nestegård. *Computer program CRSLAM for prediction of slamming pressure, Report No. 96-2039*. Det Norske Veritas Classification A.S., 2008.

[47] P. Temarel. Comparison of theoretical slamming impact pressures and forces with model test results. Technical Report MAR-D1-3-UOS-06(1), MARSTRUCT, restricted acces, 2008.

[48] W. Trouwborst. The optimal state estimation method applied to the slamming experiments of the tydeman. Technical Report 97-CMC-R0255, TNO, 1997.

[49] W. Trouwborst. Graphical user interface and optimal state estimation; user manual version 1.1 - dycoss part b. Technical Report 2000-CMC-R060, TNO, 2000.

[50] Wim Trouwborst and Frederick A. Costanzo. The optimal state estimation method, a tool to integrate full scale shock trial measurement data and numerical models. In *70th Shock and Vibration Symposium, 15-19 November 1999, Albuquerque NM USA*, 1999.

[51] Johan Tuitman and Hans van Aanhold. Using generalized modes for time domain seakeeping calculations. In *22nd International Workshop on Water Waves and Floating Bodies, Plitvice, Croatia*, 2007.

[52] J.T. Tuitman. Discription of experiment to verify the added mass for exible modes and slamming forces. Technical Report 2006-CMC-0159/TNJX, TNO, 2006.

[53] J.T. Tuitman and Š Malenica. Direct coupling between seakeeping and slamming calculations. *Journal of Engineering for the Maritime Environment*, submitted:JEME-S-09-00014, 2009.

[54] J.C.M. van den Broek. Hydroelastic response of a large, inflatable and partially rigid life raft. Master's thesis, TU Delft, 2009.

[55] G. van Oortmerssen. The motions of a moored ship in waves. Technical Report 510, MARIN.

[56] Riaan van `t Veer and Ed van Daalen. Pretti v1.3 theory manual. Technical report, CRS, 2006.

[57] Det Norske Veritas. Classification notes no. 30.7, 2003.

[58] Th. von Karman. The impact on seaplane floats during landing. Technical report, NACA TN 321, 1929.

[59] H. Wagner. Über Stoß- und Gleitvorgänge an der Oberfläche von Flüssigkeiten. *Z. Angew. Math. Mech.*, 12(4):192–235, 1932.

[60] Wikipedia. Gaussian quadrature — wikipedia, the free encyclopedia, 2009. [Online; accessed 25-May-2009].

[61] Wikipedia-bijdragers. Karel doormanklasse — wikipedia, de vrije encyclopedie, 2009. [Online; accessed 8-juni-2009].

[62] R. Zhao and O. Faltinsen. Water entry of two-dimensional bodies. *Journal of Fluid Mechanics*, 246:593–612, 1993.

[63] R. Zhao and J. Aarsnes O. Faltinsen. Water entry of arbitrary two-dimensional sections with and without flow separation. In *Twenty-First Symposium on Naval Hydrodynamics, Trondheim, Norway*, 1997.

Curriculum Vitae

The author was born in 1980 in Rotterdam. He finished his secondary education at the VWO level in 1999. Thereafter he started his academic education at the Delft University of Technology in September 1999. In 2004 he obtained his M.Sc. degree in Maritime Technology, graduating cum laude. The research for his master thesis was carried out in cooperation with the Royal Netherlands Navy. "Smeared stiffeners and re-loading for underwater shock calculations" was the title of his master thesis. Starting from October 2004 until July 2009 he worked on his Ph.D. project at the Netherlands Organisation for Applied Scientific Research (TNO) at the Center for Mechanical and Maritime Structures (CMC). This Ph.D. project has been carried out in cooperation with the Delft University of Technology and has resulted in this thesis. Since September 2009 the author has been working for TNO in the CMC group.

Acknowledgments

This thesis has been made possible by Delft University of Technology (TUD), Netherlands Organisation for Applied Scientific Research (TNO) and the Netherlands Ministry of Defence. I am grateful to these organisations for allowing me to conduct this research.

My Ph.D. research started with promotor Prof. Pinkster and copromotor Guus Hommel. Both retired during this research and Prof. Huijsmans and Theo Bosman were appointed as promotor and co-promotor, respectively. I would like to thank both Prof. Pinkster and Prof. Huijsmans for all the support and help they have provided and for allowing me to conduct this research. I am thankful to Guus Hommel for his support. Theo was the supervisor for my master graduation project and supported me with my Ph.D. research. He provided a lot of help, support and we had many good discussions. I am very grateful to him.

I would like to thank all members of the Ph.D. commission for willing to be in my commission and for their helpful comments on the draft version of this thesis.

This research was done at TNO. I have really enjoyed working together with my TNO colleagues. I received a lot of support from all colleagues within the CMC group. Hans and Theo have been my TNO supervisors for this research. Sander and Pieter have allowed me, as department managers of CMC, to do this research. Special thanks to Ingrid, Kirk, Lex, Niels, Sander and Wim for helping me with many technical problems. Both Kirk and Niels did review the draft version of my thesis very accurately which helped me to improve my thesis significantly. Jasper, Kirk, Mirre and Niels have not only done a part of the validation work presented in this thesis but with their testing, some bugs have been resolved and the programs are now more robust.

I would also like to thank Co Vink of the TUD for the great lectures on ship structures and all the support during both my master study and this Ph.D. research. I enjoyed the cooperation with Jan van Kessel, especially the "hydroelastic"-dinners and our mini-symposium. Piet de Heer supported me with all the administration matters. I would also like to thank all students who started in 1999 at the Marine Technology course of the TUD for a very nice time as student of the TUD.

Both TUD and TNO have given me the opportunity to conduct the model experiments as described in Chapter 10. I am grateful to Cees, Charles and Sebastian of TNO and Frits, Henk, Lex and Peter of the TUD for their help during the preparations and the execution of this experimental investigation.

I have done my master graduation project at the RNlN. The people of the department Bureau Militaire Maritieme Technologie did not only helped me during my master graduation project, they have also helped me during this Ph.D. research. The provided data of the measurements during the sea trail of the M-frigate provided me an excellent validation case. The RNlN provided the photograph at the cover of this thesis.

The Cooperative Ship Research group (CRS) allowed me to do a lot of research. I enjoyed all good discussions during the meetings. I would like to thank all persons participating in the CRS meetings. Especially all help and discussions with Ed, Geert, Riaan and Šime really helped me a lot during this research.

I would also like to thank Fabien, François-Xavier, Šime, Quentin and Xiao-Bo of the research department of Bureau Veritas for the very good cooperation. I am very grateful to Šime for all discussions, support and for our publications.

The OSE method software was developed by Rob Fey, currently working at the Eindhoven University of Technology, Department of Mechanical Engineering. I like to thank Rob for his support in utilizing the OSE method.

The model test with the flexible barge, discussed in Chapter 9, were carried out in BGO-First within the GIS-Hydro cooperation, with financial support of Conseil General du Var. The results of the measurements where kindly provided by F. Remy of EC Marseille.

Open source software like GNU/LINUX, GNUPLOT, VIM, PYTHON, LATEX, GFORTRAN, PARAVIEW, etc. have been extensively used during the research for this thesis. I am grateful to all developers of open source software around the World.

Every Saturday I enjoy being at the sea scout groep “Jacob Valcke”. I like to thank the other scout leaders and scouts for the pleasant Saturdays and camps.

Finally, I am very grateful to my mother and sister for their unconditional support.

Index